

RL-TR-95-47, Vol I (of two)  
In-House Report  
February 1995



# PROCEEDINGS OF THE 1994 ANTENNA APPLICATIONS SYMPOSIUM

Daniel H. Schaubert, et al



*APPROVED FOR PUBLIC RELEASE; DISTRIBUTION UNLIMITED.*

19950406 033

Rome Laboratory  
Air Force Materiel Command  
Griffiss Air Force Base, New York

DTIC SELECTED 5

This report has been reviewed by the Rome Laboratory Public Affairs Office (PA) and is releasable to the National Technical Information Service (NTIS). At NTIS it will be releasable to the general public, including foreign nations.

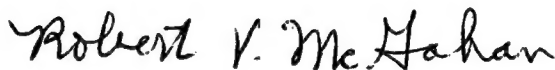
RL-TR-95-47, Vol I (of two) has been reviewed and is approved for publication.

APPROVED:



DANIEL J. JACAVANCO, Chief  
Antennas & Components Division  
Electromagnetics & Reliability Directorate

FOR THE COMMANDER:



ROBERT V. MCGAHAN  
Acting Director  
Electromagnetics & Reliability Directorate

If your address has changed or if you wish to be removed from the Rome Laboratory mailing list, or if the addressee is no longer employed by your organization, please notify RL (ERAA ) Hanscom AFB MA 01731. This will assist us in maintaining a current mailing list.

Do not return copies of this report unless contractual obligations or notices on a specific document require that it be returned.

# REPORT DOCUMENTATION PAGE

Form Approved  
OMB No. 0704-0188

Public reporting burden for this collection of information is estimated to average 1 hour per response, including the time for reviewing instructions, searching existing data sources, gathering and maintaining the data needed, and completing and reviewing the collection of information. Send comments regarding this burden estimate or any other aspect of this collection of information, including suggestions for reducing this burden, to Washington Headquarters Services, Directorate for Information Operations and Reports, 1215 Jefferson Davis Highway, Suite 1204, Arlington, VA 22202-4302, and to the Office of Management and Budget, Paperwork Reduction Project (0704-0188), Washington, DC 20503.

|  |   |  |                                   |  |  |
|--|---|--|-----------------------------------|--|--|
| 1. AGENCY USE ONLY (Leave Blank)   |   | 2. REPORT DATE<br>February 1995                            |                                   | 3. REPORT TYPE AND DATES COVERED<br>In-House                               |  |
| 4. TITLE AND SUBTITLE<br>PROCEEDINGS OF THE 1994 ANTENNA APPLICATIONS SYMPOSIUM  |   |  |                                   | 5. FUNDING NUMBERS<br>PE - 62702F<br>PR - 4600<br>TA - 14<br>WU - PW       |  |
| 6. AUTHOR(S)<br>Daniel H. Schaubert, et al   |   |  |                                   |  |  |
| 7. PERFORMING ORGANIZATION NAME(S) AND ADDRESS(ES)<br>Rome Laboratory (ERAA)<br>31 Grenier Street<br>Hanscom AFB MA 01731-3010   |   |  |                                   | 8. PERFORMING ORGANIZATION<br>REPORT NUMBER<br>RL-TR-95-47, Vol I (of two) |  |
| 9. SPONSORING/MONITORING AGENCY NAME(S) AND ADDRESS(ES)<br>Rome Laboratory (ERAA)<br>31 Grenier Street<br>Hanscom AFB MA 01731-3010  |   |  |                                   | 10. SPONSORING/MONITORING<br>AGENCY REPORT NUMBER                          |  |
| 11. SUPPLEMENTARY NOTES Rome Laboratory Project Engineer: Zachary O. White/ERAA (617) 478-3191. Volume I consists of pages 1 through 258. Volume II consists of pages 259 through 500.   |   |  |                                   |  |  |
| 12a. DISTRIBUTION/AVAILABILITY STATEMENT<br>Approved for public release; distribution unlimited.   |   |  |                                   | 12b. DISTRIBUTION CODE   |  |
| 13. ABSTRACT (Maximum 200 words)<br>The Proceedings of the 1994 Antenna Applications Symposium is a collection of state-of-the-art papers relating to phased array antennas, multibeam antennas, satellite antennas, microstrip antennas, reflector antennas, HF, VHF, UHF and various other antennas. |   |  |                                   |  |  |
| 14. SUBJECT TERMS Antennas, Satellite Antennas, Broadband Antennas, Microstrip, Reflector, HF, VHF, UHF, Multibeam Antennas, Array Antennas  |   |  |                                   | 15. NUMBER OF PAGES<br>264   |  |
|  |   |  |                                   | 16. PRICE CODE   |  |
| 17. SECURITY CLASSIFICATION<br>OF REPORT<br>UNCLASSIFIED   | 18. SECURITY CLASSIFICATION<br>OF THIS PAGE<br>UNCLASSIFIED | 19. SECURITY CLASSIFICATION<br>OF ABSTRACT<br>UNCLASSIFIED | 20. LIMITATION OF ABSTRACT<br>SAR |  |  |

# CONTENTS

## I. Special Session Honoring Paul E. Mayes

- \* Antenna Laboratory - A Brief History by T.N. Trick
- \* Antennas, Antenna Laboratory, Allerton Antenna Symposium, and Paul E. Mayes by P.W. Klock
- Analysis and Applications of Log-Periodic Monopole Arrays by P.G. Ingerson, S.C. Kuo and P.E. Mayes 1
- Polarization Extraction of Circularly Polarized Antennas by F. Colomb, J. Gentle, P. Klock, P. Mayes and J. Swanstrom 26
- Measurement of Phased Array Performance at Arbitrary Scan Angles by D.H. Schaubert, W.C. Chang and G.J. Wunsch 43
- Use of Admittance-Wall Models in the Analysis of Annular Sector Radiating line Antennas by D.J. Tammen and P.E. Mayes 71

## II. Lenses and Arrays

- Application of Polarizing Lens to a Multimode Flatplate Array Antenna by D. Collier, M. Greenspan, D. MacFadyen and L. Orwig 101
- A W-Band Active Phased Array Antenna by B.J. Edward, R.S. Webb and S. Weinreb 119
- Guided Wave Antenna Induced by Light by V.A. Manasson, L.S. Sadovnik, P.I. Shnitser and V.I. Litvinov 144
- Design and Development of Wideband Circular Array Interferometers by P. Eyring and R. Clap 158
- A Multifunction, Multiple Frequency Aperture by J. Yon, L. Parrish, T. Waterman, G. Evans and P. Hrycak 193
- Wideband Phased Array for Ionospheric Research Applications by L. Susman, P. Elliot, V. Volman, S. Carson P. Koert and J. Cha 216

- \* Not included in this volume



### **III. Analysis and Measurements**

|   |            |
|---|------------|
| <b>Infinite Microstrip Patch Array on a Biased Ferrite Substrate by F. Harakiewicz and P. Rainville</b>                                 | <b>244</b> |
| <b>A Finite Element Code for Phased Array Radiator Analysis by D.T. McGrath</b>   | <b>259</b> |
| <b>Efficient Modeling of Microstrip Antennas Using the Finite Difference Time Domain Method by S. Chebolu, J. Svigelj and R. Mittra</b> | <b>286</b> |
| <b>Pulsed Antenna Measurements with the HP8530A Microwave Receiver by J. Swanstrom and R. Shoulders</b>                                 | <b>308</b> |
| <b>Resonances in Large Circular Arrays: An Experimental Study by G. Fikioris</b>  | <b>314</b> |

### **IV. Arrays and Feeds**

|  |            |
|--|------------|
| <b>Array Failure Correction with a Digitally Beamformed Array by R. Mailloux</b>   | <b>333</b> |
| <b>A Digitally Focused X-Band Imaging Array by S. Frasier, J.B. Mead and R.E. McIntosh</b>   | <b>360</b> |
| <b>Phased Array Antennas with Neural Network Signal Processing by H. Southhall, J. Simmers and T. O'Donnell</b>                        | <b>374</b> |
| <b>A Microstrip Array Fed by a New Type of Multilayer Feeding Network by N. Herscovici and J. Klugman</b>                              | <b>382</b> |
| <b>Multi-Beam Feed for Phased Array Antenna by H. Shnitkin</b>   | <b>394</b> |
| <b>An Adaptive Matching Circuit for Phased-Array Radars by C. Lyons, W. Grammer, P. Katzin and M. Shifrin</b>                          | <b>406</b> |
| <b>An Active Monolithic Programmable Directional Coupler for Phased-Array Radars by W. Grammer, M. Shifrin, C. Lyons and P. Katzin</b> | <b>432</b> |

## V. ELEMENTS

|  |     |
|--|-----|
| From DC (0 Hz) to Daylight ( $10^{14}$ Hz); Devices, Uses and Similarities by G. Monser                | 446 |
| The Electronically Tuned HELIX by G. Ploussios   | 456 |
| Hemispherical Coverage Using a Loaded Monopole by E. Altshuler   | 477 |
| Experimental Study on Stacked Ring Coupled Triangular Microstrip Antenna by A. Naik and P.S. Bhatnagar | 497 |

|                      |  |
|----------------------|--|
| Accession For        |  |
| NTIS CRA&I           | <input checked="checked" type="checkbox"/> |
| DTIC TAB             | <input type="checkbox"/>                   |
| Unannounced          | <input type="checkbox"/>                   |
| Justification _____  |  |
| By _____             |  |
| Distribution / _____ |  |
| Availability Codes   |  |
| Dist                 | Avail and/or Special                       |
| A-1                  |  |

# ANALYSIS AND APPLICATIONS OF LOG-PERIODIC MONOPOLE ARRAYS

Dr. P. G. Ingerson<sup>1</sup> , S. C. Kuo<sup>2</sup> , and Dr. P. E. Mayes<sup>3</sup>

## Introduction and History

The publication of "Analysis and Design of the Log-Periodic Dipole Antenna," by R. L. Carrel [1] in 1961 was a milestone in modern antenna development. His report enhanced the understanding and greatly simplified the design of this type of frequency-independent antenna. After more than thirty years, his report is still being widely used as a "cookbook" for the design of the LPDA.

His analysis of the structure shown in Figure 1 showed that energy is radiated or received almost exclusively from a region of cells containing near resonant length dipoles, called the active region. This region then moves along the structure as a function of frequency. Signals are inputted or alternately received at the "feed tip" where the dipoles in the cells are well below resonance. The cascade of these cells form a transmission line region, and because they are well below resonance have little or no effect on the radiation pattern.

---

<sup>1</sup> TRW Inc., Electronics Systems & Technology Division, Redondo Beach, CA

<sup>2</sup> California Electromagnetics, Mountain View, CA

<sup>3</sup> University of Illinois, Urbana, IL

Log-periodic dipole arrays normally rely on a feed line or its equivalent at alternate elements to achieve the required active region phasing, allowing efficient radiation or collection of incident energy. When the active region includes several cells it moves smoothly along the structure, providing "frequency independent" behavior in pattern and input impedance which is characteristic of log-periodic dipole arrays.

One fundamental problem of log-periodic dipole arrays is that they lack symmetry and cannot be implemented in a monopole version. This is because the phase reversal of the excitation currents on the adjacent dipoles is provided by the transposition of the balanced transmission line, which simply cannot be realized on an unbalanced antenna.

The search for an equivalent log-periodic monopole antenna (LPMA) received a great deal of attention in the early 60's because the Navy was looking for a broadband vertically polarized antenna for their communication and direction finding systems. A vertical polarized LPDA is over 100 feet higher than an LPMA at 2 MHz. In addition, when a vertical LPDA is placed over ground in the self scaling manner, it has a periodic gain drop-out anomaly.

At about this time Dr. J. Greiser at the University of Illinois took a different approach in order to solve the monopole problem [2]. He invented two LPMAs which are different from the LPDA structure.

The LPDA has a well defined transmission line which is loaded with logarithmically scaled radiators. Dr. Greiser's antennas, the bent zigzag and the folded log-periodic antennas, are shown in Figures 2-a and b. In Greiser's antennas both radiation and phasing occur in the same elements.

Another known LPMA of the same time frame designed by F. R. Ore [3], shown in Figure 3, is also not a loaded line in the same sense as the LPDA. What these antennas' structure taught us was that the phase reversal of the excitation currents on the adjacent radiators on the LPMA could be accomplished either by a delay line or through capacitive coupling. In general, the design parameters of the delay line structures are not very critical, while the design parameters of the capacitive coupled structures are very critical.

Professor K. Mei at the University of California, Berkeley was among the first to try the delay line approach on a periodic loaded structure (shown in Figure 4). Using near-field probing, the phase progressions were measured on an LPDA, the additional phase delay was introduced to the LPMA structure using coaxial cable or stripline. After swept frequency test equipment was introduced, this structure was discovered to have an anomaly of periodic gain dropouts which were associated with corresponding high VSWR points.

This problem was later shown by Ingerson and Mayes [4] to be associated with the structural stopband in periodic structures when the phasing between loading elements is near  $1/2\lambda$  or multiples of  $1/2\lambda$  and which could easily be overcome by changing or modulating the feed line impedance. Green and Mayes [5] later used a microstrip line with modulated impedance to feed a log-periodic monopole array.

In 1965, N. Barbano's log-periodic dipole array with parasitic elements (LPPDA) [6,7], shown in Figure 5 was introduced. The active (or driven) and parasitic dipoles are arrayed alternated on this antenna. This antenna is excited using a conventional two-parallel wire balanced transmission line. The phase reversal of the excitation currents of the adjacent dipoles is accomplished by the presence of the parasitic dipoles. Thus one-half of this antenna can be placed over the ground plane and operate as a log-periodic monopole antenna. This antenna, the Log-Periodic Parasitic Monopole Antenna (LPPMA), can be fabricated either in the freestanding form or etched on PC boards. When this antenna is etched on PC boards, the active or the driven dipoles and the transmission line are etched on one side of the PC board and the parasitic dipoles on the other side. Thus the spacing between the transmission line and the parasitic dipoles is constant due to the constant thickness of the PC board. For this reason, Mr. Barbano believed that the successful operation of this antenna is due to the mutual coupling between the driven or the active dipoles and the

parasitic dipoles. It has been shown by the authors that the most important component is the capacitive coupling between the transmission line and the parasitic dipoles, as will be described in this paper.

The LPPMA has a strong advantage over the delay line implementations of monopole arrays. The disadvantage of the delay line LPMA is that it requires a larger ground plane (or volume) to accommodate the delay lines. Although the delay line can be meandered to reduce the size of the ground plane, this will limit the useful high frequency because fabrication is difficult. In addition, unless care is taken the delay line will radiate and increase the cross-polarization level.

The LPPMA by contrast can be simply photoetched on a PC board. When designed properly, this antenna will operate over a very large bandwidth. The low and high frequency cutoffs are determined by the dimension of the largest radiator and the detail of the feed point as well as the fabrication accuracy respectively. The PC board model has a smaller useful bandwidth due to the constant thickness of the conventional PC board. The freestanding models have been demonstrated with at least several times the useful bandwidth of the PC board model which is limited to about 5 or 6:1. At microwave frequencies, the freestanding models are fabricated from sheet metal.

The thickness of the material somewhat limits the bandwidth of the freestanding model. Figure 6 shows the measured VSWR of a freestanding LPPMA fabricated from 0.020" beryllium copper sheet stock. It can be seen that the VSWR is nominally under 1.5:1 at lower frequencies and starts to deteriorate at frequencies above 15 GHz.

After the introduction of the antenna, Mr. Barbano first tried to market the dipole version of this antenna for TV application. It failed because it does not have the forgiveness of the LPDA. Since this is a capacitive coupling antenna, the dimensions have to be very precise. Therefore it is more difficult to fabricate and is not tolerant of bending and distortions of the elements. In practice, a slightly bent dipole, whether driven or parasitic, will render the antenna useless near the resonant frequency of the bent dipole. In addition, this antenna usually requires a higher number of dipoles (higher scaling factor  $\tau$ ) compared to an LPDA or LPMA with delay line.

### Applications

In addition to allowing a monopole implementation for ground plane applications, LPPMAs can be used to implement multiarm feeds obtained by placing elements circumferentially around a rod, a pyramidal, or conical base cone.



Figures 7 and 8 show three and four arm configurations. The three arm configuration has been used for its ability to be packed in a hexagonal array. The four arm version could be implemented in two cross LPDAs, but the four arm LPPMAs have superior cross polarization properties at higher frequencies.

Figure 9 shows a multiarm LPPMA where the monopoles are built around a cone. These multiarm feeds can then provide tracking and angle of arrival information by exciting the arms with prescribed phase progress given by

$$V_{n,m} = A_m \exp(j 360 m n/N) \quad (1)$$

where

$n = 1, 2, \dots N$  is the arm number;

$m = +1, +2, \dots$  is the mode number; and

$A_m$  is the amplitude of the excitation of mode  $m$

The sum mode patterns are obtained for  $m = \pm 1$  and the first difference mode for  $m = \pm 2$ .

### Analysis Model

Although the development of the log-periodic monopole array with parasitic elements (LPPMA) has been empirical, the importance of coupling between the feedline and the parasitic elements has recently been demonstrated by analysis using an approximate model. In formulating the model it is postulated that the parasitic elements are

excited not only by fields due to radiation from other elements, as in Yagi-Uda arrays, for example, but also by electromagnetic coupling to the feedline, even though no conducting connections between parasitic elements and the feeder exist. So the excitation of the parasitic elements of a LPPMA differs from that of conventional parasitics, but because of the lack of conducting connections, the term “parasitic” will continue to be used to distinguish them from the driven elements.

The analysis technique is an extension of the method used by Carrel to analyze log-periodic dipole (LPD) arrays. The first step is to use image theory to convert the LPPMA to an LPD with parasitic elements (LPPDA), an array of dipoles excited by a balanced twin-fin feeder. Following Carrel, approximate field techniques are used to compute the elements of the impedance matrix,  $Z_A$  for the dipoles. All of the dipoles are driven at one extremity in the LPD, but for the LPPDA, the coupling of a parasitic element to the feeder takes place mostly in the region where the planar dipole overlays the planar feedline, forming thereby a parallel-plate capacitor. The midpoint of this region is chosen as a terminal for the parasitic element. The driven elements and the portions of the parasitic elements beyond the feedline are analyzed by a procedure very much like Carrel used to solve the “exterior problem” to find the impedance matrix for the dipoles of the LPD.

The feeder of an LPD is a uniform transmission line with conductors that are transposed between the dipoles of each adjacent pair. Terminal pairs of log-periodic spacing along the feeder provide connection points between the network representing the feeder (interior problem) and the dipoles (exterior problem). The feeder network is most easily represented by an admittance matrix,  $Y_F$ . However, in the case of the LPPDA, the feeder conductors are not transposed, and elements are added to the network representing the feedline (a) to account for the coupling between the feedline and the parasitic elements, and (b) to model the portions of the parasitic elements between the conductors of the balanced version of the feedline.

Figure 10 shows the division of an LPPDA into exterior and interior problems. A uniform line is used to represent the triangular fin conductors of the balanced feeder. The capacitances,  $C_P$ , are connected between the transmission line and the terminals of the parasitic elements. These network elements are introduced as approximate models for the proximity coupling between the feeder and the parasitics. The sections of the parasitic elements between the feeder conductors, not having been included in the exterior problem, are taken into account by connecting inductances,  $L_P$ , between the "terminals" on the parasitics.

The main component of the feeder for the planar LPPDA arrays is a coplanar, triangular-fin transmission line with small included angle of the fin and small angle of separation between the fins. Formulas for the characteristic impedance of triangular fin lines were derived by Carrel [8]. The outline drawing of Figure 11 shows the notation introduced by Carrel to describe the geometric parameters of the symmetrical, coplanar, triangular-fin line.  $\psi$  is the half angle of each fin and  $\theta_0$  is the angle between the fin axes.

Carrel shows that the characteristic impedance is given by

$$Z_0 = \eta \frac{K}{K'}$$

where  $\eta$  is the characteristic impedance of the surrounding space,  $K$  and  $K'$  are complete elliptic integrals of the first kind of moduli  $k$  and  $k'$ , respectively. The complete elliptic integral of the first kind is given by

$$K(k) = \int_0^1 \frac{dt}{\sqrt{(1-t^2)(1-k^2t^2)}} \quad (2)$$

The moduli  $k$  and  $k'$  are connected by the equation:

$$k^2 + k'^2 = 1 \quad (3)$$

and  $k$  is related to the parameters of the line by

$$k = \frac{\sin \frac{\theta_0}{2} - \sin \psi}{\sin \frac{\theta_0}{2} + \sin \psi} \quad (4)$$

For small angles,  $\psi$  and  $\theta_0$ , the values of  $k$  are less than  $\frac{1}{\sqrt{2}}$ , in which region the ratio  $K/K'$  is approximately given by

$$\frac{K(k)}{K'(k')} = \frac{\frac{\pi}{2}}{\ln \left\{ 2 \sqrt{\frac{1+k'}{1-k'}} \right\}} \quad (5)$$

The fin parameters of one of the printed antennas are  $\theta_0 = 3^\circ$ ,  $\psi = .85^\circ$ . For this case the above formula gives

$$Z_0 = 240 \text{ ohms} \quad (6)$$

This value would apply were the feeder in free space.

At the outset the capacitances in the feeder network of Figure 10 have been estimated using the parallel plate formula with the given dimensions of the overlap region between each monopole and the feeder. Note that the scaling of dimensions from element to element in a log-periodic fashion means that the area of the capacitor at the second longest parasitic element (element four) will be  $\tau^2$  times the area of the capacitor at the longest parasitic (element two).

The inductance values for the network have been estimated using the formula for the inductance per meter of a circular cylinder conductor of

radius  $a$  and the conventional equivalence between strip width,  $w$ , and cylinder radius,  $a$ ,  $w = 4a$ .

$$L_p = \frac{\mu b_p}{2\pi} \ln \left\{ \frac{2\lambda}{\pi w_p} \right\} \quad (7)$$

### Examples

The lumped circuit coupling model has been incorporated into an analysis program. Since the length of the parasitic elements is in general not related by the square root of the scale factor of the driven elements, we have chosen to define the scale factor  $\tau_A$  as the ratio between successive drive elements or parasitic elements.  $\sigma$  is also defined in terms of the length of the driven elements and the separation, as with the LPDA.

Four examples will be shown. Figure 12 shows the VSWR of a conventional 24 element LPDA with  $\tau = .948$ ,  $\sigma = .05$  (corresponding to the LPPDA of the next example) with a mean input impedance of 100 ohms. Figure 13 shows the VSWR of the same feed if the dipoles are not alternately transposed to provide the proper active region phasing. The VSWR is shown only over two log cycles.

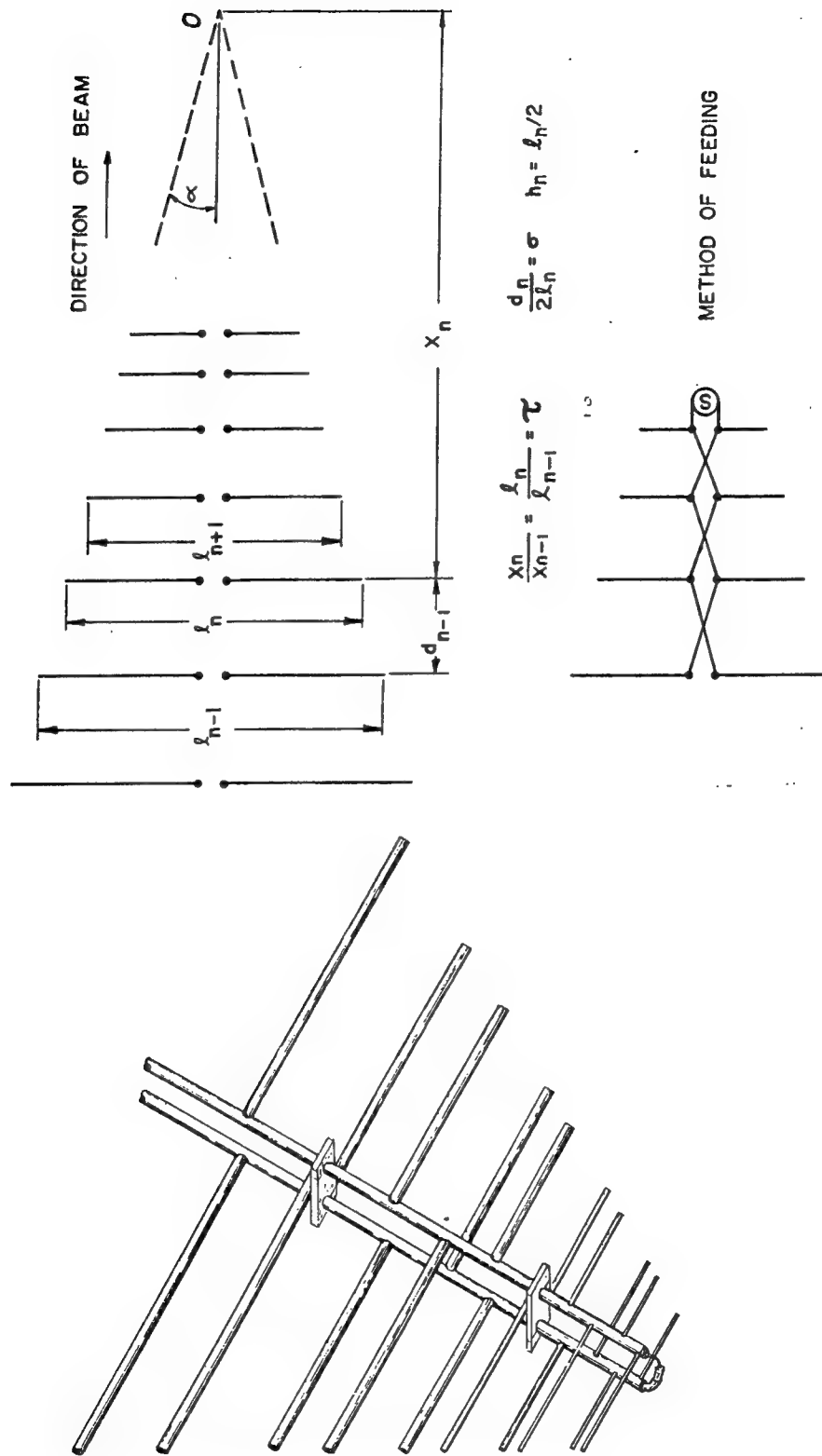
Figure 14 shows the corresponding LPPDA ( $\tau = .9$ ,  $\sigma = .1$  between driven elements) with values approximately corresponding to the current

design. Figure 15 shows the same antenna with the parasitic element to transmission line coupling set to zero. With the coupling set to zero and the length of the parasitic elements varied, it has been found that the lowest VSWR is about 6:1. With the current feed parameters the VSWR is not as good as the conventional LPDA, but shows that acceptable values well below 1.5:1 are possible.

### **Conclusion**

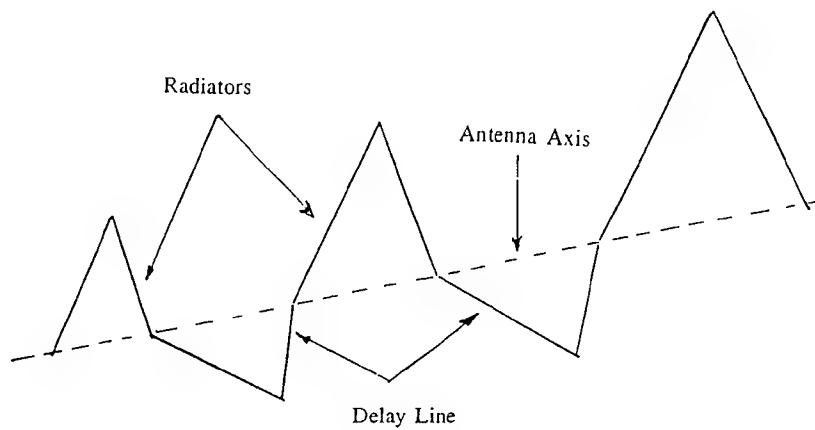
The LPPMA antenna has been demonstrated in a variety of multi-arm antennas with bandwidth up to 20:1. The current designs have been empirically determined because there was no analysis model to guide the optimization of the antenna design parameters. The analytical model described in this paper appears to be able to predict the important aspects of the antenna and should allow the designs to be optimized and modified for particular applications.

Figure 1. A log-periodic dipole antenna

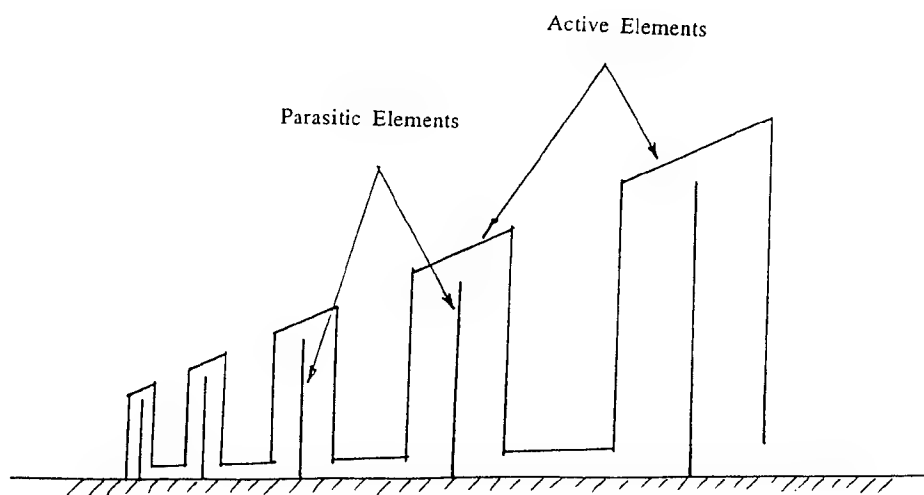


A schematic of the log-periodic dipole antenna, including symbols used in its description

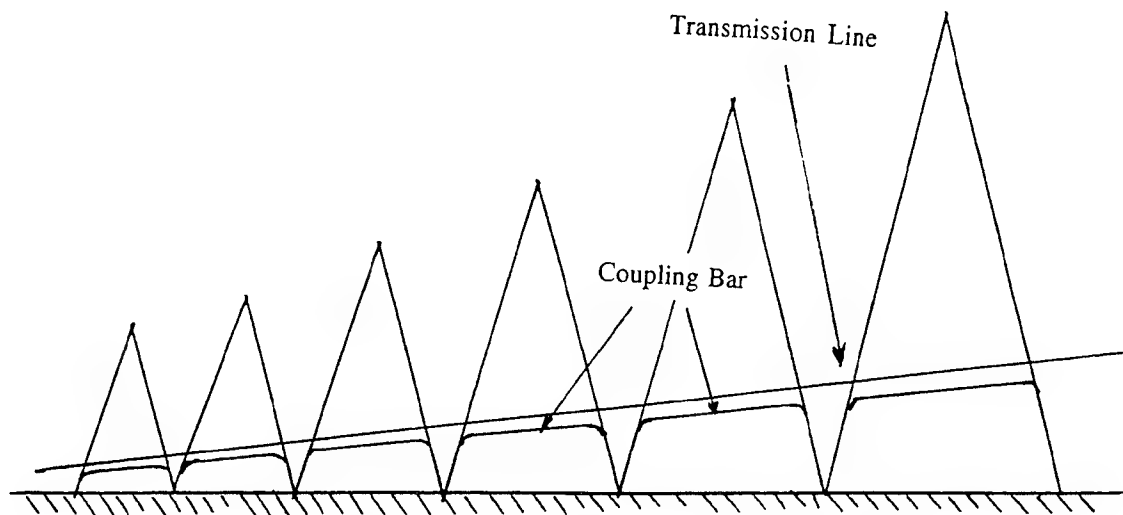




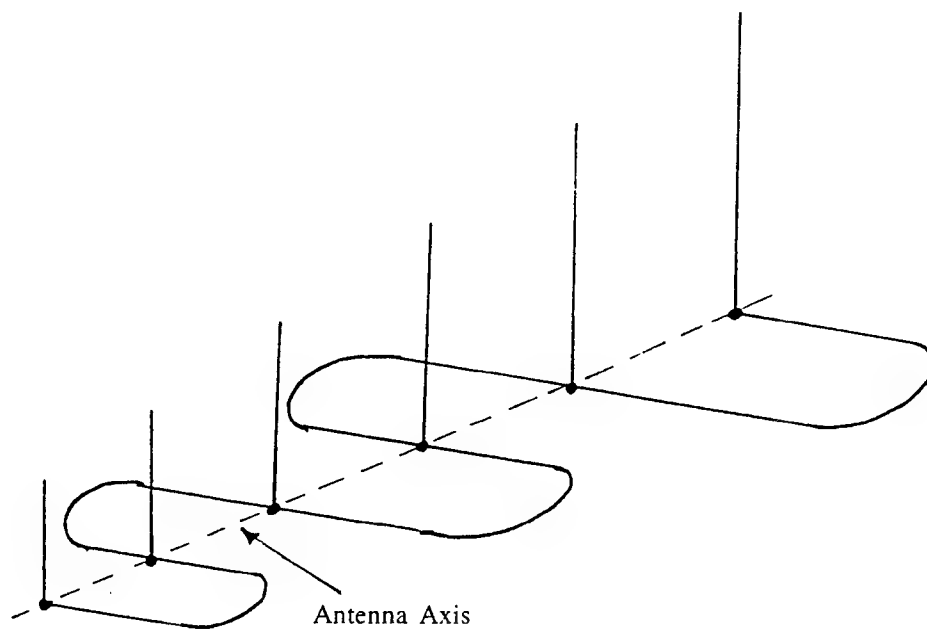
**Figure 2a. Log-periodic bent zigzag antenna**



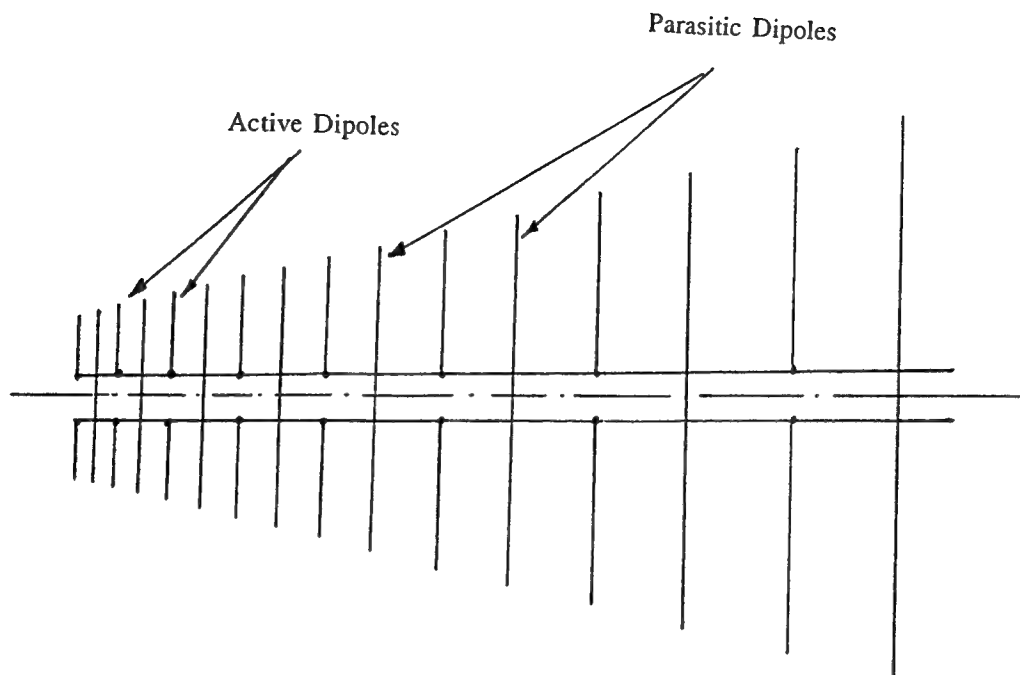
**Figure 2b. Log-periodic folded monopole antenna**



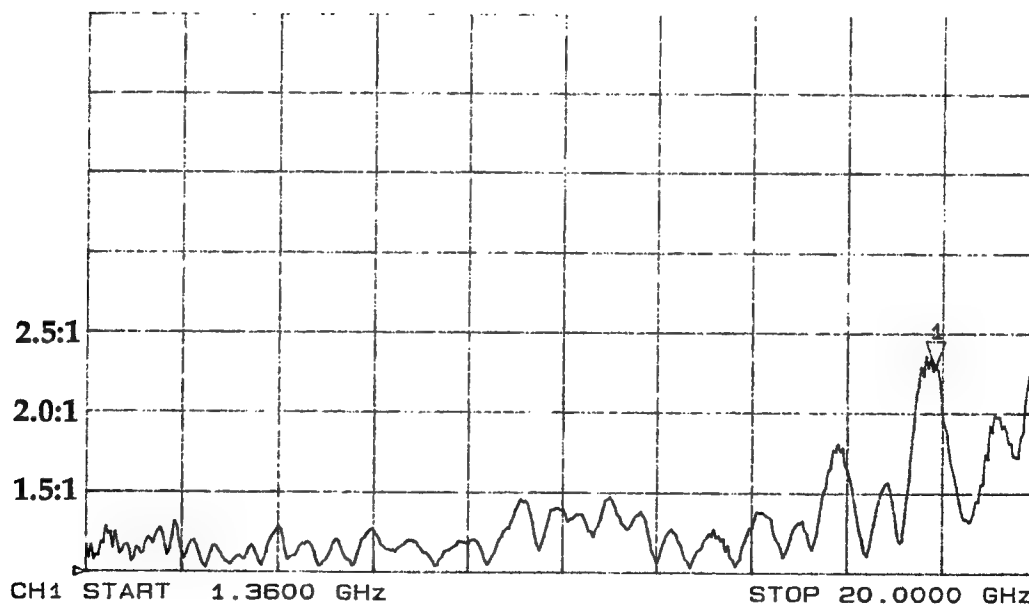
**Figure 3. Capacitive coupled log-periodic monopole antenna**



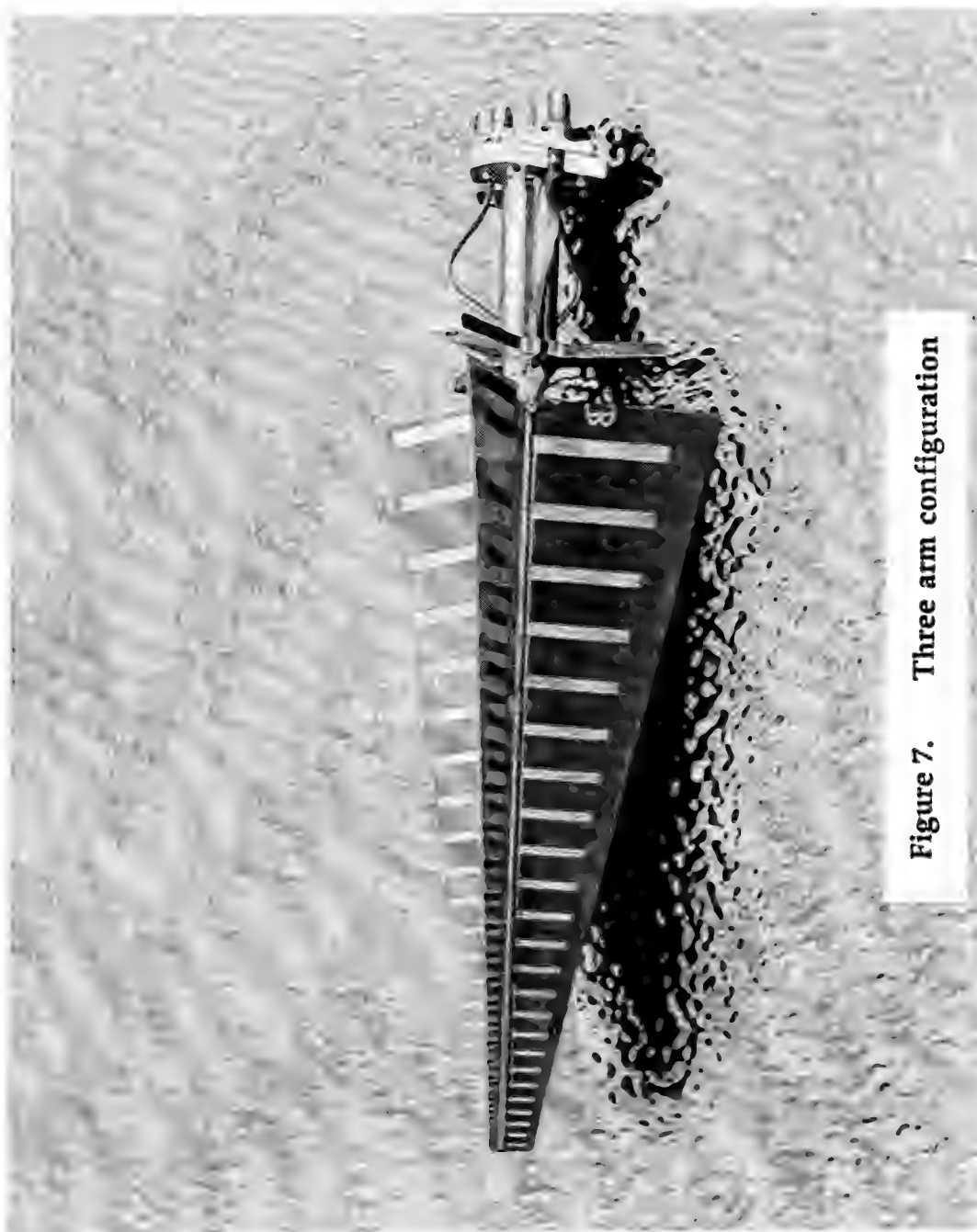
**Figure 4. Log-periodic monopole antenna with delay line**



**Figure 5. Barbano log-periodic dipole array**



**Figure 6. Measured VSWR of an LPPMA**



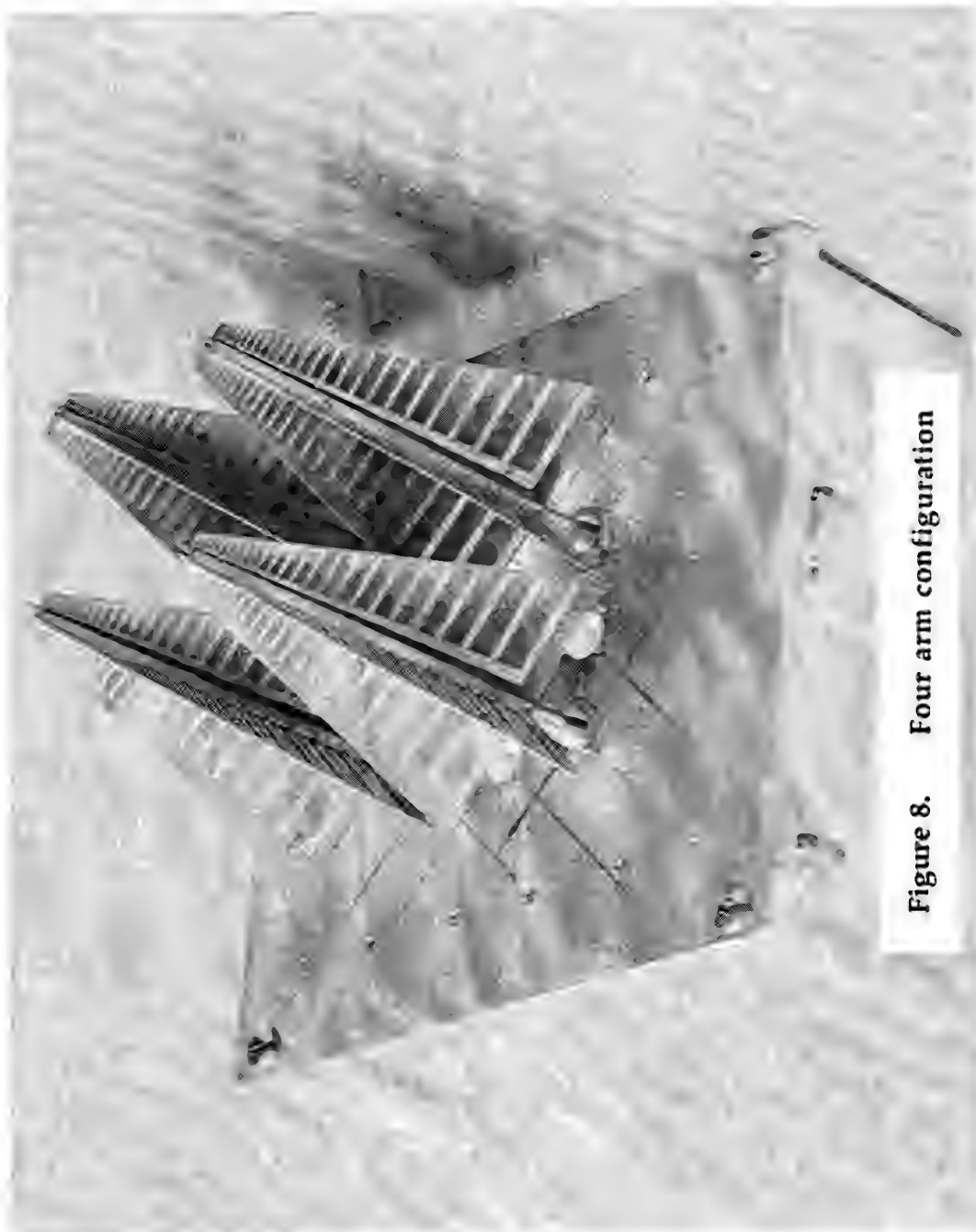


Figure 8. Four arm configuration

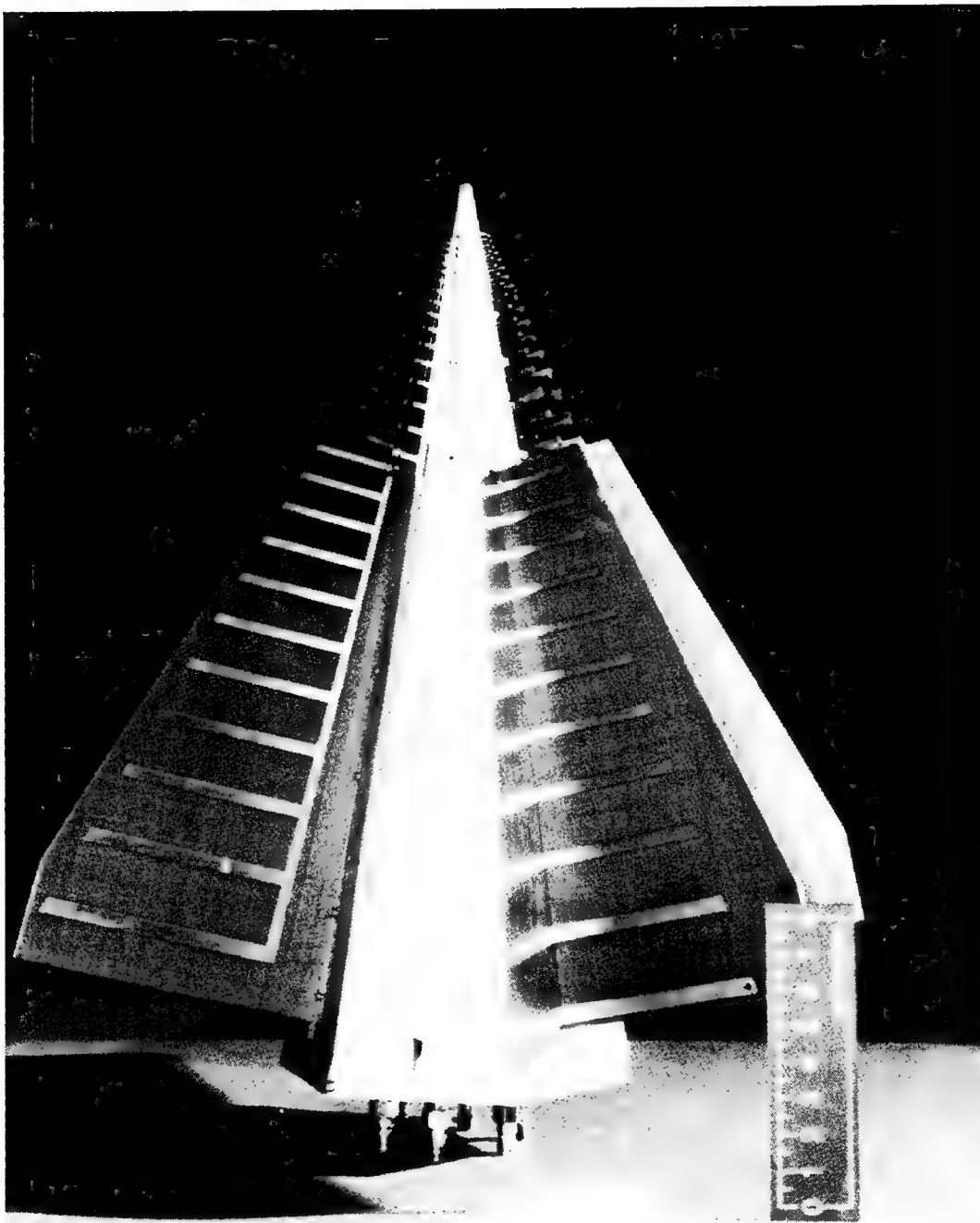


Figure 9. Multiarm configuration

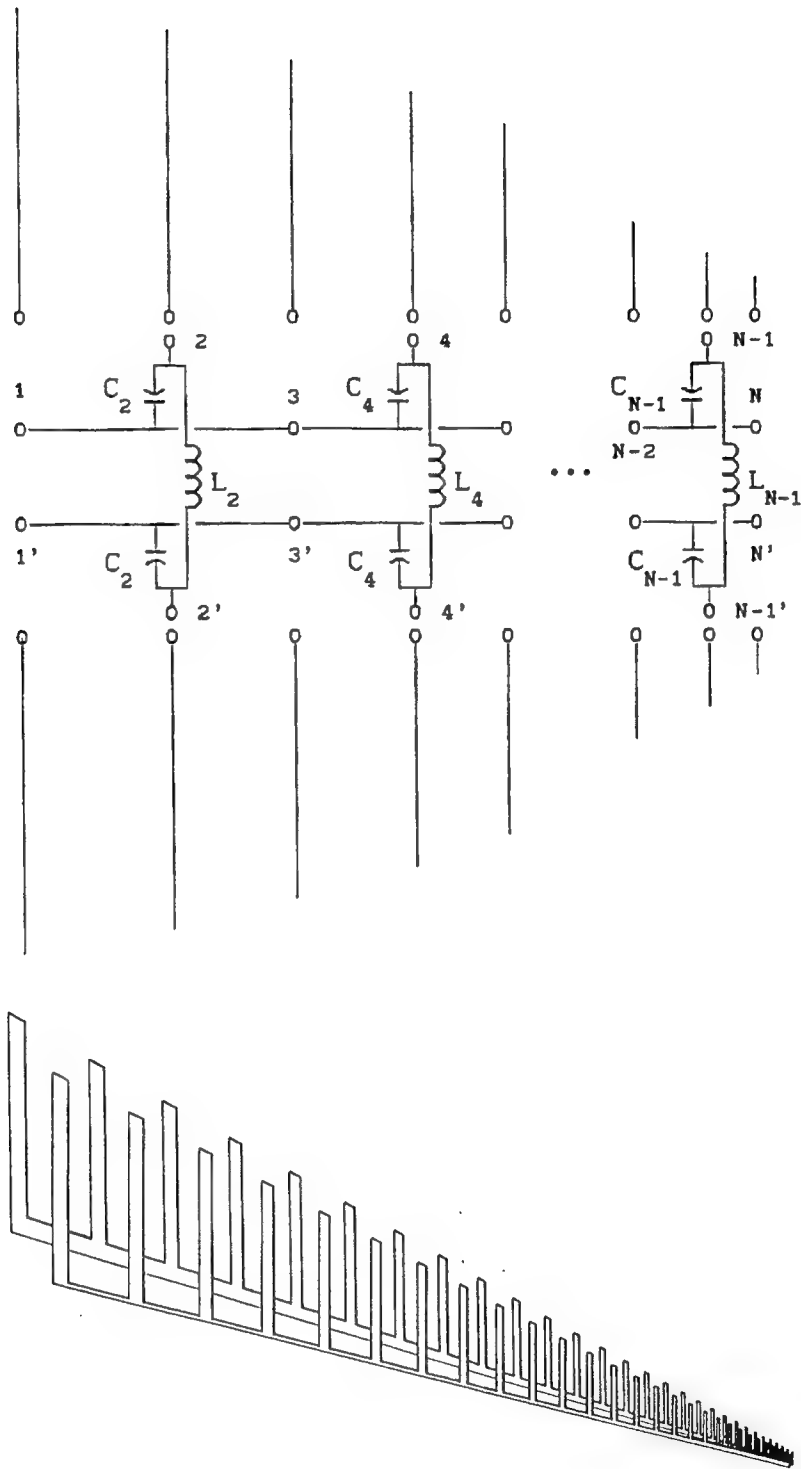


Figure 10. Log-periodic exterior and interior problems

# CHARACTERISTIC IMPEDANCE OF FIN TRANSMISSION LINE

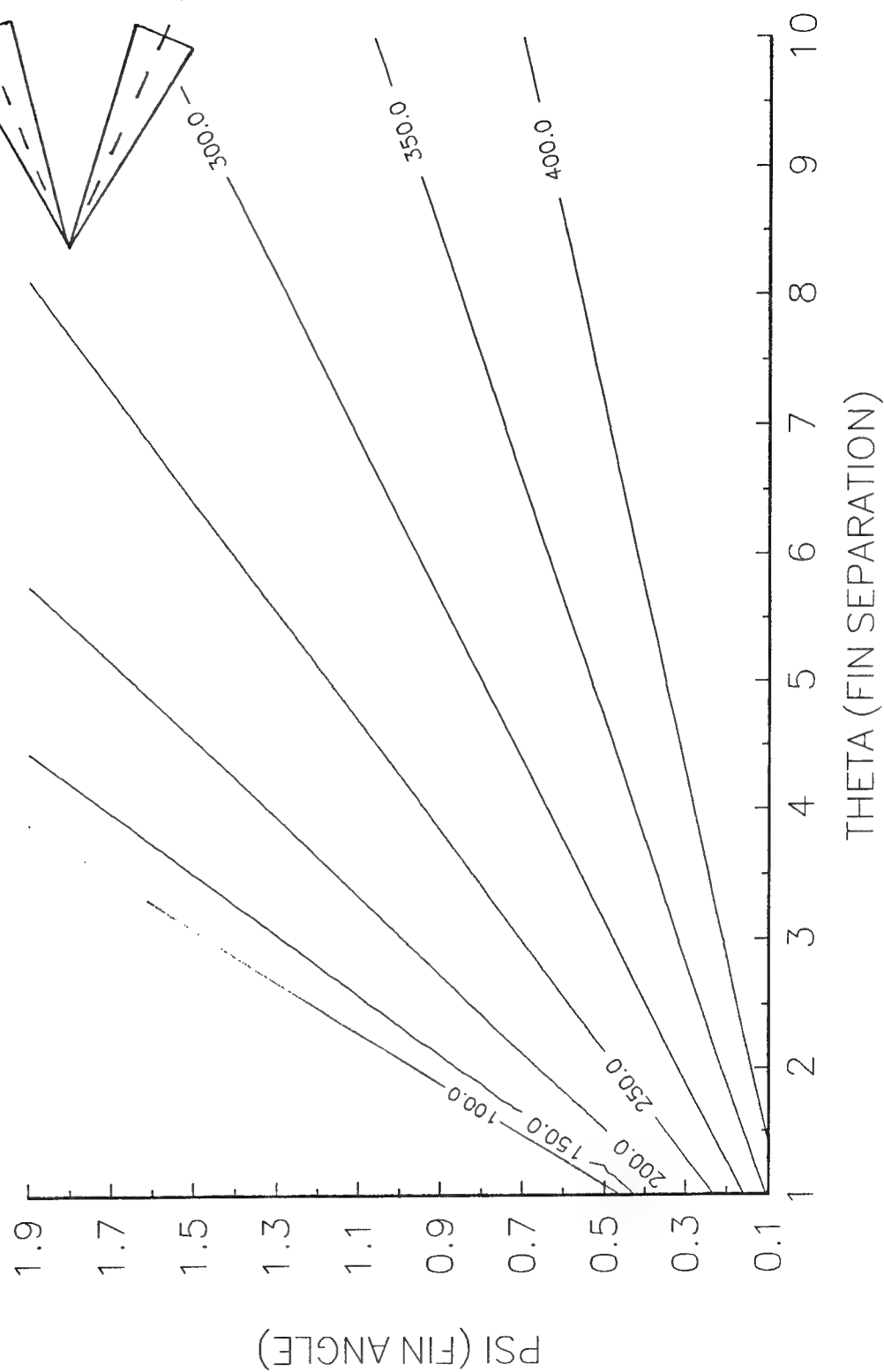


Figure 11. Characteristic impedance of fin transmission line



## Calculated VSWR for LPD

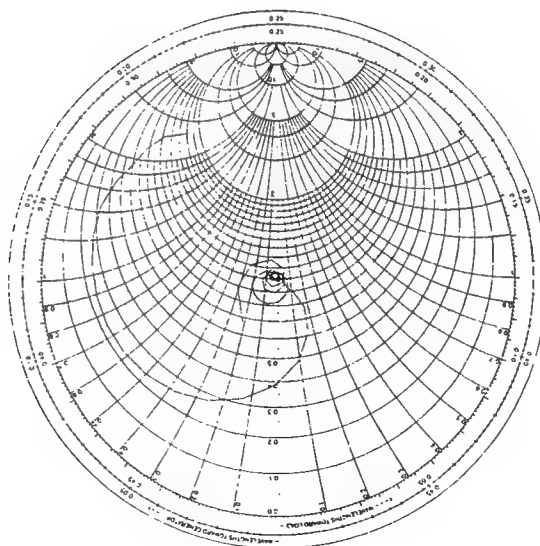


Figure 12. VSWR of Conventional LPDA

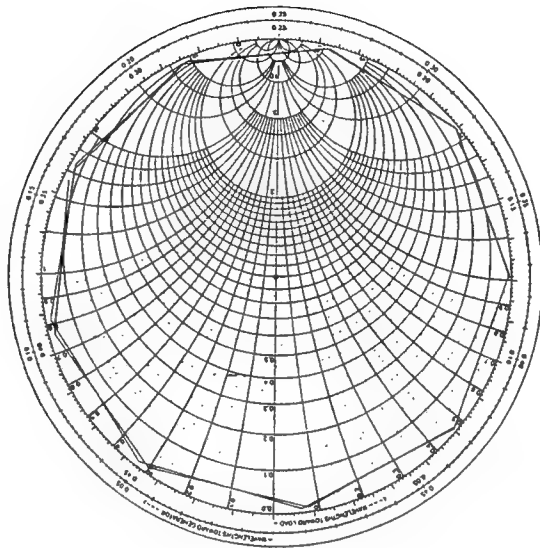


Figure 13. VSWR of LPDA without Transpose

## Calculated VSWR for LPPMA

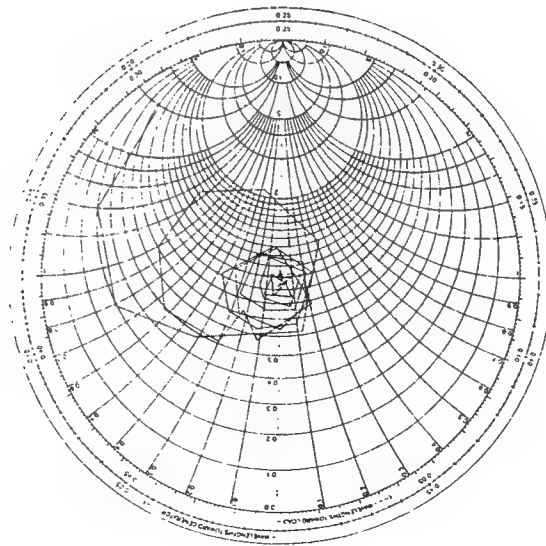
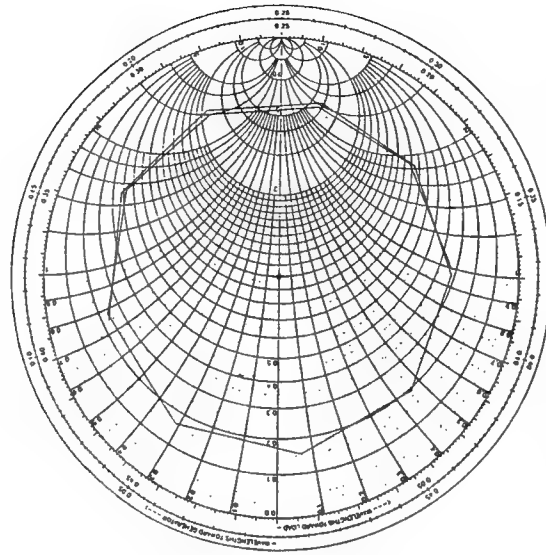


Figure 14. VSWR of Conventional LPPMA with parameters approximating current models



Optimum parasitic length — no capacitance coupling

Figure 15. VSWR of LPPMA without Capacitive Coupling between Parasitic Elements and Transmission Line

## REFERENCES

- [1] Carrel, R. L., "Analysis and Design of Log-Periodic Dipole Antenna," Technical Report No. 52, Contract AF33(616-6079), Antenna Laboratory, University of Illinois, Urbana, October, 1961. Also Ph. D. Thesis, Electrical Engineering Department, University of Illinois, Urbana, 1961.
- [2] Greiser, J. W., U. S. Patent No. 3,369,243, "Log-Periodic Antenna Structure," February 13, 1968.
- [3] Ore, F. R., "Investigation of the log-periodic coaxial fed monopole array," Technical Note No. 1, University of Illinois Radiolocation Research Laboratory, Contract NOBSR85243, October, 1963.
- [4] Ingerson, P. G. and Mayes, P. E. "Log-Periodic Antennas with Modulated Impedance Feeders," *IEEE Transactions on Antennas and Propagation*, November, 1968.
- [5] Green, P. B. and Mayes, P. E., "50  $\Omega$  Log-Periodic Monopole Array with Modulated-Impedance Feeder," *IEEE Transactions on Antennas and Propagation*, March, 1974.
- [6] Barbano, N., "Log-Periodic Dipole Array with Parasitic Elements," *Microwave Journal*, vol. 8, pp. 41-69, October, 1965.
- [7] Barbano, N., "Log-Periodic Yago-Uda Array," *IEEE Transactions on Antennas and Propagation*, vol. AP-14, no. 2, pp. 235-238, March, 1966.
- [8] Carrel, R. L., "Characteristic impedance of an infinite biconical antenna of arbitrary cross-section," Technical Report No. 15, University of Illinois Electromagnetics Laboratory, Contract AF 33(616)-3220, August, 1957.

## **POLARIZATION EXTRACTION OF CIRCULARLY POLARIZED ANTENNAS**

François Colomb  
Raytheon Company  
Research Division  
131 Spring Street  
Lexington, MA 02173

James Gentle  
Hughes Aircraft Company  
1950 East Imperial Highway  
El Segundo, CA 90245

Paul Klock  
University of Illinois  
Everitt Laboratory  
1406 W. Green Street  
Urbana, IL 61801

Paul Mayes  
University of Illinois  
Everitt Laboratory  
1406 W. Green Street  
Urbana, IL 61801

John Swanstrom  
Hewlett-Packard Company  
Santa Rosa Systems Division  
1400 Fontaingrove Parkway  
Santa Rosa, CA 95403-1799

### **ABSTRACT**

A technique is presented for obtaining the radiation patterns and the antenna gain of elliptically polarized antennas from two vector measurements of the far-field. The two measurements correspond to different polarizations which can be obtained by rotating one of the antennas around its boresight axis.

The discussion emphasizes a particularly interesting case, for which accurate radiation patterns and gain of the antenna under test (AUT) can be obtained without prior knowledge of the polarization of the second antenna.

The radiation pattern of a nearly circularly polarized (CP) antenna is conveniently represented by the CP co-polarized and cross-polarized components. The axial ratio and any other quantities commonly used to specify the antenna polarization can also be obtained since the pair of initial vector measurements completely characterize the polarization of the AUT.

This technique is illustrated by measurements performed on a CP patch antenna.

## 1.0 INTRODUCTION

Various techniques for measuring the radiation pattern and the gain of elliptically polarized antennas are available to antenna engineers from the literature. Most of these techniques are based on test range antennas of predetermined polarization. Linearly polarized (LP) antennas are rotated by 90 degrees to measure the LP components. Left-hand CP (LHCP) antennas and right-hand CP (RHCP) are interchanged to measure CP components.

An important exception is the spinning linear method in which a rotating LP antenna is used to record polarization patterns.

For consistency of terminology, the antenna that is a part of the test range at all times is referred to from here on as the second antenna.

By combining vectorially the complex responses to two different relative orientations of the AUT and the second antenna, one obtains the equivalent of a system in which the polarization of the second antenna can be configured at will. This serves as a base for the technique presented hereby. The same effect could be achieved with a fixed dual polarized antenna instead of the one-port antenna that is rotated.

After some definitions, the measurement technique is presented and illustrated with examples. It is shown that this method is equivalent to using a perfectly CP antenna as the second antenna. Standard calibration procedures can then be applied to determine the gain of the AUT. For a comparison of different antenna gain measurement techniques, see for example [1].

## 2.0 DEFINITIONS

The time convention  $e^{j\omega t}$  is adopted throughout this paper and effective values are used for all phasors.

First, the definition of the polarization of a plane wave and the associated notation as given by Lo and Lee [2] are introduced. The electric field of a plane wave propagating in an isotropic homogeneous medium is represented as

$$\mathbf{E} = C \sqrt{Z} \mathbf{u} e^{-j\mathbf{k} \cdot \mathbf{r}}$$

where  $C$  is a complex constant with units of  $\sqrt{\text{power}}/\text{m}$ ,  $Z = \sqrt{\mu/\epsilon}$ , and  $\mathbf{k}$  is the propagation vector. The complex vector  $\mathbf{u}$  is the polarization vector. It is defined only within a phase angle, thus  $\mathbf{u}$  and  $\mathbf{u} e^{j\delta}$  are the same polarization. The polarization vector satisfies the unitary condition

$$\mathbf{u} \cdot \mathbf{u}^* = 1$$

Caution must be exercised when dealing with complex vectors. A complex vector is not simply the product of a real vector and a complex scalar. Without loss of generality, the propagation will be assumed in the positive  $z$  direction unless otherwise specified. The polarization vector can then be written as the superposition of two linearly polarized components

$$\mathbf{u} = \hat{\mathbf{x}} a_x + \hat{\mathbf{y}} a_y \quad (1)$$

In phase components  $a_x$  and  $a_y$  result in linear polarization. In general however,  $a_x$  and  $a_y$  are complex and in the time domain, the electric field given by

$$\mathcal{E}(z=0, t) = \sqrt{2} \operatorname{Re} \{ \mathbf{u} e^{j\omega t} \}$$

is a vector rotating in the  $xy$  plane. The locus of the tip of the vector is the polarization ellipse.

Equal magnitude and 90 degrees out of phase components give circular polarization. The vector  $\mathbf{u}$  is then equal to one of the two unitary vectors known as the LHCP vector and the RHCP vector

$$\mathbf{L} = (\hat{\mathbf{x}} + j\hat{\mathbf{y}})/\sqrt{2} \text{ (LHCP)} \quad (2a)$$

$$\mathbf{R} = (\hat{\mathbf{x}} - j\hat{\mathbf{y}})/\sqrt{2} \text{ (RHCP)} \quad (2b)$$

In the time domain and for fixed  $z$ , the tip of the real vector associated with  $\mathbf{L}$  rotates in the left-hand sense with respect to the direction of propagation. This can be verified by observing that the  $y$  component of  $\mathbf{L}$  leads the  $x$  component.

The vectors  $\mathbf{L}$  and  $\mathbf{R}$  satisfy the conditions

$$\mathbf{L} \cdot \mathbf{L}^* = \mathbf{R} \cdot \mathbf{R}^* = 1$$

$$\mathbf{L} \cdot \mathbf{R}^* = \mathbf{R} \cdot \mathbf{L}^* = 0$$

thereby defining an orthonormal basis for  $\mathbf{u}$ . The polarization vector  $\mathbf{u}$  can then be resolved into two circularly polarized components by projecting  $\mathbf{u}$  on  $\mathbf{L}$  and  $\mathbf{R}$ .

$$a_R = \mathbf{u} \cdot \mathbf{R}^* = |a_R| e^{j\delta_R} \quad (3a)$$

$$a_L = \mathbf{u} \cdot \mathbf{L}^* = |a_L| e^{j\delta_L} \quad (3b)$$

$$\mathbf{u} = \mathbf{L} a_L + \mathbf{R} a_R \quad (4)$$

The two representations of the polarization vector (1) and (4) are equivalent and thus interchangeable. For example, using (1)-(3), the circularly polarized components can be written in terms of the linearly polarized components as

$$a_{\frac{L}{R}} = (a_x \mp ja_y)/\sqrt{2}. \quad (5)$$

This implicit notation is used for convenience. It replaces two equations where the first one is obtained by choosing the upper subscript and the upper sign and the second one by choosing the lower subscript and lower sign.

Alternatively, the LP components can be written in terms of the CP components as

$$\begin{aligned} a_x &= (a_L + a_R)/\sqrt{2} \\ a_y &= j(a_L - a_R)/\sqrt{2} \end{aligned} \quad (6)$$

The expansion of  $\mathbf{u}$  in circularly polarized components can simplify considerably the analysis of an elliptical polarization and the transmission between elliptically polarized antennas. It also leads to an easy to remember mental picture of the electric field of an elliptically polarized plane wave. In the time domain, (4) represents the superposition of two counter rotating vectors with lengths proportional to  $|a_L|$  and  $|a_R|$  as shown in Figure 1.

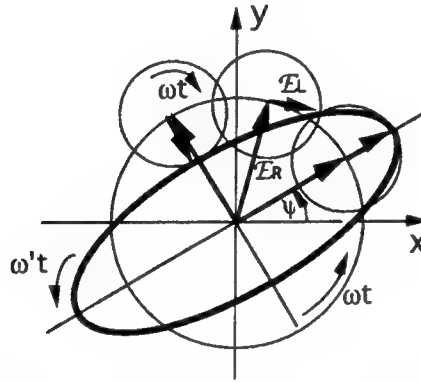


Figure 1. Polarization ellipse represented by the superposition of counter rotating vectors  $\mathcal{E}_L$  and  $\mathcal{E}_R$ .

The rotation of  $\mathcal{E}_L$  and  $\mathcal{E}_R$  means that there is a direct relationship between the phase of the voltage received by a CP antenna and its orientation in the  $xy$  plane — a fact that can be used to obtain a phase progression, without phase shifters, to steer the beam of an antenna array.



The three parameters specifying the polarization, i.e. axial ratio, orientation and sense, can be derived analytically, but can also be found directly by inspection from Figure 1.

The axial ratio, often expressed in dB, is given by

$$AR = \frac{\text{major axis}}{\text{minor axis}} = \frac{|a_L| + |a_R|}{||a_L| - |a_R||} \quad (7)$$

The orientation of the ellipse is defined as the angle  $\psi$  between  $\hat{x}$  and the major axis. It is given in terms of the circularly polarized components by

$$\psi = (\delta_R - \delta_L)/2 + m\pi \quad (8)$$

where the integer  $m$  is chosen so that  $0 \leq \psi < \pi$ .

The sense of polarization (left-hand or right-hand) is determined by the largest of the two quantities  $|a_L|$  and  $|a_R|$ .

An alternative representation of the polarization ellipse is by means of the complex number  $\Gamma$  defined as

$$\Gamma = |\Gamma| e^{j\phi} = \begin{cases} a_R/a_L, & |a_R| \leq |a_L| \\ a_L/a_R, & |a_L| \leq |a_R| \end{cases} \quad (9)$$

The axial ratio and orientation of the ellipse are given in term of  $\Gamma$  by

$$AR = \frac{1 + |\Gamma|}{1 - |\Gamma|}$$

$$\psi = \pm \phi/2, \quad |a_L| \geq |a_R|$$

A simple connection can be established between the ratio  $\Gamma$  of the circularly polarized components and a complex ratio of the linearly polarized components. If the complex number  $p$ , also known as the polarization ratio, is defined as follows

$$p = \pm j a_y/a_x, \quad |a_L| \leq |a_R|$$

one finds that  $\Gamma$  and  $p$  are related by the same bilinear transformation relating the reflection coefficient and the input admittance of a network. Thus, the toolbox of

matching techniques for microwave networks, including visualization tools such as the Smith and Carter charts, may be taken over for the discussion of elliptically polarized waves.

The Poincaré sphere provides an additional way of relating the axial ratio and the orientation of the polarization ellipse to the polarization ratio using spherical trigonometry [3]. This representation is particularly useful in evaluating the transmission between antennas of different polarizations.

Having introduced the different representations of the polarization of a plane wave, the discussion proceeds by defining the polarization of antennas and considering the transmission between elliptically polarized antennas.

There are several possibilities in choosing a set of coordinates for analyzing the transmission between two antennas. Some authors define separate sets of coordinates for each antenna with a convention specifying their relative orientation. The position adopted here is to use a unique set of coordinates at the antenna under test (AUT) with the  $z$  axis pointing towards the second antenna, see Figure 2. This avoids the need for the arbitrary convention mentioned above.

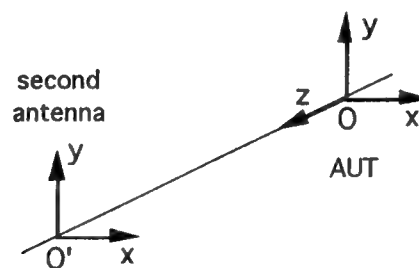


Figure 2. System of coordinates for analyzing the transmission between two antennas.

The polarization of an antenna in a given direction is defined by the polarization of the locally plane wave when the antenna is transmitting. The plane

wave is said to be in the state  $(\mathbf{k}, \mathbf{u})$ . The plane wave with state  $(-\mathbf{k}, \mathbf{u}^*)$  represents a wave propagating in the reverse direction and of *same* polarization. The change in polarization vector is due to time reversal.

The source antenna in Figure 1 produces thus a locally plane wave propagating in the  $-z$  direction with polarization vector  $\mathbf{u}_S^*$ . The voltage at the terminals of the AUT is given within a constant phase factor by

$$V = E h \mathbf{u}_{AUT} \cdot \mathbf{u}_S^* \quad (10)$$

where  $E$  is the amplitude of the plane wave at the location of the AUT and  $h$  is the antenna effective length which includes the far-field radiation pattern of the AUT and a possible mismatch between the AUT input impedance and the receiver input impedance. Equation (10) states that only the component of the wave which is parallel to  $\mathbf{u}_{AUT}$  is received by the antenna.

A polarization mismatch between the transmitting antenna and the receiving antenna results in loss of received power compared to the available power. The mismatch can be accounted for by a polarization efficiency that can be factored in the Friis transmission formula

$$\frac{P_R}{P_T} = G_T(\mathbf{k}) G_R(-\mathbf{k}) \left( \frac{\lambda}{4\pi R} \right)^2 |\mathbf{u}_T \cdot \mathbf{u}_R^*|^2 \prod_i e_i \quad (11)$$

where  $G_T$  and  $G_R$  are the gains of the transmitting and receiving antennas

respectively, the squared parenthesis is the free-space loss, the squared norm is the polarization efficiency, and  $\prod_i e_i$  represents the product of other efficiencies

accounting for example for an impedance mismatch at the terminals of the antennas and absorption occurring in the RF path.

### 3.0 POLARIZATION EXTRACTION

Enunciated in a few words, the technique to be presented consists of measuring the complex transmitted field (amplitude and phase) for two orientations of the second antenna around the propagation axis and appropriately combining the measured responses to extract the desired polarization information.

The ability to accurately determine the complex ratio of the responses is essential and has direct implications on the measurement equipment. The automated antenna test range developed at the University of Illinois is based on an HP8510B Automated Network Analyzer that is used as a conventional network analyzer or as a phased locked vector receiver for radiation pattern measurements. The details of this setup are described in Section 4.

If one had a purely linear polarized antenna, the expansion of the field radiated by the AUT into circularly polarized components could be obtained from (5) by measuring the voltage at the terminals of the second antenna when its orientation is first along  $\hat{x}$  and then along  $\hat{y}$ . The results obtained for the two possible signs of (5) would then be identical to the responses obtained with pure CP probing antennas. The algebraic manipulation of the complex responses is thus equivalent to synthesizing a new polarization of the second antenna.

In practice, the polarization of the second antenna is not ideal. Following the notation of (9), let the polarization be written as

$$u_0 = \frac{L + R \Gamma_L}{\sqrt{1 + |\Gamma_L|^2}}$$

assuming thereby that the antenna LHCP component is slightly larger than its RHCP component. The polarization of the antenna rotated by  $\pi/2$  is

$$\mathbf{u}_{\pi/2} = \frac{\mathbf{L} e^{-j\frac{\pi}{2}} + \mathbf{R} \Gamma_L e^{j\frac{\pi}{2}}}{\sqrt{1 + |\Gamma_L|^2}}$$

If one proceeds in the same way as for the LP antenna, the equivalent new polarization  $\mathbf{u}_L$  for the upper sign of (5) is

$$\begin{aligned} \mathbf{u}_L &= \frac{\mathbf{u}_0 + j \mathbf{u}_{\pi/2}}{|\mathbf{u}_0 + j \mathbf{u}_{\pi/2}|} \\ &= \frac{(\mathbf{L} + \mathbf{R} \Gamma_L) + e^{j\frac{\pi}{2}} \left( \mathbf{L} e^{-j\frac{\pi}{2}} + \mathbf{R} \Gamma_L e^{j\frac{\pi}{2}} \right)}{|\mathbf{u}_0 + j \mathbf{u}_{\pi/2}|} \\ &= \frac{2\mathbf{L}}{|\mathbf{u}_0 + j \mathbf{u}_{\pi/2}|} \\ \therefore \mathbf{u}_L &= \mathbf{L} \end{aligned}$$

A similar derivation for the minus sign leads to  $\mathbf{u}_R = \mathbf{R}$ . Thus one finds the somewhat surprising result that the equivalent polarization of the second antenna is either LHCP or RHCP irrespective of the polarization of the second antenna.

In practice, there are several potential sources of uncertainty that can degrade the quality of the measurement. These include rotational positioning accuracy, rotary joint variations, and change in radiation properties of the second antenna due to interaction with other equipment.

Once the circularly polarized components of the field radiated by the AUT have been determined, the axial ratio and orientation of the polarization ellipse are obtained in a straight forward way from (7)-(8). The envelope of a corresponding spinning linear measurement can also be obtained by forming the sum and

difference of the magnitudes of the LHCP and RHCP polarized components. Also the LP components can be extracted using (6).

This technique is illustrated with antenna measurements of a patch radiator — a dualband stacked patch antenna fed by two coaxial probes for GPS applications [4, 5]. Radiation patterns in terms of LP components and CP components are shown in Figures 3-4. Figure 5 shows the axial ratio and the orientation of the ellipse for the same cut.

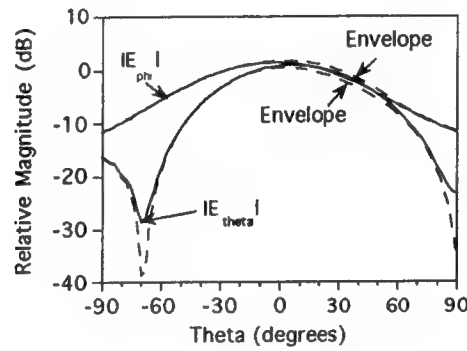


Figure 3. Linearly polarized components and envelope of corresponding spinning linear measurement measured at 1.575 GHz.

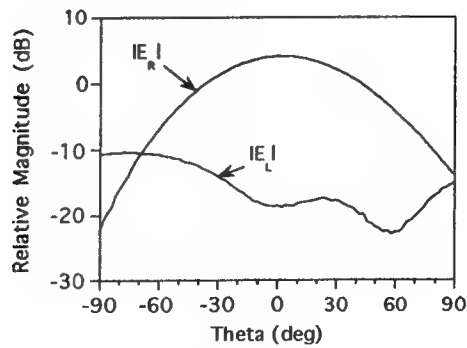


Figure 4. Circularly polarized components measured at 1.575 GHz.

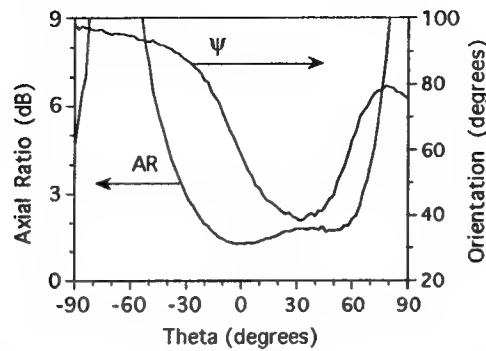


Figure 5. Axial ratio and orientation of the polarization ellipse measured at 1.575 GHz.

Polarization extraction from swept frequency measurements at boresight are shown in Figures 6-7. The axial ratio and the orientation of the ellipse for the same patch antenna are shown versus frequency in Figure 6. It is sometimes easier to visualize the polarization of an antenna by using the Poincaré sphere. The polarization efficiency is then equal to  $\cos^2(MM'/2)$  [3], where  $MM'$  is the angle spanned by the two points on the Poincaré sphere representing the polarizations of the two antennas. This representation allows to determine quickly the correction in the polarization of one or both antennas needed for reducing the polarization mismatch loss.

Charting data values on the Poincaré sphere is simplified by projecting the sphere on the equator. An orthographic projection is used in Figure 7 to show the boresight polarization of the patch antenna for two frequency intervals centered at the GPS link frequencies ( $f_{L1}=1575$  MHz,  $f_{L2}=1228$  MHz).

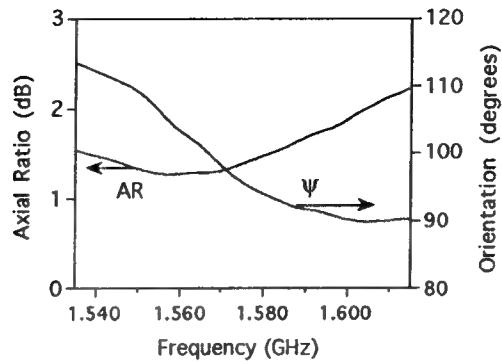


Figure 6. Axial ratio and orientation of the polarization ellipse at broadside versus frequency.

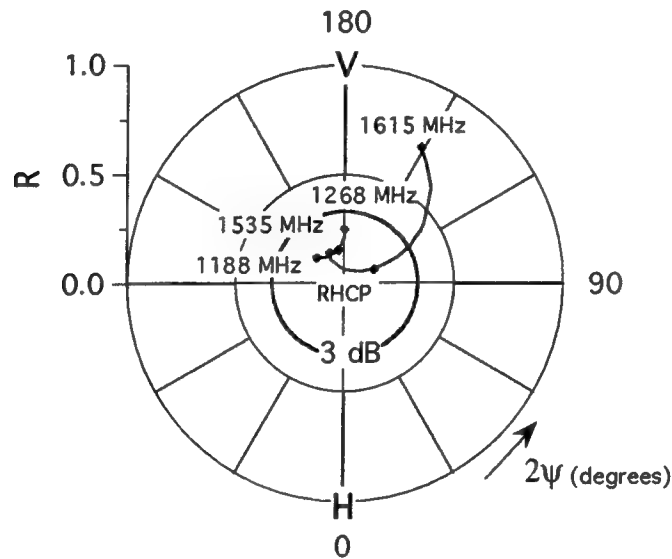


Figure 7. Polarization of the patch antenna. The radial distance  $R$  is a measure of the axial ratio  $AR$  and is given by  $R = \sin\left[\frac{\pi}{2} - 2 \tan^{-1}(1/AR)\right]$ .

#### 4.0 INSTRUMENTATION

Although the HP8510B has traditionally been dedicated to microwave network measurements, it can also be used for antenna measurements since the AUT, the second antenna, and the space in-between constitute a two-port. In



addition to providing the complex transmission coefficient for the purpose of polarization measurements, the ability to measure the input reflection coefficient of the AUT and the second antenna is advantageous since these reflection coefficients can be used to improve the accuracy of gain measurements.

The nature of pattern measurements requires however careful consideration of a number of additional factors, including free-space loss and physical distance between the test ports. The antenna test range includes a power amplifier and a separate frequency converter. The RF output of the frequency synthesizer and the IF signals fed into the network analyzer S-parameter test set can both be switched to make network measurements or antenna measurements.

Figure 8 shows a block diagram of the antenna range test set. The switched orientation of one of the couplers at the second port avoids the 20 dB attenuation in forward transmission that would otherwise be incurred in a conventional configuration. A direct consequence is that reverse transmission is not available. This does not represent a serious handicap since the two-port consisting of antennas and free-space is usually reciprocal.

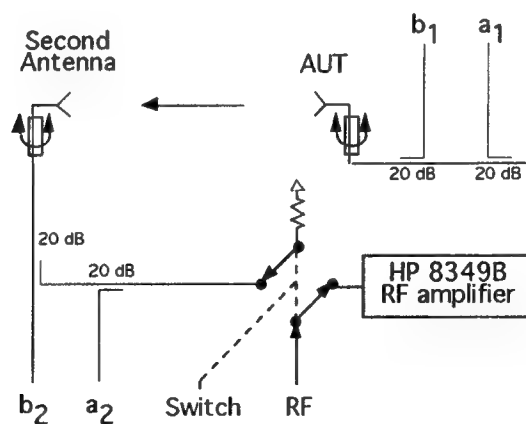


Figure 8. Antenna range test set

Not explicitly shown in Figure 8 are coils of cable in the RF path of  $a1$ ,  $a2$ , and  $b2$  that provide approximate path coherence for three of the four S-parameters. Neglecting to compensate for the path difference due mainly to the distance between the test port would produce a large phase slope of the raw scattering parameters. Significant phase errors would then result from the small but inevitable variations of the source frequency.

A program was written for automating the data acquisition with a computer that controls the network analyzer and the positioner controllers. Separate programs allow extraction and visualization of the desired information from the large files that can contain measurements at multiple frequencies and polarizations.

## 5.0 MEASUREMENT OF ANTENNA GAIN

The definition of the gain of the antenna used in this document is the gain that would be measured for matched transmitting and receiving antenna polarizations. The input impedances of the transmitting and receiving antennas are also assumed to be matched to the source and to the receiver input impedances and propagation is in free-space. With this definition, a power budget can be evaluated in any practical situation using the Friis transmission formula (11) provided that the polarizations of the two antennas are known.

Since the equivalent polarization of the second antenna is circular, the antenna test range can be calibrated to measure the gain of a CP AUT. For example, the substitution method with a LP gain standard can be applied. First the power  $PSI$  received with the gain standard in one position is measured and then the

standard gain antenna is rotated by 90 degrees on its boresight before measuring the power  $P_{S2}$ . The gain standard is then substituted by the AUT and the received power  $P_{AUT}$  is measured. The gain of the CP AUT is then obtained using

$$G_{AUT} = \frac{P_{AUT}}{P_{S1} + P_{S2}} G_0 \quad (12)$$

where  $G_0$  is the gain of the standard.

When determining the gain of an elliptically polarized antenna, a correction needs to be factored into (12) to remove the loss due to the polarization efficiency of the two antennas. This is not a problem since the polarization of both the AUT and the second antenna are known. The gain of an elliptically polarized antenna is then

$$G_{AUT} = \frac{P_{AUT}}{P_{S1} + P_{S2}} G_0 (1 + |\Gamma|^2)$$

where  $\Gamma$  is defined by (9) and  $|\Gamma|$  can be determined also from the axial ratio as

$$|\Gamma| = \frac{AR - 1}{AR + 1}$$

## 6.0 SUMMARY

A simple procedure for measuring radiation patterns and antenna gain of elliptically polarized antennas was presented and illustrated with measurements. The technique relies on the determination of the circularly polarized field components of the AUT. It is shown that the voltage obtained by appropriately combining the responses of two orthogonal orientations of the second antenna is equivalent to the voltage that would be obtained with a purely CP second antenna. This allows the accurate determination of the circularly polarized field components

of the AUT from which all other quantities describing the polarization of the AUT can be determined.

Antenna test ranges that are set up for spinning linear measurements can be upgraded to implement this technique quite easily provided that a vector receiver that can be phase locked to the source is available.

## 7.0 ACKNOWLEDGMENTS

The authors would like to thank the faculty members and the students of the University of Illinois that participated in the development and construction of the automated antenna test range. In particular, the guidance and the original ideas of Dr. D. W. Smith are gratefully acknowledged. The authors thank also J. M. Bowen for his assistance during the preparation of this document.

## REFERENCES

- [1] S. V. Parekh. The Measurements Column. IEEE Antennas Propagation Magazine, pp. 41-44, April 1990
- [2] Y. T. Lo and S. W. Lee. Antenna Handbook. Chapter 1. Van Nostrand Reinhold. New York. 1988
- [3] V. H. Rumsey, G. A. Deschamps, M. L. Kales, and J. I. Bohnert, "*Techniques for handling elliptically polarized waves with special reference to antennas*," Proc. I.R.E., pp. 533-552, May 1951
- [4] F. Y. Colomb, "*Analysis and test of patch antennas for applications in dual-band and diversity systems*," PhD Thesis, Electromagnetics Laboratory, University of Illinois, Urbana IL, May 1993
- [5] F. Y. Colomb and P. E. Mayes, "*Stacked patches with a slot in the common wall for single- and dual-band operation*," IEEE Antennas Propagat. Intl. Symp., pp. 2077-2080, Chicago IL, 1992

# MEASUREMENT OF PHASED ARRAY PERFORMANCE AT ARBITRARY SCAN ANGLES

D. H. Schaubert, W. C. Chang and G. J. Wunsch  
Antenna Laboratory  
Electrical and Computer Engineering  
University of Massachusetts  
Amherst, MA 01003

**Abstract:** A measurement technique has been developed that is useful for obtaining the active reflection coefficient of a phased array at arbitrary scan angles and frequencies. The technique utilizes a pair of moderately large arrays connected back-to-back in a constrained lens configuration and relies upon the measurement of the transmission coefficients through two such lens to evaluate the active reflection coefficient of a central element in a large array. The reflection coefficient is obtained, up to a sign ambiguity, with only a small amount of data processing. The new technique is an alternative to existing techniques for determining array performance. It is more flexible than waveguide simulators in terms of the operating conditions that can be tested and it should be less costly to implement than a fully driven array with phase scanning. For printed circuit antennas like the endfire tapered slot arrays that have been tested, the cost of implementation is also less than for active element patterns. The measurement technique and data processing algorithm have been verified by comparing several measurements to predictions from a full-wave analysis of infinite arrays of notch antennas. The results obtained to date clearly demonstrate that the technique is useful and accurate enough for antenna design and for validation of CAD simulations.

## 1. Introduction

Antenna designers are increasingly dependent upon numerical simulations for effective and efficient design of modern antennas. This is especially true in the design of high-performance phased arrays. However, before proposed designs enter production or service, they must be validated by fabrication and test of prototypes. Also, the numerical simulations and codes

that comprise the CAD/CAM being used for the design must be validated by extensive comparison to numerical and experimental results. When the antennas of interest are large, scanning phased arrays, the cost of fabricating and testing prototypes can be very large.

Typically, the parameters of interest include active element reflection coefficient or active element pattern, gain and polarization, usually measured over a band of frequencies and a range of scan angles. There are three techniques that are commonly used to assess these parameters: (i) waveguide simulator measurements, (ii) active element pattern measurements in a moderately large array with all but one element terminated in a matched load, and (iii) measurements of a fully driven array. The waveguide simulator [1] is the cheapest and easiest to use, but it yields only a limited amount of information. The scan angle is always related to the frequency, so independent evaluation of frequency and scan behavior is not possible. Furthermore, fundamental mode simulators are limited to H-plane scan and multimode simulators using several elements inside the waveguide require extensive measurements of multiport scattering parameters followed by data processing to extract the parameters of interest [2].

Active element patterns can be very useful for determining the existence of anomalies such as scan blindness. To make these measurements, a moderately large array is fabricated and the center element is connectorized so that power can be fed to it. All other elements in the array are terminated in a matched load, which may be a chip resistor or other absorber installed at the time of fabrication or a removable load that requires every element to be connectorized. Gain patterns versus frequency and scan angle provide the envelop of the array gain function. These measurements are relatively easy to perform once the moderately large array is fabricated.

Measurements of a fully driven array provide the most complete characterization of the antenna, but they require not only a moderately large array but also a fully functional feed network comprised of power dividers and phase shifters or a beam switching network. This amounts to a prototype of the entire antenna system and can be very expensive.

This paper presents an alternative measurement technique that can be used to estimate array performance at any scan angle and any frequency. The technique requires the fabrication of two constrained "lenses" comprised of moderately large arrays of the antenna under test. The transmission coefficients through the lenses are measured using an automatic network analyzer and simple data processing yields the active reflection coefficient. A typical measurement setup is depicted in Fig.1. The interconnecting lines of the constrained "lens" are all the same length so it does not actually focus the beam. Rather, it passes an incident plane wave through with no change in the direction of the beam. The measurement procedure is especially easy to implement because it requires only the relative measurement of two transmission coefficients. Neither the absolute values of the transmission coefficients nor the reflection coefficient are required. If the antennas are well matched, a strong signal passes through the lens exiting with the same "scan" angle as the incident wave. If the antennas are very poorly matched to the interconnecting line, most of the signal is reflected and the transmission is small, unless the length of interconnecting line creates a resonance. That case can be detected by the use of a second lens incorporating interconnecting lines of a different length. In fact, as shown below, the measurement of  $S_{21}$  for lenses having two different line lengths is sufficient to determine the active reflection coefficient to within a  $+/-$  sign ambiguity.

Lewis and Hessel [3] have demonstrated a measurement scheme that utilizes a plane wave incident on a lens structure similar to that depicted in Fig.1, but their method requires the insertion of a reflectometer in the interconnecting line of the central element. The reflectometer, which was a slotted line in their example, measures the reflection coefficient of the central radiating element on the exit side of the lens. No measurement of the transmission coefficient is contemplated in their work. In their work, the incident plane wave and the receiving side of the lens are used to obtain the desired amplitude and phase distribution of the excitation.

The assumptions and a description of the analysis and data processing are presented in the next section. Then several sample results that verify the validity of the method as well as illustrate its accuracy are presented.

## 2. Assumptions and Analytical Development

This paper describes a method for measuring the active reflection coefficient of a large phased array antenna at any frequency and scan angle using equipment readily available in an antenna laboratory. The primary assumption in the measurement are that the test array is sufficiently large that its gain function mimics the scan and frequency behavior of the larger, ideally infinite, array. The number of elements needed for accurate results varies with the type of antenna and the operating conditions, but some results for a 100-element array of notch antennas are shown below to agree reasonably well with numerical predictions for an infinite array. In the derivations that follow, we also include the simplifying assumption that the element spacing is sufficient to preclude grating lobes at any of the operating conditions to be tested. Under these assumptions, the lens becomes a two-port device wherein an incident plane wave ( $a_1$  in Fig. 2a) gives rise to one reflected wave ( $b_1$ ) and one transmitted wave( $b_2$ ).



The total scattering matrix of a symmetrical lens comprised of two identical faces connected by identical lengths of lossless transmission line can be obtained from the signal flow graph in Fig. 3.

$$S_{11}^T = S_{22}^T = S_{22} + \frac{S_{12}S_{21}S_{11}e^{-j2\theta}}{1 - S_{11}^2e^{-j2\theta}} \quad (1)$$

$$S_{12}^T = S_{21}^T = \frac{S_{12}S_{21}e^{-j\theta}}{1 - S_{11}^2e^{-j2\theta}} \quad (2)$$

where  $S_{11}^T = \frac{b_1}{a_1}$ ,  $S_{22}^T = \frac{b_2}{a_2}$ ,  $S_{12}^T = \frac{b_1}{a_2}$  and  $S_{21}^T = \frac{b_2}{a_1}$ .

The objective is to develop a simple measurement technique that allows the determination of the element reflection coefficient,  $b'_1/a'_1$  in Fig. 2a. Because it is difficult to accurately measure  $S_{11}^T$ , which is the bistatic radar cross-section of the lens, the procedure that is developed uses only the measurement of  $S_{21}^T$ . Furthermore, the technique utilizes the ratio of two transmission measurements, which eliminates the need for absolute calibration. It is only necessary that the position and orientation of the transmitting and receiving antennas remain fixed during the measurements.

The total transmission coefficient is measured for a lens like the one depicted in Fig. 2a and another like the one depicted in Fig. 2b, which uses identical antennas with identical physical separation, but adds a meandering section to increase the line length by approximately one-quarter wavelength at the center frequency. The exact length is not critical as long as it is known precisely and is not too close to a multiple of  $\lambda/2$ . Denote these two transmission measurements as  $S_{21}^{T'}$  and  $S_{21}^{T''}$ , and their ratio as  $R$ ,

$$R = \frac{S_{21}^{T'}}{S_{21}^{T''}} \quad (3)$$

Then it is a relatively straightforward manipulation to show that the reflection coefficient of one antenna in the array,  $S_{11} = b'_1/a'_1$ , satisfies

$$S_{11} = \pm \left[ \frac{Re^{j(\theta' - \theta'')} - 1}{Re^{-j(\theta' + \theta'')} - e^{-j2\theta''}} \right]^{\frac{1}{2}} \quad (4)$$

The right-hand side of (4) involves only quantities that are known from the construction of the array or from the measurements of the transmission coefficients. The sign ambiguity in (4) occurs because a square root operation is performed. The sign of  $S_{11}$  may be important for some applications, but it does not affect parameters such as VSWR and return loss, which often are the quantities of interest.

Some noteworthy issues related to (4) are:

1. The value of obtained from (4) is normalized with respect to the characteristic impedance of the interconnecting transmission line and the derivation assumes that this impedance is the same for the two measurements ( $S_{21}^{T'}$  and  $S_{21}^{T''}$ ). Therefore, the accuracy of the result depends upon an accurate fabrication of the lines and an accurate knowledge of their characteristic impedance. This does not usually present any significant problem.
2. The value of  $S_{11}$  obtained from (4) also depends on the electrical lengths of the interconnecting lines, so  $\theta'$  and  $\theta''$  must be accurately known. This does not usually present a problem.
3. Because the antennas in the lens are fed directly from the interconnecting transmission line, there are no connectors or transitions that may affect the results. This can be especially useful for wideband, integrated phased arrays, which may not require well-matched connectors or transitions in their final configuration. It is not necessary to

develop such a connector or transition which might be needed only for test purposes.

4. If necessary, the sign ambiguity can be resolved by fabricating a second pair of lenses with interconnecting lines having a different characteristic impedance than the first pair. Measurement of these antennas will yield  $S_{11}$  normalized to the new characteristic impedance. When the two roots are converted to absolute impedances, only one will correspond an absolute impedance obtained from the first pair of antennas. This process doubles the effort in performing this measurement, so alternative measurement procedures or other means of determining the sign of  $S_{11}$  should be considered if the sign is essential to a particular application. When comparing to computed predictions, as is done in the examples presented below, the sign ambiguity can be resolved by selecting the root that best fits the expected result.
5. The active reflection coefficient obtained from (4) corresponds to the particular frequency and scan angle employed in the measurement of the transmission coefficients. Wide-scan angle results can be obtained as easily as antenna patterns, and swept frequency measurements allow the results to be obtained over a wide bandwidth.
6. For many antennas, the fabrication and test costs for using this measurement technique may be similar to those for measuring the active element pattern. However, active element pattern measurements cannot retrieve the phase of the active reflection coefficient. Also, retrieval of the absolute magnitude of the reflection coefficient requires that the absolute gain of the active element pattern be measured. In general, active element pattern measurements readily provide information on the variation of the reflection coefficient magnitude with scan angle,

but extraction of absolute values of  $|S_{11}|$  is more difficult and no phase information is available.

### 3. Sample Results and Discussion

The measurement procedure used for the results presented here involves the installation onto an antenna positioner of a large ground plane with an opening to accommodate the lenses. The use of the ground plane is desirable because (i) the antennas usually operate in the presence of a ground plane and (ii) the large ground plane prevents unwanted coupling between the transmitting and receiving antennas of the measurement setup via diffraction around the lens. The two lenses are fabricated using techniques compatible with the element type and array configuration. The measurement technique is particularly useful for printed circuit antennas that can be fabricated in the back-to-back configuration of Fig. 2 utilizing the same number of processing steps as for the fabrication of a single-sided array. However, it can still be useful for other types of antennas if the time and expense of assembling and testing the two lenses is less than that required to obtain the same information by using one of the alternative techniques discussed in the introduction. For the notch antenna arrays described below, no transitions or connectors are needed to join the two sides of the lens, so fabrication costs are only slightly higher (due to the added substrate for the second lens face) than for a single-sided array as might be used for active element pattern measurements. Furthermore, as noted above, it is not necessary to deembed the effects of a transition from the coaxial measurement system to stripline, microstripline, waveguide, etc., that is used to feed the radiating elements and no terminations are needed for the measurements.

### 3.1 Waveguide Simulator Results

The primary assumption in the development of the measurement technique is that the array is sufficiently large that it behaves as an infinite array, with every element identical to every other element. This is, of course, only approximately true for a large finite array. However, in a waveguide simulator, the imaging properties of the waveguide walls create an equivalent array that is infinite. Therefore, the overall technique and the data processing software can be verified by performing measurements in a waveguide simulator. These measurements are restricted to H-plane scan for single-mode simulators and the scan angle is determined by the operating frequency, but the results provide useful data for assessing the performance of the measurement technique in an environment that is relatively easy to control. The configuration of the waveguides and test antennas is shown in Fig. 4. The signal is inserted through the coax-to-waveguide adapter at the left. The TE<sub>10</sub> mode in the waveguide illuminates the left-hand side of the "lens" with a field that is equivalent to a pair of plane waves. The "lens" transfers a signal to the output waveguide, which is then coupled out through the receive port. By using two sets of antennas having different interconnecting line lengths, the total transmission coefficients  $S_{21}^{T'}$  and  $S_{21}^{T''}$  are obtained. The data processing proceeds as described above and the active reflection coefficient is obtained and no terminations are needed for the measurements.

#### 3.1.1 CWSA Antenna

A Constant Width Slot Antenna (CWSA) array has been extensively analyzed with method of moments computer programs [4,5]. The dimensions of a single antenna from an infinite array are shown in Fig. 5. This antenna is not well matched for any frequencies within the useful range

of the waveguide simulator, but it is an interesting example because the numerical computations predict that the antenna will have a reflection coefficient of unit magnitude in the vicinity of 4.25 GHz. The antenna has been tested in a waveguide simulator and this anomaly has been observed. The measured results are compared to the computations in Fig. 6 and the agreement is reasonably good over the frequency range of the measurements. The discrepancies at the upper end of the band are most likely due to higher order modes in the waveguide simulator. These modes begin to propagate at about 6.3 GHz and previous work with this waveguide simulator has produced unusual results for frequencies above 5.6 GHz.

The discrepancies in the reactance that occur at the lower end of the band are probably due to errors in the fabrication of the antennas. Computations show that the reactance at the lower frequencies is very sensitive to the length of the open circuited stripline stub. Errors in etching or alignment that increase the stub length by less than 0.5mm could create the discrepancies that are observed here. However, this error in stub length has a negligible effect on the impedance in the middle and upper portions of the band.

Two features of the measured data plots are important to note. The first is the gap in the data around 4.2 GHz. Because the reflection coefficient is nearly unity in this frequency range, the transmitted signal that is needed to determine  $S_{21}^{T'}$  and  $S_{21}^{T''}$  is very small; so small that noise corrupts the measurements and the data processing algorithm produces a reflection coefficient that varies wildly, sometimes appearing outside the Smith chart. This problem is not crucial for most antenna development because antennas with unity reflection coefficient are usually avoided. In any case, it is

evident from both the measured  $S_{21}^T$  and the processed value of the reflection coefficient that the antenna has a large reflection coefficient and this is usually sufficient information for the designer.

The second feature is the anomalous spike in the curve at 4 GHz. The cause of this is readily apparent from equation (2). If the antenna is very poorly matched so that the magnitude of  $S_{11}$  is nearly unity and if its phase is equal to  $+\theta$ , then the dominator of (2) vanishes. In that case, the data processing algorithm becomes ill-conditioned and is once again very sensitive to noise in a situation where the transmission coefficient that is measured is very small. Since this condition can only exist if  $|S_{11}|$  is nearly unity, it rarely occurs in practical antenna design.

### 3.1.2 LTSA Antenna

A Linearly Tapered Slot Antenna (LTSA) array has also been measured in the waveguide simulator. This antenna does not display any anomalies within the frequency range of the measurements. The dimensions of the antenna are shown in Fig. 7 and the measured results are compared to calculations in Fig. 8. The agreement here is quite good. The waveguide simulator cross-sectional dimensions for all of the measurements reported in this paper are 2.215 cm  $\times$  4.755 cm and the length of each waveguide section is 14.5 cm.

### 3.1.3 Vivaldi Antenna

A final example of the method applied to waveguide simulator measurements is the Vivaldi antenna in Fig. 9. The measured and computed results are plotted in Fig. 10, where the agreement is seen to be quite good.

### 3.2 Free-Field Results

A  $10 \times 10$  array of Broken Tapered Slot Antennas (BTSA) has been constructed and tested in a nine meter long tapered anechoic chamber that was modified by the addition of a receiving antenna so that the new measurement technique could be utilized. A schematic diagram of the setup is shown in Fig. 11. The test setup need not be symmetric. In this case, the transmit antenna is a standard gain horn and is located about seven meters from the lens. The receive antenna is an open-ended waveguide and is located about two meters from the lens.

The BTSA antenna dimensions are shown in Fig. 12 and a photo of the array installed in the ground plane is shown in Fig. 13. The grid spacing of the array is  $a = b = 1.4$  cm. The 10 printed circuit cards that make up the array are sandwiched between 11 aluminum bars. These bars are attached to a pair of  $4' \times 8'$  galvanized steel ground planes that are separated by 1.9 cm, the physical length of the shorter interconnecting line in Fig. 2(a). Measured and computed results for several scan angles are shown in Figs. 14-16. The results for the  $10 \times 10$  array agree reasonably well with predictions for the infinite array at broadside and 30 degrees in the E-plane (Figs. 14 and 15). The H-plane data exhibit an anomaly at about 9.5 GHz, where the computer simulation predicts a reflection coefficient of unity. The measurements also display an anomaly at this frequency, but the reflection coefficient is, of course, not unity for the finite array. The relationship between the anomalies predicted for the infinite array and observed for the finite array is being studied. However, with regard to the new measurement technique, it is sufficient to note here that it provides a clear indication that an anomaly may exist.



#### 4. Summary

A measurement technique has been developed for the study of phased array antennas. The technique utilizes back-to-back antenna arrays in a constrained "lens" configuration in order to experimentally determine the active reflection coefficient of elements in a large phased array. Data for arbitrary scan planes and frequencies can be obtained with relative ease and without the expense of an array feed network. It is not necessary to connectorize the array, so the expense of microwave connectors is avoided, as is the complication of deembedding a transition from a coaxial measurement system to the transmission medium used for the array elements. Comparison of measured results with computations for infinite arrays of notch antenna elements demonstrates that the method easily detects catastrophic effects like scan blindness or element resonances. It also provides reasonably accurate predictions of the active reflection coefficient, up to a sign ambiguity, for antennas that are well matched. In particular, waveguide simulator measurements employing the technique agree very well with predictions. Free field measurements of a  $10 \times 10$  element array of BTSA notches also agree reasonably well with predicted values obtained from an analysis of infinite arrays.

The new measurement technique is an alternative to existing measurement techniques, such as active element patterns, single- and multiple-element waveguide simulators, and fully driven arrays. Further development of the technique is in progress and it is anticipated that it will become another tool in the antenna engineer's kit of solutions to problems of antenna array design.

## 5. Acknowledgement

The authors thank Joon Shin and Eyal Gerecht who assisted with some of the measurements and computations. This work was supported in part by the U.S. Army Research Office under grant number DAAL03-92-G-0295.

## 6. References

- [1] P.W. Hannan and M.A. Balfour, "Simulation of a Phased-Array Antenna in Waveguide," *IEEE Trans. Ant. Propagat.*, AP-13, pp. 342-353, May 1965.
- [2] J.J. Gustincic, "The Determination of Active Array Impedance with Multielement Waveguide Simulators," *IEEE Trans. Ant. Propagat.*, AP-20, pp. 589-595, September 1972.
- [3] L.R. Lewis and A. Hessel, "A Novel Small Array Technique for Phased Array Impedance Measurement," *IEEE Trans. Ant. Propagat.*, pp. 107-110, January 1972.
- [4] M.E. Cooley, D.H. Schaubert, N.E. Buris and E.A. Urbanik, "Radiation and Scattering Analysis of Infinite Arrays of Endfire Slot Antennas with a Ground Plane," *IEEE Trans. Ant. Propagat.*, AP-39, pp. 1615-1625, November 1991.
- [5] D.H. Schaubert, J.A. Aas, M.E. Cooley, and N.E. Buris, "Moment Method Analysis of Infinite Stripline-Fed Tapered Slot Antenna Arrays with a Ground Plane," to appear, *IEEE Trans. Ant. Propagat.*, August 1994.

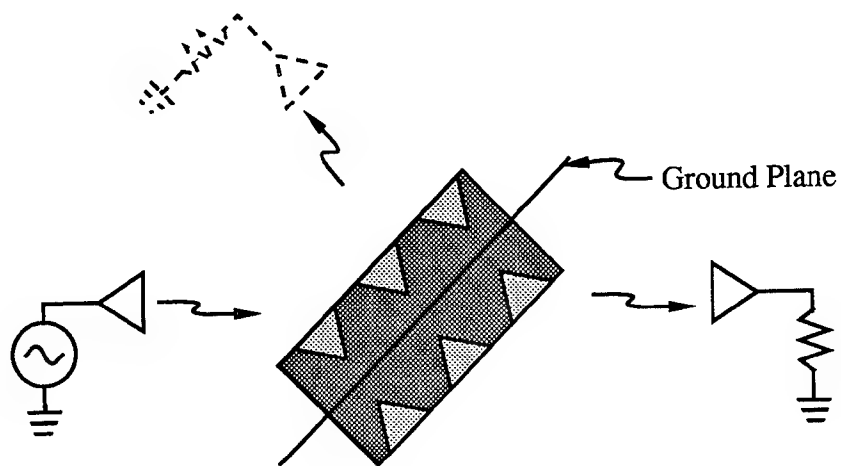
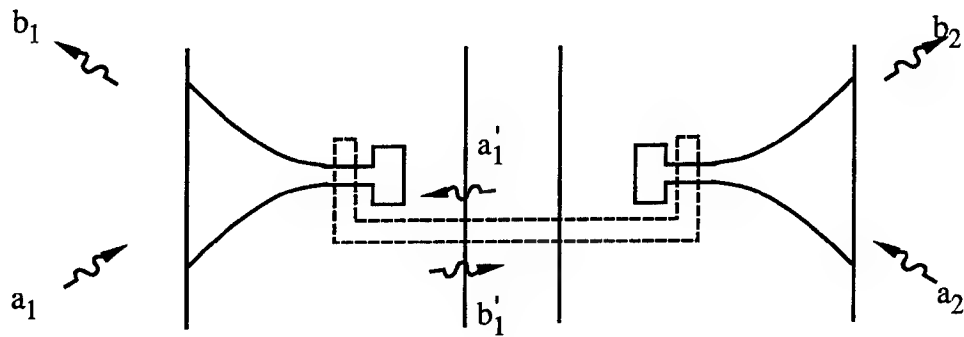
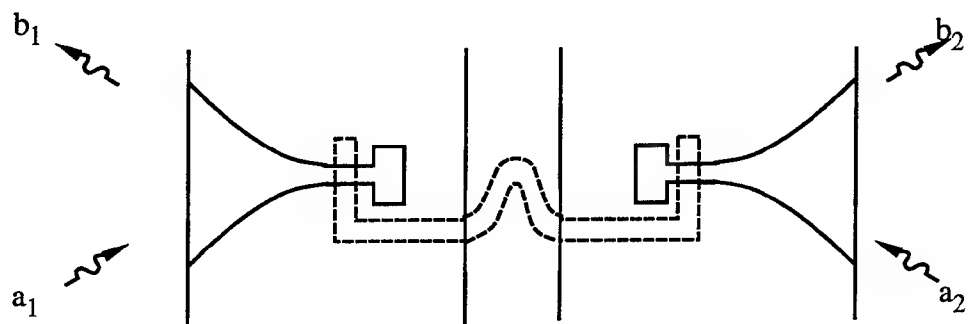


Figure 1. Transmission measurement through back-to-back arrays. Reflected signal measurements are not required for the determination of active reflection coefficient.



(a)



(b)

Figure 2. Pair of elements from lens. (a) Short interconnecting line. (b) Longer interconnecting line.

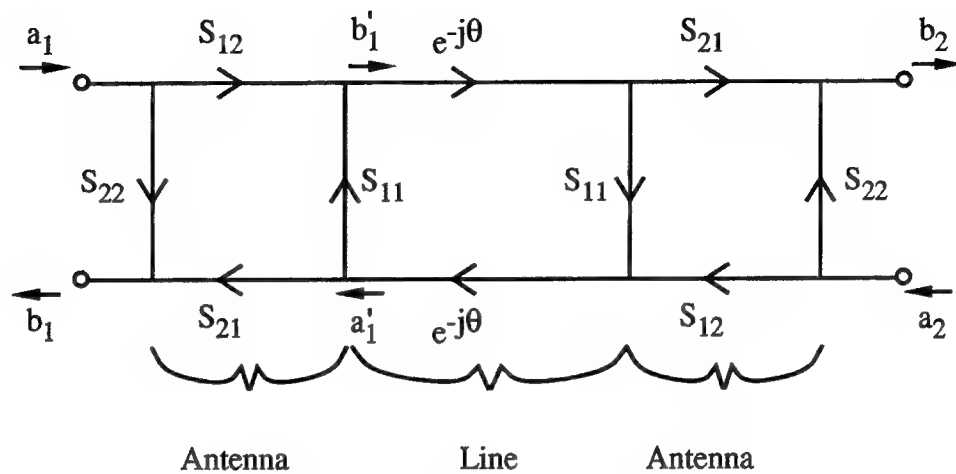


Figure 3. Signal flow graph for a pair of antennas in the lens.

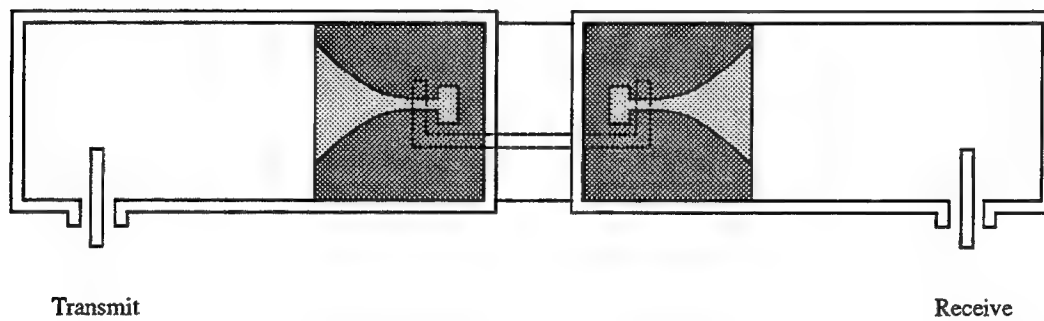


Figure 4. Connectorless measurement of active reflection coefficient utilizing waveguide simulator methodology.

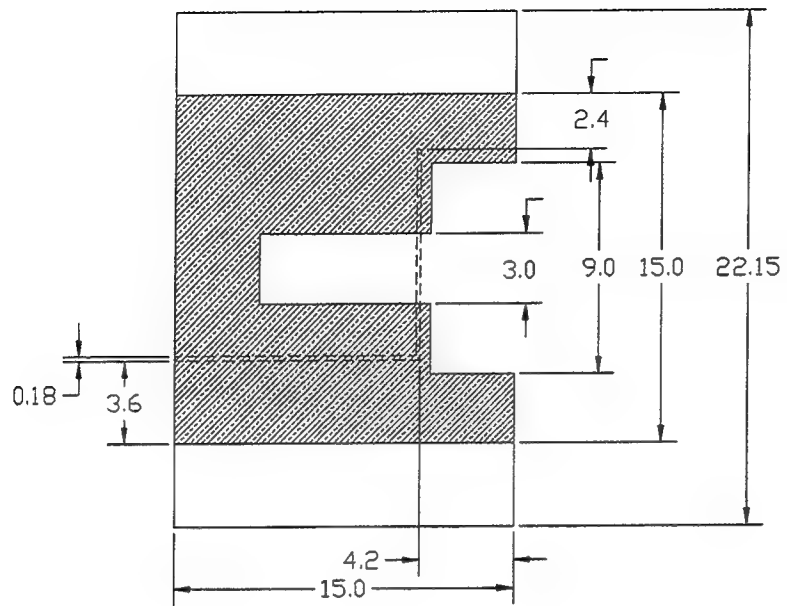


Figure 5. CWSA antenna for use in waveguide simulator.

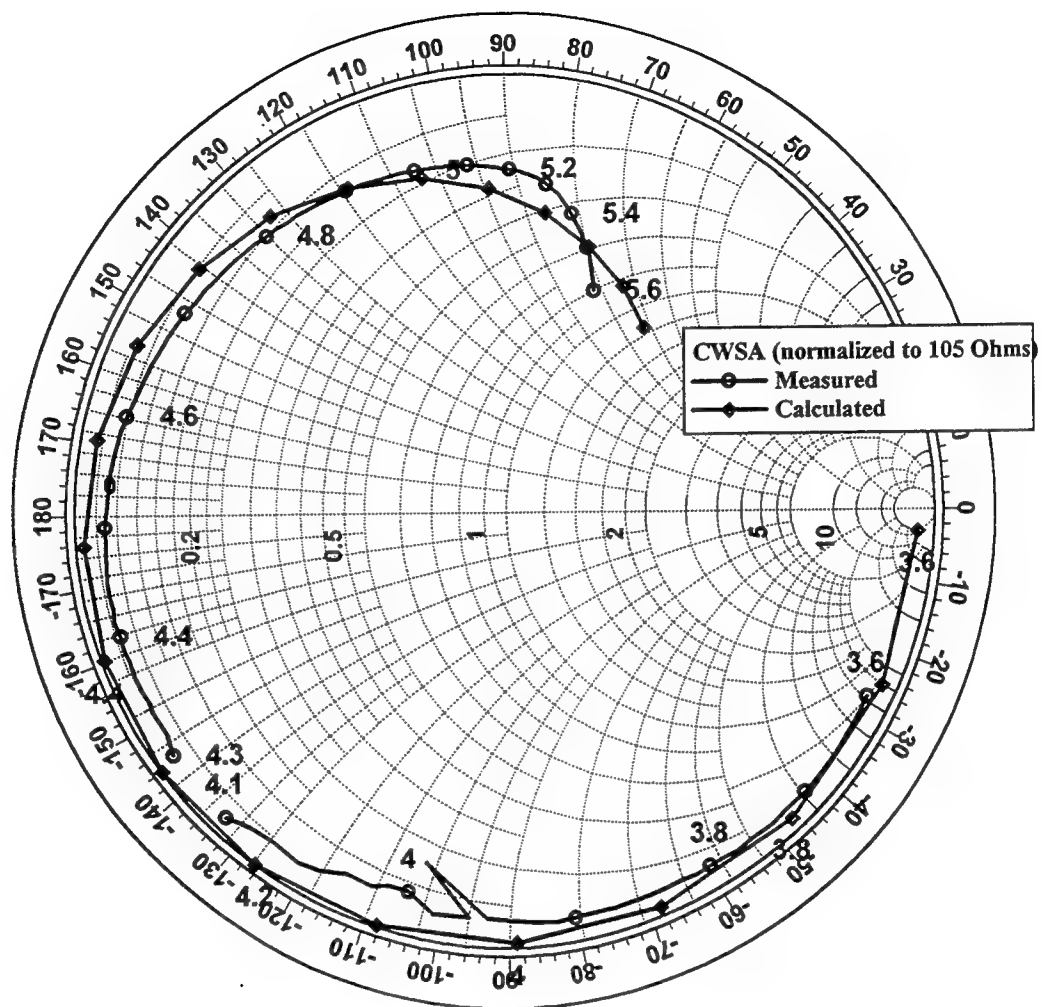


Figure 6. Measured and computed input impedance of CWSA antenna array. Array grid:  $a = 2.38$  cm,  $b = 2.22$  cm. Antenna thickness:  $t = 0.1$  cm,  $\epsilon_r = 2.2$ . Frequency increment = 0.2 GHz.

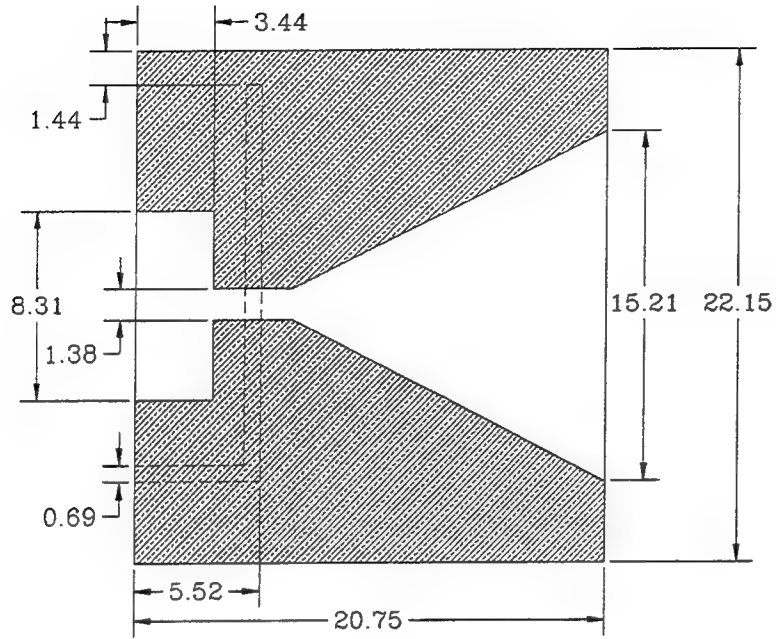


Figure 7. LTSA antenna for use in waveguide simulator.



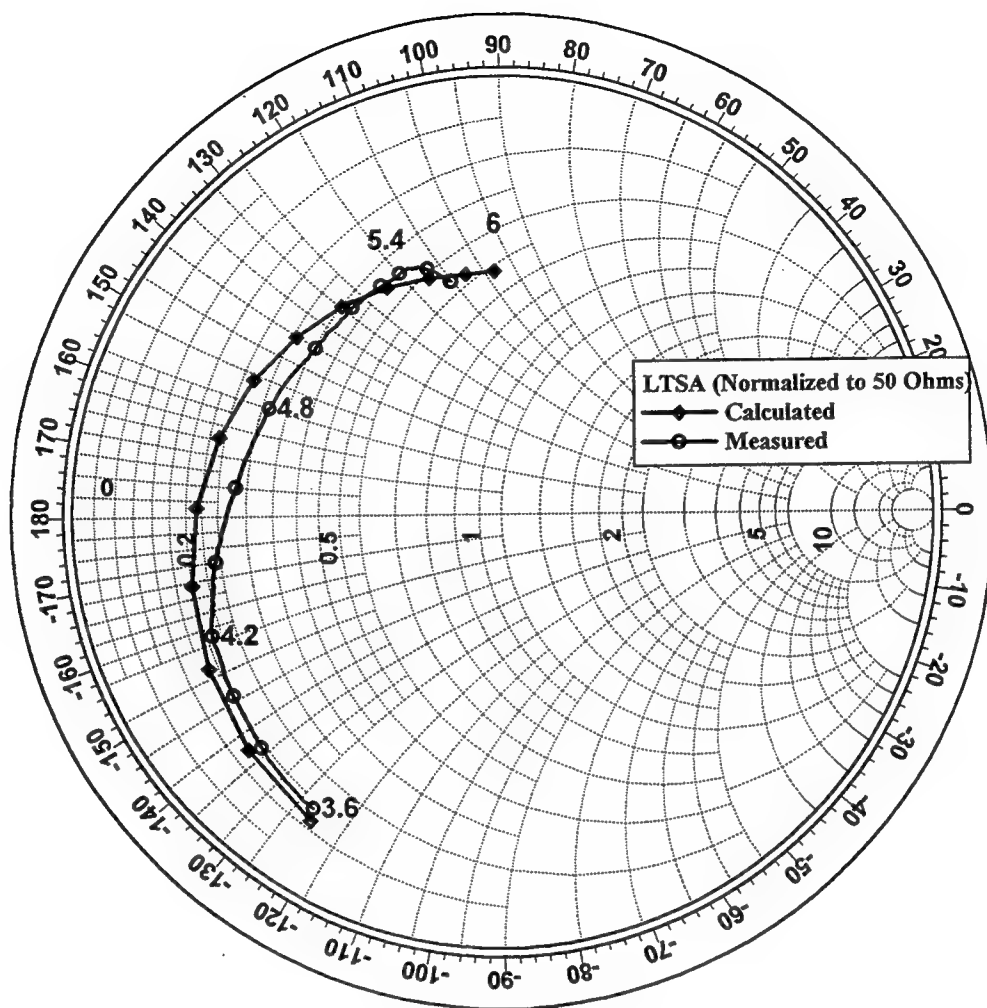


Figure 8. Measured and computed input impedance of LTSA antenna.  $a = 2.38$  cm,  $b = 2.2$  cm,  $t = 0.1$  cm,  $\epsilon_r = 2.2$ . Frequency increment = 0.2 GHz.

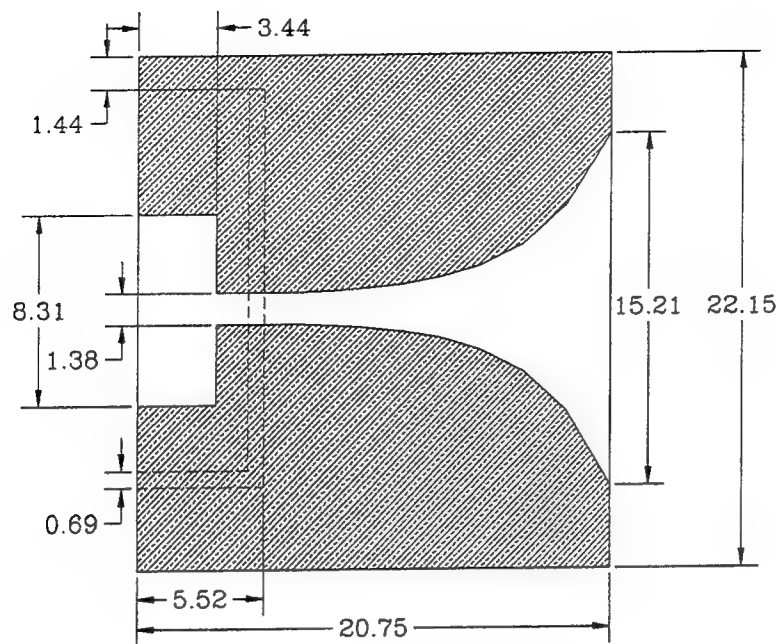


Figure 9. Vivaldi antenna for use in waveguide simulator.

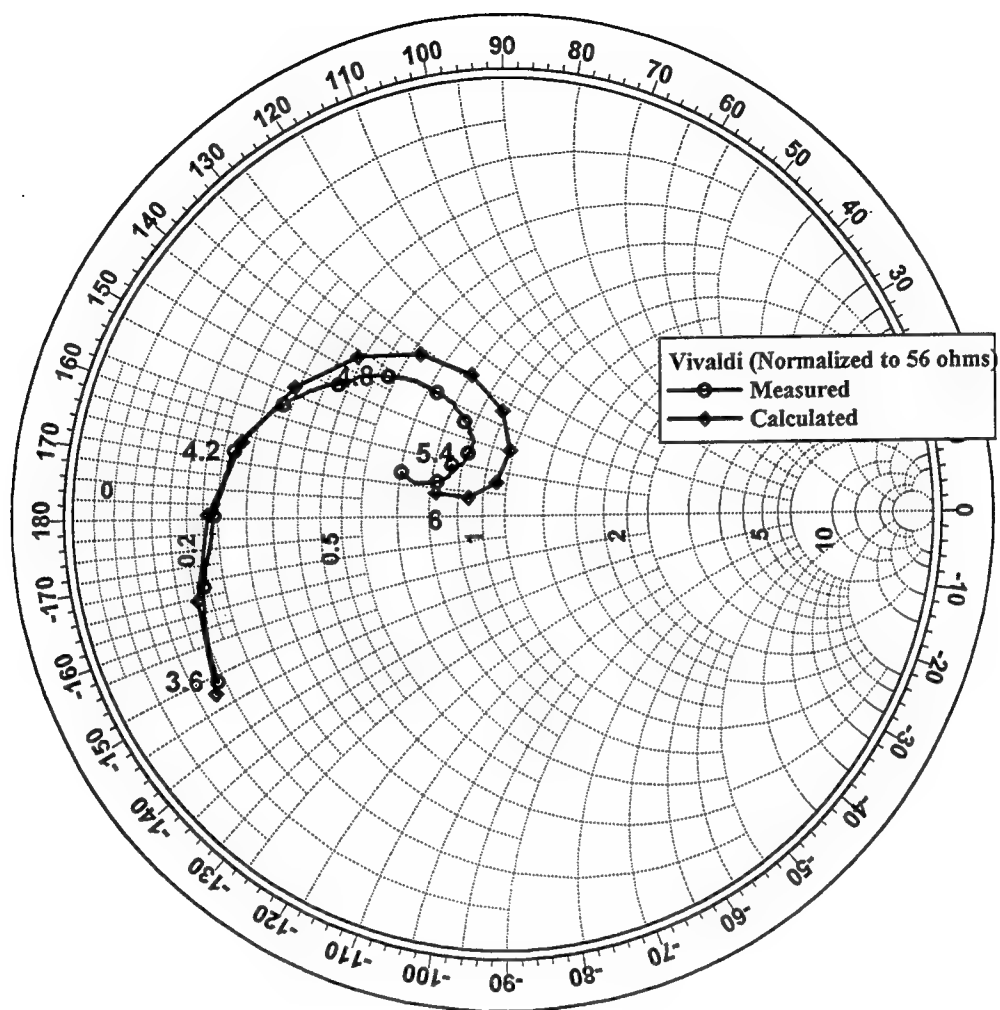


Figure 10. Measured and computed input impedance of Vivaldi antenna.  $a = 2.38$  cm,  $b = 2.22$  cm,  $t = 0.1$  cm,  $\epsilon_r = 2.2$ . Frequency increment = 0.2 GHz.

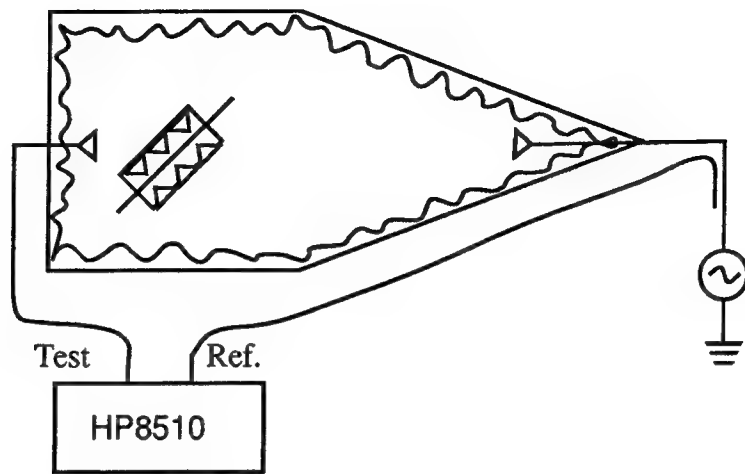


Figure 11. Setup for free-field measurements in tapered anechoic chamber.

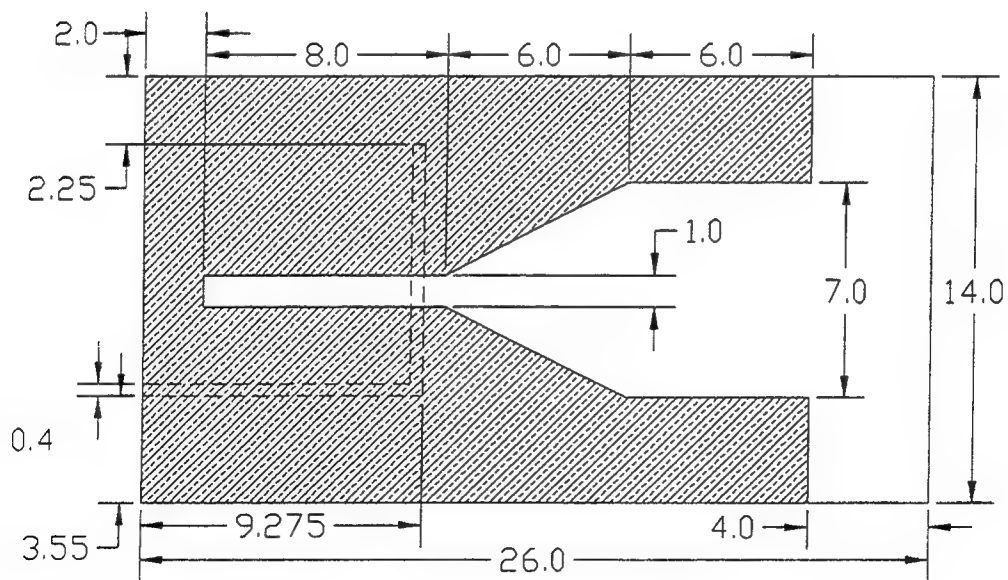


Figure 12. BTSA element used in  $10 \times 10$  array.

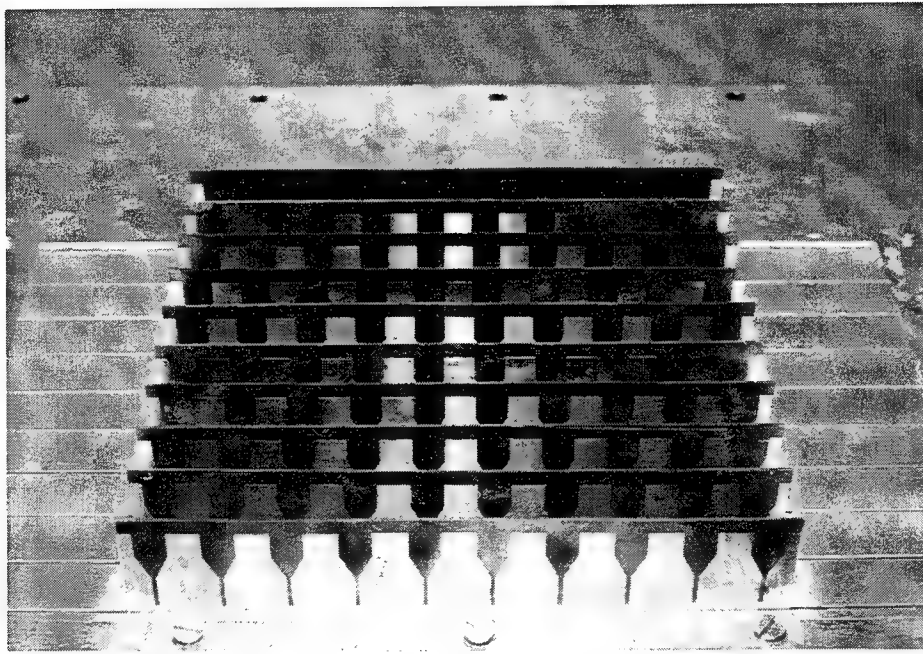


Figure 13.  $10 \times 10$  array of BTSA elements mounted in ground plane.

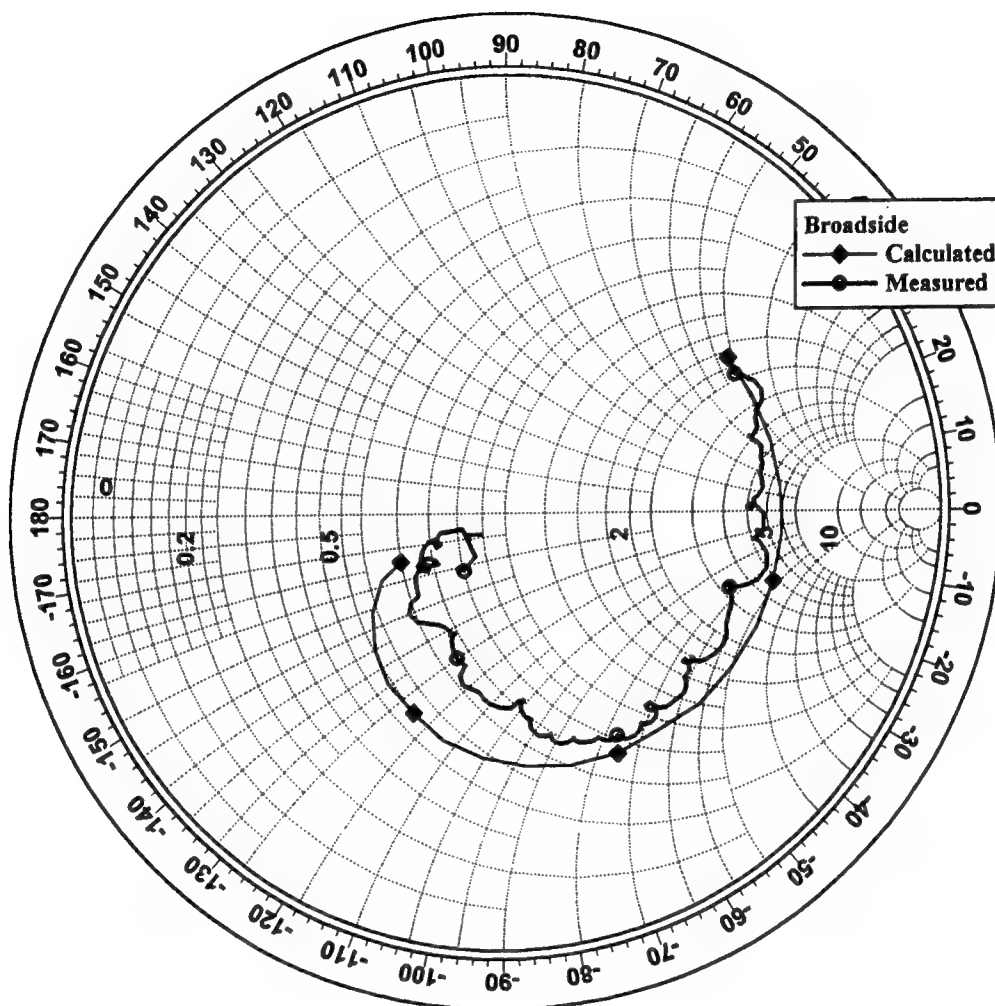


Figure 14. Measured impedance for 10 x 10 array of BTSA and computations for infinite array. Broadside scan. Frequency = 8-12 GHz, increment = 1 GHz.

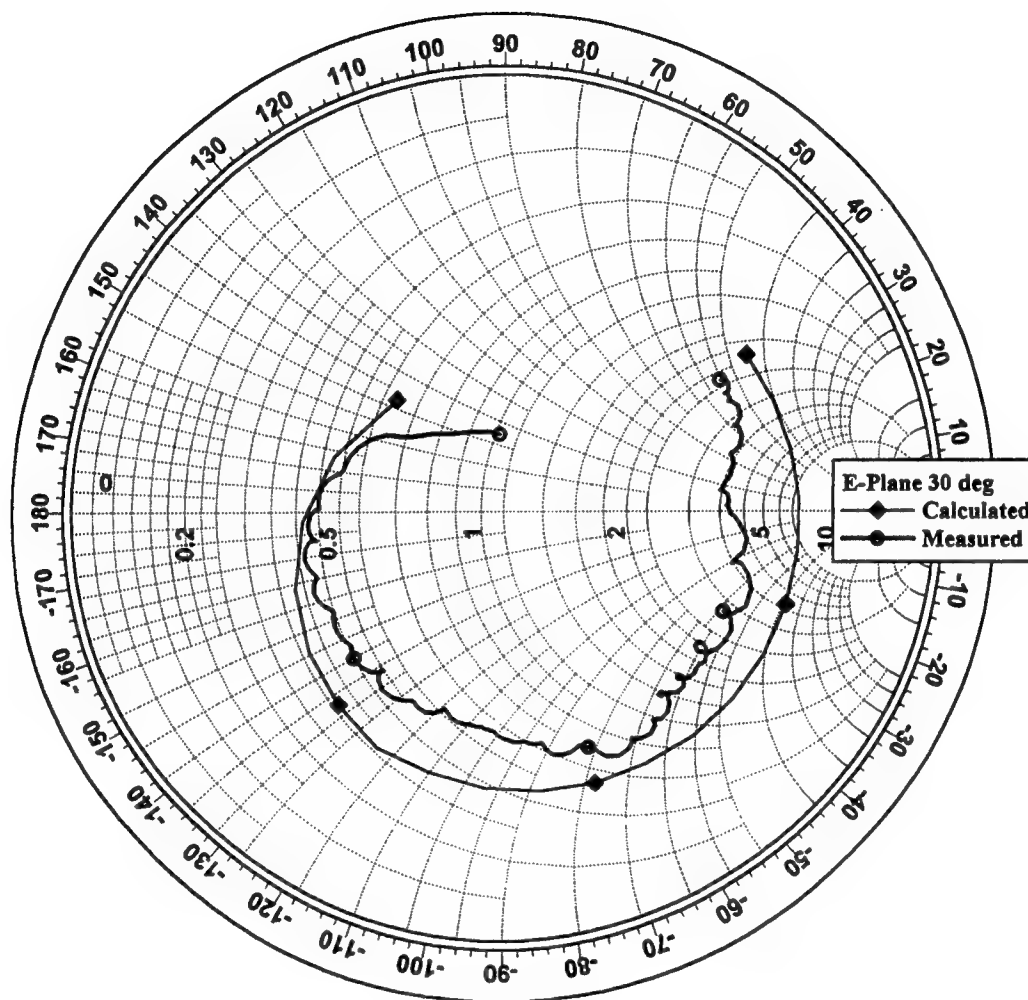


Figure 15. Measured impedance for 10 x 10 array of BTSA and computations for infinite array. Scanned  $30^\circ$  in E-plane. Frequency = 8-12 GHz, increment = 1 GHz.

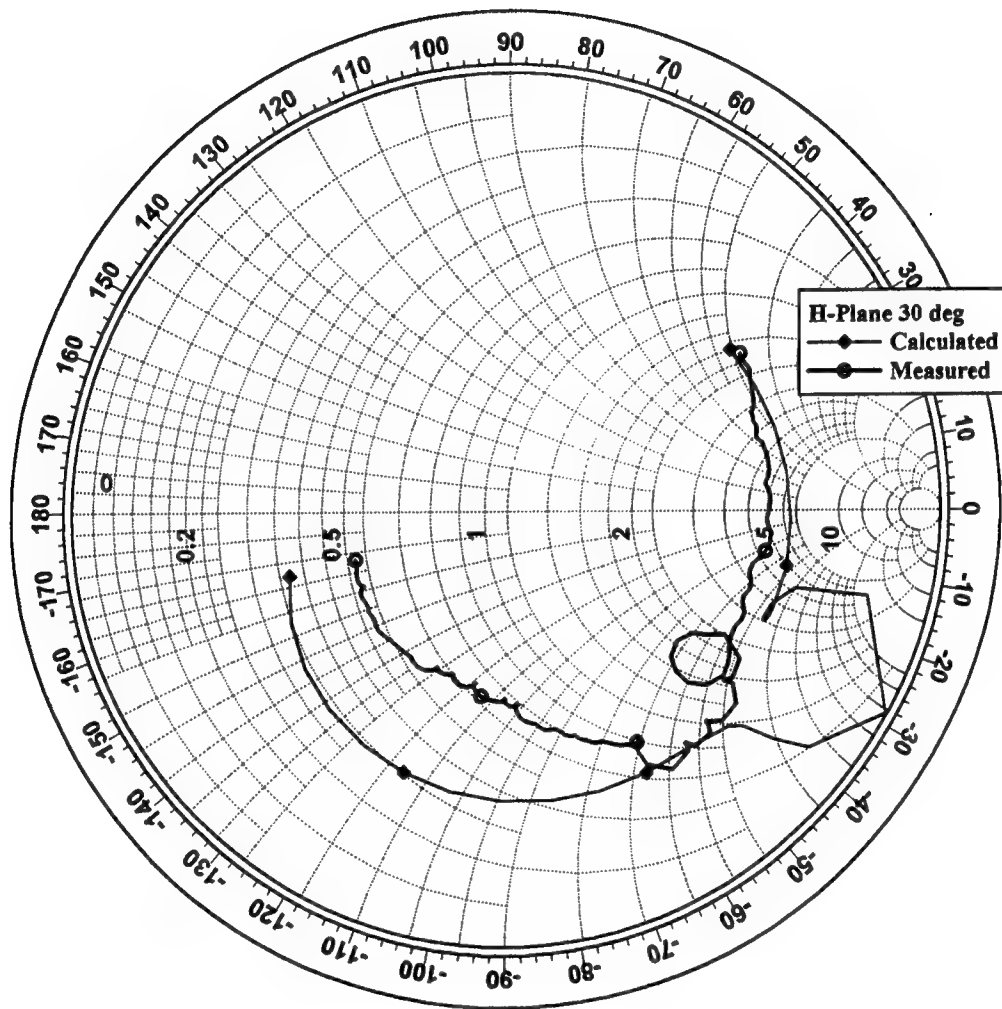


Figure 16. Measured impedance for 10 x 10 array of BTSA and computations for infinite array. Scanned  $30^\circ$  in H-plane. Frequency = 8-12 GHz, increment = 1 GHz.



## USE OF ADMITTANCE-WALL MODELS IN THE ANALYSIS OF ANNULAR SECTOR RADIATING LINE ANTENNAS

D. J. Tammen  
Communications Research Laboratory  
Motorola  
Schaumburg, IL

P. E. Mayes  
Electromagnetics Laboratory  
University of Illinois  
Urbana, IL

### Abstract

This paper describes the development of analytical models for the Annular Sector Radiating Line (ANSERLIN) antenna. The models provide data and insights into the operation of the antenna without requiring large amounts of computation. A first-order model is obtained by solving for the fields of a closed waveguide with perfect electric conducting (PEC) top and bottom walls and perfect magnetic conducting (PMC) side walls. The propagation constant obtained from these fields of the closed waveguide is then used in the equivalent magnetic current filaments to obtain the radiated fields. Use of the propagation constant of the closed waveguide fields does not include the fringing and radiation behavior. A second-order model was developed in which the radiation loss and fringing fields are included by putting a small complex admittance on the side walls rather than having PMC side walls. Two formulations were developed to include the radiation loss in the representation: a coupled-mode formulation and an eigenvalue formulation. The coupled-mode formulation, which is similar to that described by Schelkunoff for a waveguide with lossy conductors, is used to obtain the complex-valued propagation constant. In the eigenvalue formulation, the eigenvalues obtained from the solution of the characteristic equation of the waveguide with admittance side walls are used to obtain the complex-valued propagation constant. This complex-valued propagation constant, which includes the fringing and radiation behavior, is then used in the equivalent magnetic current filaments to obtain the radiated fields. Good agreement was found between measured results and results computed using the eigenvalue formulation for thin antenna structures. The agreement was not as good for thicker structures or for results obtained using the coupled-mode formulation. The general characteristics of the radiation patterns of ANSERLIN elements can be obtained using only a small number of circularly polarized spherical modes in the field expansion. A study of the modal distribution as a function of frequency was done for the ANSERLIN antenna. For a given geometry, it was found that as the frequency was increased more coupling into the higher-order circularly polarized free space modes occurred. This shifting of the mode mixtures with changing frequency explains the beam tilt observed for the ANSERLIN antenna.

### 1. Introduction

In the past few years there has been significant interest in low-profile, circularly polarized antennas. In many applications, unidirectional, broadside radiation is desired. Low-profile, circularly polarized antennas are often used on aircraft for communication, threat warning and direction-finding applications. For such applications, the antenna

would be flush mounted on the wings or the fuselage. Low-profile, circularly polarized antennas are often used for other mobile communication systems.

In the course of studies of cavity-backed spiral antennas, a single-turn spiral was tested to evaluate the amount of power radiated [1]. The one-turn spiral with a port on each end displayed useful properties and led to the development of the Annular Sector Radiating Line (ANSERLIN) antenna [1], [2]. The ANSERLIN provides a very simple antenna with moderate bandwidth, greater than that of circularly polarized microstrip patches, even those with multiport feeds, but less than that of the larger, more complex multiarm spirals. The geometry of a typical probe-fed ANSERLIN element is given in Figure 1. As seen in the figure, an ANSERLIN element is a two-port antenna composed of a wide, curved strip transmission line with air dielectric. The triangular-shaped feed transitions at the ends of the annular microstrip line are needed to maintain a constant impedance as the height of the line is reduced for the feed gap. Either sense of circular polarization can be realized by simply exciting the appropriate port of the antenna while maintaining a good impedance match at the other port.

Unlike the resonant microstrip patch antennas, the ANSERLIN antenna was found to have a very broad impedance bandwidth and a fairly broad pattern bandwidth. It also has a simple feed structure. Since the ANSERLIN elements are inherently two-port devices, they are particularly well-suited for use in series-fed arrays [3]. Various array excitations can be achieved by controlling the fraction of input power that is radiated by each element. This can be done by varying the height while changing the width to maintain the impedance. ANSERLIN elements have also been found to exhibit a tilt of the main beam as a function of frequency. This phenomenon has proved useful in the design of arrays for low-angle coverage. Initially, the relationships between the element geometry and the relative power radiated and that between the beam tilt and frequency were obtained experimentally [1], [2]-[4].

Wood developed a theoretical analysis of a curved radiating line antenna similar to the ANSERLIN [5]. In his analysis, he used a single magnetic current filament of uniform amplitude and traveling-wave phase located at the center radius of the annular line to obtain far-field radiation patterns and an approximation to the total power radiated. From the power radiated, he obtained the power radiated per unit length of arc. He then recalculated the radiation patterns including the radiation loss in the current distribution. Drewniak also investigated the radiation from an annular arc of magnetic current (but along the outer periphery) for both a uniform amplitude traveling wave and a traveling wave with a propagation constant that included the radiation loss as computed from S-

parameter measurements of ANSERLIN elements [1]. Bowen used a wire-grid model with the Numerical Electromagnetics Code (NEC) to model an ANSERLIN element [4]. The radiation patterns found using NEC agreed reasonably well with measured results, but the predicted power radiated was found to be less than that measured. Smith modeled the ANSERLIN antenna using a surface patch implementation of the moment method (MOM) technique [6]. The computed radiation patterns agreed well with measurements. The power radiated from the ANSERLIN antenna computed using the MOM code also agreed well with measured data. However, the amount of computation necessary to obtain a solution was considerable and provided little intuition about performance. It was the goal of the research presented in this paper to develop a model for the ANSERLIN antenna that would provide design information without requiring large amounts of computation and that would also furnish an alternate interpretation for the radiation mechanism. A more accurate representation of the  $\phi$ -dependence of the fields and magnetic currents utilizing a technique which included the radiation loss of the antenna in the representation will be described. Formulations were developed which separately considered the interior closed waveguide problem and the external radiation problem through the use of a complex admittance on the side walls of the annular waveguide system.

For the annular geometry a complex propagation constant for the  $\phi$ -direction will result from the solution of coupled-mode and eigenvalue formulations. The starting point for the methods is a closed waveguide problem with perfect electric conducting (PEC) top and bottom walls and perfect magnetic conducting (PMC) side walls. The waveguide in this case is a toroidal waveguide with rectangular cross section as depicted in Figure 2. Solving the source-free boundary-value problem for this waveguide gives expressions for the electric currents in the top and bottom walls and magnetic currents in the side walls for the various modes. The PEC top and bottom walls and PMC side walls can then be replaced by the induced sources in free space determined from the appropriate tangential components of the fields. For this set of induced sources, the fields in the region bounded by the sources will be the same as those for the waveguide with the PEC top and bottom walls and PMC side walls. The fields beyond the sources will be zero as in the original waveguide.

The ANSERLIN antenna corresponds to a toroidal waveguide from which the PMC walls have been removed (corresponding to removal of the induced magnetic currents). It is asserted that removing the PMC side walls will not appreciably affect the currents in the PEC walls, particularly when the vertical height is small. Hence, the fields of the ANSERLIN structure can be determined approximately by using the electric currents of

the lowest-order closed waveguide mode. Therefore, these currents can be used to find transverse ( to  $\rho$  ) near fields in the aperture at the edges of the ANSERLIN element. To the extent that these fields have a constant ratio, complex-valued wall admittances can be found. These admittances include not only the effect of radiation, but also the stored energy of the fringing field at the edge of the conductor. The complex-valued wall admittances can then be used as new boundary values in both the coupled-mode and eigenvalue formulations. Solutions of the resulting equations result in complex-valued propagation constants for the  $\phi$ -direction. The propagation constant found using either formulation can then be used to calculate the radiation loss of the ANSERLIN structure as well as substituted into the circularly polarized multipole-field expansion to obtain far-field radiation patterns.

The coupled-mode formulation for the circular geometry of the ANSERLIN is similar to that developed for a linear geometry. The complex wall admittance results in the coupling of the previously uncoupled toroidal waveguide modes. The coupling of the lowest-order waveguide mode to the higher-order modes alters the propagation constant in  $\phi$  of this lowest-order mode.

In the eigenvalue formulation for the toroidal waveguide geometry, the  $\phi$  behavior is not explicitly separable from the radial behavior. Therefore, it is necessary to obtain the modified  $\phi$  behavior from the root of the characteristic equation that is obtained by application of the small complex admittance boundaries in place of the magnetic walls. The root to be found is the order of the Bessel functions in the characteristic equation. The complex boundaries cause the order of the Bessel functions to become complex-valued. This complex order of the Bessel functions (multiplied by  $j$ ) is the propagation constant for the  $\phi$ -direction.

Measurements made by Drewniak on the ANSERLIN structure demonstrated that the radiation patterns are primarily circularly polarized over a wide portion of a broad beam in the direction broadside to the plane of the antenna [1], [2]. This suggests that the fields might be simply expressed using the radiation modes of spherical coordinates. The broad beamwidth and azimuthal phase variation proportional to angle indicate that only a relatively small number of circularly polarized modes would be needed. A circularly polarized multipole-field expansion of the fields of the ANSERLIN antenna was developed following a procedure outlined by Liang and Lo [7]. Multipole coefficients for the TE and TM to  $r$  modes were derived for an annular magnetic current filament with traveling-wave (in the  $\phi$ -direction) behavior using the standard multipole expansion given in Jackson [8]. A comparison of the computed far-field radiation patterns to measured

results for an appropriate ANSERLIN antenna found that the general characteristics of the radiation patterns could be obtained using only a few circularly polarized modes.

## 2. Review of Fields for Toroidal Waveguide Geometry

The pertinent fields for the toroidal waveguide geometry shown in Figure 2 will be presented. The most desirable coordinate system in which to express the fields for the toroidal geometry is cylindrical coordinates ( $\rho, \phi, z$ .) For a thin (in  $z$ ) waveguide the general TM field expressions in cylindrical coordinates are given by [9]

$$E_z = \frac{k^2}{j\omega\epsilon} [A J_v(k\rho) + B N_v(k\rho)] e^{\pm jv\phi} \quad (1a)$$

$$H_\rho = \pm \frac{jv}{\rho} [A J_v(k\rho) + B N_v(k\rho)] e^{\pm jv\phi} \quad (1b)$$

$$H_\phi = -k [A J_v'(k\rho) + B N_v'(k\rho)] e^{\pm jv\phi} \quad (1c)$$

where  $J_v(k\rho)$  is the Bessel function of the first kind and  $N_v(k\rho)$  is the Bessel function of the second kind.

For the closed waveguide, the boundary conditions for TM modes are

$$H_\phi|_{\rho=a} = H_\phi|_{\rho=b} = 0 \quad (2)$$

Applying these boundary conditions to (1c) and solving for the characteristic equation for the closed toroidal waveguide with PMC side walls results in

$$J_v'(ka)N_v'(kb) - J_v'(kb)N_v'(ka) = 0 \quad (3)$$

The transcendental equation given by (3) was solved using the Mathematica software to give plots of  $ka$  as a function of  $v$  for  $b/a$  ratios of 4., 2.5 and 1.75. These plots are given in Figures 3 to 5, respectively. The Mathematica software allowed solutions for Bessel functions of complex and imaginary orders. Therefore, the evanescent behavior of the annular waveguide modes could be obtained. The dominant mode is seen to have no cutoff frequency as expected. The higher-order modes, which are associated with higher-order zeros of (3), have cutoff frequencies which increase with decreasing  $b/a$  as is

observed for linear waveguide geometries. Thus, the higher-order modes of narrower toroidal waveguides would be expected to decay more rapidly below cutoff for a given frequency than the higher-order modes of wider waveguides. For fixed impedance ANSERLIN elements, the height of the element must be increased as the width of the annular microstrip line is increased. Therefore, use of only the dominant closed waveguide mode in calculation of the equivalent currents would be expected to give better results for thin (in  $z$ ) structures than for thicker structures.

### 3. Coupled-mode Formulation for the ANSERLIN Geometry

Using the field expressions developed in the preceding section as a starting point, a coupled-mode formulation similar to that given by Schelkunoff for a lossy waveguide [10] can be derived for the ANSERLIN antenna shown in Figure 1. This derivation was done in detail in the technical report by Tammen and Mayes [11] and the resulting modal propagation constants and coupling coefficients were found to be

$$\gamma_m = \sqrt{Z_{mm} Y_{mm}} = \sqrt{-v_m^2 + j \frac{2dk\eta}{N_m^2} \left( Y_{w1} a \psi_m^2 \Big|_{\rho=a} + Y_{w2} b \psi_m^2 \Big|_{\rho=b} \right)} \quad (4a)$$

$$c_{mn} = \frac{1}{2} z_m Y_{mn} z_n = \frac{2dk\eta N_m^{-1} N_n^{-1} \left( Y_{w1} a \psi_n \psi_m \Big|_{\rho=a} + Y_{w2} b \psi_n \psi_m \Big|_{\rho=b} \right)}{\left[ v_m^2 - j \frac{2dk\eta}{N_m^2} \left( Y_{w1} a \psi_m^2 \Big|_{\rho=a} + Y_{w2} b \psi_m^2 \Big|_{\rho=b} \right) \right]^{\frac{1}{4}} \left[ v_n^2 - j \frac{2dk\eta}{N_n^2} \left( Y_{w1} a \psi_n^2 \Big|_{\rho=a} + Y_{w2} b \psi_n^2 \Big|_{\rho=b} \right) \right]^{\frac{1}{4}}} \quad (4b)$$

$$\text{where } z_m = \left( \frac{Z_{mm}}{Y_{mm}} \right)^{1/4}$$

$$\text{with } \psi_n = \left[ J_{v_n}(k\rho) - \frac{J_{v_n}'(ka)}{N_{v_n}'(ka)} N_{v_n}(k\rho) \right] \quad (5)$$

$n$  = the index which orders the roots of (3)

$$N_n^2 = \int_{-d}^d \int_a^b \frac{\psi_n^2}{\rho} d\rho dz \quad (6)$$

$Y_{w1}$  = the complex admittance at  $\rho=a$  and  $Y_{w2}$  = the complex admittance at  $\rho=b$

The value of  $\gamma_1$  found from (4a) is the propagation constant of the lowest-order waveguide mode found using the coupled-mode formulation. Initially it is assumed that the radiation loss due to the open side walls can be found from the imaginary portion of  $\gamma_1$  only. Equation (4b) shows that there will be coupling of energy to the higher-order curved waveguide modes for non-zero  $Y_{w1}$  and  $Y_{w2}$  since  $\psi$  is not zero in general. However, any energy coupled to the higher-order modes will be attenuated since the fields will be decaying for the higher-order modes.

The admittances  $Y_{w1}$  and  $Y_{w2}$  used in the preceding expressions can be found from the ratio of  $H_\phi$  and  $E_z$  in the apertures  $\rho=a$  and  $\rho=b$ . Near-field expressions for  $H_\phi$  and  $E_z$  can be derived for the radiating line using the direct method [12]. It is assumed that the electric currents in the top and bottom conductors are nearly the same for the radiating case as for the case with PEC top and bottom walls and PMC side walls. The equivalent electric currents can thus be determined from the fields of the closed waveguide case.

#### 4. Eigenvalue Formulation for the ANSERLIN Geometry

The geometry and orientation of the ANSERLIN antenna are shown in Figure 2. The general characteristic wave function for the TM to z representation of the fields for thin (in z) structures is given by (3). Expressions for the TM to z fields are given in (1a) to (1c). To derive the transcendental characteristic equation for the toroidal waveguide geometry with complex-valued admittance boundaries the ratio of the transverse (to  $\rho$ ) field expressions is found at  $\rho=a$  and  $\rho=b$ . From the boundary condition on one wall, the unknown coefficient relating the Bessel functions can be found. Application of the other boundary condition results in a transcendental equation from which the complex value of the order of the Bessel functions can be determined [11].

$$\begin{aligned}
& J_v'(kb)N_v'(ka) - J_v'(ka)N_v'(kb) + j\eta \frac{H_\phi}{E_z} \Big|_{\rho=a} \left[ J_v(ka)N_v'(kb) - N_v(ka)J_v'(kb) \right] \\
& = j\eta \frac{H_\phi}{E_z} \Big|_{\rho=b} \left[ J_v(kb)N_v'(ka) - N_v(kb)J_v'(ka) \right] \\
& + (j\eta)^2 \frac{H_\phi}{E_z} \Big|_{\rho=a} \frac{H_\phi}{E_z} \Big|_{\rho=b} \left[ N_v(kb)J_v(ka) - J_v(kb)N_v(ka) \right]
\end{aligned} \tag{7}$$

If the admittance boundaries at  $\rho=a$  and  $\rho=b$  are replaced with perfect magnetic conducting material, the more general characteristic equation given by (7) reduces to the characteristic equation found earlier for the closed annular waveguide case. For the ANSERLIN, the propagation constant would be expected to be complex to account for the attenuation of the fields due to radiation. The propagation constant is given by the order of the Bessel functions in (7). Thus, a complex-valued order for the Bessel functions would be the expected solution of the transcendental equation. In order to solve (7) for the complex order, the ratios of the transverse fields ( $H_\phi/E_z$ ) were determined.

##### 5. Attenuation Due to Radiation

As a test of the coupled-mode and eigenvalue formulations, a comparison was done of the attenuation of the dominant mode as determined from measured results and that computed by the two formulations. The attenuation of the dominant mode due to radiation can be found experimentally for a well-matched ANSERLIN antenna (neglecting conductor and dielectric losses) from a measurement of the transmission S-parameter ( $S_{21}$ ). The attenuation can be computed from the real part of the propagation constant in the  $\phi$ -direction found using the coupled-mode and eigenvalue formulations.

The propagation constant in the  $\phi$ -direction for the lowest-order waveguide mode using the coupled-mode formulation is given by (4a) and can be found directly once the complex values of the wall admittances  $Y_{w1}$  and  $Y_{w2}$  have been determined from the near fields at the apertures. The integral expressions for the transverse aperture fields ( $H_\phi$  and  $E_z$ ) were integrated numerically using a two-dimensional Romberg integrator to obtain values for  $Y_{w1}$  and  $Y_{w2}$ . The observation angle was chosen to be  $180^\circ$ . An annular arc of current of  $270^\circ$  extent was used since that is the approximate angular extent of the annular sector of the ANSERLIN antennas measured. Uniform amplitude was used between



sinusoidal spline end transitions (See Figure 6) which were of 45° angular extent with the spline fraction set to a value of 0.5.

To calculate the propagation constant using the eigenvalue formulation, the transcendental equation given by (7) must be solved. The Mathematica program was used to determine the solution since it has provisions for determination of the value of Bessel functions of complex order. It also includes a routine which solves for the roots of transcendental equations. The ratios of  $H_\phi/E_z$  at  $\rho=a$  and  $\rho=b$  were determined by numerical integration of the expressions for  $H_\phi$  and  $E_z$ . The initial guesses required for the transcendental equation solver were obtained from small perturbations of the values found using the coupled-mode technique.

The real part of the propagation in the  $\phi$ -direction was calculated using the coupled-mode and eigenvalue formulations for two different annular waveguide structures. Tables 1 and 2 give the results for two cases. A comparison between the measured and calculated percent power radiated was done. The percent power radiated is given by  $(1 - |S_{21}|^2) \times 100\%$ . The value for  $|S_{21}|^2$  was calculated from the computed values of the real part of the propagation constant in the  $\phi$ -direction ( $\alpha$ ) using an angular extent of 270° (1.5 $\pi$  radians)

$$|S_{21}|^2 = e^{-2\alpha\phi} = e^{-3\pi\alpha} \quad (8)$$

The propagation constants from Tables 1 and 2 were used in (8) to obtain the calculated radiation loss. Measured results [1] are compared to calculated results for an ANSERLIN with  $b/a=2.5$ ,  $w/h=3.5$  and  $b=3.5$  cm in Figure 7 and for an ANSERLIN with  $b/a=1.75$ ,  $w/h=4.285$  and  $b=3.5$  cm in Figure 8.

The eigenvalue formulation gives a good value for the radiation loss for a thin (in  $z$ ) ANSERLIN structure but does not work as well for thicker structures. The coupled-mode formulation does not work as well for thin ANSERLIN structures as the eigenvalue formulation, but does seem to give values similar to those obtained from the eigenvalue formulation for thick structures. This suggests that the error in both methods for the thicker structures is most likely due to a failure of the part of the model which is common to both formulations. The decay of the evanescent modes for thicker annular structures was slower than that for thin structures (Figures 3 to 5). Therefore, any higher-order modes introduced at the feedpoint would not be attenuated as quickly for the thicker structures as for the thin structures. Any changes in the radiation due to the presence of

these higher-order modes have been neglected. It was found in [11] that the near fields are not uniform in the  $\phi$ -direction near the ends of the annular current arcs for thicker structures. This nonuniform behavior has also been neglected in the present model.

## 6. Calculation of the Far-field Radiation Patterns

For calculation of the far fields in the upper half space, a planar Huygens' equivalent surface can be placed at  $z=d$ . The equivalent sources on the Huygens' surface are then given by  $\bar{J}_s = \hat{z} \times \bar{H}$  and  $\bar{M}_s = \bar{E} \times \hat{z}$ . The equivalent magnetic current will be of limited extent in  $\rho$  since the tangential E-field is zero for the region with the PEC conductor and is assumed to decay rapidly with distance from the edge for a thin ANSERLIN structure. Thus the magnetic surface currents can be approximated by  $\phi$ -directed magnetic current filaments at  $\rho=a$  and  $\rho=b$ . Next, the region beneath the Huygens surface can be filled with PEC (since the fields are zero there.) Using image theory, the equivalent magnetic current filaments on the surface of the PEC are replaced by magnetic current filaments in free space with twice the magnitude, while the contribution from the electric currents is zero. The  $\phi$ -directed equivalent magnetic currents are proportional to  $E_\rho$  (from  $\bar{M}_s = \bar{E} \times \hat{z}$ ). The radial component of the E-field,  $E_\rho$ , is due to the fringing of  $E_z$  at the conductor edges. Thus,  $E_\rho$  is proportional to  $E_z$ . Since the fringing of  $E_z$  at  $\rho=a$  and  $\rho=b$  is oppositely directed (in  $\rho$ ), the equivalent magnetic current filament at  $\rho=a$  has the opposite sign of the filament at  $\rho=b$ . The relationship of the magnitudes of the equivalent magnetic current filaments is given approximately by the relationship between  $E_z$  at  $\rho=a$  and  $E_z$  at  $\rho=b$ . Sinusoidal spline functions were used at both ends of the annular magnetic current filaments to provide a smooth transition of the magnetic currents with both the functions and their derivatives being zero at the ends of the current distribution. This prevents a buildup of magnetic "charge" from occurring at the ends due to a discontinuity of the currents. The resulting magnetic current distribution is a superposition of two magnetic current rings at  $\rho=a$  and  $\rho=b$  given in spherical coordinates by

$$\bar{M} = [M_b \delta(r-b) - M_a \delta(r-a)] \delta\left(\theta - \frac{\pi}{2}\right) e^{\mp jQ\phi} F(\phi) \frac{1}{r} \hat{\phi} \quad (9)$$

The function  $F(\phi)$  is the function with the spline endcaps shown in Figure 6. The complex variable  $Q$  is the complex phase constant determined from the solution of the transcendental equation of the eigenvalue formulation (7) or from the coupled-mode formulation (4a). The constants  $M_a$  and  $M_b$  are determined from  $E_z$  at  $\rho=a$  and  $\rho=b$  as

discussed above. The minus sign corresponds to propagation in the waveguide in the  $+\phi$  direction for  $+j\omega t$  harmonic excitation, while the plus sign corresponds to propagation in the  $-\phi$  direction. For the cases considered here,  $b=3.5$  cm and  $a$  is determined from the ratio  $b/a$ .

The far-field radiation patterns were determined from the current distribution given by (9) using the multipole expansion of the fields to obtain circularly polarized far fields as well as the modal distribution which provides some insight into the operation of ANSERLIN elements. For the circularly polarized multipole expansion, the current distribution given by (9) was substituted into the expressions for the electric and magnetic multipole coefficients as found in Jackson [8]. These coefficients were then substituted into the expression for the circularly polarized expansion given by Liang and Lo [7] to obtain the right-hand and left-hand circularly polarized multipole coefficients and the circularly polarized far fields. Circularly polarized representations of the far fields were obtained from the results found. The components  $E_{\max}$  and  $E_{\min}$  are found by taking  $\|E_L\| + \|E_R\|$  and  $\|E_L\| - \|E_R\|$ , respectively. The values found for  $E_{\max}$  and  $E_{\min}$  for the computed results correspond to the edges of the envelope which would be obtained from spinning linear measurements of circularly polarized fields.

## 7. Comparison of Measured and Calculated Radiation Patterns

An ANSERLIN antenna which has  $b/a=1.75$ ,  $w/h=4.285$  and  $b=3.5$  cm was mounted on a 3 ft aluminum disc and far-field radiation patterns measurements were made. To obtain the circularly polarized response of the antenna, cuts with two orthogonal positions of the receive antenna were taken. The circularly polarized response was determined by combining the two orthogonal linear responses (magnitude and phase) with the appropriate phase shift.

The far-field radiation patterns were calculated for an ANSERLIN antenna with  $b/a=1.75$ ,  $w/h=4.285$  and  $b=3.5$  cm using the formulation described in the preceding section. The orientation of the antenna for the measurements and calculations is shown in Figure 9. For the results described, the antenna was excited at port 1, which would result in a traveling wave in the  $+\phi$  direction. The feedpoint was taken to be the  $0^\circ$  reference point in the  $\phi$  direction for the magnetic current given by (9). The cuts were taken in elevation with the  $0^\circ$   $\theta$  angle being normal to the plane containing the antenna and the  $-90^\circ$   $\theta$  angle corresponding to the plane containing the antenna on the feed side of the antenna. A matched load was placed on the opposite port.

In Figures 10 to 15 measured and computed radiation patterns are compared at 1.6 GHz, 1.8 GHz and 2.0 GHz for both  $90^\circ$  and  $0^\circ$  cuts. An angular extent of  $270^\circ$  of current was used in the integration of the currents required to calculate the complex wall admittances required for the eigenvalue formulation. An angular extent of  $270^\circ$  with  $45^\circ$  sinusoidal-spline endcaps was used when calculating the far-field radiation patterns with the circularly polarized multipole expansion. For this set of patterns, the number of modes used in the expansion was 120.

Looking at the radiation patterns for the  $90^\circ$  cuts given in Figures 10, 12 and 14, the computed patterns are seen to model the general characteristics of the measured results. The basic lobe structure for  $E_{\min}$  is predicted, but there is a difference in the location of the pattern nulls in the direction opposite the beam tilt. Good agreement between the measured and computed results was found for the beam tilt as a function of frequency. The beamwidth of  $E_{\min}$  for the computed patterns was seen to be narrower than the measured patterns for the  $0^\circ$  cuts as seen in Figures 11, 13 and 15. The beamwidth of  $E_{\max}$  for the computed patterns was seen to be wider for the  $0^\circ$  cuts and narrower for the  $90^\circ$  cuts than the beamwidth of the measured patterns. The differences between the measured and computed patterns are most significant for angles near the plane of the antenna. Much of this difference is likely due to the fact that an infinite ground plane was assumed for the calculated fields whereas the actual antenna measured was mounted on a finite structure.

## 8. Modal Distribution for the Multipole Expansion of the Fields

It was demonstrated that the far-field radiation patterns could be obtained for the ANSERLIN geometry using an expansion of a relatively small number of circularly polarized modes. In this section, an investigation of how the magnitudes of the different modal coefficients vary as a function of the geometry will be presented.

The modal coefficients whose magnitudes were larger than 0.001 of the magnitude of the mode with the largest magnitude are given in order of decreasing magnitude for frequencies of 1.6 GHz, 1.8 GHz, and 2.0 GHz for an ANSERLIN with  $b/a=1.75$ ,  $w/h=4.285$  and  $b=3.5$  cm in Tables 3 to 5. As was done for the calculation of the radiation patterns, an angular extent of  $270^\circ$  of current was used in the integration of the currents required to calculate the complex wall admittances required for the eigenvalue and coupled mode formulations. An angular extent of  $270^\circ$  with  $45^\circ$  sinusoidal-spline endcaps was used when calculating the modal coefficients from the propagation constant obtained from the eigenvalue formulation. Three-dimensional surface plots of the

magnitudes of the modal coefficients are given for the frequencies of 1.6 GHz, 1.8 GHz and 2.0 GHz (eigenvalue) in Figures 16 to 18.

Looking at the magnitudes of the modal coefficients as presented in the tables and in the three-dimensional figures, it is seen that the order of the modal coefficients with larger magnitudes shifts as the frequency is changed. For frequencies of 1.6 GHz and 1.8 GHz the mode coefficient with the largest magnitude is the  $m=-1, n=1$   $(-1,1)$ . (An excitation of a traveling wave on a single magnetic current ring in the  $+\phi$  direction with  $m'=1$  would couple most strongly to this mode.) For a frequency of 2.0 GHz, the  $(-1,2)$  mode coefficient has the largest magnitude, and the  $(-1,1)$  coefficient is now number two in the ordering. The ordering of the first 5 modes at 1.6 GHz is  $(-1,1)$ ,  $(0,1)$ ,  $(-1,2)$ ,  $(1,1)$ , and  $(2,2)$ . At 1.8 GHz the ordering is seen to be  $(-1,1)$ ,  $(-1,2)$ ,  $(0,1)$ ,  $(-2,2)$ , and  $(2,2)$  and at 2.0 GHz the ordering is  $(-1,2)$ ,  $(-1,1)$ ,  $(-2,2)$ ,  $(-1,3)$ ,  $(-3,3)$ . As the frequency is increased, mode coefficients of higher  $m$  and  $n$  values increase in magnitude. At 2.0 GHz, the magnitude of the mode coefficient for  $(-2,2)$  is nearly as large as that for  $(-1,1)$ . This stronger coupling to the higher-order  $(-2,2)$  mode results in a tilting of the beam away from the feedpoint at 2 GHz for the  $90^\circ$  cut (Figure 14). At 1.6 GHz, coupling is stronger to the  $(0,1)$  and  $(1,1)$  modes than at 1.8 GHz. This results in a tilting of the beam towards the feed for the  $90^\circ$  cut (Figure 10).

## 9. Conclusions

Coupled-mode and the eigenvalue formulations were developed for the ANSERLIN antenna and used to find the complex propagation constant in the  $\phi$ -direction. The coupled-mode formulation uses a system of coupled toroidal waveguide modes to find the propagation constant. In the eigenvalue formulation, the root is found of the characteristic equation that is obtained by applying small complex admittance boundaries to the side walls. This root, which is the complex order of the Bessel functions of the characteristic equation, multiplied by  $j$  is the propagation constant in the  $\phi$ -direction.

Use of the eigenvalue formulation produced good agreement between the computed and measured results for radiation loss for the case of a thin ANSERLIN structure. The radiation loss computed using the propagation constant determined from the coupled-mode formulation was found to be larger than the measured loss. For thicker structures, the radiation losses computed using the propagation constants determined from the eigenvalue and coupled-mode techniques agreed with each other but were found to be larger than the measured loss. Thus, the eigenvalue formulation accurately predicts the radiation loss for thin ANSERLIN structures.

Radiation patterns were computed from magnetic current filaments with radii corresponding to the edges of the annular waveguide and propagation constants in the  $\phi$ -direction determined from the eigenvalue and coupled-mode formulations. A circularly polarized multipole expansion was used to determine the far-field radiation patterns. Good agreement was found between the computed and measured radiation patterns for a thin ANSERLIN structure when the propagation constant determined from the eigenvalue formulation was used. The computed patterns predicted the beam tilt found in the radiation patterns as well as matched many of the general pattern characteristics for both  $0^\circ$  and  $90^\circ$  cuts. It was found that only a few circularly polarized modes are needed in the multipole expansion.

An investigation was done of the modal distribution of the multipole-field expansions. It was found that as frequency was increased, the magnitudes of the mode coefficients of modes with higher values of  $m$  and  $n$  (higher-order circularly polarized spherical modes) increased. This coupling to the higher-order mode causes the characteristic beam tilt as a function of frequency observed for the ANSERLIN structure.

## 10. References

- [1] J. L. Drewniak and P. E. Mayes, "Broadband, circularly polarized, radiating-line antennas with an application to a series-fed array," University of Illinois Electromagnetics Laboratory, Urbana-Champaign, Tech. Rep. 87-4, July 1987.
- [2] J. L. Drewniak and P. E. Mayes, "ANSERLIN: A broad-band, low-profile, circularly polarized antenna," *IEEE Trans. Antennas Propagat.*, vol. AP 37, pp. 281-288, March 1989.
- [3] J. L. Drewniak and P. E. Mayes, "The synthesis of patterns using a series-fed array of Annular Sector Radiating Line (ANSERLIN) elements: Low-profile, circularly polarized radiators," *IEEE Trans. Antennas Propagat.*, vol. AP 39, pp. 184-189, Feb. 1991.
- [4] J. M. Bowen and P. E. Mayes, "Microstrip-fed ANSERLIN antennas and arrays," University of Illinois Electromagnetics Laboratory, Urbana-Champaign, Tech. Rep. 88-3, July 1988.
- [5] C. Wood, "Curved microstrip lines as compact wideband circularly polarised antennas," *IEE J. Microwaves, Opt. & Acoust.*, vol. 3, pp. 6-13, January 1979.
- [6] D. W. Smith and P. E. Mayes, "Numerical and experimental analysis of circularly polarized, radiating line antennas," University of Illinois Electromagnetics Laboratory, Urbana-Champaign, Tech. Rep. 90-4, Sept. 1990.
- [7] C. S. Liang and Y. T. Lo, "A multipole-field study for the multiarm log-spiral antennas," *IEEE Trans. Antennas Propagat.*, vol. AP 16, pp. 656-664, Nov. 1968.

- [8] J. D. Jackson, *Classical Electrodynamics*. New York: John Wiley and Sons, 1975.
- [9] R. F. Harrington, *Time-Harmonic Electromagnetic Fields*. New York: McGraw-Hill, 1961, pp. 198-202.
- [10] S. A. Schelkunoff, "Conversion of Maxwell's equations into generalized telegraphist's equations," *Bell Syst. Tech. J.*, pp. 995-1043, Sept. 1955.
- [11] D. J. Tammen and P. E. Mayes, "Use of admittance-wall models in analysis of radiating line antennas," University of Illinois Electromagnetics Laboratory, Urbana-Champaign, Tech. Rep. 93-3, June 1993.
- [12] P.E. Mayes, Advanced Antennas Class Notes, University of Illinois at Urbana-Champaign, Fall 1984.

Table 1 Real Part of the Propagation Constant in the  $\phi$  Direction Computed Using the Coupled-mode and Eigenvalue Formulations for an ANSERLIN with  $b/a=2.5$ ,  $w/h=3.5$  and  $b=3.5$  cm

| Freq (GHz) | $\alpha_{\text{coupled-mode}}$ | $\alpha_{\text{eigenvalue}}$ |
|------------|--------------------------------|------------------------------|
| 1.994      | 0.050822                       | 0.051129                     |
| 2.000      | 0.051270                       | 0.051623                     |
| 2.189      | 0.066554                       | 0.068695                     |
| 2.200      | 0.067492                       | 0.069762                     |
| 2.382      | 0.083368                       | 0.087816                     |
| 2.400      | 0.084923                       | 0.089595                     |
| 2.574      | 0.100312                       | 0.107283                     |
| 2.600      | 0.102525                       | 0.109828                     |

Table 2 Real Part of the Propagation Constant in the  $\phi$  Direction Computed Using the Coupled-mode and Eigenvalue Formulations for an ANSERLIN with  $b/a=1.75$ ,  $w/h=4.285$  and  $b=3.5$  cm

| Freq (GHz) | $\alpha_{\text{coupled-mode}}$ | $\alpha_{\text{eigenvalue}}$ |
|------------|--------------------------------|------------------------------|
| 1.756      | 0.029106                       | 0.013547                     |
| 1.931      | 0.037395                       | 0.017469                     |
| 2.000      | 0.040770                       | 0.019074                     |
| 2.105      | 0.045925                       | 0.021538                     |
| 2.200      | 0.050466                       | 0.023734                     |
| 2.280      | 0.054208                       | 0.025572                     |
| 2.400      | 0.059517                       | 0.028264                     |
| 2.455      | 0.061782                       | 0.029450                     |
| 2.600      | 0.067260                       | 0.032491                     |



Table 3 Magnitudes of the Modal Coefficients Determined from the Eigenvalue Formulation for an ANSERLIN with  $b/a=1.75$ ,  $w/h=4.285$  and  $b=3.5$  cm for a Frequency of 1.6 GHz

| <b>m</b> | <b>n</b> | <b><math> A_{\text{left}}(m,n) </math></b> | <b><math> A_{\text{left}}(m,n) </math><br/>normalized</b> |
|----------|----------|--|---|
| -1       | 1        | 0.073911                                   | 1.0000  |
| 0        | 1        | 0.042734                                   | 0.57818   |
| -1       | 2        | 0.042167                                   | 0.57051   |
| 1        | 1        | 0.011162                                   | 0.15101   |
| 2        | 2        | 0.0084091                                  | 0.11377   |
| 1        | 2        | 0.0063678                                  | 0.086155  |
| -1       | 3        | 0.0058423                                  | 0.079045  |
| -2       | 2        | 0.0049808                                  | 0.067388  |
| -3       | 3        | 0.0020906                                  | 0.028285  |
| 3        | 3        | 0.0016869                                  | 0.022824  |
| 0        | 3        | 0.0015229                                  | 0.020604  |
| 1        | 3        | 0.00088226                                 | 0.011937  |
| -1       | 4        | 0.00084379                                 | 0.011416  |
| 2        | 3        | 0.00069853                                 | 0.0094510   |
| -2       | 3        | 0.00041374                                 | 0.0055978   |
| -4       | 4        | 0.00035934                                 | 0.0048617   |
| 4        | 4        | 0.00018324                                 | 0.0024791   |
| 2        | 4        | 0.00017068                                 | 0.0023093   |
| 1        | 4        | 0.00012742                                 | 0.0017240   |
| -2       | 4        | 0.00010110                                 | 0.0013678   |
| -1       | 5        | 7.5894e-05                                 | 0.0010268   |

Table 4 Magnitudes of the Modal Coefficients Determined from the Eigenvalue Formulation for an ANSERLIN with  $b/a=1.75$ ,  $w/h=4.285$  and  $b=3.5$  cm for a Frequency of 1.8 GHz

| <b>m</b> | <b>n</b> | <b><math> A_{left}(m,n) </math></b> | <b><math> A_{left}(m,n) </math><br/>normalized</b> |
|----------|----------|-------------------------------------|--|
| -1       | 1        | 0.065270                            | 1.0000   |
| -1       | 2        | 0.054407                            | 0.83357  |
| 0        | 1        | 0.026764                            | 0.41005  |
| -2       | 2        | 0.013916                            | 0.21320  |
| 2        | 2        | 0.0084835                           | 0.12998  |
| -1       | 3        | 0.0075045                           | 0.11498  |
| 1        | 1        | 0.0074715                           | 0.11447  |
| 1        | 2        | 0.0062281                           | 0.095420   |
| -3       | 3        | 0.0037761                           | 0.057854   |
| 3        | 3        | 0.0021232                           | 0.032529   |
| -2       | 3        | 0.0014358                           | 0.021998   |
| -1       | 4        | 0.0013233                           | 0.020275   |
| 0        | 3        | 0.0011731                           | 0.017973   |
| 2        | 3        | 0.00087530                          | 0.013410   |
| 1        | 3        | 0.00085905                          | 0.013162   |
| -4       | 4        | 0.00059896                          | 0.0091767  |
| -2       | 4        | 0.00034989                          | 0.0053607  |
| 4        | 4        | 0.00028506                          | 0.0043674  |
| 2        | 4        | 0.00021330                          | 0.0032680  |
| -3       | 4        | 0.00015163                          | 0.0023231  |
| 1        | 4        | 0.00015148                          | 0.0023209  |
| -1       | 5        | 0.00011881                          | 0.0018203  |
| 3        | 4        | 8.5254e-05                          | 0.0013062  |

Table 5 Magnitudes of the Modal Coefficients Determined from the Eigenvalue Formulation for an ANSERLIN with  $b/a=1.75$ ,  $w/h=4.285$  and  $b=3.5$  cm for a Frequency of 2.0 GHz

| m  | n | $ A_{left}(m,n) $ | $ A_{left}(m,n) $<br>normalized |
|----|---|-------------------|---------------------------------|
| -1 | 2 | 0.080518          | 1.0000                          |
| -1 | 1 | 0.046515          | 0.57769                         |
| -2 | 2 | 0.036348          | 0.45143                         |
| -1 | 3 | 0.011017          | 0.13682                         |
| -3 | 3 | 0.0079127         | 0.098272                        |
| 2  | 2 | 0.0075901         | 0.094266                        |
| 0  | 1 | 0.0070512         | 0.087573                        |
| -2 | 3 | 0.0051486         | 0.063942                        |
| 1  | 2 | 0.0043935         | 0.054565                        |
| 3  | 3 | 0.0027640         | 0.034327                        |
| -1 | 4 | 0.0025827         | 0.032076                        |
| 1  | 1 | 0.0025381         | 0.031522                        |
| -2 | 4 | 0.0012487         | 0.015508                        |
| -4 | 4 | 0.0011826         | 0.014688                        |
| 2  | 3 | 0.0010751         | 0.013352                        |
| 1  | 3 | 0.00060111        | 0.0074655                       |
| 4  | 4 | 0.00050438        | 0.0062641                       |
| -3 | 4 | 0.00042242        | 0.0052462                       |
| 0  | 3 | 0.00041651        | 0.0051729                       |
| 2  | 4 | 0.00026075        | 0.0032384                       |
| -1 | 5 | 0.00023114        | 0.0028707                       |
| 3  | 4 | 0.00014755        | 0.0018326                       |
| 1  | 4 | 0.00014093        | 0.0017502                       |
| -3 | 5 | 0.00013890        | 0.0017251                       |
| -5 | 5 | 0.00012200        | 0.0015151                       |
| -2 | 5 | 0.00010599        | 0.0013163                       |

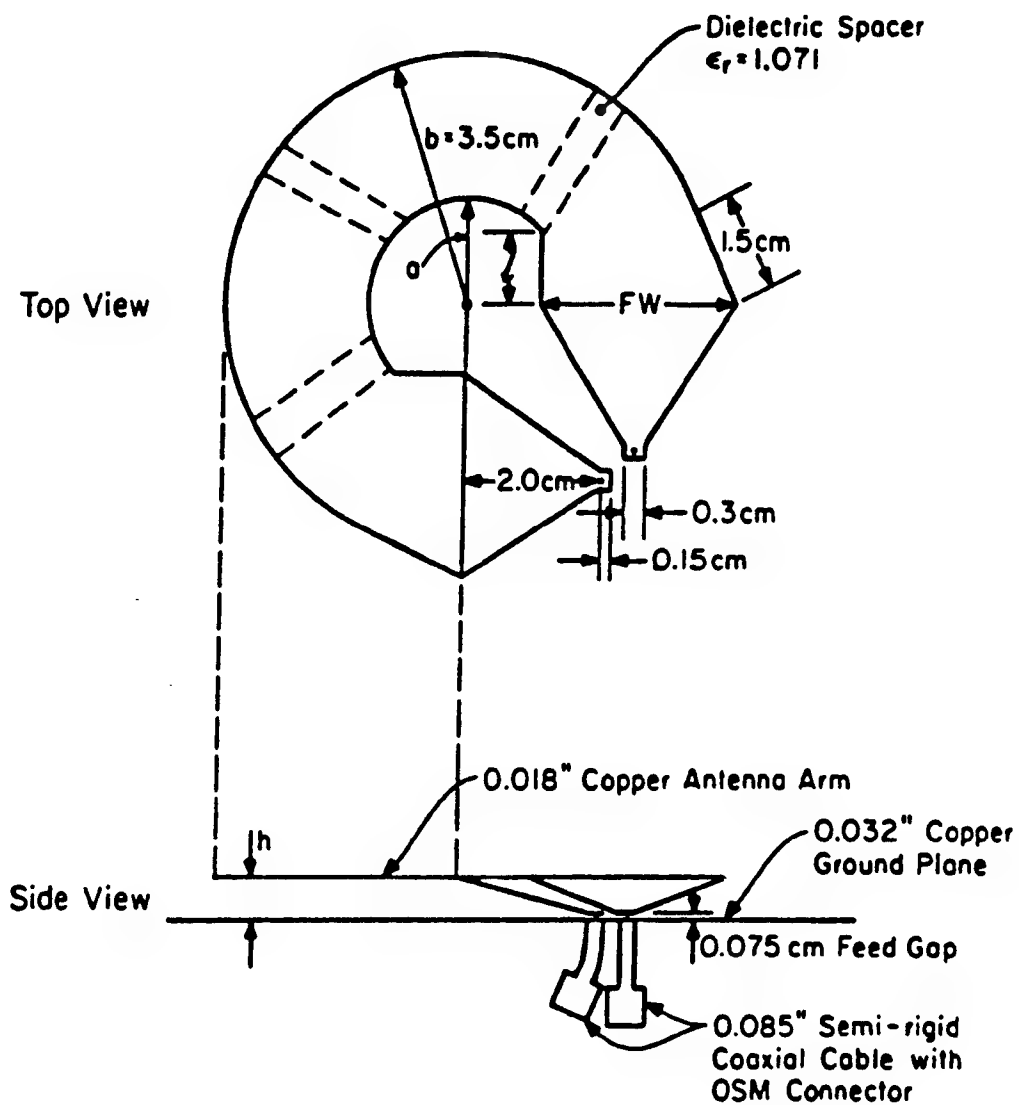


Figure 1 Probe-fed ANSERLIN element [1].

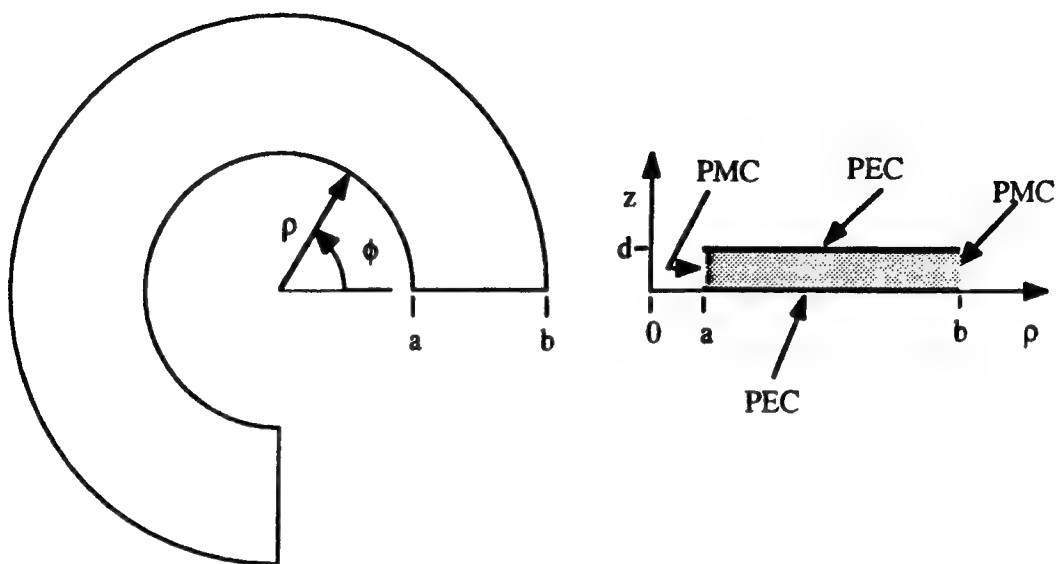


Figure 2 Toroidal waveguide model of ANSERLIN element.

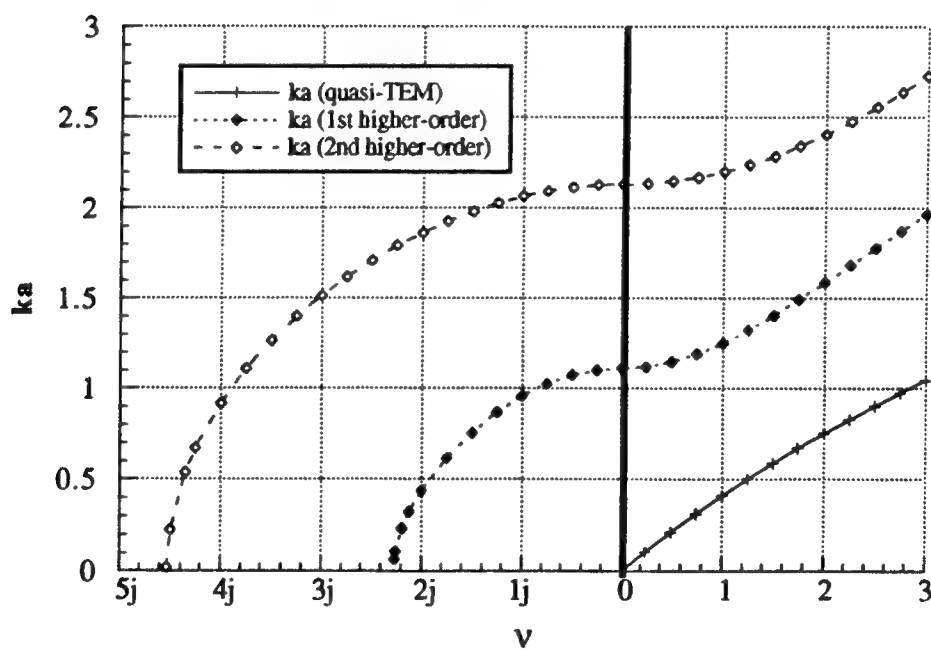


Figure 3 Solution of characteristic equation of toroidal waveguide with  $b/a = 4$ .

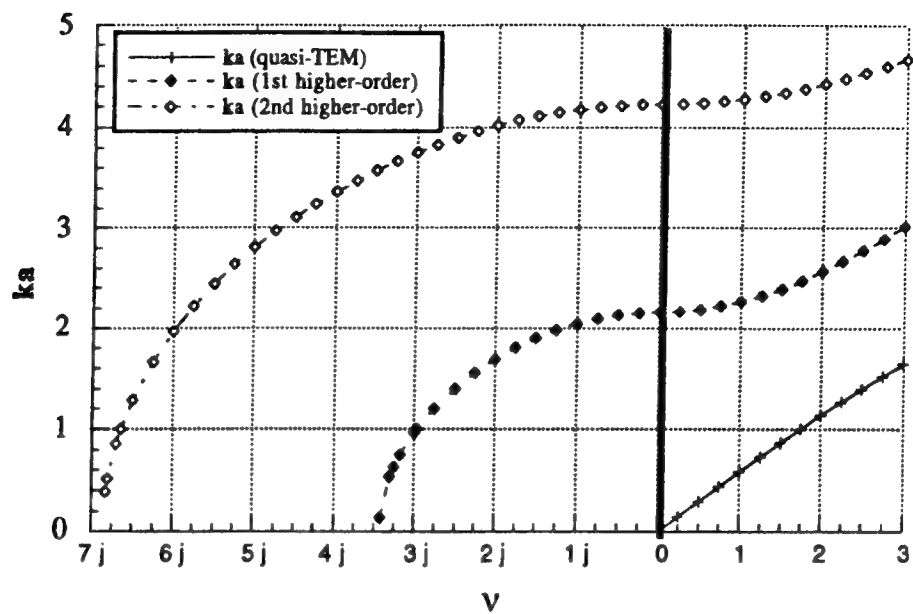


Figure 4 Solution of characteristic equation of toroidal waveguide with  $b/a = 2.5$ .

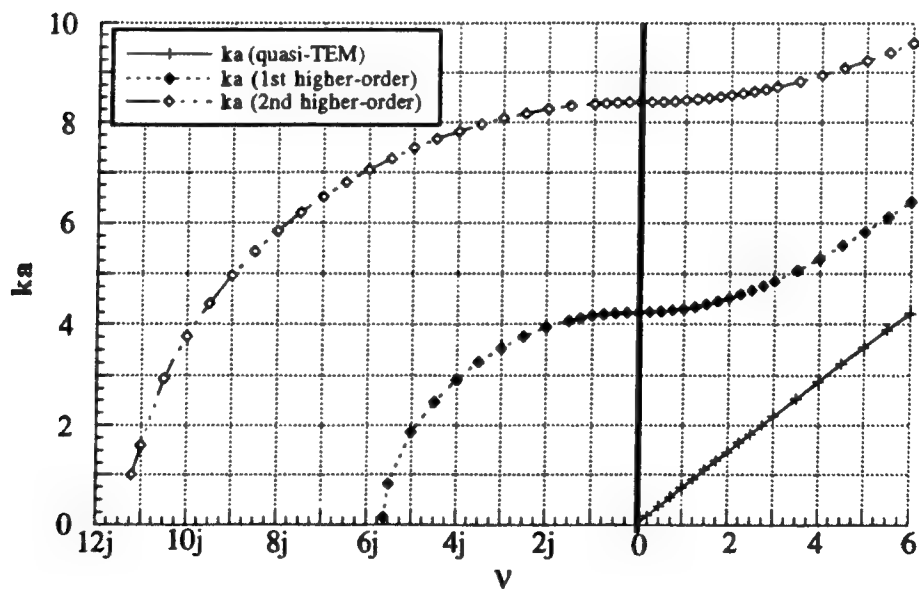


Figure 5 Solution of characteristic equation of toroidal waveguide with  $b/a = 1.75$ .

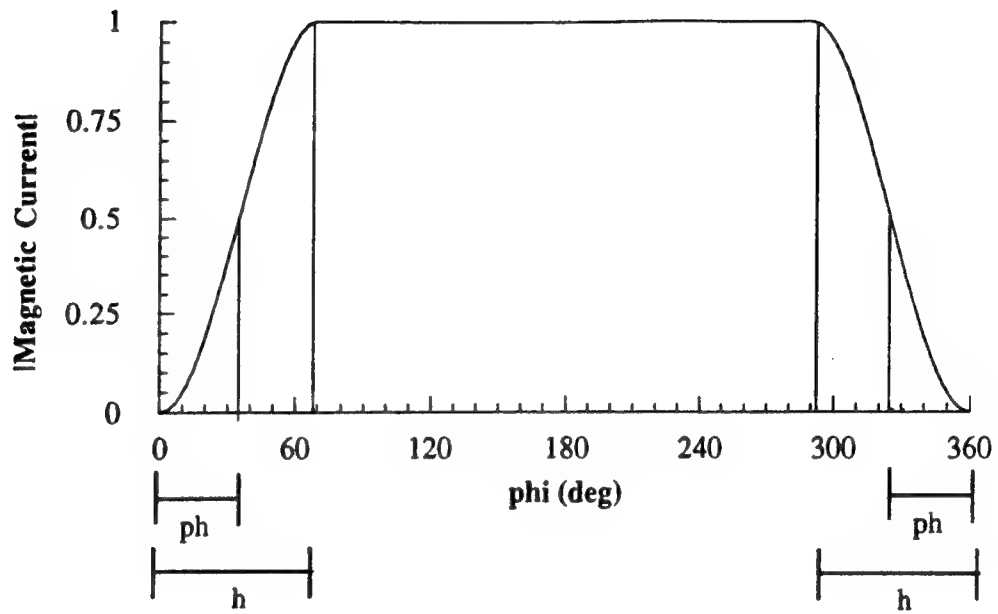


Figure 6 Magnitude of magnetic current distribution with sinusoidal-spline endcaps.

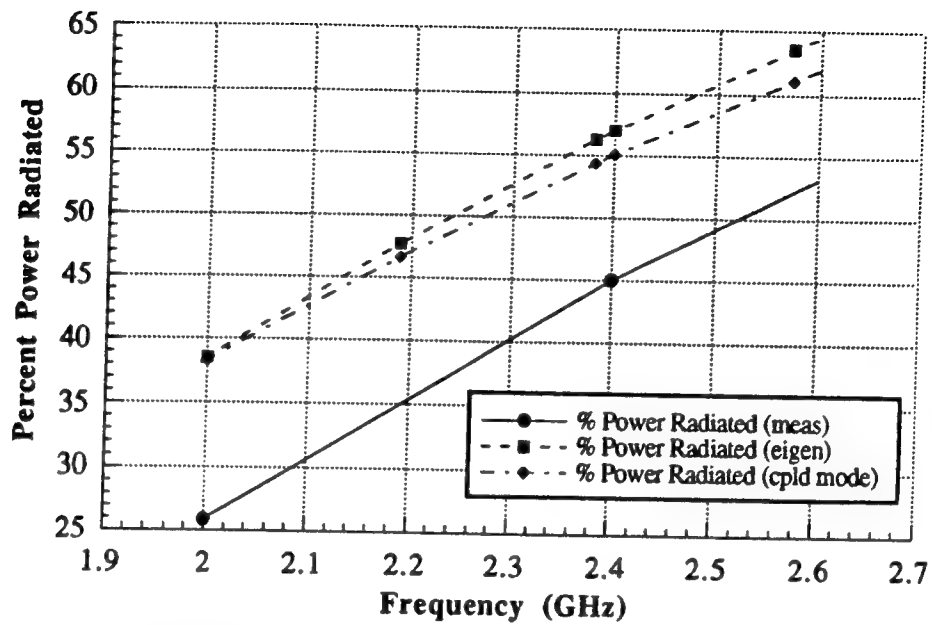


Figure 7 Comparison of measured and computed percent power radiated for ANSERLIN with  $b/a = 2.5$ ,  $b = 3.5$  cm,  $w/h = 3.5$ .

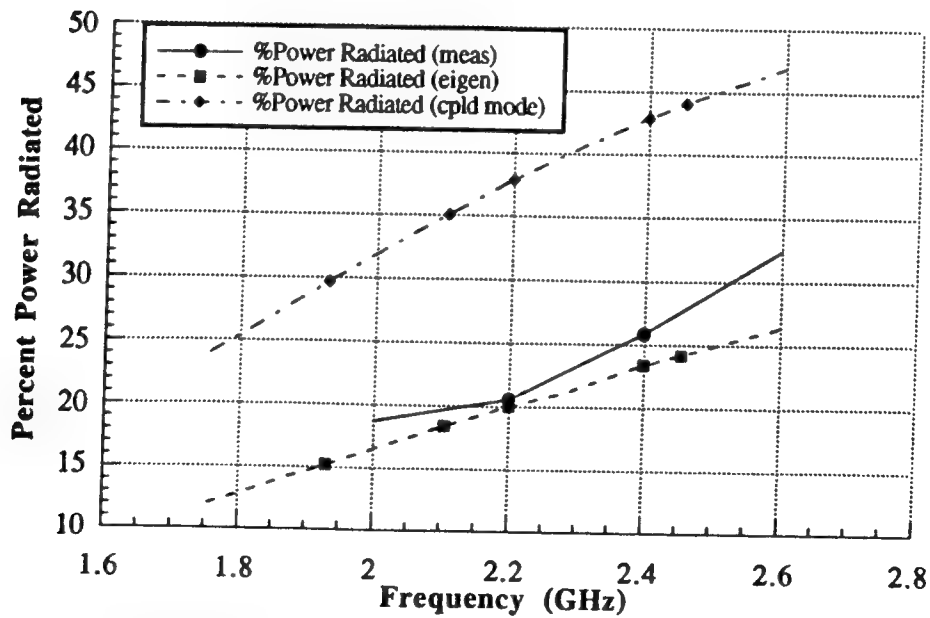


Figure 8 Comparison of measured and computed percent power radiated for ANSERLIN with  $b/a = 1.75$ ,  $b = 3.5$  cm,  $w/h = 4.285$ .



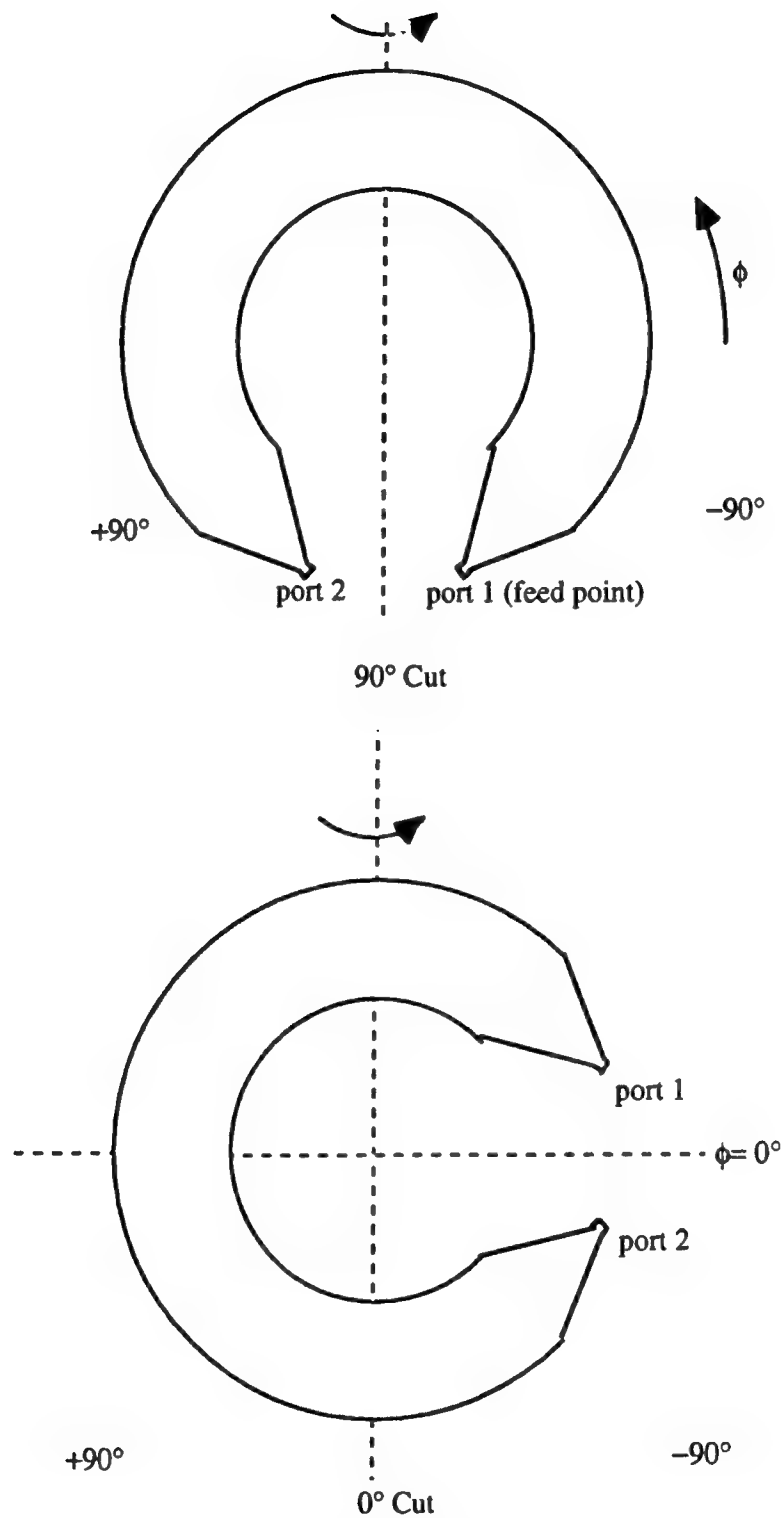


Figure 9 Orientation of ANSERLIN antenna for radiation pattern measurements for  $0^\circ$  and  $90^\circ$  cuts.

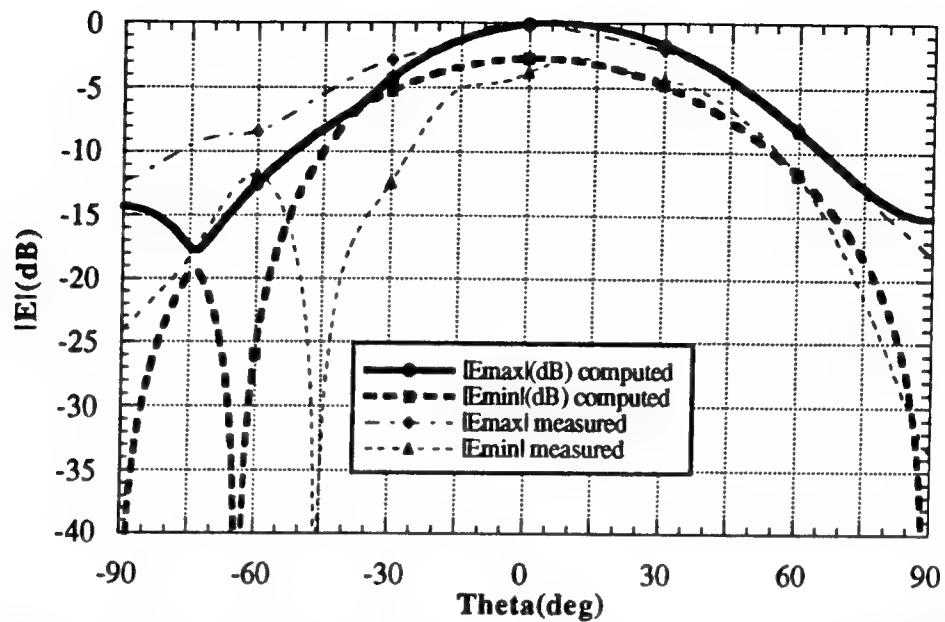


Figure 10 Comparison of measured and computed patterns for ANSERLIN with  $b/a = 1.75$ ,  $w/h = 4.285$ ,  $b = 3.5$  cm,  $270^\circ$  arc,  $\text{freq} = 1.6$  GHz,  $90^\circ$  cut.

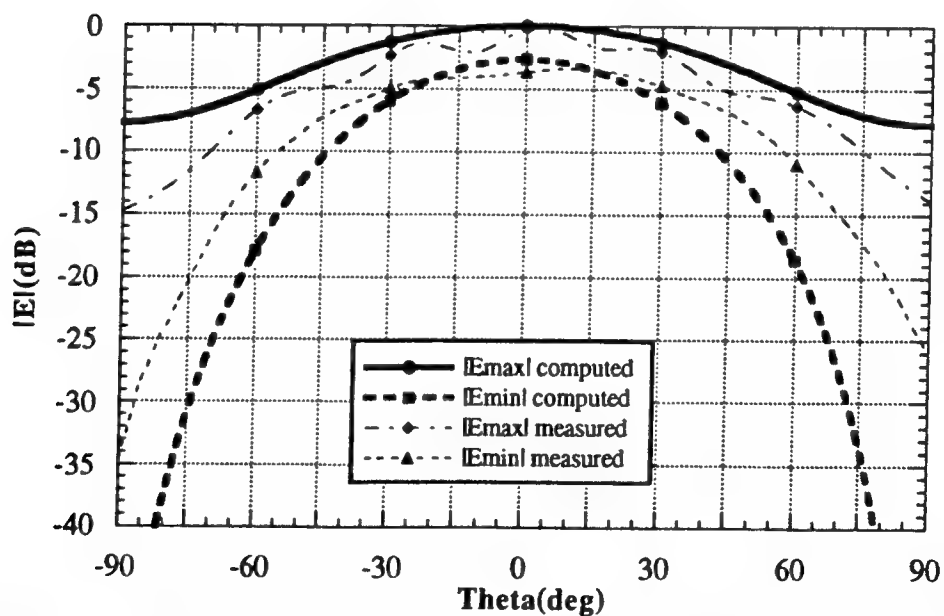


Figure 11 Comparison of measured and computed patterns for ANSERLIN with  $b/a = 1.75$ ,  $w/h = 4.285$ ,  $b = 3.5$  cm,  $270^\circ$  arc,  $\text{freq} = 1.6$  GHz,  $0^\circ$  cut.

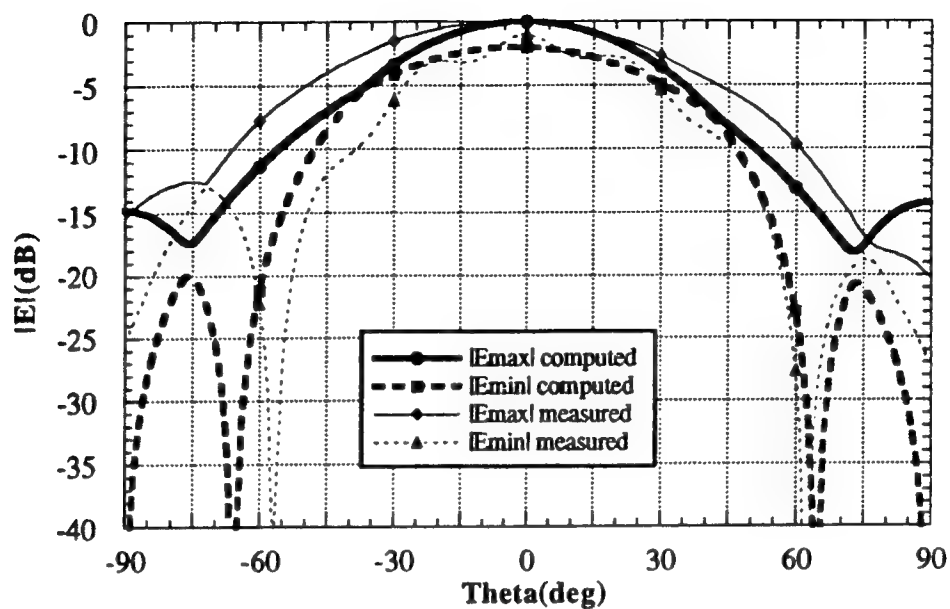


Figure 12 Comparison of measured and computed patterns for ANSERLIN with  $b/a = 1.75$ ,  $w/h = 4.285$ ,  $b = 3.5$  cm,  $270^\circ$  arc, freq= 1.8 GHz,  $90^\circ$  cut.

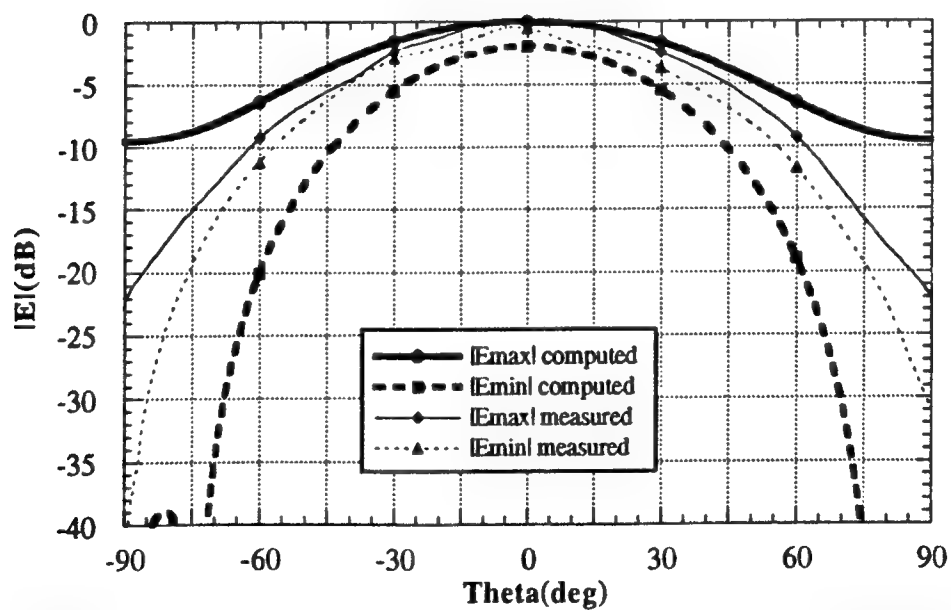


Figure 13 Comparison of measured and computed patterns for ANSERLIN with  $b/a = 1.75$ ,  $w/h = 4.285$ ,  $b = 3.5$  cm,  $270^\circ$  arc, freq= 1.8 GHz,  $0^\circ$  cut.

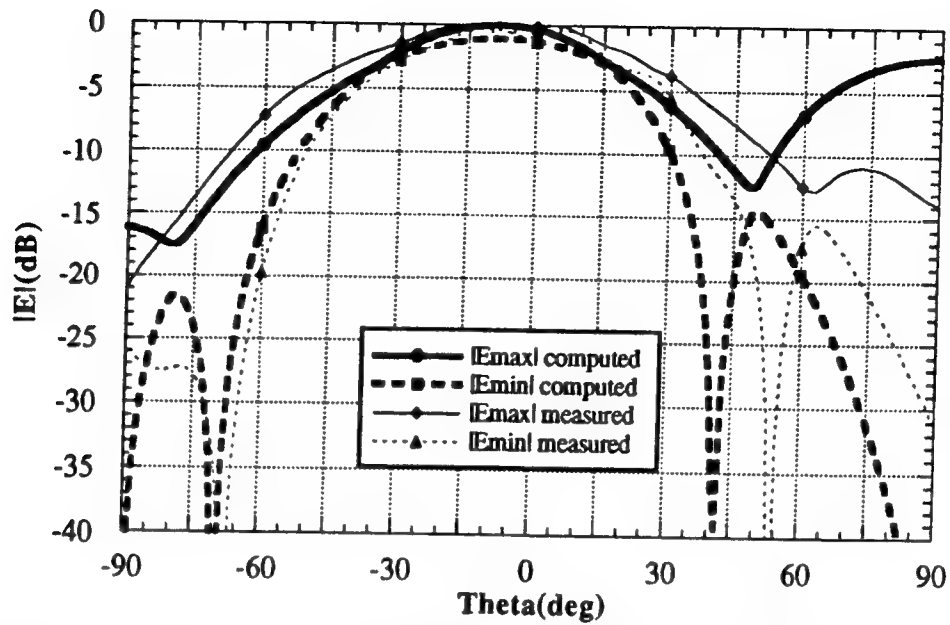


Figure 14 Comparison of measured and computed patterns for ANSERLIN with  $b/a = 1.75$ ,  $w/h = 4.285$ ,  $b = 3.5$  cm,  $270^\circ$  arc, freq= 2.0 GHz,  $90^\circ$  cut.

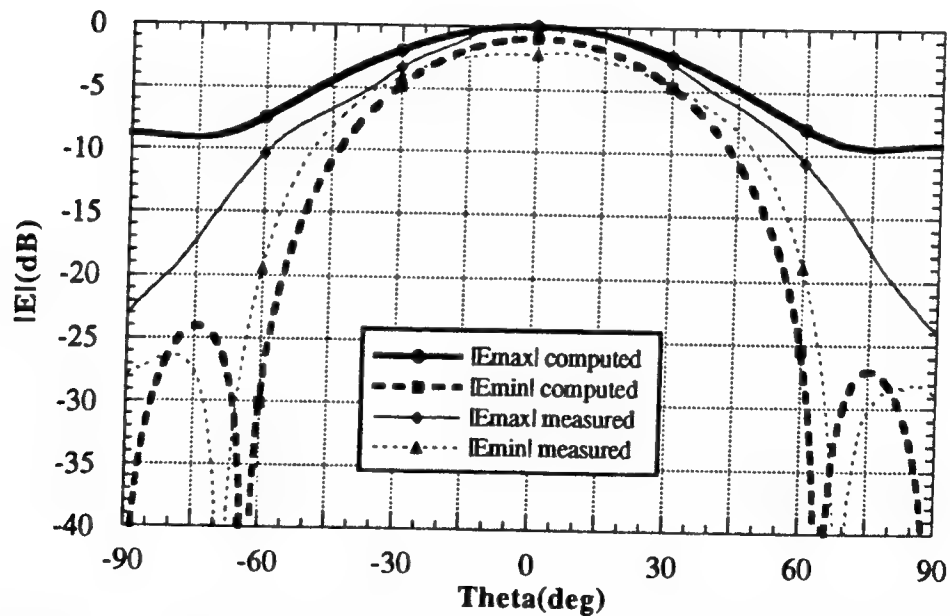


Figure 15 Comparison of measured and computed patterns for ANSERLIN with  $b/a = 1.75$ ,  $w/h = 4.285$ ,  $b = 3.5$  cm,  $270^\circ$  arc, freq= 2.0 GHz,  $0^\circ$  cut.

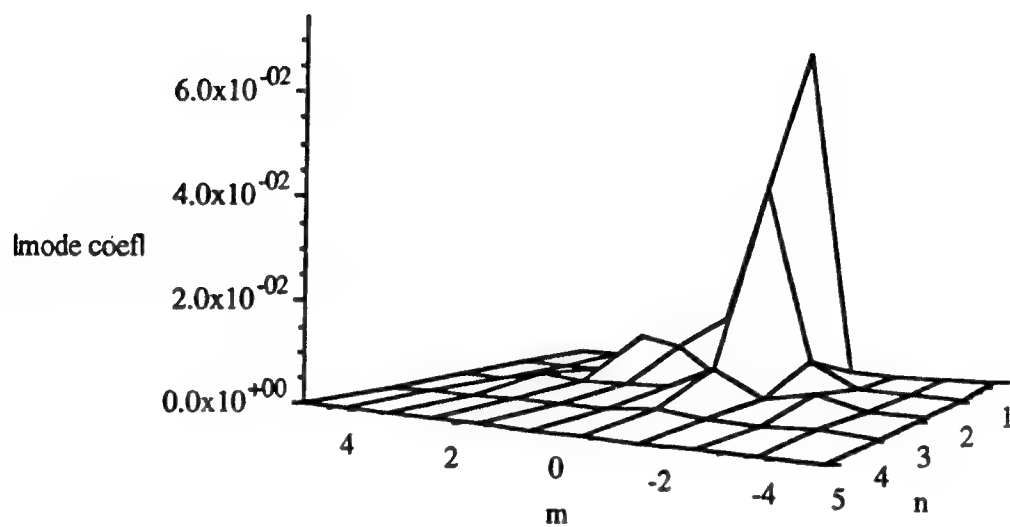


Figure 16 Modal distribution for ANSERLIN at 1.6 GHz, 150° view.

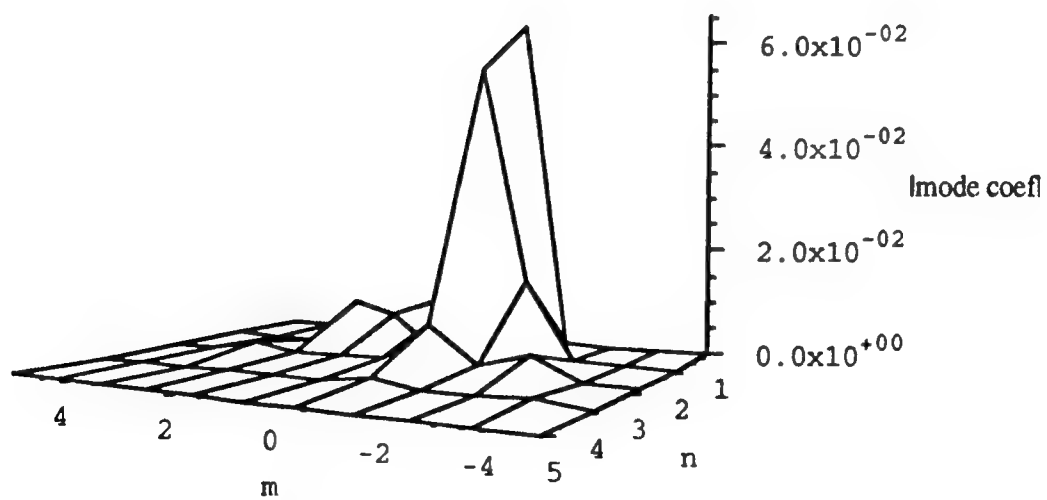


Figure 17 Modal distribution for ANSERLIN at 1.8 GHz, 150° view.

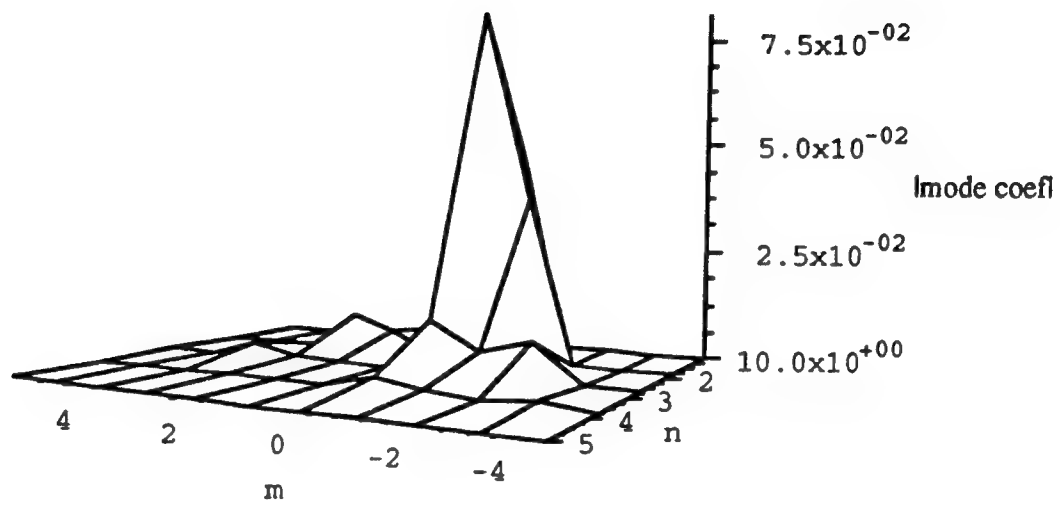


Figure 18 Modal distribution for ANSERLIN at 2.0 GHz, 150° view.

**APPLICATION OF A POLARIZING LENS TO A MULTIMODE  
FLATPLATE ARRAY ANTENNA**

**Don Collier**

**Marshall Greenspan**

**Dave MacFadyen**

**Larry Orwig**

**Westinghouse Norden Systems, Inc.**

**P.O. Box 5300**

**Norwalk, CT 06856, USA**

**ABSTRACT:**

In a previous paper presented at the 1991 Antenna Applications Symposium, "Multimode Performance From a Single Flatplate Array Antenna", three military antennas were described which functioned in a multiplicity of concurrent as well as switchable modes. One of these was a slotted waveguide array containing five elliptical apertures. The largest aperture was a four quadrant monopulse with sum, azimuth difference and elevation difference ports. Below this array, there were three apertures which functioned as an azimuth interferometer. Finally, there was a small array that performed a guard function.

Under a recent IR&D project the capability of this array has been expanded to include polarization diversity for Automatic Target Recognition (ATR). A light-weight, meanderline polarizer has been designed, which transmits linearly polarized RF and receives simultaneously horizontally and vertically polarized target returns on boresight. An optional configuration transmits right-hand circular and receives simultaneously right- and left-hand circular polarized returns. Either configuration detects two correlated polarization scattering states. Such data are useful in target identification either through partial polarization whitening of the image or by supplying feature information for matching against a target model. The addition of an RF switch to the design allows alternating transmission of both polarizations; in this case the full polarization scattering matrix can be obtained.

The linearly polarized apertures of the original array design permit the antenna to perform air-to-air pulse doppler monopulse, high resolution synthetic aperture (SAR) ground mapping, and ground moving target indication (GMTI) and track. The high gain and efficiency of the flatplate array, combined with pulse

compression techniques and high transmitter power, give the system a long range, high resolution, ground mapping capability unusual in a nose mounted radar system. With the incorporation of the polarizer lens, the new ATR capability makes this antenna a more powerful tool in air-to-ground combat and surveillance.

## **1.0 THE MULTIFUNCTION, FLATPLATE ARRAY ANTENNA**

### **1.1 Background: The Bandwidth Trade-off**

The slots on any flatplate antenna are excited by waveguide runs located behind the front plate of the antenna aperture. RF energy travels through these waveguides and is emitted from the slots whenever a component of E-field within the waveguide is normal to the slot center line. The slots are precisely spaced to insure that the RF from each slot is in phase with that of its neighbor [1]. The aperture is subdivided into resonant subarrays to simplify the feed network. This simplification limits the operational frequency band however, and for this reason, antennas with good sidelobe characteristics at center frequency show higher sidelobes and VSWR at the band edges. This deterioration can be minimized by keeping the waveguide runs short. As energy travels down the guide from the RF feed port, the phase error of the RF increases as it reaches each successive slot. Therefore, if the antenna aperture were divided into small subarrays, and each subarray were fed by a separate RF feed port, the phase errors could be kept to a minimum. However, this method is expensive, as it requires a complex feed network attached to the back of the flatplate antenna. Figure 1 illustrates the complexity of the array feed network.

The array used on this project has 60 subarrays with short waveguide runs, achieves a 3% operating bandwidth, and has elevation pencil beam sidelobes -23 dB and azimuth pencil beam sidelobes -25 dB below main beam peak.



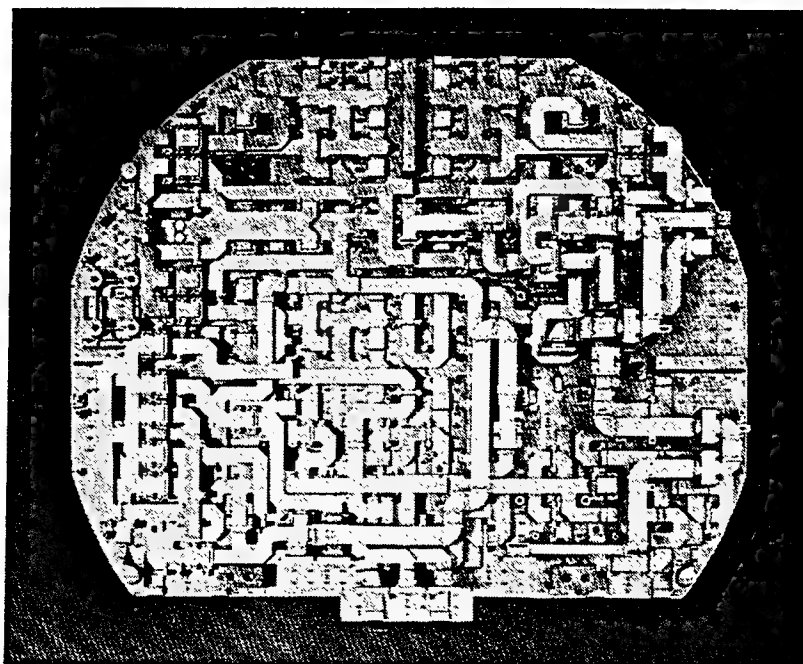


**Figure 1. Reverse Side of Multimode Flatplate Array Antenna Showing Waveguide Feed Network.**

### **1.2 Desired Modes of Operation**

A multiple aperture antenna can support many modes of operation. The large array, which is divided into quadrants, forms a pencil beam for long range target location, for monopulse air-to-air tracking, for SAR (Synthetic Aperture Radar) ground target identification and track, as well as for a terrain clearance mode. In addition, P. Smith of Norden Systems developed and patented a means to create a CSC<sup>2</sup> elevation beam from the same flatplate array by 1) switching the power to only the upper half of the radiating aperture and 2) introducing a fixed phase shift into the lowest row of the active aperture [2]. This invention permits the inclusion of modes requiring a shaped beam, such as ground mapping, and facilitates ground and ship target location.

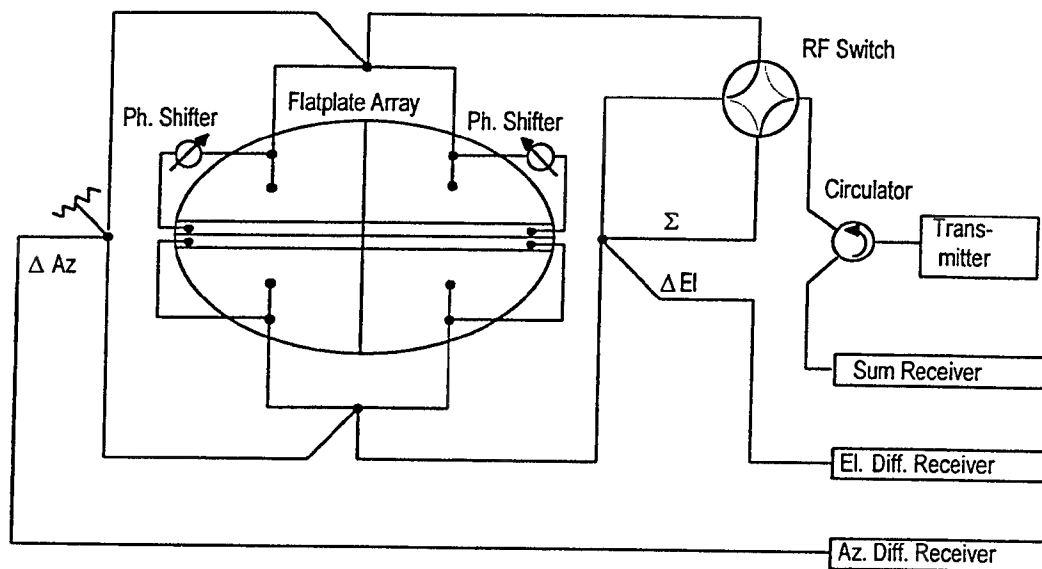


**Figure 2. Simplified Electrical Schematic of Monopulse Aperture**

Power switching is accomplished by inclusion of an RF switch in the feed manifold as shown in Figure 2.

## 2.0 THE LENS CONCEPT

For optimum operation in an automatic target classification environment, Synthetic Aperture Radar (SAR) requires measurement of the target's polarimetric response; i.e., transmission of polarized RF energy and the reception simultaneously of co-polarized and cross-polarized target echo's. To date, polarimetric SAR has been practical only when separate apertures were employed. The configuration applied in this program utilizes a vertically polarized monopulse planar array antenna, to which has been added a pair of opposite-sensed, circularly polarized lenses covering the upper and lower half apertures. This approach, together with novel radar control and signal processing techniques, will demonstrate the capability of producing a wide variety of high quality polarimetric target data. For the first time, it will be practical to incorporate

polarimetric SAR and ATR modes into a system that employs only a single slotted flatplate antenna.

Attached to the antenna and covering the monopulse aperture are two polarizer lenses, illustrated in Figure 3. One, which produces right-hand circular polarization, covers the upper half of the antenna. The other, which produces left-hand circular polarization, covers the lower half of the antenna. The first objective of the study was to determine the nature of the polarization of the RF energy in the far field.

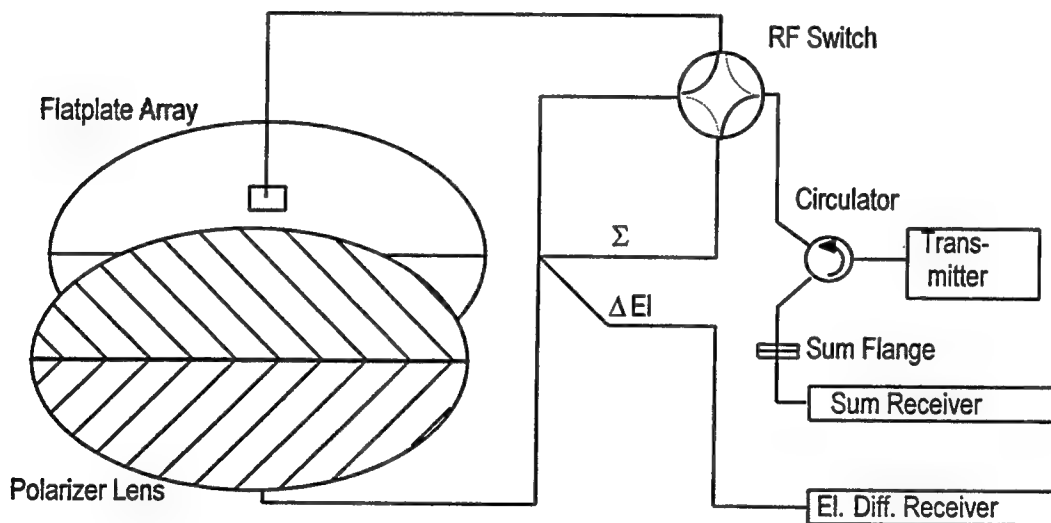


**Figure 3. Flatplate Array With Polarizer Lenses Covering Aperture.  
The Polarizer Lens**

Polarization modifying gratings or lenses were designed and built in the 1940's, and were described by Marcuvitz [3]. The meanderline lens used in this application is similar to the design outlined by Young, Robinson and Hacking in 1973 [4]. The layout is shown in Figure 4, in which microstrip meanderlines set at a 45 degree angle are etched into copperclad dielectric sheets.

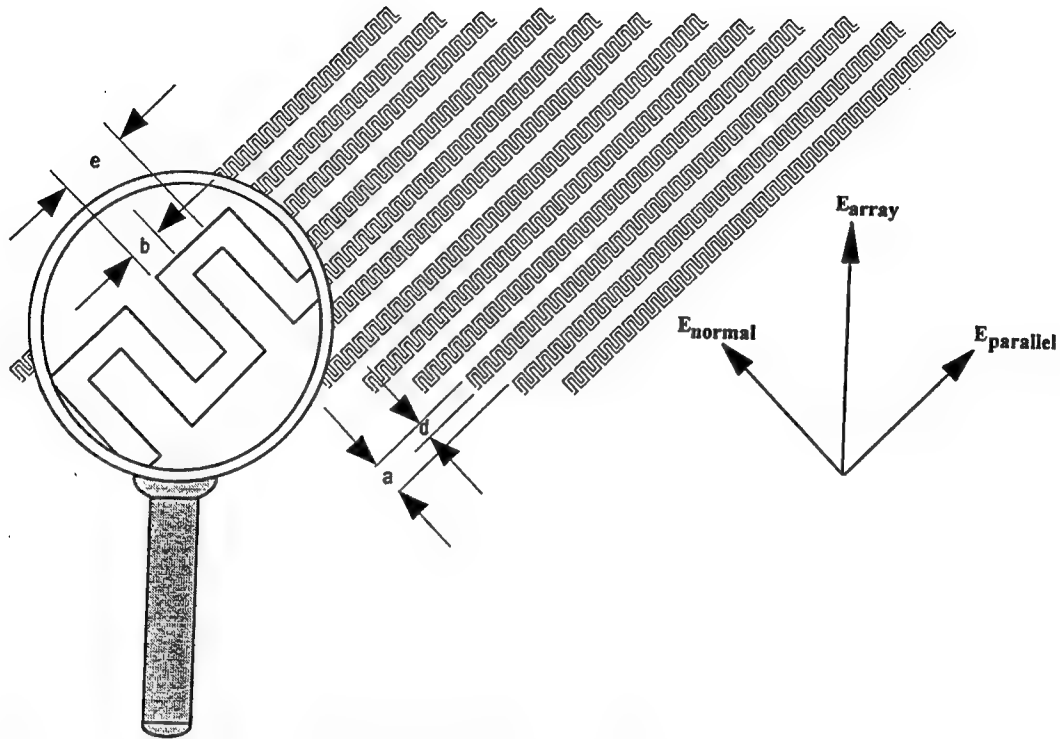


**Figure 4. Microstrip Meanderline Layout of Polarizer Lens.**

Vertically polarized RF energy emitted from the array slots impinges on the polarizer sheet, located approximately 0.5 inches in front of the antenna aperture. The radiated voltage vector  $\mathbf{E}_{\text{array}}$  consists of two components or legs, one parallel to the meanderline strips,  $\mathbf{E}_{\text{parallel}}$ , and one perpendicular to the meanderline strips,  $\mathbf{E}_{\text{normal}}$ . As  $\mathbf{E}_{\text{normal}}$  passes through the lens, it undergoes a phase retard, since the lens acts as a capacitive reactance to this leg of the RF signal. The admittance is determined by the meanderline dimensions:

$$\frac{B_c}{Y_0} \approx \frac{4a}{\lambda} \left[ \ln \left( \frac{2a}{\pi d} \right) + \frac{1}{2} \left( \frac{a}{\lambda} \right)^2 \right] \quad (\text{Eq. 1})$$

where  $\frac{B_c}{Y_0}$  is the normalized lens capacitive susceptance, the dimensions  $a$  and  $d$  are shown in Figure 4 and  $\lambda$  is the RF wavelength. The phase retard is then found:

$$\Phi_D = -2 \tan^{-1} \left( \frac{B_c}{2Y_0} \right) \text{ degrees.} \quad (\text{Eq. 2})$$

In similar manner, the vector  $E_{\text{parallel}}$  undergoes a phase advance, since the lens acts as an inductive reactance to this leg of the RF vector. The reactance is approximately

$$\frac{X_L}{Z_0} \approx \frac{a}{\lambda} \left[ \ln \left( \frac{2a}{\pi d} \right) + \frac{1}{2} \left( \frac{a}{\lambda} \right)^2 \right] \quad (\text{Eq. 3})$$

where  $\frac{X_L}{Z_0}$  is the normalized lens inductive reactance and the other variables are the same as in Eq. 1. The phase advance is then

$$\Phi_D = 2 \tan^{-1} \left( \frac{B_L}{2Y_0} \right) \text{ degrees} \quad (\text{Eq. 4})$$

where  $\frac{B_L}{Y_0} = \frac{Z_0}{X_L}$ .

An inaccuracy is introduced in this result by a reactance caused by the capacitance existing between parallel strips of each individual meanderline. From Figure 4,

the dimensions  $b$  and  $e$  can be substituted into **Eq. 1**, the phase retard calculated, and the result subtracted from the solution of **Eq. 4**.

The full 90 degree phase differential is not normally achieved with a single layer. The structure must be matched to free space to minimize RF reflections, so that three or more layers are used in the manner of spacial filters, each one shifting the RF phase a fraction of the desired total. When the 90 degree separation between vector components has been obtained, the linearly polarized energy becomes circular by definition.

## 2.1 Polarization of Array and Lens on Boresight

As explained in the previous section, vertically polarized RF is emitted from the flatplate array slots at 0 deg. elevation angle. The circularly polarized meanderline lens causes the vector components to undergo a phase *advance* if the vector component is *parallel* to the meanderline. The vector component undergoes a phase *retard* if the vector component is *normal* to the meanderline. See Figures 5 and 6.

### Propagation Through Upper Half of Polarizer Lens

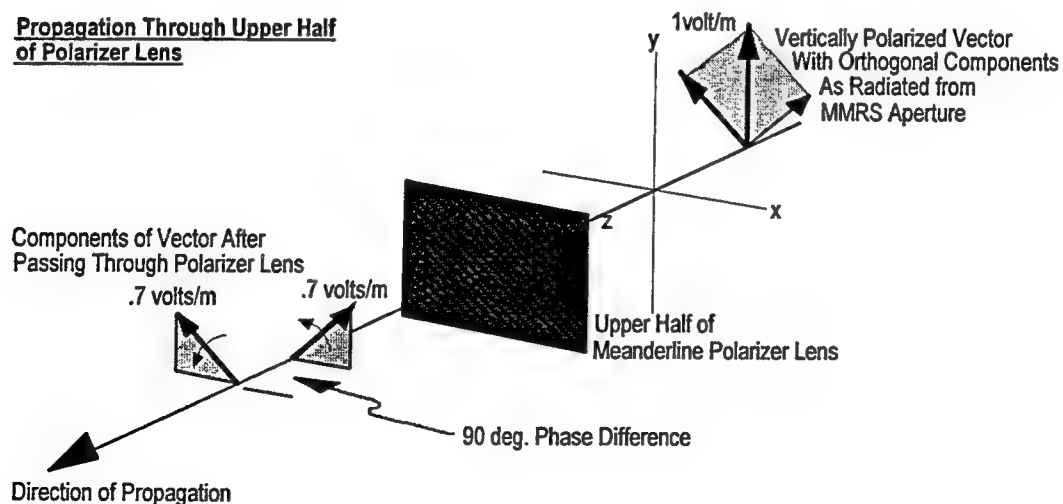


**Figure 5. Propagation Through Upper Half of Polarizer Lens**

In general, a linearly polarized electromagnetic wave propagating through space along the Z axis may be characterized in the time domain in the following manner:

$\vec{E} = E_x \sin(\omega t + \Psi) \hat{i} + E_y \sin(\omega t + \Psi) \hat{j}$  where  $\Psi$  is the phase distance from the wave source and  $\omega t$  is the instantaneous angular displacement over time.

The pair of rotating vectors illustrated in Figure 5 may then be expressed in time and space by the equation

$$\vec{E}_{upper} = E_1 \left[ -.5 \sin(\omega t + 45^\circ) \hat{i} + .5 \sin(\omega t + 45^\circ) \hat{j} + .5 \sin(\omega t - 45^\circ) \hat{i} + .5 \sin(\omega t - 45^\circ) \hat{j} \right] \quad (\text{Eq. 5})$$

v/m

where  $E_1 = 1 \text{ volt/m.}$  and  $\hat{i}$  and  $\hat{j}$  are unit vectors along the X and Y axes, respectively.

#### Propagation Through Lower Half of Polarizer Lens

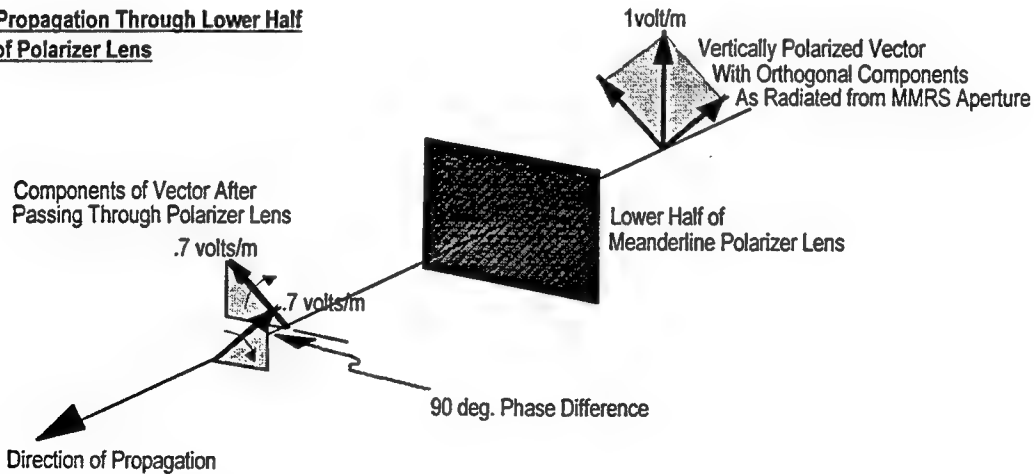


**Figure 6. Propagation Through Lower Half of Polarizer Lens**

The pair of rotating vectors in Figure 6 may be expressed in time and space by the equation

$$\vec{E}_{\text{lower}} = E_2 \left[ .5 \sin(\omega t + 45^\circ) \hat{i} + .5 \sin(\omega t + 45^\circ) \hat{j} - .5 \sin(\omega t - 45^\circ) \hat{i} + .5 \sin(\omega t - 45^\circ) \hat{j} \right] \quad (\text{Eq. 6})$$

v/m

where  $E_2 = 1 \text{ volt/m.}$  and  $\hat{i}$  and  $\hat{j}$  are unit vectors along the X and Y axes, respectively.

Four rotating vector components,  $U_{\text{normal}}$  and  $U_{\text{parallel}}$  from the upper half and  $L_{\text{normal}}$  and  $L_{\text{parallel}}$  from the lower half of the array, combine in the far field as shown in Figure 7. On boresight then, the resultant RF polarization is linear vertical.

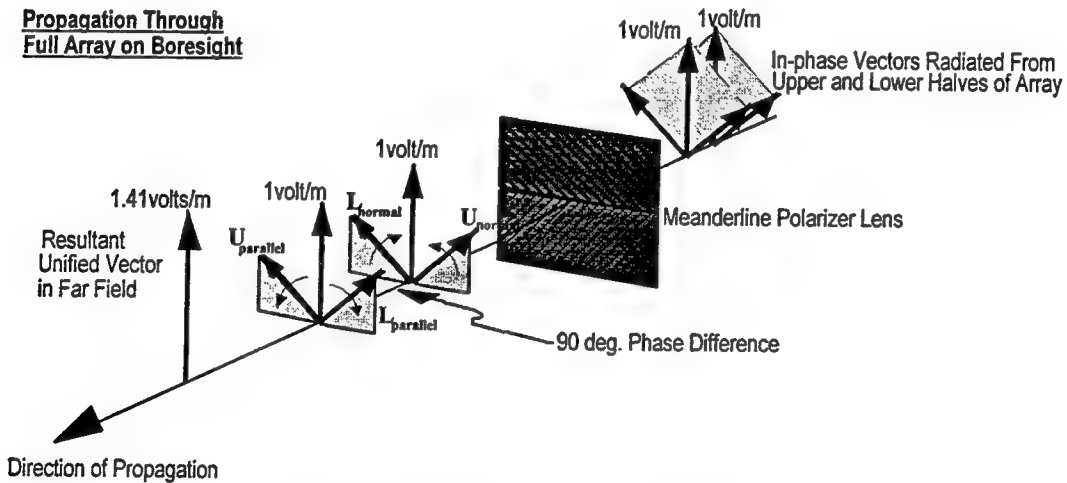


**Figure 7. Propagation Through Full Array on Boresight**



Performing mathematically what has been illustrated pictorially, **Eq. 5** is added to **Eq. 6**. After some manipulation using trigonometric identities, the resultant total E-field is

$$\bar{E}_t = 1.41 \sin \omega t \hat{j} \text{ v/m} \quad (\text{Eq. 7})$$

proving that the field resulting from the two apertures with circular polarization having contrary senses of rotation, is *vertical linear* on boresight, since vertically polarized transmissions are denoted by the  $\hat{j}$  term in each equation and horizontally polarized transmissions correspond to the  $\hat{i}$  term in each equation.

However, energy has been lost along the boresight axis. For instance, if each half aperture emits 1 volt/m. or 1 watt/m<sup>2</sup> of vertically polarized RF, these vectors will combine in the far field as a vertically polarized vector of 1.41 volts/m. or 2 watts/m<sup>2</sup>. Without the polarizer lens, each half aperture emits 1 volt/m, but since the upper and lower vectors are in phase, they would combine in the far field as 2 volts/m. or 4 watts/m<sup>2</sup>. Use of the polarizer has therefore resulted in a one-way loss of -3 dB plus approximately 0.2 dB I<sup>2</sup>R ohmic losses.

## 2.2 Polarization of Array and Lens Off Boresight

To consider the behavior of the RF voltage vector off boresight, a look at the more general far field equations provides a starting point. In Figure 8, a side view of the array aperture reveals the following phase relationships in the elevation plane:

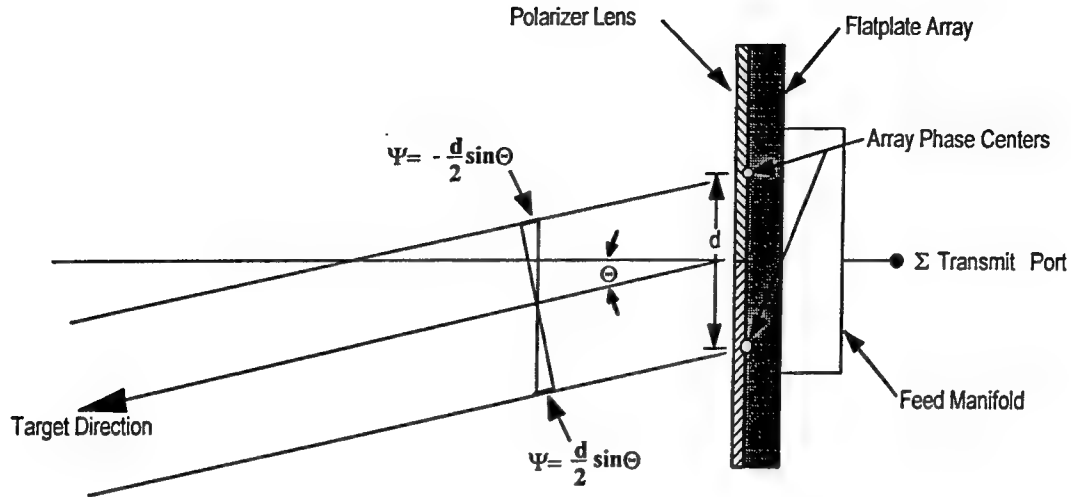


**Figure 8. Spatial Phase Relationships in the Elevation Plane**

As an example, if  $\Theta$  were 1 degree below boresight and  $d = 4.68$  inches (6.5 wavelengths at the array operating frequency), the upper and lower half apertures would be spatially out of phase by  $d \sin \Theta$ , or approximately 40 degrees.

The general time and space varying equations for any RF energy passing through the polarizer sheets on or off boresight would then be

$$\bar{E}_{upper} = -.5 \sin(\omega t - \Psi + 45^\circ) \hat{i} + .5 \sin(\omega t - \Psi + 45^\circ) \hat{j} + .5 \sin(\omega t - \Psi - 45^\circ) \hat{i} + .5 \sin(\omega t - \Psi - 45^\circ) \hat{j} \quad (\text{Eq. 8})$$

v/m

$$\bar{E}_{lower} = .5 \sin(\omega t + \Psi + 45^\circ) \hat{i} + .5 \sin(\omega t + \Psi + 45^\circ) \hat{j} - .5 \sin(\omega t + \Psi - 45^\circ) \hat{i} + .5 \sin(\omega t + \Psi - 45^\circ) \hat{j} \quad (\text{Eq. 9})$$

v/m

Propagation Through  
Full Array 1 Deg. Off  
Center Axis

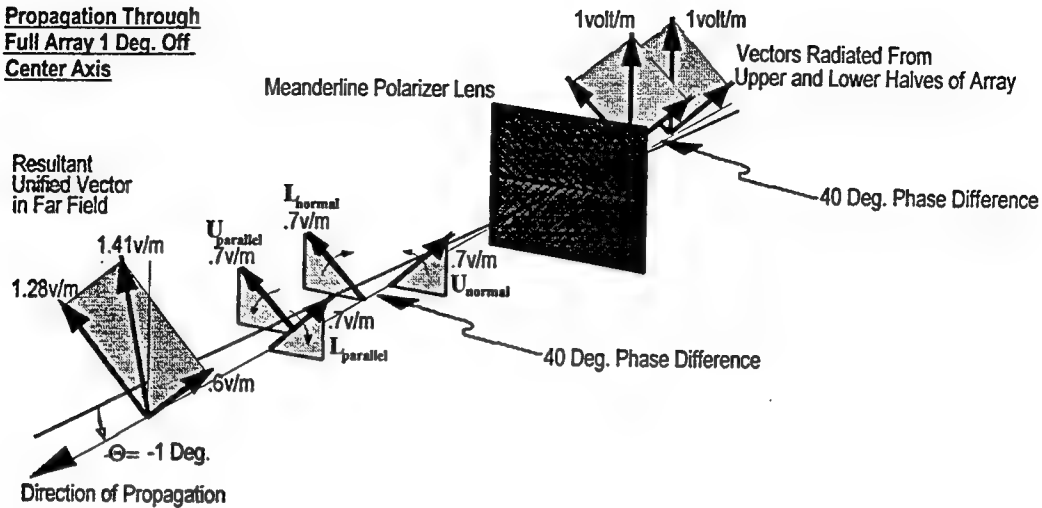


**Figure 9. Propagation Through Full Array 1 Deg. Off Center Axis**

From Figure 9 it is apparent that the total RF energy transmitted off boresight will still be linearly polarized, but the resulting vector will have an orientation other than vertical. In fact, if both halves of the array transmit simultaneously, *the combined vectors in the far field will always be linearly polarized, even though each half aperture is circularly polarized.* By combining Eq. 8 with Eq. 9 and manipulating trigonometric identities, a general expression for the radiated RF energy is found:

$$\bar{E}_t = 1.41 \sin \omega t \left[ -\sin \left( \frac{d}{2} \sin \Theta \right) \hat{i} + \cos \left( \frac{d}{2} \sin \Theta \right) \hat{j} \right] \text{ v/m} \quad (\text{Eq. 10})$$

As the angle of depression is increased, the resultant far field vector will continue to rotate until it becomes horizontally polarized. Referring back to Figure 8, this condition will occur when  $d \sin \Theta$  is a half wavelength, or for this test aperture, when  $\Theta = -4.4$  degrees. This prediction was borne out accurately in the far field patterns measured on the Westinghouse Norden compact range. Utilizing an approach similar to that used for the preceding mathematical development, it can

be demonstrated that were the difference channel to transmit, the RF energy radiated would be expressed thus:

$$\bar{\mathbf{E}}_t = 1.41 \cos \omega t \left[ -\cos \left( \frac{d}{2} \sin \Theta \right) \hat{\mathbf{i}} + \sin \left( \frac{d}{2} \sin \Theta \right) \hat{\mathbf{j}} \right] \text{ v/m} \quad (\text{Eq. 11})$$

In Eq. 10, the  $\hat{\mathbf{i}}$  term is zero when  $\Theta$  is zero on boresight, and the  $\hat{\mathbf{j}}$  term is maximum. The reverse is true for Eq. 11.

Table I summarizes the relative RF phase and amplitude in each channel according to the polarization of the returning radar signal.

|                                      | Sum Channel RF   | Difference Channel RF  |
|--------------------------------------|--|--|
| <b>Vertically Polarized Return</b>   | $1.41 \sin \omega t \left[ \cos \left( \frac{d}{2} \sin \Theta \right) \right]$  | $1.41 \cos \omega t \left[ \sin \left( \frac{d}{2} \sin \Theta \right) \right]$  |
| <b>Horizontally Polarized Return</b> | $-1.41 \sin \omega t \left[ \sin \left( \frac{d}{2} \sin \Theta \right) \right]$ | $-1.41 \cos \omega t \left[ \cos \left( \frac{d}{2} \sin \Theta \right) \right]$ |

**Table I. Relative Amplitude and Phase of RF in Receiver Sum and Difference Channels**

As can be observed from the table, the total far field pattern of the flatplate array with the split polarizer lens is linearly polarized upon transmission, with a polarization vector whose orientation varies according to the elevation depression angle  $\Theta$ . 3 dB of radiated power is lost by using the lens when transmitting through lower and upper half-apertures simultaneously. However, the radar system is then sensitive to both horizontally and vertically polarized returns.

### 3.0 MODES OF OPERATION

Two polarimetric modes are possible in the baseline RF configuration of Figure 3:

**3.1** Transmit from the full aperture (linear polarization, vertical on elevation boresight); receive at sum and elevation difference ports (vertical and horizontal linear polarization respectively on elevation boresight). Isolation between the two orthogonal receive polarizations is estimated to be more than 30 dB on boresight. A background system-level RF injection capability maintains the gain balance and phase alignment between the co- and cross-pol channels at approximately 0.1 dB and 1.0° respectively.

**3.2** Transmit from the upper half aperture only (righthand circular polarization); receive at upper and lower aperture ports (right and lefthand circular polarizations), which are connected to the sum and elevation difference receivers, respectively.

In order to support interferometric applications while maintaining weather penetration, the three interferometers should be covered by a lens, as well. For maximum separation of aperture phase centers, they should work in conjunction with the upper half of the monopulse array, and should therefore be like-sense polarized (righthand circular).

Another configuration, shown in Figure 10, would create a fully polarimetric system. It requires an additional RF switch and slight modification to the waveguide runs. A fully polarimetric linear system is defined as one which transmits alternately Vertical and Horizontal, and receives both Vertical and Horizontal (HH, VV, HV). A fully polarimetric circular system is defined as one which transmits alternately righthand and lefthand circular, and receives both right- and lefthand circular (RL, LR). Righthand circular is abbreviated R and lefthand circular is L, while linear vertical is V and linear horizontal, H.

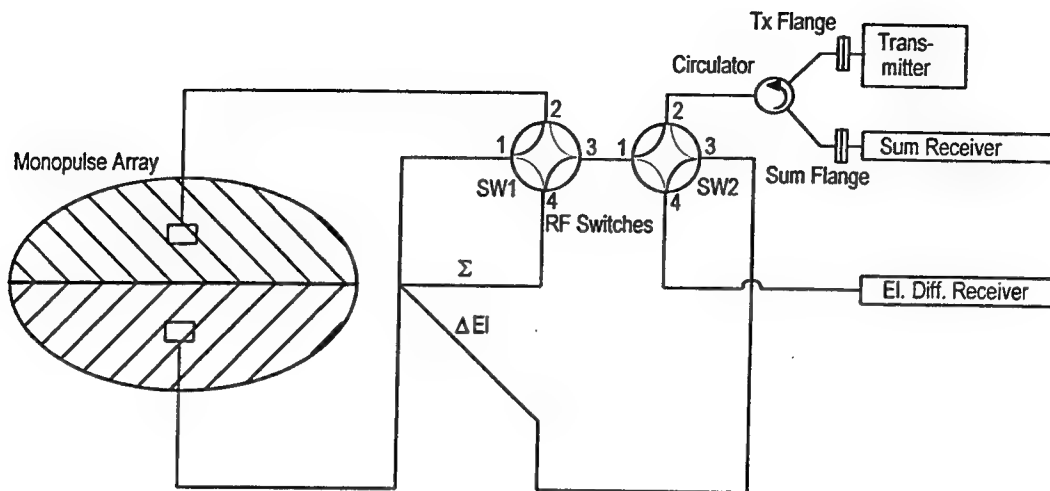


**Figure 10. Simplified Electrical Schematic of Fully Polarimetric Monopulse Aperture**

Table II lists the modes possible with the various switch positions.

| SW1<br>Position | SW2<br>Position | Modes   |
|-----------------|-----------------|---|
| 1-2,3-4         | 1-2,3-4         | Transmit V on boresight, receive co-linear at Sum Rcvr;<br>receive orthogonal linear at El Difference Rcvr. |
| 1-2,3-4         | 1-4,2-3         | Transmit H on boresight, receive co-linear at Sum Rcvr;<br>receive orthogonal linear at El Difference Rcvr. |
| 1-4,2-3         | 1-2,3-4         | Transmit R, receive R at Sum Rcvr, receive<br>L at El Difference Rcvr.                                      |
| 1-4,2-3         | 1-4,2-3         | Transmit L, receive L at Sum Rcvr, receive<br>R at El Difference Rcvr.                                      |

**Table II. Possible Modes of Operation With Fully Polarimetric Monopulse Aperture**

#### 4.0 HARDWARE TEST PROGRAM

A comprehensive flight test and evaluation program is being funded which will encompass the following phases:

4.1 A lens design has been established which permits the polarizing lens to be installed on the test antenna in a flightworthy fashion, and removed with no damage to the array face. A lens will be fabricated and installed on the array, and pattern tests will be performed by the lens contractor.

4.2 A polarization data collection mode will be developed to permit polarization testing and evaluation using the test radar hardware on the Norden Gulfstream II aircraft. The Gulfstream II is a test vehicle utilized by Norden Systems for flight testing of their various airborne radar systems. This will include collection of the data necessary to evaluate the use of the lensed system for airborne automatic target recognition (ATR).

It is expected that data will also be collected to support evaluation of a sum channel transmission mode with the antenna rolled  $45^\circ$  about boresight, or equivalently, off-elevation boresight reception in a region where the polarization vector is oriented at  $45^\circ$  from the vertical. This method yields HH-VV and HH+2HV+VV polarimetric data (HH-VV alone is known to be a useful target-clutter discriminant).

4.3 I and Q radar data will be recorded on high speed digital tape together with GPS/INS (Global Positioning Satellite/Inertial Navigation Satellite), IMU (Inertial Measuring Unit) and time tag data. Also, the in-flight radar display shall be recorded on video tape.

## **5.0 DATA PROCESSING AND EVALUATION**

Upon completion of the flight test, data will be processed and evaluated.

5.1 The in-flight video tapes will be reviewed and hard copies of selected scenes will be created. The I/Q data will be ground-processed to create representative imagery. This imagery may include SAR (Synthetic Aperture Radar) with 10-, 3-, and 1-foot resolution, GMTI (Ground Moving Target Indication) relocated and overlaid on SAR, and IMTF (Interferometric Moving Target Focussing) imagery.

Images may represent either polarization channel, ratios of the two channels, or linear combinations of the two channels. At least four images will be provided.

5.2 High range resolution (1 ft.) data will be motion-compensated and clutter-cancelled, and provided to Wright Laboratory in Dayton, Ohio for time domain range profile studies.

5.3 A partial polarization whitening filter (PWF) shall be designed, based on the fully polarimetric PWF technique introduced by L. Novak at MIT/Lincoln Laboratory in Cambridge, Mass. [5,6]. The partial PWF filter will then be applied to the test imagery to evaluate its applicability for clutter reduction, using measurements of effectiveness as published by Novak.

5.4 All processed data will be available to Wright Laboratory for evaluation.

## 6.0 REFERENCES:

- [1] "Antenna Engineering Handbook", Edited by R.C. Johnson and H. Jasik, McGraw-Hill Book Co., 1984, pp. 9-20 to 9-26.
- [2] "Multimode Antenna Array", P.W. Smith, U.S. Patent No. 4,376,281 (1983).
- [3] "Waveguide Handbook", N.Marcuvitz, Dover Publications, Inc., 1951, pp. 280-285.
- [4] "Meander-line Polarizer", Leo Young, Lloyd A. Robinson and Colin A. Hacking, *IEEE Transactions on Antennas and Propagation*, May 1973.
- [5] "Optimal speckle reduction in polarimetric SAR imagery", L. M. Novak and M. C. Burl, *IEEE Trans A&ES*, v 26, pp 293-305, March 1990.
- [6] "Joint spatial-polarimetric whitening filter to improve SAR target detection performance for spatially distributed targets", Les Novak et al, *SPIE Conference on Algorithms for SAR Imagery*, Orlando, Fla., April 1994.



## **A W-BAND ACTIVE PHASED ARRAY ANTENNA**

B. J. Edward, R. S. Webb, S. Weinreb\*

Martin Marietta Laboratories-Syracuse, NY

\*Martin Marietta Laboratories-Baltimore, MD

### **ABSTRACT**

The design and fabrication details for 94 GHz active receive and transmit array-modules are presented. These modules comprise eight elements in a line array configuration and can be readily combined to realize larger one- or two-dimensional systems. Amplifiers and phase shifters are located with each element to achieve high receive sensitivity or high transmit power generation efficiency, along with electronic positioning of the antenna beam. An innovative approach for fabricating the modules employing a multi-layer DC/control substrate onto which is mounted the RF substrates, active and passive circuit chips including MMICs, package wall, and top lid is described. Printed dipole-style radiating elements which mount directly to the front of the modules are also detailed. The measured performance of an eight-element demonstration array assembled from a receive module with the radiating elements operating in conjunction with a corner reflector is presented.

## 1.0 INTRODUCTION

The development of millimeter wave MMIC circuits has made the cost and performance advantages of active phased arrays available at frequencies up through W-band (94GHz). Active, electronically steered arrays have significant performance advantages over conventional antenna designs and are rapidly becoming cost competitive as MMIC and packaging developments continue. In this paper we describe a recently developed eight element array-module that can be used to build up active phased arrays in a variety of configurations optimized for each application.

A wide diversity of applications exists for W-band phased array systems. Some of the more common include; terminal guidance for precision munitions ("smart bombs"); self protection system sensors for armored vehicles, acquisition and guidance for TMD and NMD interceptors, precision landing guidance for aircraft, and obstacle warning/collision avoidance for highway vehicles. These all have common requirements for weather penetration, good acquisition range, high angular accuracy while fitting a small aperture, and affordability. A building block module such as the array-module described in this paper, can be configured in a variety of arrays to meet the requirements of these various applications.

Precision guided munitions (PGMs) typically require a terminal guidance sensor having an acquisition range of a few kilometers, beam agility scanning over  $\pm 30^\circ$ , data rate to support target discrimination, and sufficient angular accuracy to hit a selected aim-point. This performance should not be significantly degraded by operation in fog, dust, smoke, or rain. Analysis and experiment have shown that the required performance for a PGM sensor can be obtained with an array having an average power in the range of two to ten watts, and an aperture near ten centimeters. For some applications, an aperture composed of orthogonal linear arrays will suffice, at considerable savings in cost, volume, and weight. Fabrication of linear arrays is readily accomplished using the basic eight-element building block.

Ballistic missile defense (BMD), particularly against theatre missiles, can be significantly enhanced by having interceptors which can operate in the atmosphere. Active millimeter-wave phased array

seekers can provide terminal guidance with sufficient range and accuracy to support kinetic "hit-to-kill" interceptor designs. Compared to PGM sensors, BMD seekers must have longer acquisition range and operate against targets having much smaller radar cross sections. A typical seeker design for this application, operating at 94 GHz, would have a 12 cm diameter aperture populated with approximately 2200 transmit/receive modules, each having a 100 - 150 mW power amplifier, on a grid spacing that supports  $\pm 30^\circ$  scanning. Arrays using this two-dimensional architecture can be readily fabricated using the array-module described in this paper.

Active arrays – i.e., arrays having elemental low noise and power amplifiers at the array face – have a large signal to noise ratio advantage by eliminating losses between radiating elements and amplifiers incurred in conventional systems. This advantage can range upwards from 8 dB, and can be used for improved performance, or reduced cost. Other advantages of electronically steered arrays include ready implementation of monopulse tracking, capability for electronic beam stabilization, and beam agility to support multiple target tracking.

## **2.0 ARRAY-MODULE DESIGN**

Eight-element line array-modules constitute the building blocks for W-band active receive and transmit arrays. Multiple array-modules are combined to realize larger one- or two-dimensional systems. The modules incorporate amplifiers and phase shifters at each radiating element to achieve high receive sensitivity or high transmit power generation efficiency, along with electronic positioning of the antenna beam. An innovative approach is employed for fabricating the modules consisting of a multi-layer DC/control substrate onto which is mounted RF substrates, active and passive circuit chips including MMICs, package wall, top lid, and radiating elements. Exclusive of the radiating elements, the modules are only 0.652 inches in width, 1.114 inches deep, and 0.072 inches thick. The overall module size is compatible with contiguous placement of units to form two-dimensional arrays. The module weight is only 0.15 ounces.

The block diagram for the transmit array-module is presented in Figure 1.

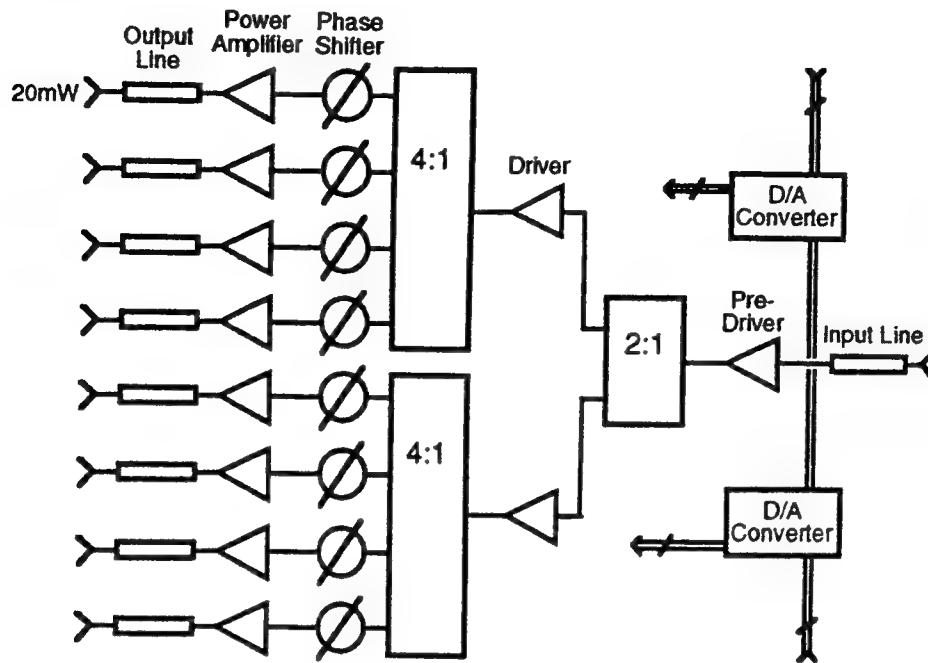


**Figure 1. Transmit Array-Module Architecture.** The receive module architecture is identical with the exception of having low-noise amplifiers in place of the transmit unit's power amplifiers.

The basic architecture for both receive and transmit modules is identical, with the exception of the receive module having low-noise amplifiers where the transmit unit has power amplifiers. Referring to the transmit line-up, the input signal is applied to a pre-driver amplifier, split into two channels, and directed to driver amplifiers. The output of each driver is further divided into four channels and sent to the elemental phase shifters and power amplifiers. The output of the final power amplifiers is connected directly to the radiating elements. The successive levels of amplification is required to compensate for the power splitting inherent in forming the multiple channels and for the dissipative losses incurred in the divider networks. All amplifiers in the transmit array-module are of a common design – a three-stage GaAs MMIC with pHEMT devices. The phase shifter MMIC is an analog design having varactor diodes. D/A converters within the module translate digital control input words to the analog voltages required for setting the phase. An analog control voltage is also generated and applied to the gate biasing of the amplifiers to achieve channel gain control. The transmit output power is nominally 20 mW per radiating element.

The receive array-module substitutes low noise amplifiers for the transmit's power amps. All amplifiers are of a common four-stage pHEMT design. The other componentry is identical to that of the transmit unit. The receive gain is nominally 48 dB per channel with a gain control range in excess of 30 dB and a noise figure on the order of 5.5 dB.

An exploded view of the array-module is provided in Figure 2.

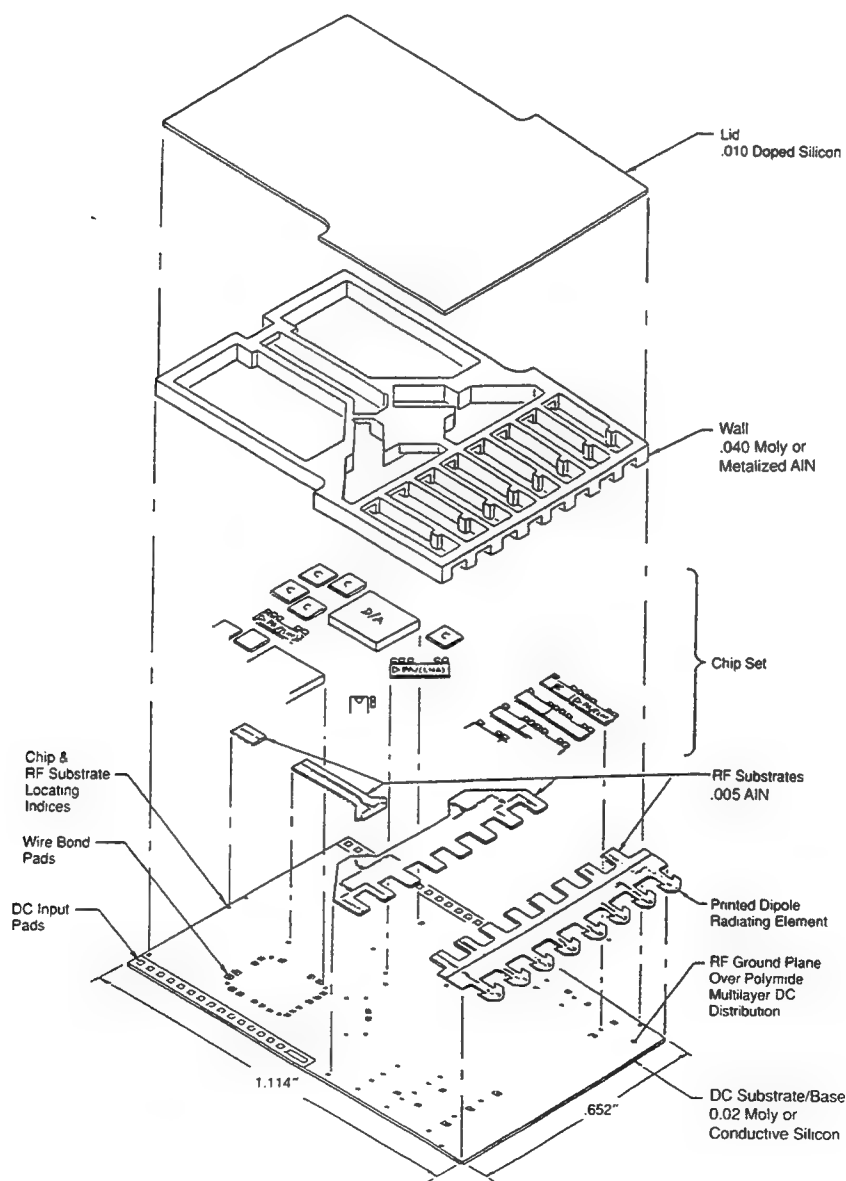


**Figure 2. Exploded View of the Array-Module.** A multi-layer DC distribution substrate serves as the base to which all other module components are mounted.

A multi-layer DC and control signal substrate/base, and RF substrates provide for all the interconnects within the module. Active and passive circuit chips, a package wall, top lid, and radiating elements are the remainder of the components. The package is identical for both the receive and transmit array-modules. Both employ the same analog phase shifter circuit, and the low noise and power amplifier MMICs are of the same size and have identical RF and DC bond pad locations. Therefore, only one package design is fabricated and it is populated by either low noise or power amplifiers respectively for the receive or transmit application. Figure 3 shows the principal module componentry.

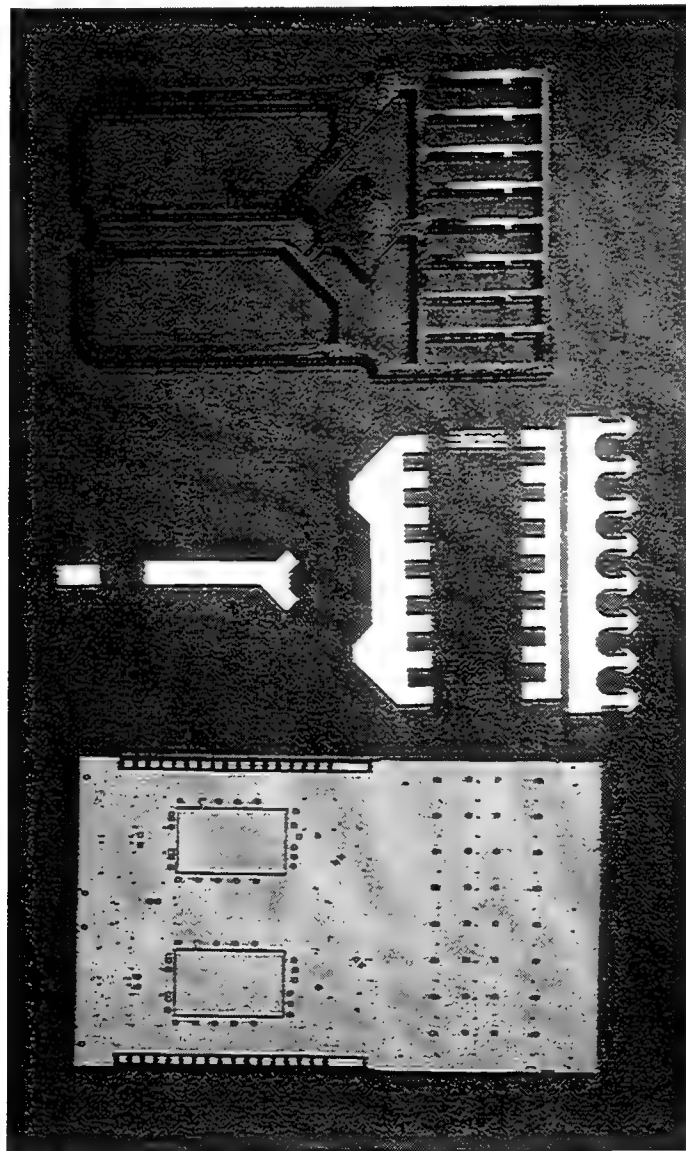


**Figure 3. Array Module Componentry.** From the top, package wall EDM'd from molybdenum, GaAs MMIC amplifier, laser cut AlN RF substrates and radiating elements, and multi-layer DC substrate.

The DC substrate, depicted in cross section in Figure 4, consists of a 0.020 inch thick molybdenum base onto which is deposited multiple layers of copper conductors and polyimide insulation.

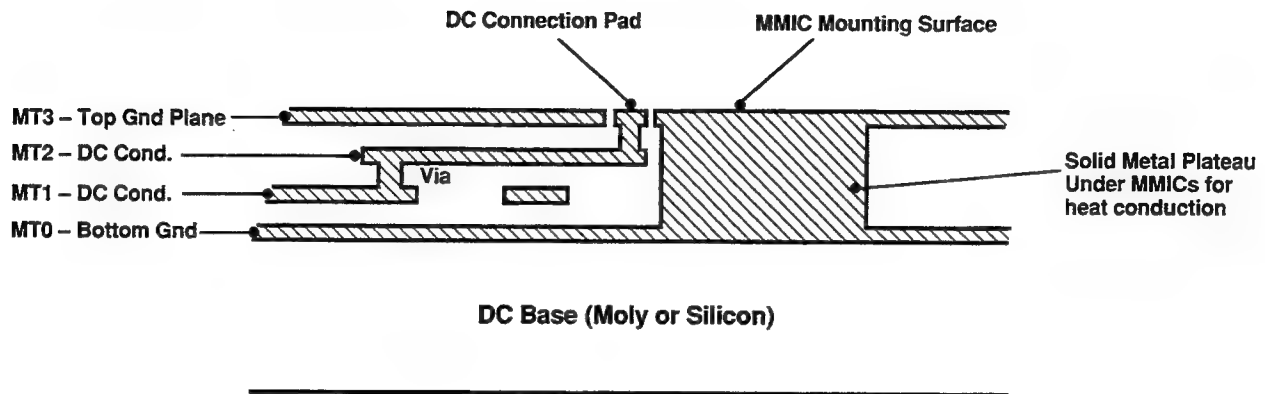


**Figure 4. Cross-Section of the Multi-Layer Polyimide/Copper DC Substrate.** Since conductor traces can cross each other and run under module components, very dense interconnects are realized.

Molybdenum exhibits high thermal conductivity for efficient extraction of heat from the power amplifiers, has a coefficient of thermal expansion that is well matched to the other module components (thereby minimizing stresses), and can be prepared with a surface finish suitable for the multi-layer process. For lower power densities, conductive silicon, which has all the favorable properties of molybdenum with the exception of high thermal conductivity, may be used. Conductor traces distribute the DC power and control signals throughout the module, running within the layers of polyimide and coming to connection pads on the top surface next to the circuit chips. Since multiple layers of these traces are formed that can cross each other and even run under other module components, very dense interconnects are realized. Input DC and control contact pads are located along both sides of the module. When multiple modules are mounted side-to-side to form larger arrays, DC and control signal distribution is achieved by jumpering these contacts between modules in daisy-chain fashion. The top surface of the DC substrate is almost entirely gold-plated copper, with openings only at the connection pad locations and small fiducials to facilitate positioning of module components. This extensive conductive surface shields

the DC traces from RF signals, greatly diminishing stray coupling via these paths. All of the other module components are mounted directly onto this surface. The DC substrate is batch fabricated, six units per a molybdenum or silicon wafer. Figure 5 shows a wafer at process completion.

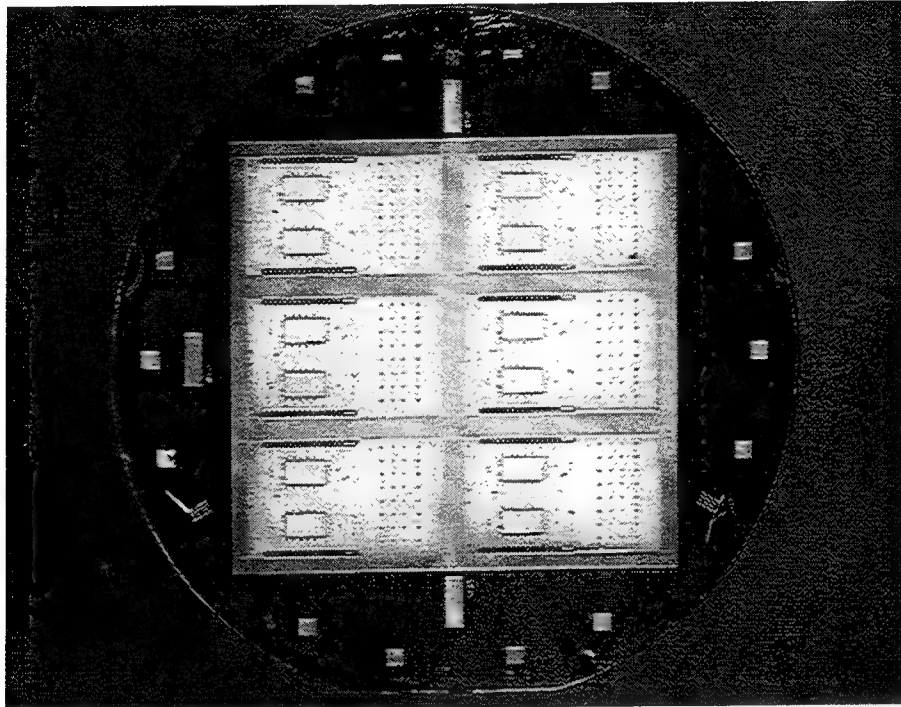


**Figure 5. Multiple DC Substrates Fabricated on a Single Wafer.** Molybdenum or conductive silicon wafers are used, with moly selected for higher power applications where efficient heat removal is required.

The individual substrates are either sawn or electro-discharge machined out of the wafer.

The RF substrates are low-loss ceramic, 0.005 inch thick, patterned with microstrip interconnects. Aluminum nitride material was used for the W-band array-modules, but alumina can also be employed. The unique shapes of the various RF substrates (refer to Figure 3) are defined by laser machining. These substrates are attached with either conductive epoxy or solder directly to the DC substrate. Chip components (MMICs, capacitors, etc.) are also mounted onto the DC substrate. When a high thermally conductive path is required directly under a component, such as under the power amplifiers, the DC substrate is designed to have exclusively metal layers at that component location.



At microstrip interface locations, such as at MMICs and radiating elements, grounded pads are provided at each side of the microstrip in a coplanar waveguide fashion to facilitate RF probing at these points and enable a three ribbon bond interconnect (ground-signal-ground). This design, in conjunction with the continuous common ground plane under the MMICs and RF substrates, results in a very high-performance millimeter-wave interface that is tolerant to a wide range of spacings between the components. Connections between chips and the DC pads are implemented with wire bonds.

The package wall also mounts to the DC substrate. The walls used in assembling the W-band modules were electro-discharge machined from 0.040 inch thick molybdenum. Walls laser machined from alumina and then metalized were also successfully fabricated. The conductive wall in conjunction with the continuous top metal of the DC substrate forms shielded enclosures for the circuitry, improving stability by electrically isolating various portions of the module assembly. A top lid mounts to the wall, completing the enclosure. The lid is fabricated from 0.010 inch thick silicon, optimally doped to attenuate waveguide modes within the enclosures. The outer surface of the silicon lid is metalized for shielding.

Printed dipole radiating elements also mount to the DC substrate, overhanging the front edge of the module. These elements connect directly to the final power amplifiers through a short length of microstrip line. They are spaced at 0.082 inches to support electronic beam scan to 30° from array broadside without the formation of grating lobes.

### **3.0 MODULE COMPONENTS**

#### **3.1 MMICs**

Our design for the array-module is based on three advanced, high performance MMIC circuits – power amplifier, low noise amplifier, and phase shifter – recently developed at our Baltimore laboratories.

#### Power Amplifier MMIC [1]:

We have developed at our Baltimore laboratories, a monolithic, three stage, W-band power amplifier using pseudomorphic HEMTs which has exhibited record gain, power per unit gate width, and power per unit area. Figure 6 is a photograph of four of the power amplifier MMIC.

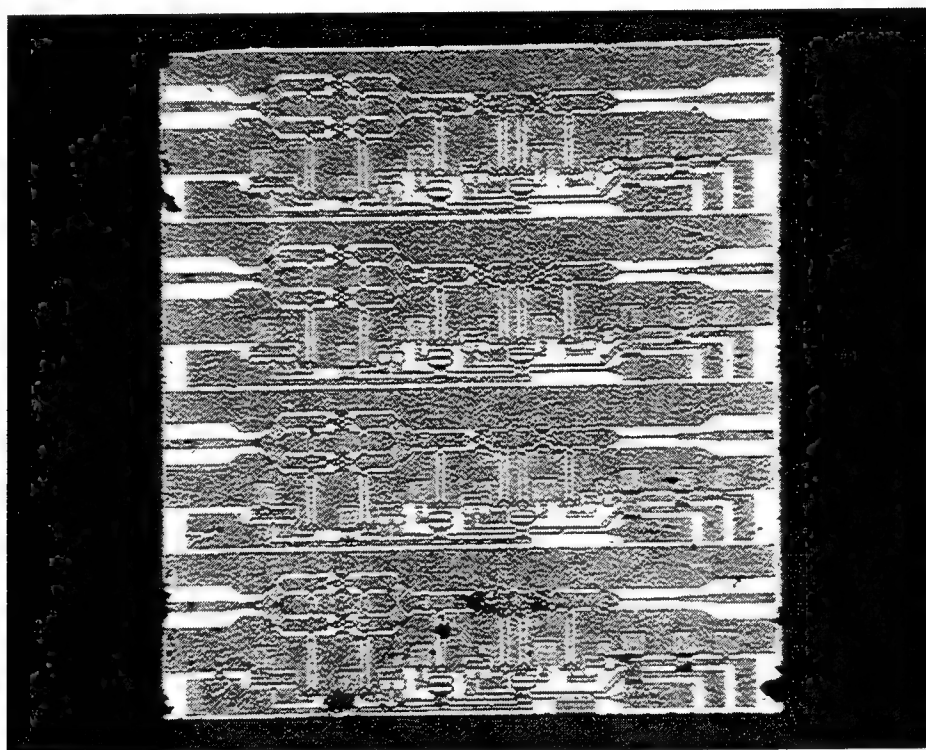


**Figure 6. W-Band Power Amplifier MMIC:** Photograph of four monolithic, pHEMT, three stage, W-band power amplifier MMIC used in demonstration array-module. Power output 37 mW with gain of 10 dB.

The W-band amplifier has a small signal gain of 22 dB, and an output power of 37 mW with an associated gain of 10 dB and an overall efficiency of 4.7%. The efficiency for the output stage is 9.4%.

These circuits achieved a power per unit gate width at W-band of 185-mW/mm, which to the best of our knowledge is the highest yet reported. Total chip area has also been minimized; power per unit area, 10-mW/mm<sup>2</sup> is a significant improvement over previous results.

### Low Noise Amplifier [2]:

The receive version of the array-module uses a monolithic W-band LNA MMIC based on 0.1  $\mu\text{m}$  AlGaAs/InGaAs/GaAs pHEMT technology recently developed in our Baltimore laboratories. A photograph of the amplifier is shown in Figure 7.

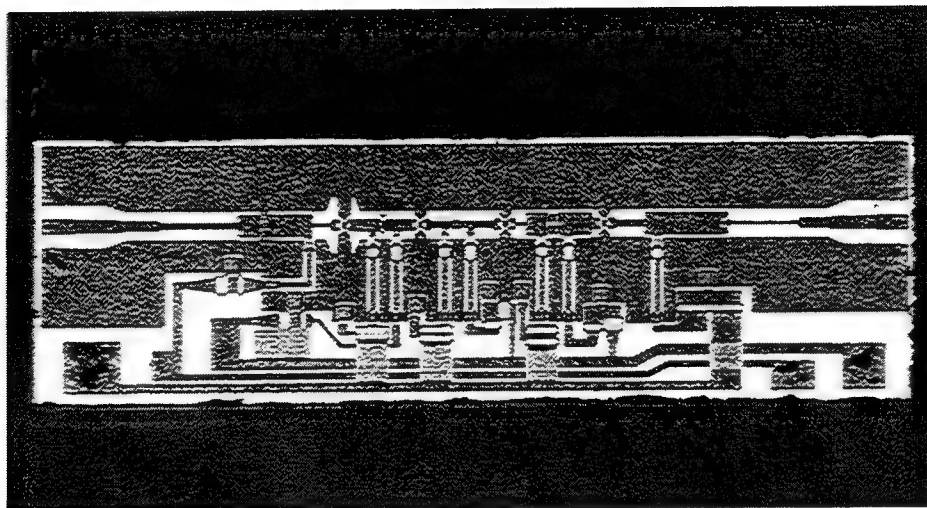


**Figure 7. W-Band LNA MMIC:** Photograph of monolithic, pHEMT low noise W-band amplifier used in demonstration array-module. Gain 26 dB and noise figure 4.6 dB.

The amplifier performance was measured with bias optimized, respectively, for maximum gain and minimum noise figure. With maximum gain bias, the amplifier has a peak gain of 31.7 dB and a noise figure of 5.9dB at 102 GHz. With minimum noise bias, the amplifier has a gain of 26 dB and noise figure of 4.6 dB at 98 GHz.

Phase Shifter [3]:

Both transmit and receive versions of the array-module use an analog phase shift MMIC, shown in Figure 8.

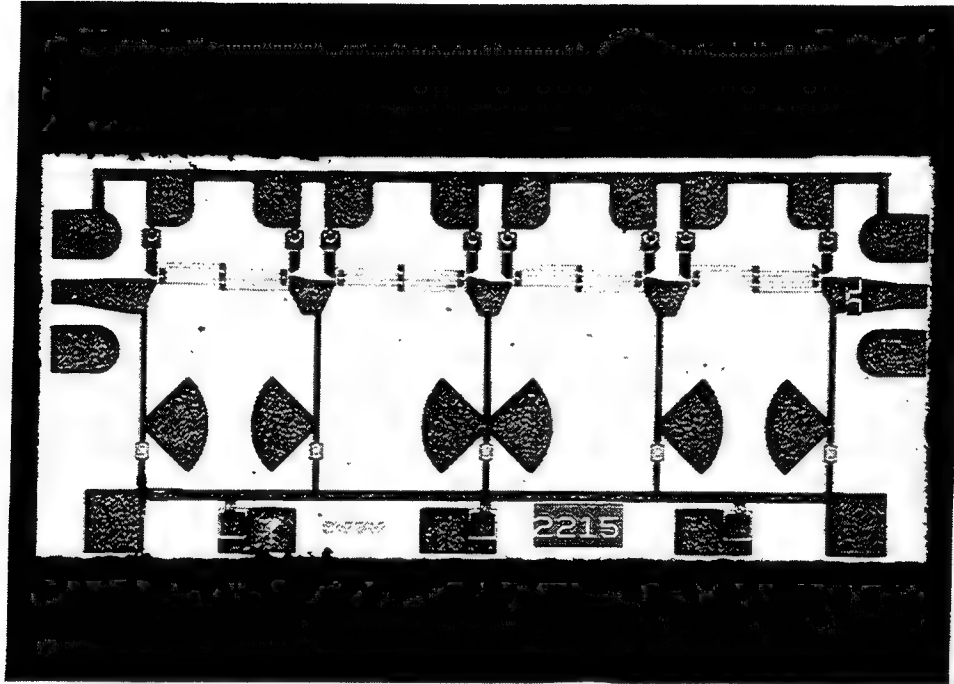


**Figure 8. W-Band Phase Shifter MMIC:** Photograph of analog varactor MMIC phase shifter used in demonstration array-module.

Analog phase shifters driven by D/A converters offer digital control with phase step size dependent upon the number of D/A bits and the non-linearity in the phase vs control voltage curve. With an 8-bit D/A converter, the phase shifter described here has an average phase step of  $1.4^\circ$  and a worst case phase step of  $9^\circ$ . Our design uses four zero to  $90^\circ$  sections to achieve a total range of  $360^\circ$ . Figure 8 shows the four sections of our phase shifter. The MMIC process includes thin-film bypass and coupling capacitors and resistors for bias isolation. Input and output connections are in the form of co-planar waveguide pads to allow probe testing and ready circuit insertion. This circuit demonstrates a phase shift range of  $358^\circ$  for a bias voltage change from 0.2V forward to 12V reverse. The variation of loss and phase shift with frequency is adequate to support a system with a bandwidth of less than 3 GHz.

### 3.2 Radiating Elements

Printed dipole radiating elements are employed for the W-band array. Samples of these elements are shown in Figure 9.



**Figure 9. Printed Dipole Radiating Elements.** Fabricated on the same material as the RF substrates and having a microstrip feed that interfaces directly with the active circuitry, these elements readily integrate with the receive and transmit modules.

The elements are printed on 0.005 inch thick aluminum nitride substrates, with the dipole radiating arms on one side; the microstrip feed line on the other; and the shorted coplanar strip and microstrip open stubs, which form the balun, using both substrate sides. This element type was selected for its ease of integration with the array-modules. Since the element is designed for the same material as the modules' RF substrates, it can be printed as part of these interconnects. The microstrip feed also enables a direct connection to other module componentry, in this case the MMIC amplifiers. Similar printed dipoles have been developed for 20, 35, 44, and 60 GHz arrays, so the 94 GHz design effort represented an extension of that work.

To realize the required H-plane beamwidth, the line array elements are located within a corner reflector. The design process, therefore, considered the reflector's included angle and depth, the dipole height with respect to the reflector apex, and the dipole's arm lengths in order to establish the H-plane beamwidth, to achieve an E-plane beamwidth compatible with line array's beam scan requirements, and to result in a dipole impedance that may be matched to the active circuitry. A dipole was modeled using a method-of-moments code with images to mimic the reflector. This work together with published experimental data [4] established the above design parameters.

The layout of the radiating element and its transmission line equivalent circuit are given in Figure 10 [5].

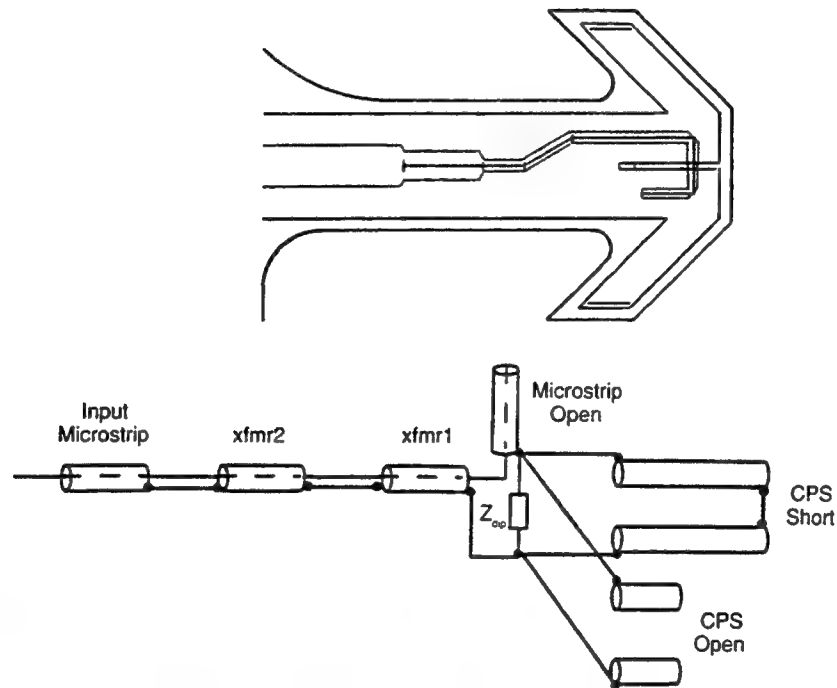


**Figure 10. Radiating Element Layout and Equivalent Circuit.** The stubs which form the balun together with the input transmission lines perform impedance matching to the dipole's resonant impedance.

The stubs which form the balun together with the input transmission lines perform matching of the approximately  $138\Omega$  dipole resonant impedance, as determined by the moment code modeling, to the nominally  $50\Omega$  impedance of the active circuitry. The stubs and transmission line discontinuities were individually modeled using Sonnet Software's "em" to determine appropriate compensation factors in the physical layout of the element.

A baseline element design together with samples having perturbations in stub and dipole arm lengths were printed onto aluminum nitride and cut out by laser. These elements were individually mounted into a corner reflector test fixture, shown in Figure 11, and measured for input impedance using an RF coaxial/coplanar waveguide probe in conjunction with our W-band automatic network analyzer.

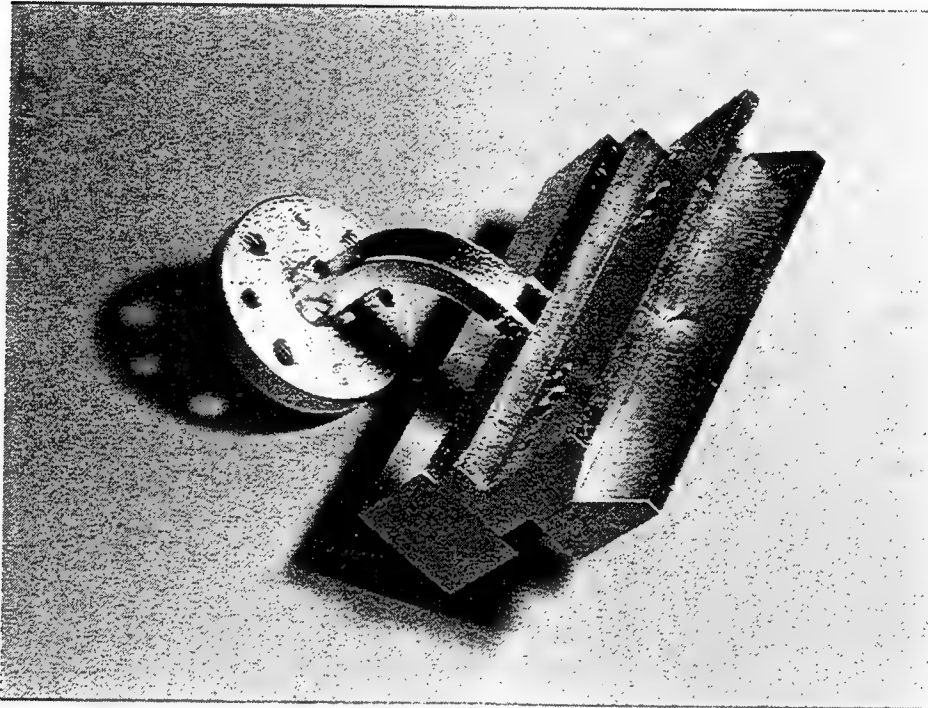


**Figure 11. Dipole Element Mounted into a Corner Reflector Test Fixture.** Sample elements having perturbations in stub and dipole arm lengths were evaluated for impedance match and radiation patterns.

The return loss characteristics of the selected design are presented in Figure 12. The element exhibits a better than 2:1 VSWR (return loss greater than 10 dB) over a 15 percent bandwidth.

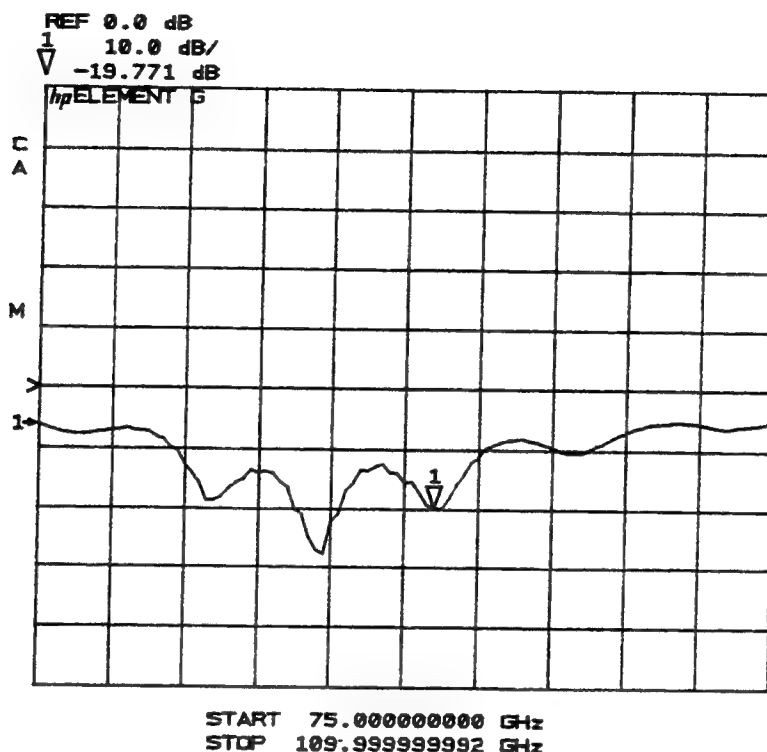


**Figure 12. Measured Return Loss of the Printed Dipole Radiating Element within the Corner Reflector.** The element features a better than 2:1 VSWR over a 15 percent bandwidth.

The radiation patterns of the selected design were also measured. The element was mounted in the corner reflector test fixture mated with a waveguide to microstrip transition (evident in Figure 11) to facilitate connection to the anechoic chamber test apparatus. Measured data at 94 GHz is presented in Figure 13.



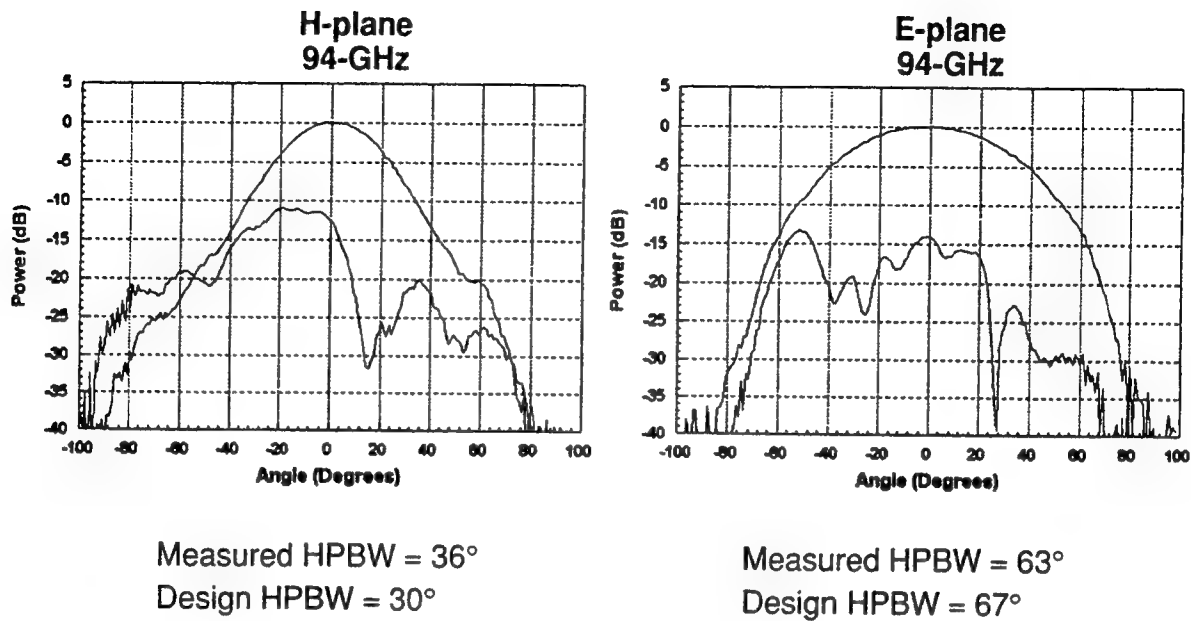


**Figure 13. Measured Radiation Patterns of the Printed Dipole Radiating Element within the Corner Reflector.** The element exhibits symmetric patterns in both principal planes with half-power beams very close to design values.

The patterns are very symmetric in both principal planes. Half-power beamwidths are very close to the design values, with them being somewhat wider than anticipated in the H-plane and slightly narrower in the E-plane.

### 3.3 Package Lid

The module compartment, defined by the package wall, containing the elemental amplifier and phase shifter has its lowest rectangular cavity resonant frequency at 97 GHz. Since the amplifiers have gain up to 110 GHz, the cavity must be damped to avoid possible oscillations. An attractive way to do this is to make the module lid out of doped silicon which is plated only on the (outside) top and edges. The plating on the lid top provides a conducting layer which shields the entire module, but leaves the

lossy layer exposed on the inside to provide the damping. With this approach, both the damping and shielding functions are provided in a single part.

Insertion loss of the cavity when excited by open circuit microstrip stubs placed at each end was analyzed using Sonnet Software's "em." The cavity (0.062" w X 0.262" l X 0.010" h) was loaded with 0.005" thick alumina ( $\epsilon_r = 9.8$ ) on the bottom, and 0.010" thickness of silicon on top ( $\epsilon_r = 12$ ), leaving 0.035" air. The results are plotted in Figure 14 for various doping levels of silicon. Figure 14a shows values of loss tangent between 0.001 and 0.5;

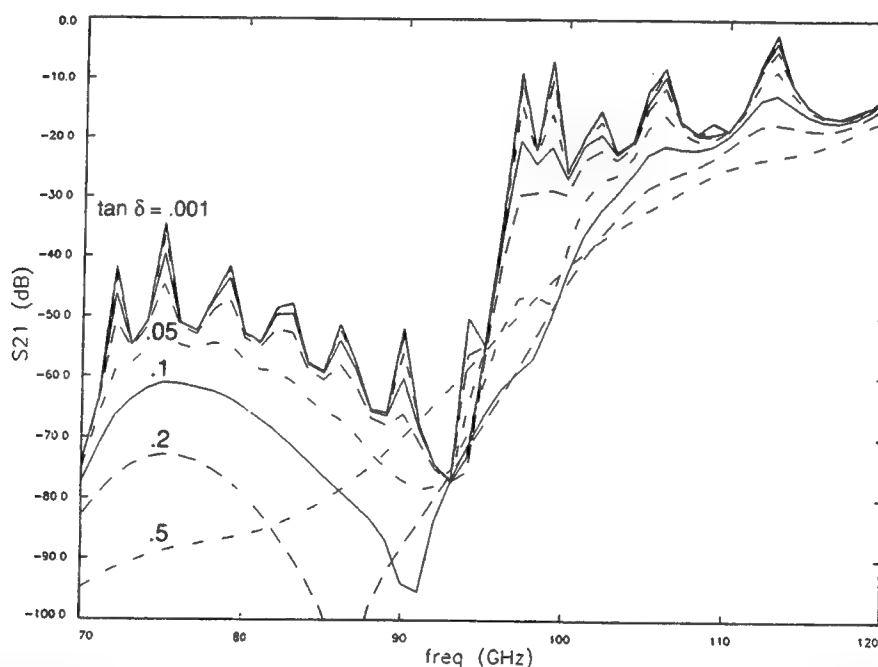


**Figure 14a. Amplifier/Phase Shifter Cavity Loss vs Frequency for Various Lid Doping Levels.** Loss tangent values between 0.001 and 0.5. A silicon lid loss tangent of 0.5 optimally dampens the rectangular cavity-modes to preclude amplifier instabilities.

Figure 14b shows values between 1 and 500.

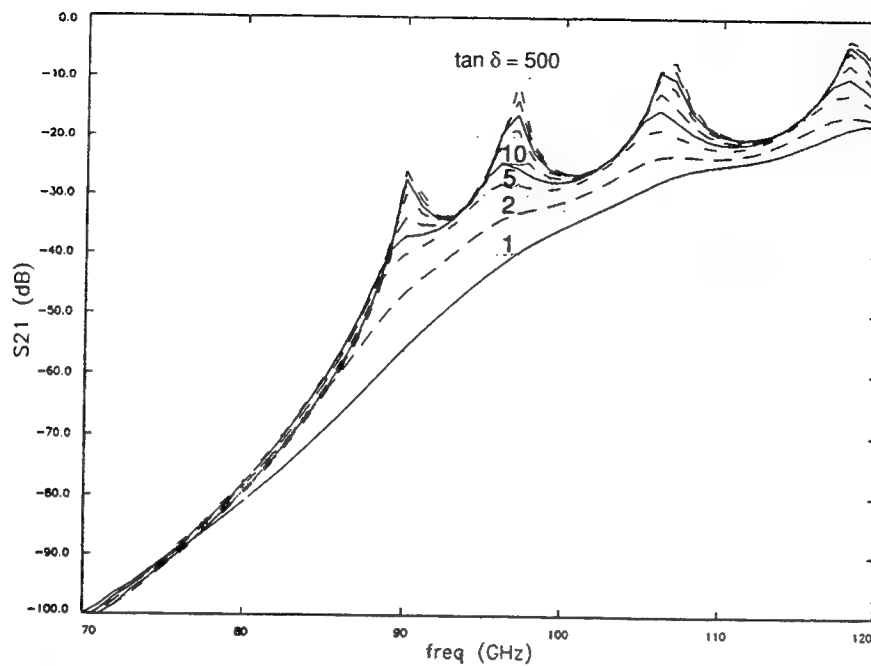


**Figure 14b. Amplifier/Phase Shifter Cavity Loss vs Frequency for Various Lid Doping Levels.** Loss tangent values between 1 and 500.

The chosen loss tangent value of 0.5 provides the highest loss in the cavity up to 110GHz. The corresponding resistivity is given by

$$R = [ \omega \epsilon_r \epsilon_0 \tan \delta ]^{-1}$$

giving a value of 3.2 ohm-cm at 94 GHz.

#### 4.0 DEMONSTRATION ARRAY

Receive and transmit eight-element array-modules have been assembled. The receive array has been fully tested for individual channel characteristics using the network analyzer, which was followed by radiation pattern and beam steering performance measured in the anechoic chamber. Testing of the transmit array is now beginning.

An assembled receive module is shown in Figure 15.

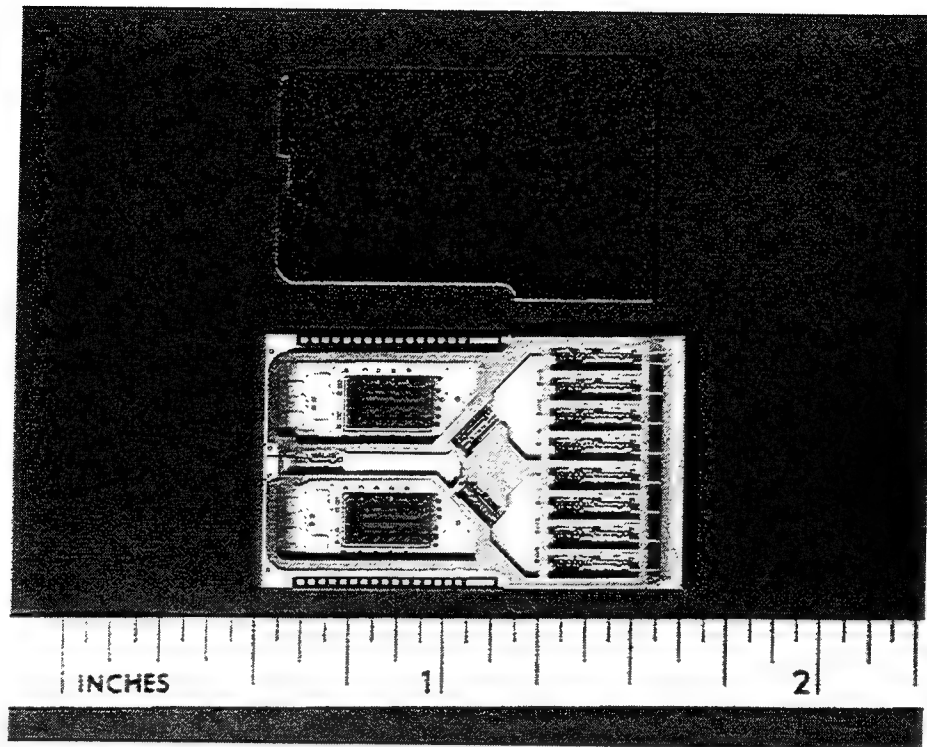
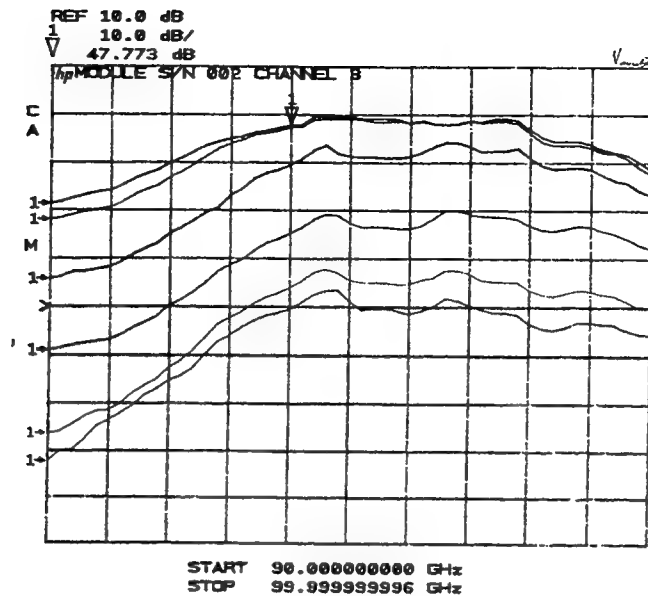
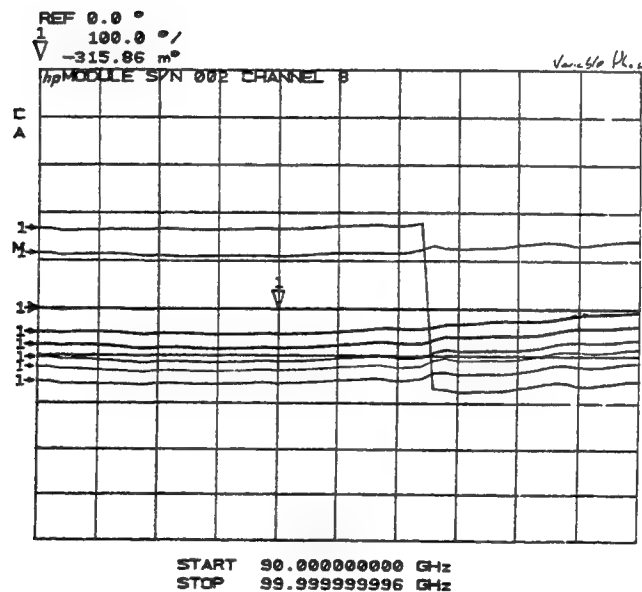


**Figure 15. Assembled Receive Module.** After RF probe testing of individual channels on the network analyzer, radiating elements are attached (right side of module in photo) and radiation pattern measurements performed.

Each compartment, defined by the package wall, in the right of the figure contains the low noise amplifier and phase shifter MMICs for one channel. Chip bypass capacitors and isolation resistors are mounted along side the MMICs, and wire bonds run from the MMIC DC pads to the passive chip components and to the pads on the surface of the DC substrate. The large silicon chips in the compartments towards the left of the module are the D/A converters for controlling phase and gain of each channel. The radiating elements are not yet mounted to allow two-port measurements of each channel using RF probes.



Gain Control Performance



Phase Control Performance

**Figure 16. Gain and Phase Characteristics of a Channel of the Receive Module.** Peak gain is equal to the anticipated level, and a full range of gain and phase control is achieved.

Measured gain and phase characteristics through one of the eight channels is reported in Figure 16. At 94 GHz the maximum gain is 47.8 dB, essentially equal to the anticipated level of 48 dB. A gain control range of 38 dB is exhibited. A full range of phase control is achieved over an extremely wide bandwidth.

The eight-element module mounted within the test fixture for radiation pattern measurements is shown in Figure 17.

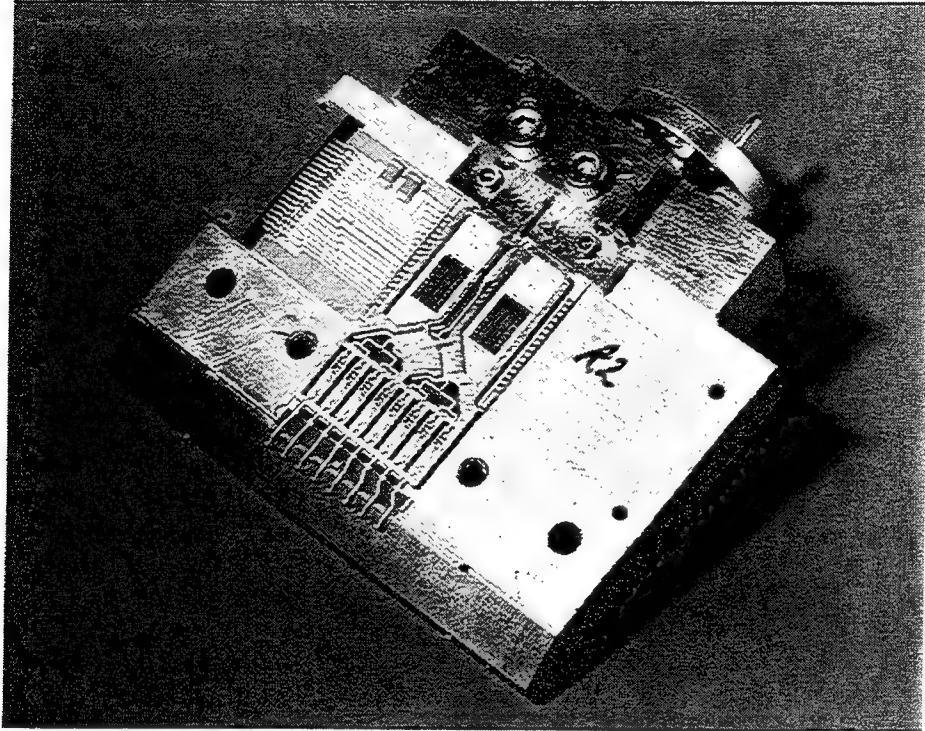


**Figure 17. Eight-Element Receive Array Mounted for Radiation Pattern Measurements.** The lower portion of the corner reflector is formed in the base of the test fixture, the top half is in an upper piece which has been removed for the photo.

The bottom portion of the corner reflector is evident in the photo. The top of the reflector is formed in the fixture's upper piece, which has been removed for the photograph. A microstrip to waveguide transition of the design used in pattern testing individual radiating elements, is also employed here. The substrate in the upper-left brings the DC power and control signals from the connector to the contact pads on the module's DC substrate.

Measured broadside radiation patterns are presented in Figure 18.

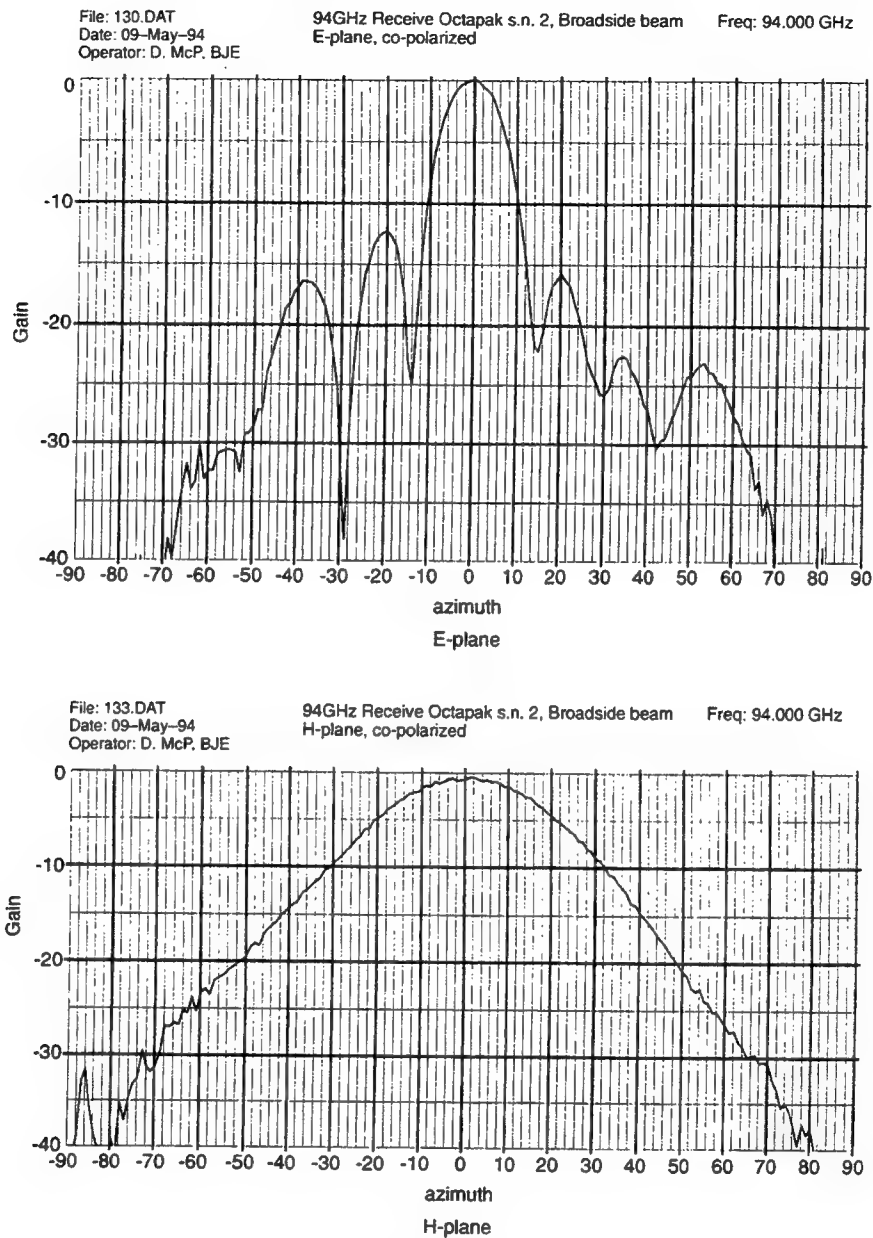


**Figure 18. Receive Array Broadside Radiation Patterns.** Patterns are well formed in both principal planes with beamwidths and sidelobe levels close to predicted values. Patterns for both E-plane and H-plane are shown.

Patterns are well formed in both principal planes. In the E-plane the half-power beamwidth is close to 12 degrees and the peak sidelobe level is -12.5 dB, both very close to the anticipated values. In the H-plane the beamwidth measures 33 degrees, a couple of degrees broader than the design value.

Patterns for the beam commanded to broadside,  $\pm 10^\circ$ ,  $\pm 20^\circ$ , and  $\pm 30^\circ$  are given in Figure 19.

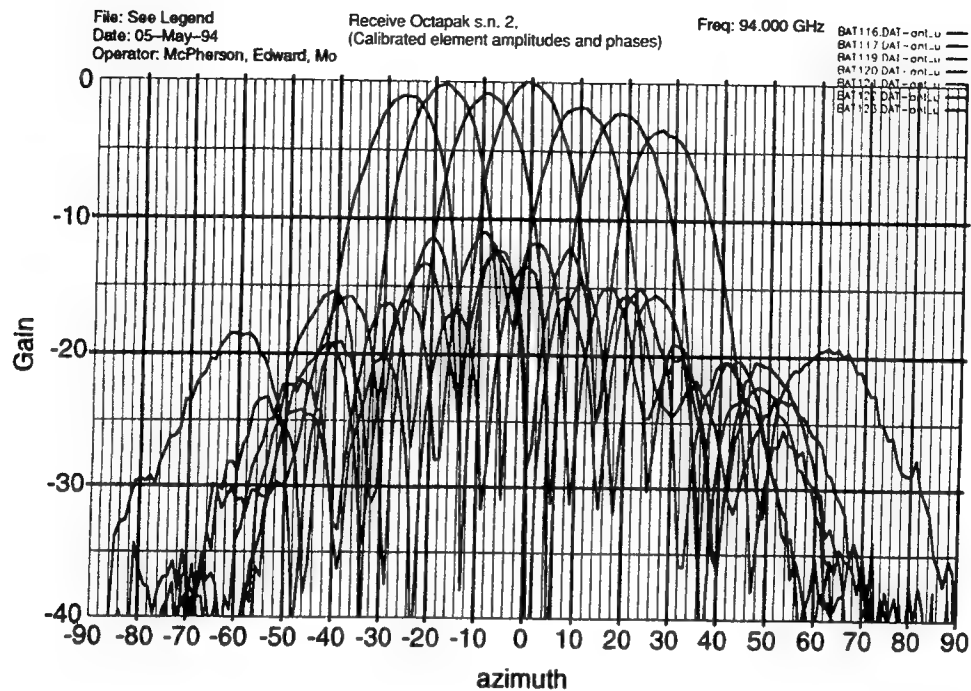


**Figure 19. Receive Array Scanned Beam Patterns.** Beams are commanded to broadside,  $\pm 10^\circ$ ,  $\pm 20^\circ$ , and  $\pm 30^\circ$ .

All scanned beams are very well formed. The effects of the element pattern are evident in the beams at extreme scan, with their peak occurring somewhat closer to broadside than the actual commanded position.

## 5.0 CONCLUSION

W-band active receive and transmit array-modules have been successfully designed and fabricated. These modules comprise eight elements in a line array configuration and can be readily combined to realize larger one- and two dimensional systems. An innovative approach for fabricating the modules employing a multi-layer DC substrate onto which all other module components are mounted has been demonstrated. A receive array has been assembled and shown to have excellent performance. To the best of our knowledge, this represents the first active phased array demonstrated at 94 GHz.



## 6.0 ACKNOWLEDGMENT

Special recognition on this project goes to Bill Jewett who generated design and layout detail for all module components, Dave Helms for module RF design, Aziz Benalla for radiating element design, Don McPherson and Luke Smith for power supply, controller, and software development, Bryan Cleaveland for cavity analysis, Ron Browne for module component fabrication, Howie Steiner for module assembly, and Dave Prichard for module characterization.

## 7.0 REFERENCES

- [1] Duncan, S.W. et al, "Compact high gain W-band and V-band pseudomorphic HEMT MMIC power amplifiers," *1994 IEEE MTT-S Digest*, May 1994.
  
- [2] Tu, D-W, et al, "High gain monolithic P-HEMT W-band four stage low noise amplifier," *IEEE 1994 Microwave and Millimeter-Wave Monolithic Circuits Symposium*.
  
- [3] Weinreb, S, et al, "Monolithic varactor 360° phase shifters for 75-110 GHz," *International Semi-Device Conference, ISDRS, Digest of Papers*, Charlottesville, VA, Dec 1-3, 1993.
  
- [4] A. C. Wilson and H. V. Cottony, "Radiation Patterns of Finite-Size Corner-Reflector Antennas," *IRE Trans. Ant. Propagat.*, vol. AP-8, pp. 144-57, March 1960.
  
- [5] B. J. Edward and D. E. Rees, "A Broadband Printed Dipole with Integrated Balun," *Microwave Journal*, vol. 30, pp. 339-44, May 1987.

# GUIDED WAVE ANTENNA INDUCED BY LIGHT

V. A. Manasson, L. S. Sadovnik, P. I. Shnitser, and V. I. Litvinov  
Physical Optics Corporation  
Research and Development Division  
20600 Gramercy Place, Suite 103  
Torrance, CA 90501

**Abstract:** A millimeter wave antenna has been demonstrated in which beamforming is performed by creating, by optical means, a diffraction grating on the surface of a silicon rod. Generation of an optically induced hologram in a semiconductor medium is a promising approach to the control of MMW antennas. A photogenerated electron-hole plasma can effectively change the dielectric function of the semiconductor medium at MMW frequencies. Diffusion of the plasma grating and changes in the index of refraction and extinction coefficient have been numerically simulated as a function of semiconductor material parameters. Direction of millimeter wave radiation by the photoinduced plasma grating has been experimentally observed at 90 GHz.

## 1.0 INTRODUCTION

An optically controlled semiconductor MMW antenna can be made according to various designs. One of them, the theory of which is discussed in Ref. [1], is a leaky-wave antenna formed by a periodically induced electron-hole plasma on an all-semiconductor rod. To the best of our knowledge, there has been no reported experimental demonstration of this kind of antenna. A modification of this design, in which the bulky semiconductor rod was replaced with a dielectric rod or slab coated with a thin semiconductor layer, has been investigated both theoretically [2] and experimentally [3]. The main obstacle to the operation of the all-semiconductor antenna is the diffusion of carriers from where the rate of their photogeneration across the whole volume of the semiconductor rod.

In the work reported here, we used numerical simulation to study the diffusion of the photoinduced grating in a silicon rod antenna, and experimentally demonstrated its operation with a photoinduced plasma grating.

## 2.0 THEORETICAL MODEL

Our calculations took into consideration the main parameters of the silicon rod which can affect the distribution of photogenerated carriers: volume recombination rate, surface recombination velocity, and light penetration depth. Two cases, steady state illumination and pulse illumination, were considered. The sources of illumination were also taken into account. The illuminating pattern representing the periodic structure is shown in Figure 1.

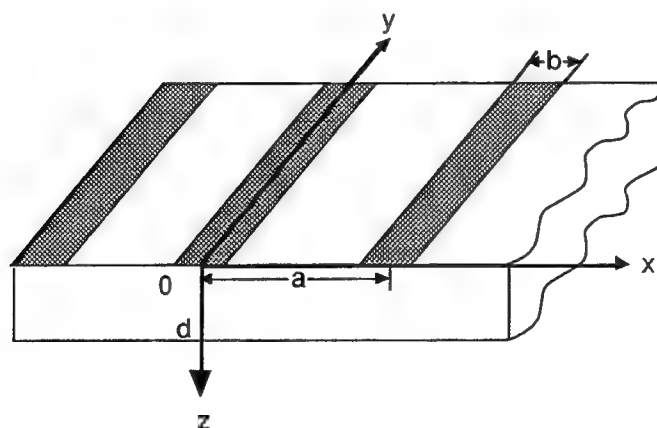


Figure 1  
Illuminating pattern.

To calculate carrier distribution  $\Delta N(x,z,t)$  we solved the two-dimensional inhomogeneous equation

$$\frac{\partial N}{\partial t} + \frac{\Delta N}{\tau} - D \nabla^2 \Delta N = g(x,z,t) , \quad (1)$$

where  $D = 2D_n D_p / (D_n + D_p)$ ,  $D_n$  and  $D_p$  are the electron and hole diffusion coefficients,  $\tau$  is the carrier lifetime, and  $g$  is the carrier generation rate:

$$g(x,z,t) = g(x) \exp(-\alpha z) \exp\left(-\frac{t}{t_p}\right) \left[1 - \exp\left(-\frac{t}{t_p}\right)\right] , \quad (2)$$

$\alpha$  is the light absorption coefficient,  $t_p$  is a temporal parameter of pumping light,  $g(x)$  is a periodic function of  $x$ , and

$$g(x) = \begin{cases} \alpha I_0 , & \text{when } -\frac{b}{2} + aj \leq x < \frac{b}{2} + aj, j = 0, \pm 1, \pm 2, \dots \\ 0, & \text{otherwise} \end{cases} . \quad (3)$$

$I_0$  is the density of the photon flux.

The boundary conditions at illuminated and nonilluminated surfaces are, respectively:

$$D\left(\frac{d\Delta N}{dz}\right)_{z=0} = s_1 \Delta N|_{z=0} , \quad (4)$$

$$D\left(\frac{d\Delta N}{dz}\right)_{z=d} = s_2 \Delta N|_{z=d} , \quad (5)$$

where  $s_1$  and  $s_2$  are surface recombination velocities.

In the steady state condition, we substitute the time independent equations

$$\frac{\Delta N}{\tau} - D\nabla^2 \Delta N = g(x, z) \quad (6)$$

$$g(x, z) = g(x) \exp(-\alpha z) . \quad (7)$$

for Eqs. (1) and (2).

The change in the dielectric constant of the semiconductor medium caused by photoinduced plasma was calculated using the Drude model:

$$\epsilon = \epsilon_{\infty} \left[ 1 - \frac{\omega_n^2}{\omega \left( \omega + \frac{i}{\tau_n} \right)^2} - \frac{\omega_p^2}{\omega \left( \omega + \frac{i}{\tau_p} \right)^2} \right] , \quad (8)$$

where  $\epsilon_{\infty}$  is the high frequency dielectric constant of silicon,  $\tau_{n,p}$  are electron and hole momentum relaxation times,  $\omega_{n,p}$  are electron and hole plasma resonance frequencies,  $\omega$  is the MMW frequency,  $\tau_{n,p} = \frac{\mu_{n,p} \cdot m_{n,p}}{q}$ ,  $\mu_{n,p}$  are electron and hole mobilities,  $m_{n,p}$  are electron and hole effective masses, and  $q$  is electron charge.

The plasma resonance frequency is given by

$$\omega_{n,p} = \left( 4\pi q \frac{\Delta N}{m_{n,p} \epsilon_0} \right)^{1/2}. \quad (9)$$

The refractive index  $n$  and extinction coefficient  $k$  were calculated according to the formulas:

$$n = R_e(\epsilon)^{1/2} \quad (10)$$

$$k = I_m(\epsilon)^{1/2}. \quad (11)$$

### 3.0 RESULTS OF CALCULATION

The equilibrium material parameters used for calculation are the following:  $\epsilon_{\infty} = 11.8$ ;  $m_n = 0.26 m_0$ ;  $m_p = 0.39 m_0$ ;  $\mu_n = 1300 \text{ cm}^2/\text{Vs}$ ;  $\mu_p = 600 \text{ cm}^2/\text{Vs}$ ;  $s_1 = 10^3 \text{ cm/s}$ ;  $s_2 = 10^6 \text{ cm/s}$ , and  $N_0 = 10^{14} \text{ cm}^{-3}$ . To satisfy single-mode

operation requirements, the rod thickness in the z-direction was chosen to be  $d=0.45$  mm. The grating parameters were  $a = 1.25$  mm and  $b = a/3$ .

Figure 2 diagrams the development over time of nonequilibrium carrier distribution under illumination by the short pulse shown in Figure 3. From Figure 2 one can see that the well-defined photoinduced plasma grating is confined to the first few microseconds. The maximum contrast between illuminated and nonilluminated areas is achieved after  $\sim 30$   $\mu$ s, with subsequent diffusion of the plasma grating across the entire waveguide body. By the time the pumping pulse reaches its maximum ( $t = 100$   $\mu$ s), the photoinjected carriers have been distributed uniformly and the grating has vanished.

For steady-state illumination, Figure 4 shows the carrier distribution along the z-direction at the center of an illuminated strip (solid lines) and at the center of a nonilluminated space (dashed lines). The curves were generated using carrier lifetime as a parameter ( $\tau = 10^{-3}$ ,  $10^{-4}$ ,  $10^{-5}$  and  $10^{-6}$  s). For  $\tau = 10^{-3}$  and  $10^{-4}$  s, diffusion totally destroys the photoinduced grating (solid and dashed lines coincide). But for shorter carrier lifetimes ( $\tau = 10^{-5}$ ,  $10^{-6}$  s) the grating still exists. The distribution of change in refractive index,  $\Delta n$ , and extinction coefficient,  $\Delta k$ , follow the carrier distribution and are shown in Figures 5(a) and (b).

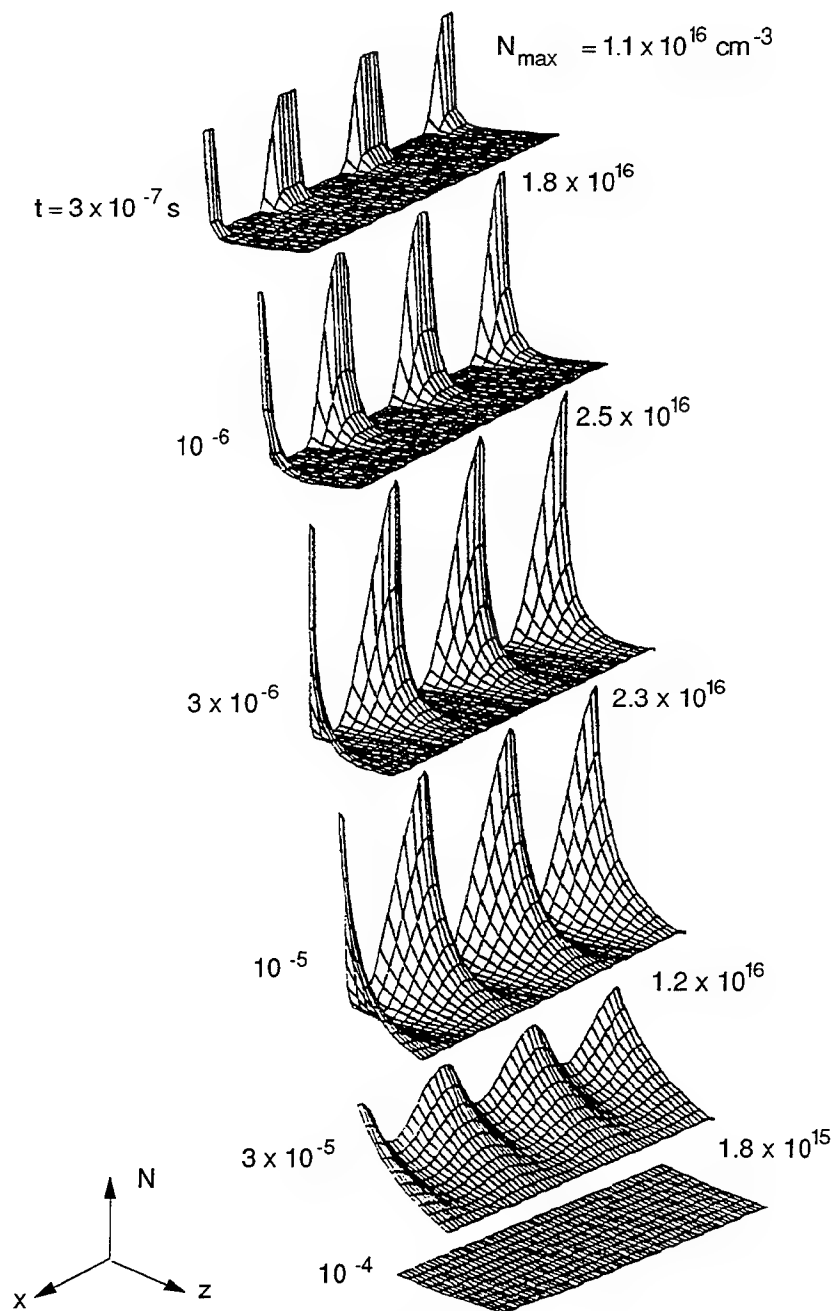


Figure 2  
Development of carrier distribution over time.  $t = 10^{-4} \text{ s}$ ;  $I_0 = 10^{16} \text{ cm}^{-2} \text{ s}^{-1}$ ,  
 $\alpha = 10^5 \text{ cm}^{-1}$ ;  $s_1 = 10^3 \text{ cm s}^{-1}$ ;  $s_2 = 10^6 \text{ cm s}^{-1}$ ;  $a = 0.125 \text{ cm}$ ;  $b = 0.042 \text{ cm}$ ;  $d =$   
 $0.045 \text{ cm}$ ; and  $N_0 = 10^{14} \text{ cm}^{-3}$



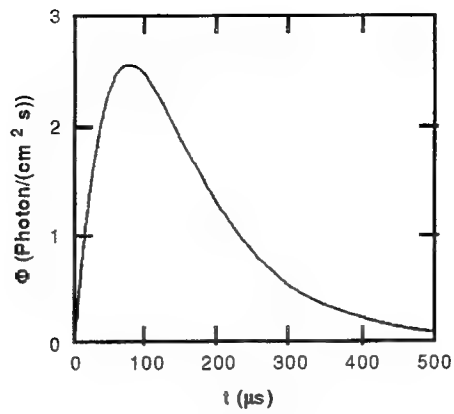


Figure 3  
Time shape of the illuminating pulse.

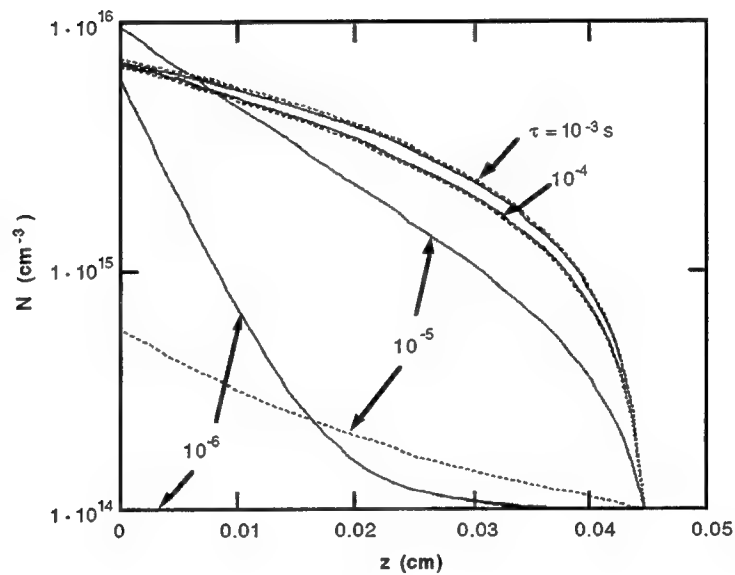
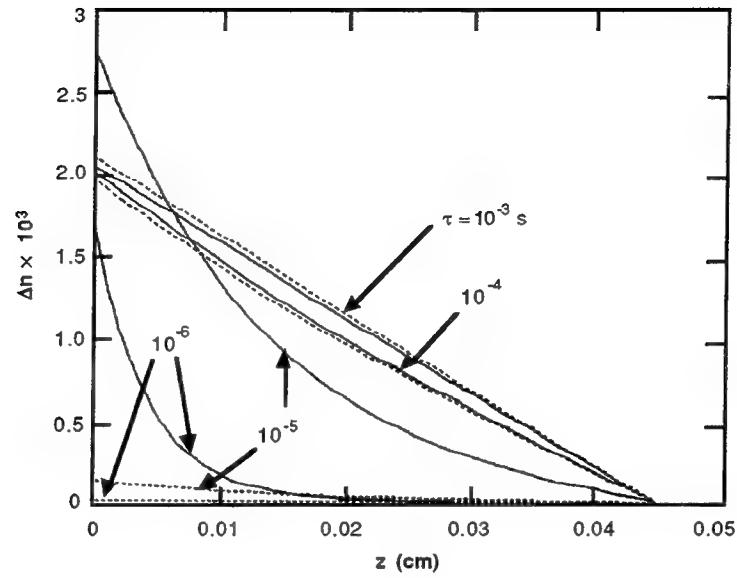
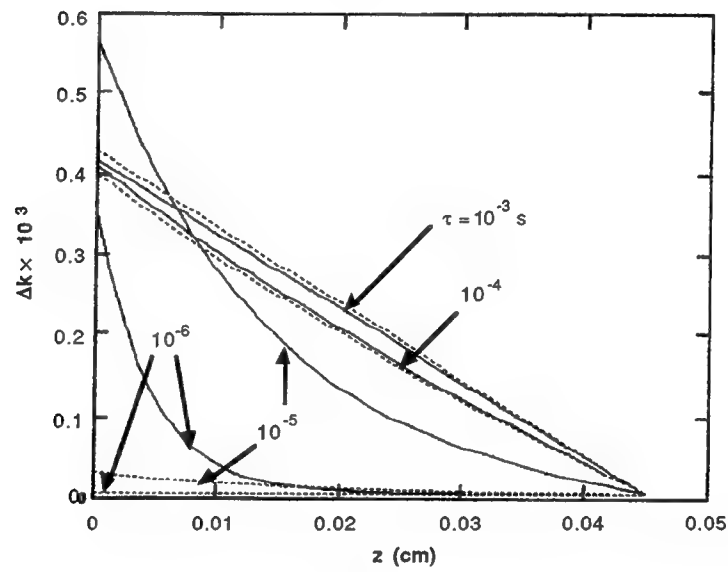


Figure 4  
Carrier distribution under steady-state illumination (solid lines correspond to the center of an illuminated strip, dashed lines to the center of a nonilluminated space).  
 $a = 0.125$  cm,  $b = 0.042$  cm,  $d = 0.045$  cm,  $I_0 = 3 \times 10^{19}$  cm<sup>-2</sup> s<sup>-1</sup>,  $\alpha = 10^5$  cm<sup>-1</sup>,  
 $s_1 = 10^3$  cm s<sup>-1</sup>,  $s_2 = 10^6$  cm s<sup>-1</sup>, and  $N_0 = 10^{14}$  cm<sup>-3</sup>.



(a)



(b)

Figure 5  
Distribution of change in refractive index  $\Delta n$  (a) and in extinction coefficient,  $\Delta k$  (b) caused by the photoinduced plasma. The legend is the same as for Figure 4.

Figures 5(a) and (b) show that the highest contrast in  $\Delta n$  and  $\Delta k$  for illuminated and nonilluminated strips occurs when carrier lifetime is shorter than  $10^{-5}$  s.

The influence of the spectral composition of the pumping light on the distribution of  $\Delta n$  or  $\Delta k$  is shown in Figure 6.

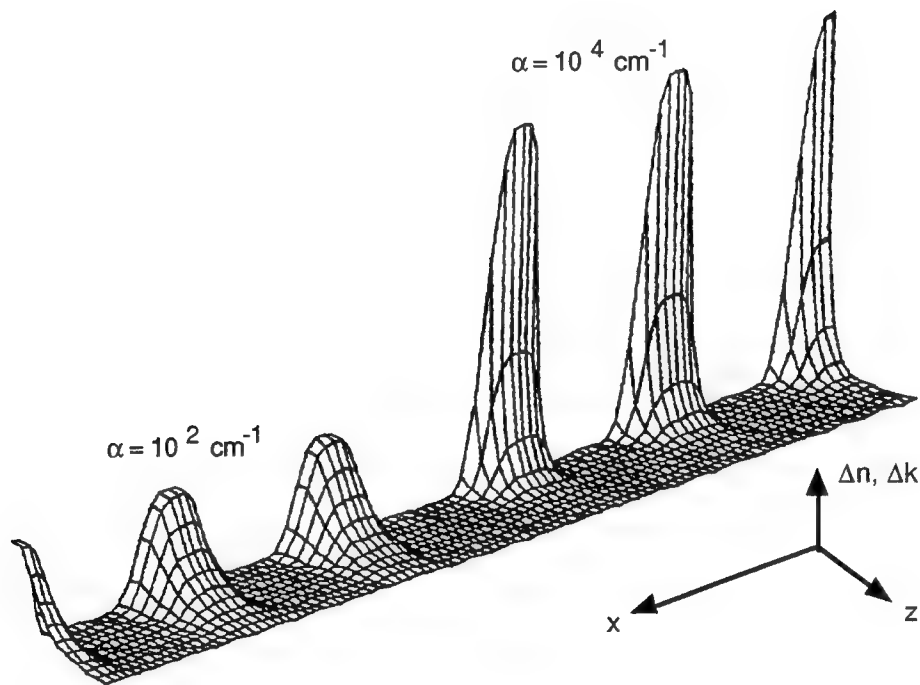


Figure 6  
Distribution of  $\Delta n$  (or  $\Delta k$ ) under IR illumination ( $\alpha = 10^2 \text{ cm}^{-1}$ ) (left side) and with green light ( $\alpha = 10^4 \text{ cm}^{-1}$ ) (right side).  $\Delta n$  and  $\Delta k$  are shown in relative units.  $\tau = 10^{-6}$  s. Other parameters are the same as for Figure 4.

Both the confinement of the plasma-injected grating and the grating amplitude are much better using shorter wavelength illumination.

The calculations above show that a plasma-induced grating can be confined even under steady-state illumination if the carrier lifetime is shorter than  $10^{-5}$  s and short wavelength light is used for illumination.

#### 4.0 EXPERIMENT

Figure 7 shows the experimental setup.

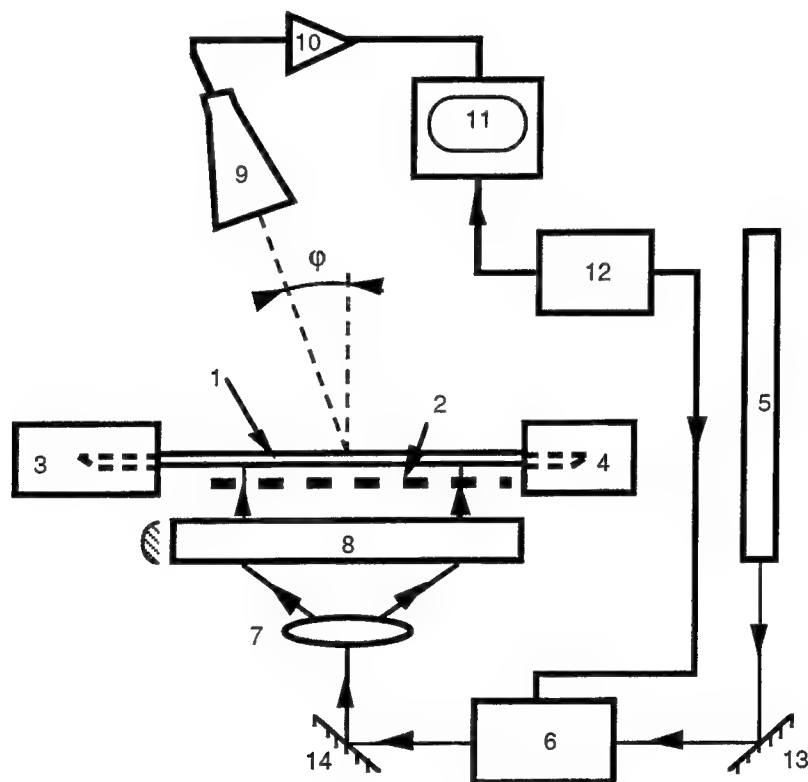


Figure 7  
Experimental setup.

The silicon-rod single mode antenna (1) is illuminated through a transparency (2). The rod is fed by a 90 GHz Gunn oscillator (3) and loaded at the other end by an absorber (4). The light pumping system consists of a 2 W Ar laser (5), an acousto-optic modulator (6), a microlens (7), and a cylindrical lens (8). Millimeter waves radiating from the silicon rod are detected by a horn antenna attached to a GaAs Schottky diode (9). The detected signal is amplified by a low-frequency amplifier (10) and displayed on an oscilloscope (11). A pulse generator (12) controls the acousto-optic modulator and synchronizes the oscilloscope.

The silicon rod was prepared from float zone high resistivity ( $> 1 \text{ k}\Omega\text{cm}$ ) material. Its dimensions are  $0.45 \times 1.25 \times 77 \text{ mm}$ . The illuminated surface was polished by a chemical-mechanical process to achieve low surface recombination. The other sides were lapped to achieve high surface recombination. The ends of the silicon rod were tapered for efficient coupling of the MMW between the silicon rod and the metal waveguides. The light-induced grating has a period of 1.27 mm; the ratio of the transparent strip width to the grating period is 1:3. The illuminating power is  $1.1 \text{ W/cm}^2$ , the pulse duration is  $200 \text{ }\mu\text{s}$ , the duty cycle is 1:20, and the wavelength is  $\lambda = 514 \text{ nm}$ , which corresponds to an absorption coefficient  $\alpha = 8 \times 10^3 \text{ cm}^{-1}$ .

The direction in which the maximum radiation was detected ( $\phi = 22^\circ$ ) corresponds to the propagation constant  $\beta = 2.8$  for the  $\text{TE}_1$  mode.

The waveform of the detected signal in the -1 diffraction order is shown in Figure 8. The fall-time of the pulse allows us to estimate the carrier lifetime, which was about 50  $\mu$ s.

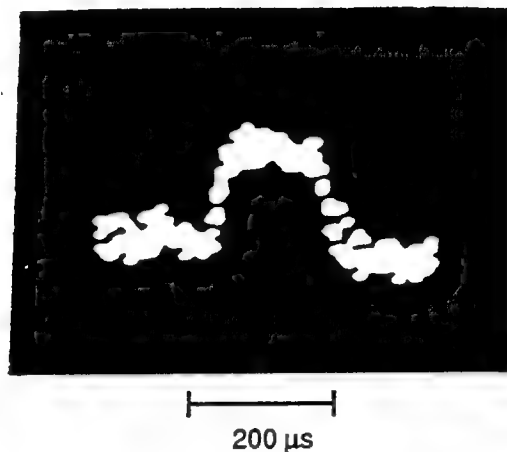


Figure 8  
Diffracted beam pulse.

This long carrier lifetime is probably the main reason that the radiating light is rather weak. In our future work, the silicon material will be treated in order to decrease  $\tau$ .

## 5.0 ACKNOWLEDGMENT

This work was partially supported by the Office of Naval Research under the Contract No. N00014-93-C-0116 and Electronic System Center, Hanscom AFB under Contract No. F19628-93-C-0084. The technical support of the program monitors, Mr. William Miceli and Mr. Harvey Tobin, is greatly appreciated.

## 6.0 REFERENCES

- [1] M. Matsumoto, M. Tsutsumi and N. Kumagai, "Millimeter-Wave Radiation Characteristics of a Periodically Plasma-Induced Semiconductor Waveguide", *Electron. Lett.*, vol. 22, pp. 710-711, 1986.
- [2] M. Matsumoto, M. Tsutsumi and N. Kumagai, "Radiation of Millimeter Waves from a Leaky Dielectric Waveguide with a Light-Induced Grating Layer", *IEEE Trans. Microwave Theory Tech.*, vol. MTT-35, pp. 1033-1042, 1987.
- [3] P. J. Stabile, R. E. Marx, G. A. Evans, A. Rosen, R. Amantea, E. J. Denlinger and J. K. Butler, "Millimeter-Wave Surface Emitters with Optically Induced Gratings", *OE6.1*, p. 279, 1992.
- [4] M. Matsumoto, M. Tsutsumi and N. Kumagai, "Bragg Reflection Characteristics of Millimeter Waves in a Periodically Plasma-Induced Semiconductor Waveguide", *IEEE Trans. Microwave Theory Tech.*, vol. MTT-34, pp. 406-411, 1986.

# DESIGN AND DEVELOPMENT OF WIDE-BAND CIRCULAR ARRAY INTERFEROMETERS

by  
Paul Eyring and Randolph Clapp  
AIL Systems Inc.  
Commack Road  
Deer Park, NY 11729

**Abstract:** Circular array interferometer (CAI) systems utilize a circular array antenna connected to a Butler matrix mode-forming network to provide angle-of-arrival (AOA) measurement over a full 360-deg instantaneous field-of-view (IFOV). The theory of operation for CAI's and design considerations such as element pattern requirements, choosing the number of array elements, and selecting which phase modes to utilize for wide-band AOA determination are discussed. The development of wide-band Butler matrices, providing 0.5-dB rms amplitude tracking and 3.5-deg rms phase tracking from UHF to millimeter-wave frequencies, and a high performance, light weight (10 lb), 8-element, 4:1 bandwidth CAI utilizing resistively loaded dipole elements are described. In addition, a unique, high accuracy 16-element, 3:1 bandwidth CAI is presented. It simultaneously provides both a wide open full 360-deg IFOV and a narrower IFOV high-gain directional-beam operating state capable of 360-deg coverage via electronic scanning. Finally described is an AIL patented circular array utilizing log-periodic array elements with the potential to provide future systems with a 1-deg AOA accuracy over a 10:1 or 20:1 frequency bandwidth.

## 1. Introduction

Wide-band, high-accuracy, angle-of-arrival (AOA) measurement over a full 360-deg instantaneous field-of-view (IFOV) has been identified by the Department of Defense (DoD) as a required ESM/ELINT capability for battlefield surveillance and targeting systems. There are two types of phase interferometer configurations which can provide the required AOA accuracies: one utilizes three linear interferometers while the other utilizes a single circular array interferometer.

Linear interferometers utilize three or four antenna elements and provide instantaneous coverage over a 120-deg angular sector. Utilizing multiplexers, three linear interferometers can be utilized to provide a 360-deg FOV with three or four receiver channels. However, since only one linear interferometer is connected to the



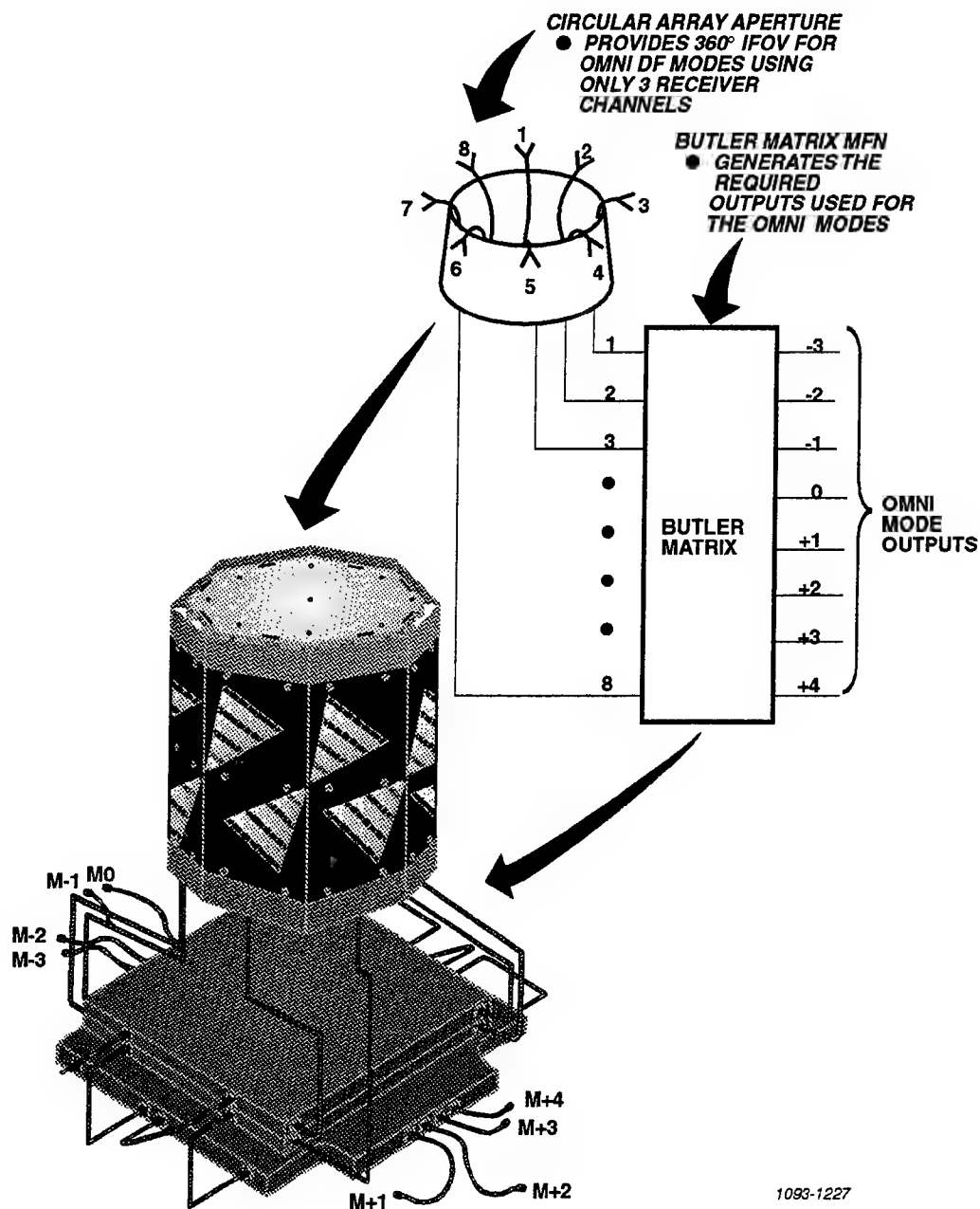
receivers at a given instant in time, this configuration provides only a 120-deg IFOV. To obtain a 360-deg IFOV, each element of the three linear interferometers must be connected directly to a receiver channel; therefore, 9 or 12 receiver channels must be used.

Circular array interferometers (CAI's) inherently provide instantaneous coverage over a full 360-deg IFOV. The number of antenna elements is chosen based on AOA accuracy requirements and physical size constraints but is always a power of two. Typical CAI's utilize 4, 8, or 16 antenna elements. Each antenna element in the circular array is connected to a Butler matrix input port as shown in the block diagram of Figure 1. The outputs of the Butler matrix are omnidirectional phase modes. Only three omnidirectional phase modes are required for AOA determination, independent of the number of antenna elements. Therefore, CAI's need only three receiver channels compared to the 9 or 12 required for a 360-deg IFOV linear interferometer system. This translates into smaller, less complex, lower cost, 360-deg IFOV ESM/ELINT systems.

This paper presents a comprehensive introduction to the theory of operation of CAI systems including: a system description, AOA determination, bandwidth considerations, and AOA accuracy considerations. In addition, the paper includes a discussion of the following CAI technology:

- Wide-band Butler matrices which typically provide 0.5-dB rms amplitude tracking and 3.5-deg rms phase tracking from 0.3 – 40.0 GHz
- An 8-element, 4:1 bandwidth CAI utilizing resistively loaded dipole elements

**A CAI UTILIZES A CIRCULAR ARRAY ANTENNA CONNECTED TO A BUTLER MATRIX MODE FORMING NETWORK (MFN). THE BUTLER MATRIX OUTPUTS ARE THE PHASE MODES OF THE CAI**



1093-1227

Figure 1. An Eight-Element CAI

- A unique 16-element, 3:1 bandwidth CAI which simultaneously provides both a 360-deg IFOV and a high-gain directional-beam capable of 360-deg coverage via electronic scanning
- A frequency independent circular array utilizing log-periodic microstrip patch arrays

## **2. Technical Discussion**

### **2.1 System Description**

A CAI system utilizes a circular array antenna connected to a Butler matrix mode-forming network. The block diagram of a typical eight-element CAI is given in Figure 1. The elements of a circular array antenna are located at equiangular distances around the circumference of a circle. While each individual element typically has only a 90- to 120-deg IFOV, the array's circular geometry inherently gives a circular array a full 360-deg IFOV.

A Butler matrix is a network which performs a discrete Fourier transform on a set of the antenna element signals at its input using analog signal processing in real-time. The results are the modal outputs of the CAI. The matrix is implemented as a set of 3-dB directional couplers (either quadrature or 0/180 hybrids) and phase shift networks that are interconnected by a labyrinth of transmission lines. The block diagram of an eight-input/eight-output Butler matrix utilizing 3-dB quadrature couplers is given in Figure 2. While the total number of modal outputs is inherently equal to the number of antenna element inputs, only three of the modal outputs are required to accurately determine the AOA of incoming signals. Therefore, only three receiver channels are required for 360-deg IFOV AOA determination.

**A BUTLER MATRIX UTILIZES 3-dB DIRECTIONAL COUPLERS AND PASSIVE PHASE SHIFT NETWORKS TO PERFORM A DISCRETE FOURIER TRANSFORM AT MICROWAVE FREQUENCIES IN REAL-TIME**

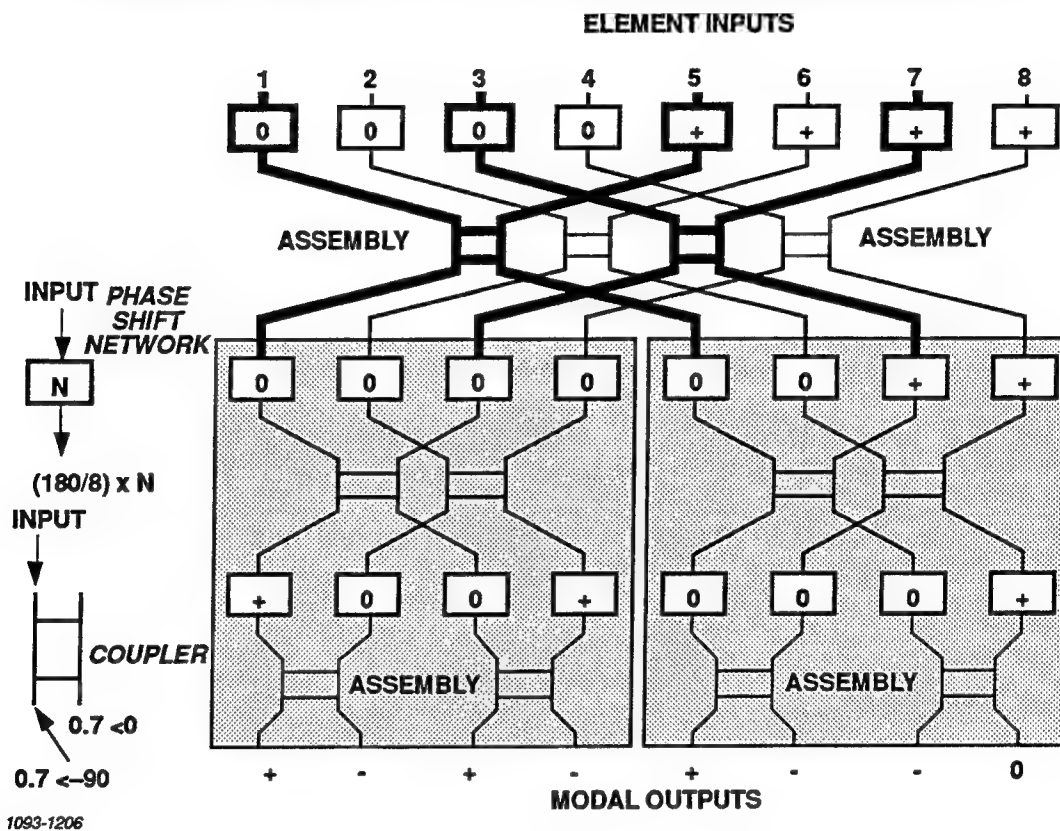


Figure 2. Block Diagram of an Eight-Input/Eight-Output Butler Matrix Realized as Four Assemblies

For applications where high gain, sensitivity, and selectivity are required, AIL has developed an enhanced CAI system with a unique high gain, narrow beam width operating mode. This antenna can operate in both a wide open full 360-deg IFOV mode and a narrower IFOV high-gain directional-beam mode capable of full 360-deg coverage via electronic scanning. The block diagram of a 16-element implementation of this system is given in Figure 3. Low-noise preamplifiers are located at the output of each antenna element to mask the losses of the Butler matrix and digital phase shifters for maximum sensitivity. The modal outputs of the Butler matrix are connected to digital phase shifters. The phase shifter outputs are combined to form high-gain mode monopulse (sum and difference) directional beams. Beam steering is accomplished by appropriate control of the phase shifter settings. The omnidirectional operating mode is obtained using directional couplers to couple-off selected modal outputs of the Butler matrix. Therefore, both operating modes are available simultaneously and can be independently controlled.

## **2.2 AOA Determination**

Fourier series theory can be used to model a circular array's excitation as a sum of phase mode components. These components have omnidirectional amplitude and phase which varies as a harmonic multiple of azimuth angle. The phase of these modes can be compared to accurately determine the AOA of an incoming signal. As was mentioned previously, using a Butler matrix in conjunction with a circular array gives us direct access to the phase modes of the CAI; they are the Butler matrix outputs.

**THIS ANTENNA SIMULTANEOUSLY PROVIDES BOTH A WIDE OPEN FULL 360° IFOV AND A NARROWER IFOV HIGH-GAIN DIRECTIONAL-BEAM OPERATING STATE CAPABLE OF 360° COVERAGE via ELECTRONIC SCANNING**

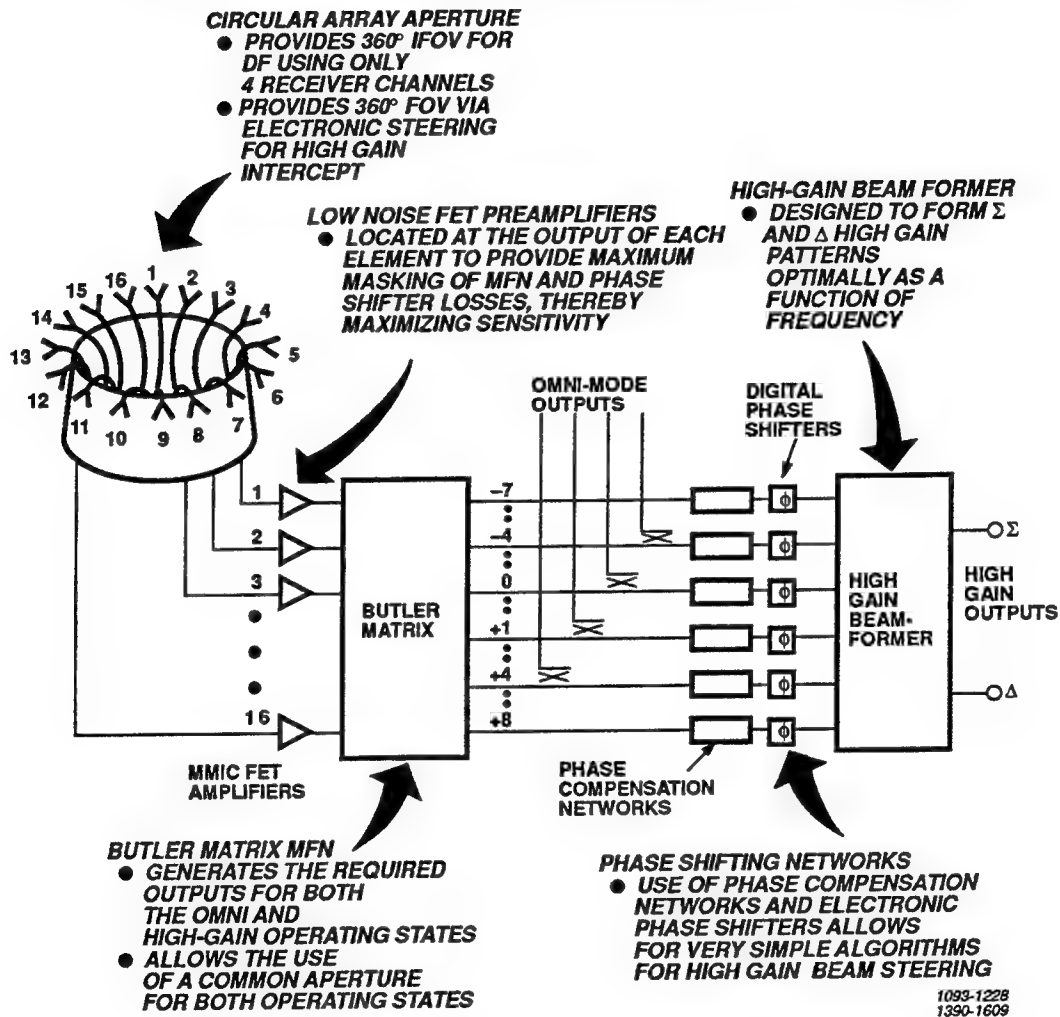


Figure 3. Block Diagram of AIL's Dual-Mode CAI System

Consider the case of a continuous circular array with an excitation  $f(\phi)$ , where  $\phi$  is the angular variation around the array. Since the array is circular,  $f(\phi)$  must be periodic in  $\phi$ , with a period of  $2\pi$  radians. It can therefore be represented in terms of a Fourier series:

$$f(\phi) = \sum_{m=-N}^N F_m(\phi) = \sum_{m=-N}^N C_m e^{jm\phi} \quad (1)$$

where:  $\phi$  = Azimuth angle

$F_m(\phi)$  = The  $m^{\text{th}}$  phase mode excitation

$C_m$  = Complex Fourier coefficient of excitation

$N$  = Maximum spatial harmonic of excitation (0, 1, 2, etc.)

$m$  = Mode number (0,  $\pm 1$ ,  $\pm 2$ , etc.)

Consider  $F_m(\phi) = C_m e^{jm\phi}$ , the  $m^{\text{th}}$  phase mode excitation of the array. This excitation has a constant amplitude, but a phase which varies linearly with  $\phi$  around the array. Since the phase term is  $m\phi$ , there are  $m$  complete cycles of phase around the array. The far-field antenna pattern,  $D_m$ , resulting from the excitation of the  $m^{\text{th}}$  phase mode can be expressed as:

$$D_m(\phi) = \frac{1}{2\pi} \int_0^{2\pi} [C_m e^{jm\phi'} G(\phi - \phi') e^{j\beta r \cos(\phi - \phi')}] d\phi' \quad (2)$$

where:  $G(\phi)$  = Far field pattern of an individual antenna element

$\beta$  =  $2\pi/\lambda$  = Propagation constant in free space

$r$  = Radius of circular array

The radiation pattern  $G(\phi)$  of an elemental radiator in the array, or “element pattern”, must be periodic in  $\phi$ , with a period of  $2\pi$  radians. Thus, it can also be expressed as a Fourier series:

$$G(\phi - \phi_0) = \sum_{k=-P}^P [B_k e^{jk(\phi - \phi_0)}] \quad (3)$$

where:  $B_k$  = Complex Fourier coefficient of element pattern  
 $P$  = Maximum spatial harmonic of element pattern (0, 1, 2, etc.)  
 $\phi_0$  = Constant (angular position of element pattern peak)

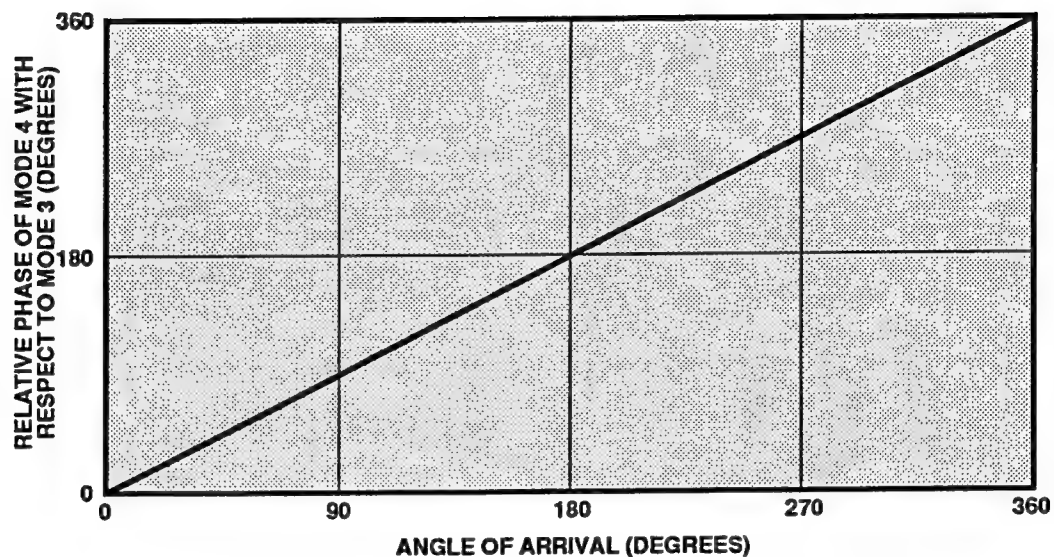
Using the element pattern representation given in Eq. (3), the far-field pattern of the  $m^{\text{th}}$  phase mode can be expressed as a sum of Bessel functions:

$$D_m = C_m e^{jm\phi} \sum_{k=-P}^P [B_k j^{m-k} J_{m-k}(\beta r)] \quad (4)$$

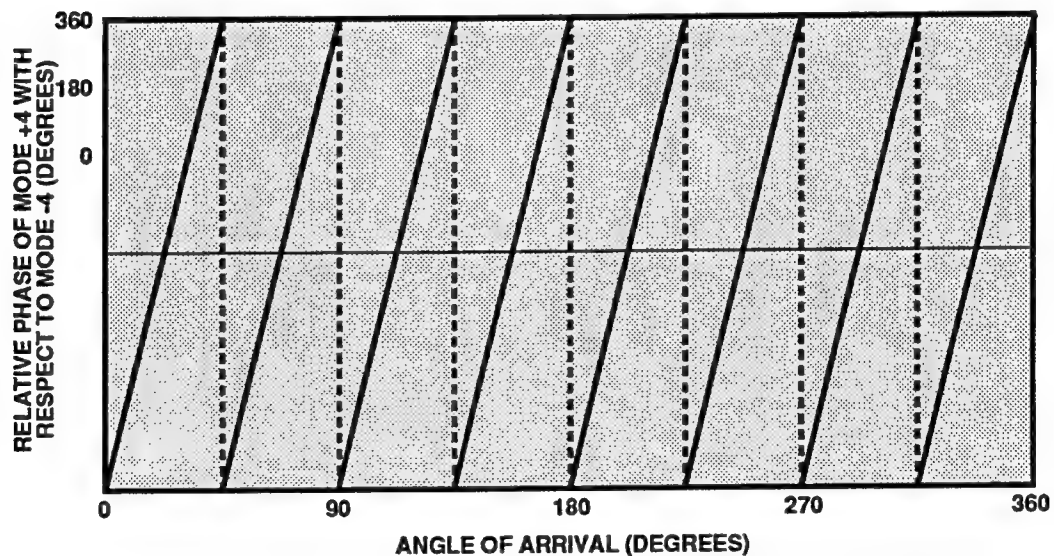
where :  $j = \sqrt{-1}$   
 $J_m(x)$  = Bessel Function of the First Kind of Order  $m$

Note that the phase of the  $m^{\text{th}}$  phase mode's far field pattern is  $e^{jm\phi}$ . Therefore, when a circular array is used as a receive antenna, the phase of the  $m^{\text{th}}$  phase mode is equal to  $m$  times the angle of arrival of the incident signal. AOA determination can be accomplished by comparing the phase difference between two phase modes. Comparing phase modes of adjacent orders ( $m = 4$  and  $m = 3$  for example), is sufficient to determine AOA without ambiguity because there is a one-to-one correspondence between electrical phase and angle of arrival (Figure 4). However, this results in a one-to-one relationship between system phase errors (due to antenna element variations, Butler matrix phase errors, and receiver phase errors)





**A. A PAIR OF ADJACENT (IN MODE NUMBER) MODES ARE USED TO PROVIDE NONAMBIGUOUS COARSE AOA INFORMATION**



**B. A PAIR OF WIDELY SPACED (IN MODE NUMBER) MODES ARE USED TO PROVIDE HIGH ACCURACY AOA – ANTENNA AND RECEIVER PHASE TRACKING ERRORS ARE DEMAGNIFIED BY THE MODE NUMBER DIFFERENTIAL; 8 IN THIS EXAMPLE**

1093-1209

Figure 4. AOA Determination

and AOA errors; each electrical degree of system phase error causes one degree of AOA error. To “demagnify” the system phase errors, phase modes of widely different orders are compared. For example, if mode  $m = -4$  is compared with mode  $m = +4$ , the phase difference would be equal to eight times the angle of arrival. Therefore, the system phase errors are “demagnified” by eight (i.e., system phase errors of 8 deg result in an AOA error of 1 deg). However, as depicted in Figure 4, there are seven ambiguities when modes  $m = +4$  and  $m = -4$  are compared. So simultaneous comparison of a mode adjacent to mode  $m = +4$  (or mode  $m = -4$ ) is required to resolve the ambiguity.

### 2.3 Bandwidth Considerations

The bandwidth of conventional CAI systems is limited by two phenomena which result from the array’s circular geometry:

- The need for a directive element pattern
- The use of a discrete number of wide-band elements along a circle of fixed physical diameter

These factors limit present CAI’s to 3:1 or 4:1 operating bandwidths, depending upon AOA accuracy requirements and system error levels. The paragraphs that follow will contain a discussion on: (1) the need for a directive element pattern in wide-band CAI’s, using the equations for a continuous circular array, and the drop-off in modal gain for small array diameters that imposes the low frequency limit on a CAI’s operating bandwidth; (2) the introduction of a discrete number of elements into the array introducing residual terms which impose the high-frequency limit on the CAI’s operating bandwidth; and (3) the AIL-patented Frequency Independent Circular Array [1], which does not suffer from these inherent bandwidth limitations.

## 2.4 Affect of Element Pattern Directivity

The Fourier series of an omnidirectional element is given simply by:

$$G(\phi) = 1 \quad (5)$$

So, from Eq. (4), the far field pattern of the  $m^{\text{th}}$  phase mode of a continuous circular array employing omnidirectional elements is:

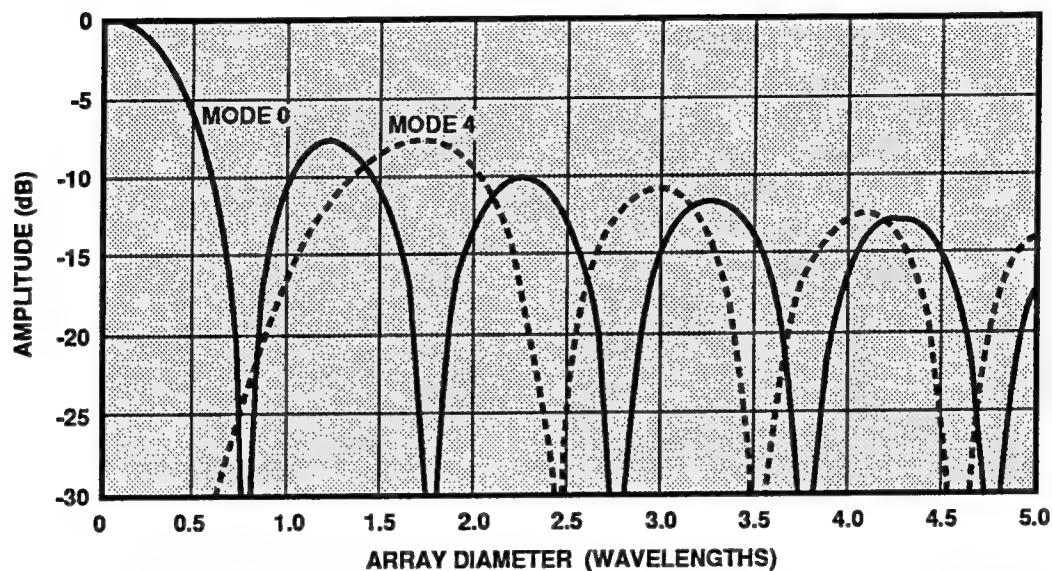
$$D_m = C_m e^{jm\phi} j^m J_m(\beta r) \quad (6)$$

where:  $C_m$  = Complex Fourier coefficient of excitation  
 $m$  = Mode number (0,  $\pm 1$ ,  $\pm 2$ , etc.)  
 $J_m(\beta r)$  = Bessel function of the first kind of order  $m$   
 $\beta$  =  $2\pi/\lambda$  = Propagation constant in free space  
 $r$  = Radius of circular array

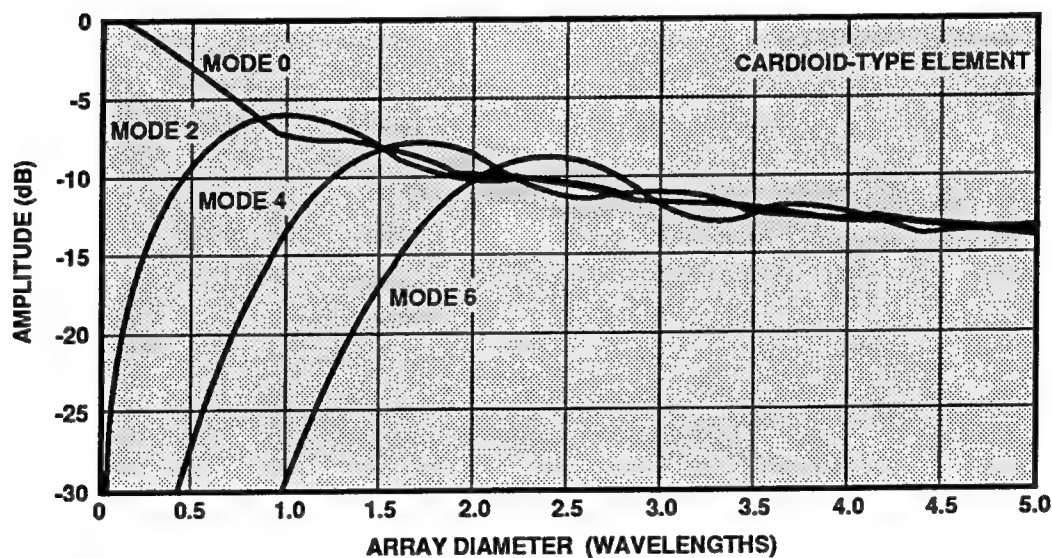
As Eq. (6) shows, the amplitude of the far field pattern is proportional to the Bessel function  $J_m(\beta r)$ . This Bessel function goes to zero for certain values of its argument,  $\beta r$ . This means that the far-field phase mode cannot be excited for certain operating frequencies or certain array diameters. The amplitudes of mode 0 and mode 4 are plotted as a function of the array diameter in wavelengths in Figure 5. Periodic nulls in the modal amplitudes place a severe limitation on the operating bandwidth of a circular array with omnidirectional elements.

The use of directional elements eliminates these periodic amplitude nulls. A cardioid element pattern will be utilized below to illustrate this fact because of its simple Fourier series representation. However, ALL's Antenna Systems Department has found that the conclusions are valid for any element which provides at least a

**A DIRECTIONAL ELEMENT PATTERN REMOVES THE UNDESIRABLE  
NULLS IN THE MODAL GAIN RESPONSE ENABLING OPERATION OVER  
WIDE FREQUENCY BANDWIDTHS**



**A. ARRAY RESPONSE WITH OMNIDIRECTIONAL ELEMENTS**



**B. ARRAY RESPONSE WITH DIRECTIONAL ELEMENTS**

1093-1210

**Figure 5. Affect of Element Directivity on Array Gain  
Versus Frequency Response**

10 dB front-to-back gain ratio (10 dB more gain directly in front of the antenna, at boresight, than directly behind the antenna, 180 deg away from boresight). Elements which meet this requirement over a wide bandwidth include flared notches, a shaped dipole backed by a conducting ground plane, and a shaped monopole backed by a conducting ground plane. AIL has designed and manufactured CAI's which utilize flared notch antennas and shaped dipoles backed by a conducting ground plane.

Consider a cardioid element pattern of the form  $G(\phi) = 1 + \cos(\phi)$ . This element pattern has the following Fourier series representation:

$$G(\phi) = \sum_{k=-1}^1 [B_k e^{jk\phi}] \quad (7)$$

where :

$$\begin{aligned} B_0 &= 1 \\ B_{-1} &= B_1 = \frac{1}{2} \end{aligned}$$

Using Eq. (7) in Eq. (4) gives the far field pattern for the  $m^{\text{th}}$  phase mode of an array utilizing cardioid elements:

$$D_m = C_m e^{jm\phi} \left[ j^m J_m(\beta r) + \frac{1}{2} j^{m+1} J_{m+1}(\beta r) + \frac{1}{2} j^{m-1} J_{m-1}(\beta r) \right] \quad (8)$$

where:  $C_m$  = Complex Fourier coefficient of excitation  
 $m$  = Mode number (0,  $\pm 1$ ,  $\pm 2$ , etc.)  
 $J_m(\beta r)$  = Bessel function of the first kind of order  $m$   
 $\beta$  =  $2\pi/\lambda$  = Propagation constant in free space  
 $r$  = Radius of circular array

Comparing Eq. (8) to Eq. (6) shows that the affect of using a cardioid element pattern is to replace the single Bessel function term in Eq. (6) with a series of Bessel functions. As Figure 5 shows, the sum of the Bessel function series does not go to zero for a circular array of finite diameter. Therefore, circular arrays with directive elements can be designed for wide bandwidth operation. However, the gain drop-off experienced by the higher order modes for small electrical diameters (Figure 5), imposes the low frequency limit on the CAI's operating bandwidth.

#### 2.4.1 Affect of Using a Finite Number of Antenna Elements

This section shows that when directive elements are utilized, the upper frequency of a conventional CAI's operating bandwidth is limited by the discreteness of the array.

The discrete array is a sampled version of the continuous array. The sampling rate is determined by the element spacing in wavelengths. As in signal processing, the sampling rate imposes bandwidth limitations. The modal excitation of a discrete array of  $N$  elements,  $F_m^d(\phi)$ , can be obtained by multiplying the continuous array modal excitation,  $F_m(\phi) = C_m e^{jm\phi}$ , by a sampling function of unit impulses at each element location [2]:

$$F_m^d(\phi) = C_m e^{jm\phi} S(\phi) \quad (9)$$

$$S(\phi) = \sum_{q=0}^{\infty} e^{jNq\phi} \quad (10)$$

Using this excitation in Eq. (2) gives the resulting far field pattern of the  $m^{\text{th}}$  phase mode:

$$D_m^d(\phi) = \frac{1}{2\pi} \sum_{q=-\infty}^{\infty} \int_0^{2\pi} C_m e^{j(m+Nq)\phi'} G(\phi-\phi') e^{j\beta r \cos(\phi-\phi')} d\phi' \quad (11)$$

Expressing the element pattern in the Fourier series of Eq. (3) enables us to express Eq. (11) as a sum of Bessel functions:

$$D_m^d(\phi) = C_m \sum_{k=-P}^P B_k \sum_{q=-\infty}^{\infty} \left[ j^{(m+Nq-k)} e^{j[(m+Nq)\phi]} J_{(m+Nq-k)}(\beta r) \right] \quad (12)$$

The  $q = 0$  term in Eq. (12) represents the  $m^{\text{th}}$  phase mode's far field pattern for a continuous array. The remaining terms in the  $q$  summation represent the pattern distortion caused by the discreteness of the  $N$  element array. While this is an infinite summation, it converges rapidly and only the first three or four terms need to be included during an analysis. To illustrate the affect of the distortion terms, let us examine the case of a discrete array of cardioid elements. For cardioid elements, Eq. (12) becomes:

$$D_m(\phi) = C_m A_m e^{jm\phi} + C_m \sum_{q=1}^{\infty} \left[ A_{(Nq+m)} e^{j(Nq+m)\phi} + A_{(m-Nq)} e^{j(m-Nq)\phi} \right] \quad (13)$$

where:

$$A_m = j^m J_m(\beta r) + \frac{1}{2} j^{m+1} J_{m+1}(\beta r) + \frac{1}{2} j^{m-1} J_{m-1}(\beta r) \quad (14)$$

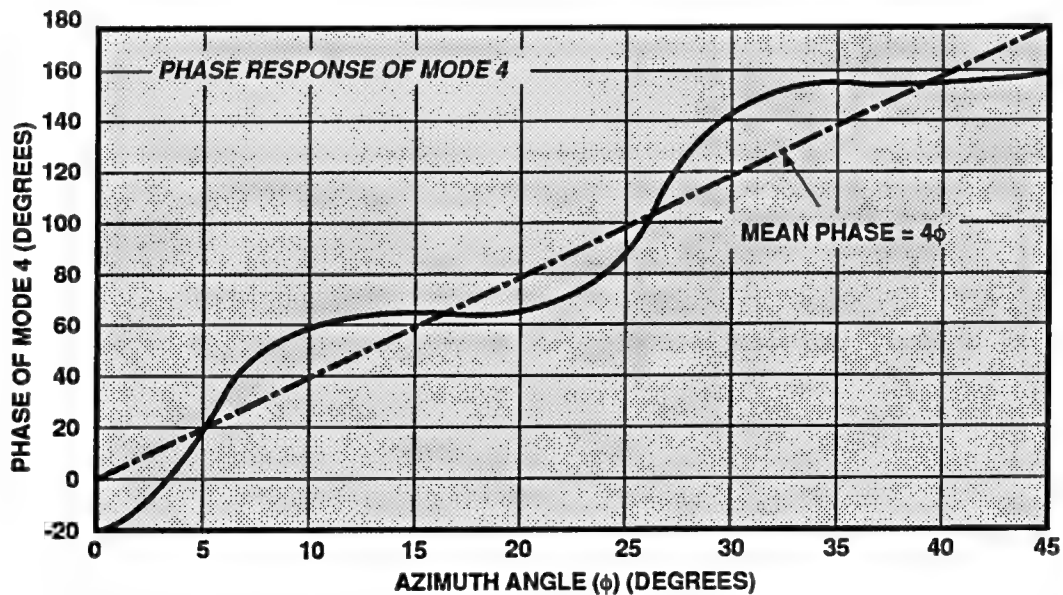
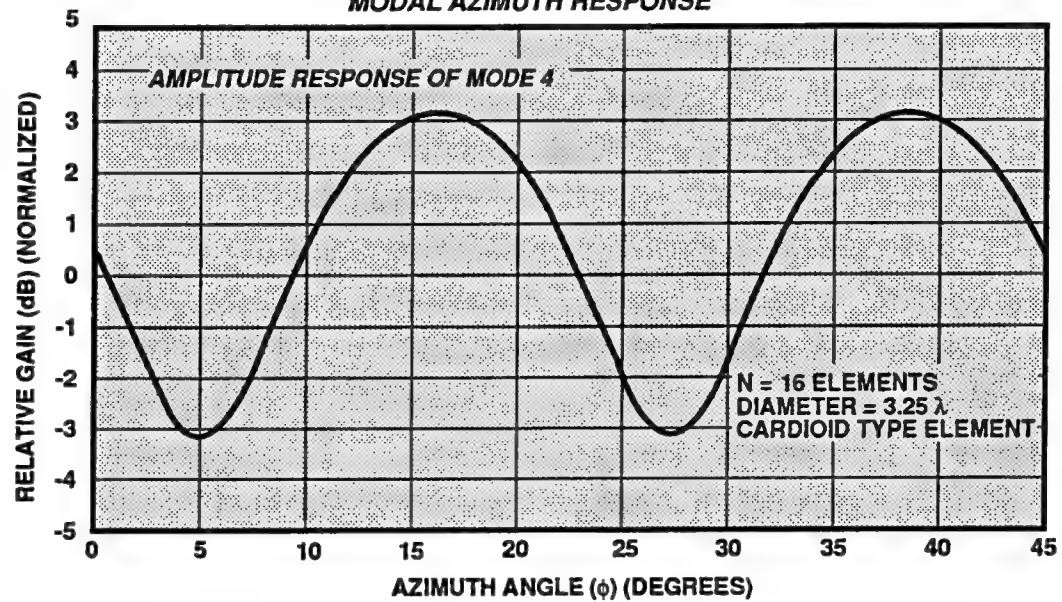
The first term in Eq. (13) is the desired far field phase mode pattern (the principle term). It is linear with azimuth and mode number. The remaining residual terms in Eq. (13) represent higher-order pattern distortions whose relative magnitudes increase with increasing frequency. It is these residual terms which limit the upper frequency of a conventional CAI's operating bandwidth. An example of the amplitude and phase ripple these residual terms introduce into the modal azimuth response is given in Figure 6. The peak-to-peak phase ripple as a function of element spacing in wavelengths is shown in Figure 7. Consider mode 3: At  $0.2\lambda$  and  $0.4\lambda$  element spacings there is practically no phase ripple from the discreteness of the array. For  $0.6\lambda$  element spacing the phase ripple increases to 10 deg, which is still tolerable in most cases. However, at  $0.8\lambda$  element spacing the 120-deg phase ripple makes the array unusable as the phase response becomes too distorted. This effect limits the highest frequency of operation for a given design.

Figure 7 shows the relative gain of the phase modes versus element spacing for modes 0, 2, 4, and 6. The negative modes behave identically to their positive counterparts. The odd numbered modes behave similarly, and were left off the figure for clarity. All of the modal gains were normalized to the maximum gain of mode 0. At the low end of the band, decreasing frequency causes an increasingly rapid gain fall-off for the higher order modes. As was discussed previously, it is desirable to use higher order modes because they potentially maximize AOA accuracy by demagnifying system errors. This gain fall-off limits the lowest frequency of operation for a given design.

These affects, low modal gain at the low end of the band and next large phase ripple at the high end of the band, limit conventional circular array designs to 3:1 or 4:1 operating bandwidths depending upon system error levels and AOA accuracy requirements. As is discussed AIL has patented a circular array design which eliminates these inherent bandwidth limitations.



THE DISCRETENESS OF THE ARRAY GIVES RISE TO RESIDUAL TERMS WHICH  
INTRODUCE AMPLITUDE AND PHASE RIPPLE TO THE  
MODAL AZIMUTH RESPONSE

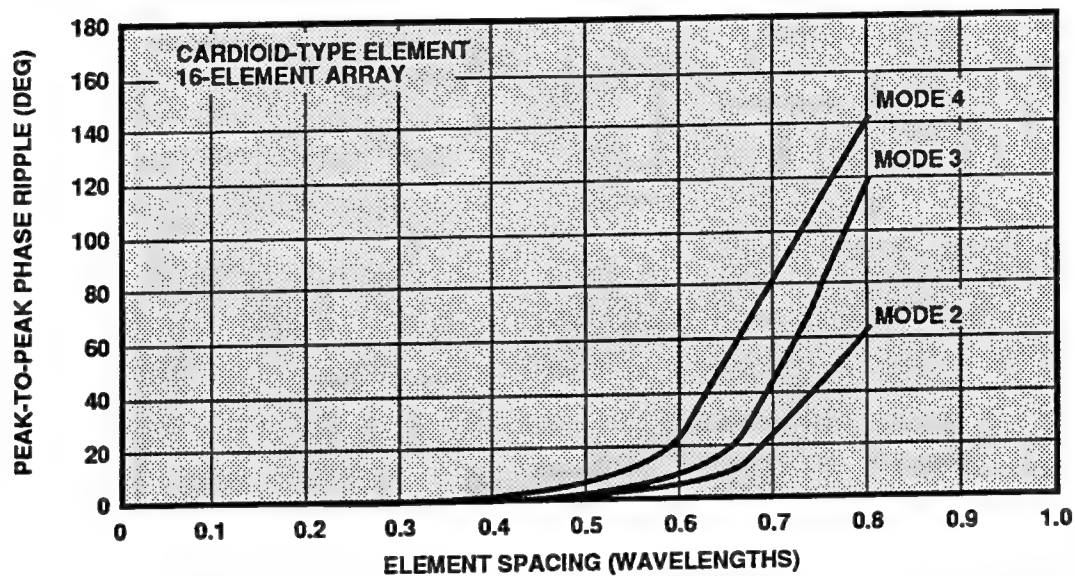


NOTE: AZIMUTH EXPANDED FOR CLARITY  
RESPONSE REPEATS EVERY 45 DEGREES

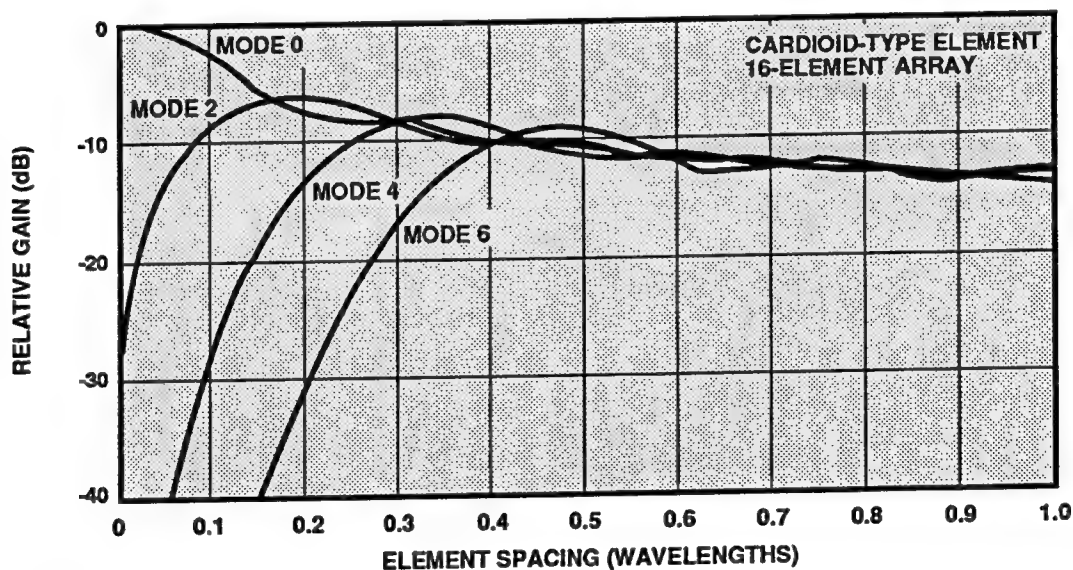
1093-1211

Figure 6. The Directness of the Array Causes Amplitude and Phase Ripple

**LARGE PEAK-TO-PEAK PHASE RIPPLE AT THE HIGH END OF THE BAND AND LOW MODAL GAIN AT THE LOW END OF THE BAND, LIMIT CONVENTIONAL CIRCULAR ARRAY DESIGNS TO 3:1 OR 4:1 OPERATING BANDWIDTHS**



**A. PEAK-TO-PEAK PHASE RIPPLE AS A FUNCTION OF ELEMENT SPACING**



**B. RELATIVE MODAL GAIN AS A FUNCTION OF ELEMENT SPACING**

1093-1212

**Figure 7. Phenomena Which Limit the Bandwidth of Present CAI Systems**

#### **2.4.2 Frequency Independent Circular Array**

AIL is designing, as part of an Independent Research and Development (IRAD) program, a circular array antenna which does not suffer from the inherent frequency limitations of conventional circular arrays. In principle, this antenna design is frequency independent and in practice will make it possible to design high accuracy CAI's which cover ultrabroadband (10:1 or 20:1) frequency bands with no degradation in AOA accuracy across the band. The concept of this frequency independent circular array is described below.

A conventional circular array utilizes individual elements which cover the entire operating band. As Figure 8 shows, the fixed physical diameter of these arrays causes their electrical diameter to vary linearly with frequency. As was discussed earlier, this limits conventional circular arrays to a maximum 4:1 operating bandwidth. As shown in Figure 8, what is desired is an antenna which operates at a constant electrical diameter independent of frequency. AIL has patented [1] an antenna which possesses these desirable properties. The Frequency Independent Circular Array, shown in Figure 9, utilizes log-periodic arrays of narrow-band patch antennas as the elements of the circular array. When a log-periodic array is constructed with these narrow-band patches, the phase center of that array moves along the array's length as a function of frequency. By placing a discrete number of these log-periodic arrays at equiangular distances around the surface of a cone, the movement of the log-periodic array's phase center gives the resulting circular array an electrical diameter which remains nearly constant with frequency. This type of array has no inherent bandwidth limitations because its bandwidth can be extended simply by adding more narrow-band patch elements, with the proper resonant frequencies, to each log-periodic array. However, adding more patch elements increases the height of the array; so this design trades-off antenna aperture height for bandwidth. For ship and ground based ESM/ELINT

systems this is an acceptable trade-off. But for submarine periscope and certain unmanned airborne vehicle (UAV) applications, where aperture height is extremely limited, the trade-off is not acceptable.

**TO REALIZE ULTRA-WIDEBAND PERFORMANCE AN ANTENNA WHICH OPERATES AT A CONSTANT ELECTRICAL DIAMETER INDEPENDENT OF FREQUENCY IS REQUIRED**

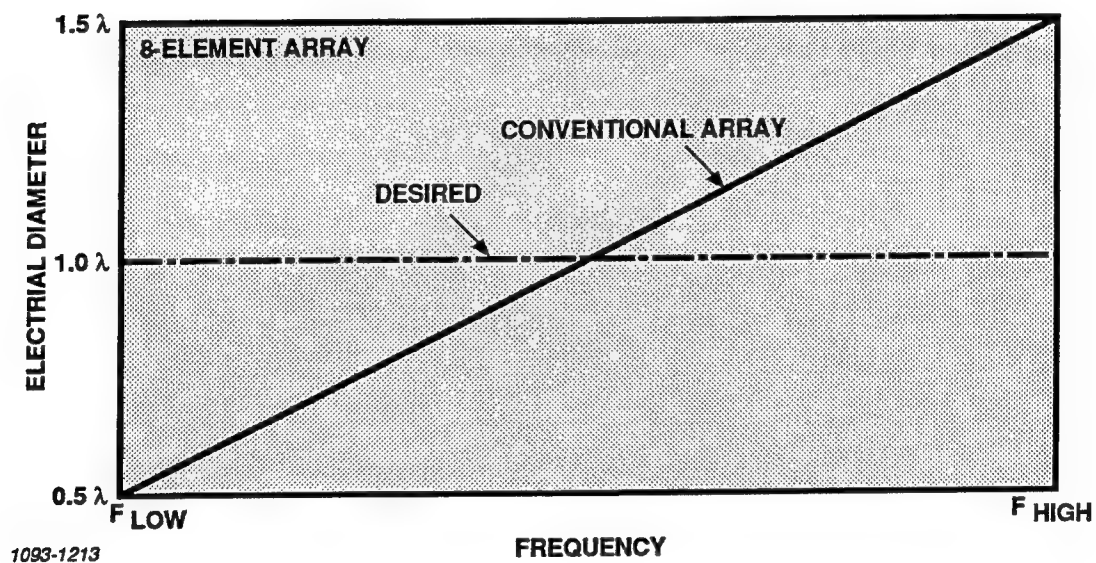


Figure 8. Antenna Electrical Diameter

THIS AIL PATENTED ANTENNA WILL PROVIDE CONSTANT PERFORMANCE OVER  
A MULTIOCTAVE OPERATING BAND AND IS SUITABLE FOR GROUND BASED AND  
SHIPBOARD APPLICATIONS

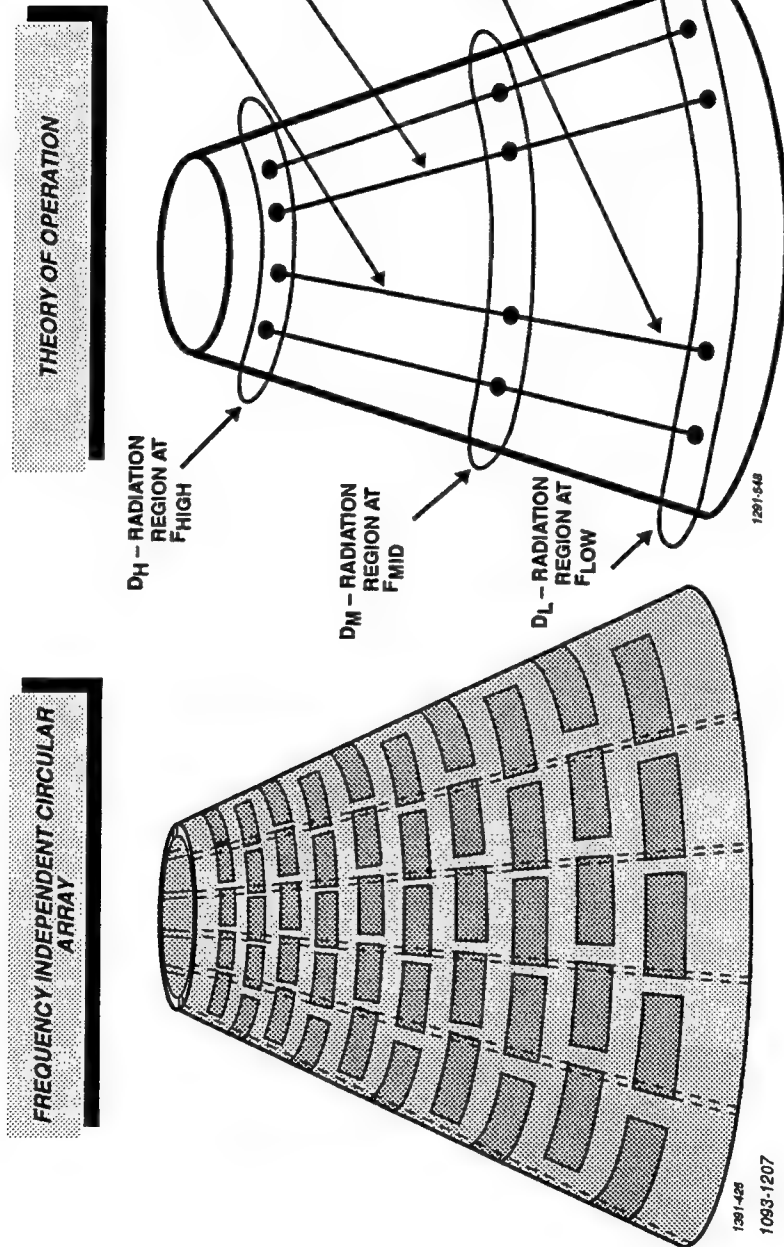


Figure 9. Frequency Independent Circular Array

### **3. AOA Accuracy Considerations**

CAI systems using 8 or 16 elements are capable of providing an AOA accuracy of 1- to 3-deg rms. The factors which affect the AOA accuracy of a CAI system include:

- The operating bandwidth
- The mode pairs used for AOA determination
- Antenna element and Butler matrix error levels
- Receiver error levels
- Calibration method (if any)

An engineering trade-off must be performed to determine the configuration which provides the best combination of AOA accuracy, physical size, and system cost. For ESM systems, an ultrabroadband frequency range, which must be divided into subbands, is usually specified. As was discussed previously, it is desirable to use higher order phase modes for AOA determination because they demagnify the affect of system errors on AOA accuracy. But, the higher order modes exhibit performance degradation at the band edges and the amount of degradation increases with increasing mode number (i.e., the performance of mode 4 degrades more rapidly than the performance of mode 2). Therefore, the optimum bandwidth of each subband must be determined by trading-off the order of the mode pairs used for AOA determination against antenna, Butler matrix, and system error levels.

Keeping error levels small is desirable because it facilitates the use of lower order phase modes to obtain a given AOA accuracy, which in turn, increases the achievable bandwidth. However, developing more accurate system components (antenna elements, Butler matrix, and receiver) is not always feasible and usually increases development time and costs.

In many applications a system calibration is required to obtain the desired AOA accuracy levels. This can be a universal calibration, which is identical for every production unit, or a custom calibration, where every production unit receives its own specific calibration. A custom calibration provides more accuracy, but is undesirable because it increases unit cost and inhibits the use of field replaceable subassemblies; if a component fails in the field and gets replaced, the entire system must be recalibrated.

AIL has developed a sophisticated AOA accuracy analysis tool, the Circularly Disposed Antenna Array (CDAA) computer code, which facilitates the performance of the design trade-offs discussed. This program models a circular array of broadband antenna elements and the Butler matrix which is used to form the phase modes. The CDAA program incorporates deterministic models of components with a user-specified performance variation as a function of frequency. In addition, the user can specify statistical error levels to be placed at the antenna elements and/or at Butler matrix components. AIL's Antenna Systems Department utilizes an extensive design library of measured data to ensure that realizable error levels are used in the analysis. Program outputs include phase and amplitude error variation with either angle or frequency, and for single modes or mode pairs.

#### **4. Present AIL Circular Array Technology**

AIL's CAI technology development is a multifaceted effort which is opening new business areas for the company. Both the U.S. Army and the U.S. Navy have recently awarded AIL contracts to develop high performance, state-of-the-art CAI hardware. The High-Gain Phased Array Antenna is a small, lightweight-antenna which is compatible with Unmanned Airborne Vehicles (UAV's).

A Butler matrix is the heart of every CAI system. AIL's cutting-edge Butler matrix designs have produced AIL winning results with the U.S. Navy to develop small, high performance matrices for deployment in Type 18 periscopes, and a

commercial contract for an ultrabroadband Butler matrix. In addition, several Butler matrices have been designed and fabricated as part of IRAD projects. A sampling of AIL's extensive line of small, lightweight, high performance Butler matrices is presented below.

#### 4.1 Butler Matrices

AIL has over 25 years of experience designing and manufacturing Butler matrices with state-of-the-art performance. We have developed almost a dozen different Butler matrix designs which cover the entire frequency range from 0.3 to 40 GHz. The thick film etching expertise of AIL's AIC group is one of the key elements that enables AIL to produce low cost, high performance Butler matrices. Utilizing statistical process control (SPC), they can repeatedly obtain thin film etching tolerances ( $\pm 0.3$  mils) on 1/2-ounce copper. This enables us to significantly reduce our production costs without sacrificing electrical performance by using low cost, thick film Duroid circuits instead of more expensive, thin film alumina circuits. The performance of AIL's Butler matrices is summarized in Table 1.

Table 1. Butler Matrix Performance Summary

| Butler Matrix   |              | VSWR<br>(In/Out) | Amplitude<br>Matching | Phase<br>Matching |
|-----------------|--------------|------------------|-----------------------|-------------------|
| 0.3 – 2.0 GHz   | 4 x 2 Unit   | 2.0:1 max        | 0.46 dB rms           | 2.3 deg rms       |
| 0.5 – 2.0 GHz   | 8 x 8 Unit   | 2.0:1 max        | 0.48 dB rms           | 3.5 deg rms       |
| 2.0 – 6.0 GHz   | 8 x 8 Unit   | 2.0:1 max        | 0.56 dB rms           | 3.6 deg rms       |
| 6.0 – 18.0 GHz  | 8 x 8 Unit   | 2.2:1 max        | 0.52 dB rms           | 3.4 deg rms       |
| 6.0 – 18.0 GHz  | 16 x 16 Unit | 3.0:1 max        | 0.79 dB rms           | 6.7 deg rms       |
| 2.0 – 18.0 GHz  | 8 x 8 Unit   | 2.0:1 max        | 0.50 dB rms           | 7.3 deg rms       |
| 18.0 – 40.0 GHz | 4 x 2 Unit   | 2.2:1 max        | 0.94 dB rms           | 4.5 deg rms       |



Typical amplitude and phase tracking performance from an 8-input, 8-output 2 – 18 GHz Butler matrix which could be used to feed a Frequency Independent Circular Array is given in Figure 10. Four Butler Matrices designed for use with conventional circular array antennas are shown in Figure 11. The 0.5 to 2.0 GHz and the 2.0 to 6.0 GHz units employ high dielectric constant ( $k = 10.8$ ) soft substrate material to shrink the size of the couplers and phase shift networks. The published coupled stripline design equations are not valid for this high- $k$  material, so AIL has developed custom design curves to facilitate the design and optimization of the required components. The 6.0 to 18.0 GHz unit utilizes unique “pseudocontinuously” tapered couplers which provide the performance of continuously tapered designs in the same physical length as a discretely stepped coupler; a continuously tapered coupler’s overall length is a quarter wave longer. The 18.0 to 40.0 GHz unit utilizes preamplification on the input ports to mask the insertion losses of the

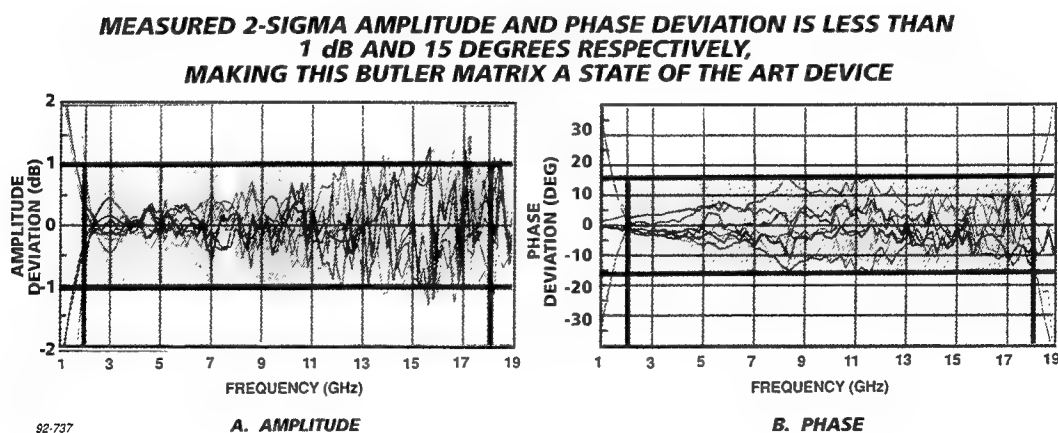
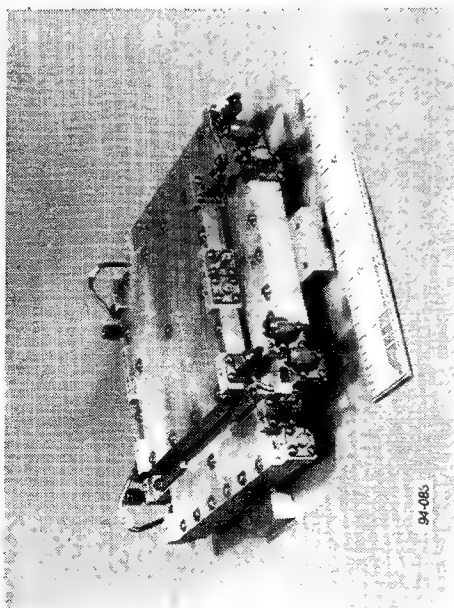
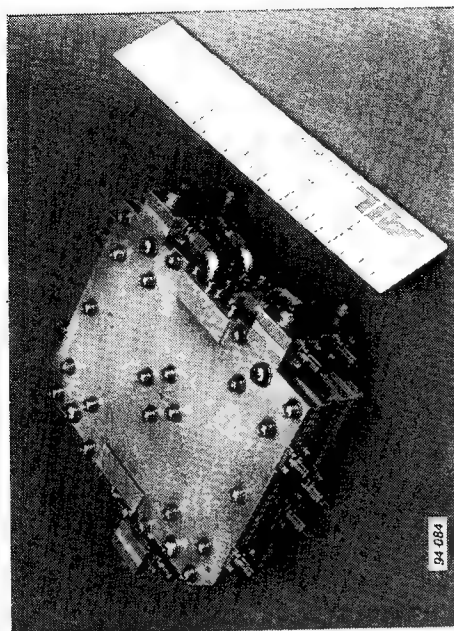


Figure 10. Measured Deviation of All Ports of 2.0 – 18.0 GHz 8 x 8 Butler Matrix Relative to the Median of Error Distribution for Mode –2

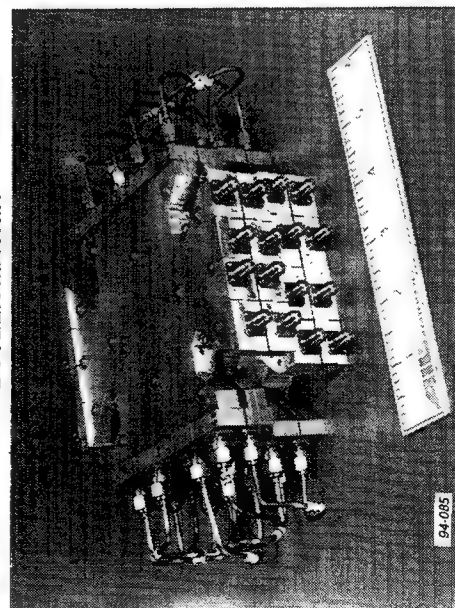
**AIL'S SMALL, LIGHTWEIGHT BUTLER MATRICES PROVIDE OUTSTANDING PERFORMANCE OVER THE ENTIRE BAND FROM UHF TO MILLIMETER-WAVE FREQUENCIES**



**0.5 - 2.0 GHz 8 x 8  
BUTLER MATRIX**

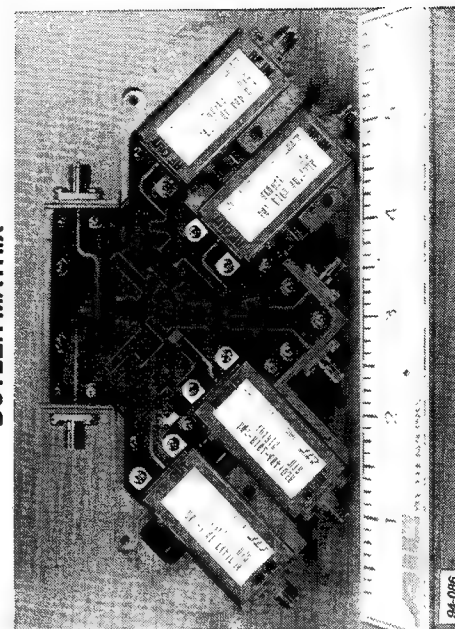


**2.0 - 6.0 GHz 8 x 5  
BUTLER MATRIX**



**6.0 - 18.0 GHz 16 x 16  
BUTLER MATRIX**

**93-1214**



**18.0 - 40.0 GHz 4 x 4  
BUTLER MATRIX**

**Figure 1.1. Butler Matrices Designed and Manufactured by AIL**

device. This matrix design employs 0/180-deg hybrids which utilize a unique combination of microstrip and slotline transmission media to provide outstanding performance in a very compact configuration.

#### **4.2 High-Gain Phased Array Antenna**

The High-Gain Phased Array Antenna (HGPAA) is an in-progress program to develop a high accuracy AOA circular array antenna with two simultaneous operating states. The first provides omni (360-deg IFOV) phase DF over a 36:1 frequency band. The second provides a narrower IFOV high-gain directional beam capable of full 360-deg coverage via electronic scanning. The antenna is comprised of three separate antenna subsystems each covering a 3:1 or larger segment of the operating frequency band. AIL has currently completed development of the high- and low-band antenna subsystems, and plans to complete the mid-band antenna subsystem.

#### **4.3 High-Band Antenna Subsystem**

The high-band antenna subsystem covers a 3:1 frequency band and has both the omni and high gain modes of DF operation. The developed antenna subsystem is shown in Figure 12. The radiating aperture, shown in Figure 13, is a biconical horn fed by a horizontally polarized circular array of 16 printed circuit flared-notch elements. The passive VSWR of a flared-notch radiator in the 16-element array is given in Figure 14. Element VSWR is under 2.0:1 for the upper 60 percent of the frequency band and peaks at just over 3.0:1 near the low end of the band. The feed for the 16-element flared-notch array is shown in Figure 15. A twist-grid polarizer, designed using the procedure discussed in [3], at the aperture face provides the desired slant-45-degree final polarization state.

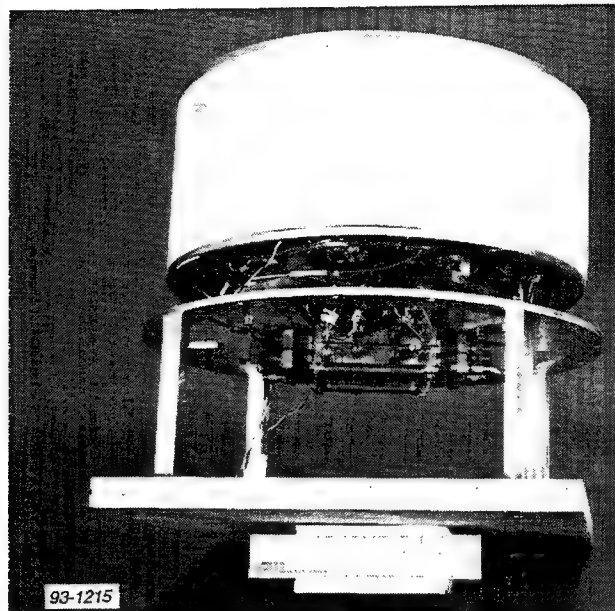


Figure 12. High-Band Antenna Subsystem

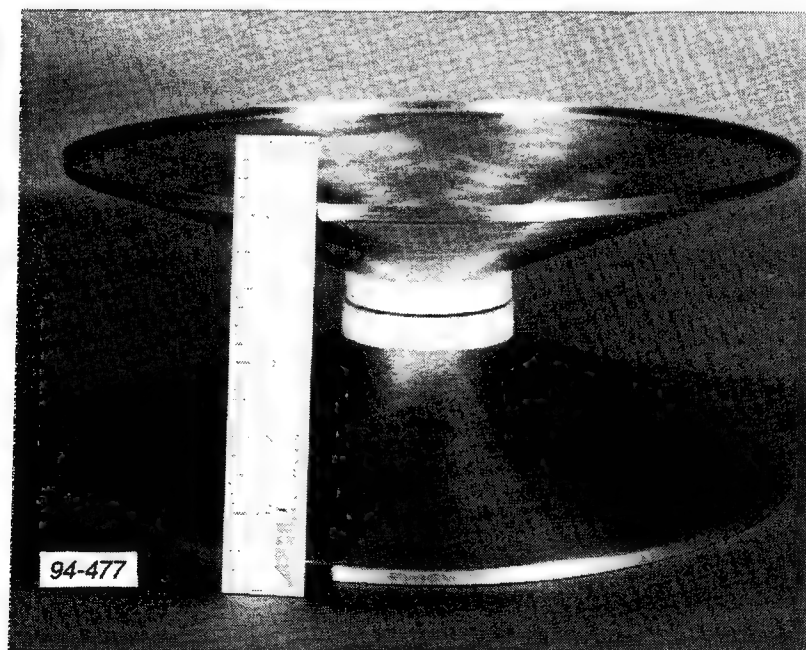


Figure 13. 3:1 Bandwidth Biconical Horn Fed by Circular Array of 16 Printed Circuit Flared-Notch Elements

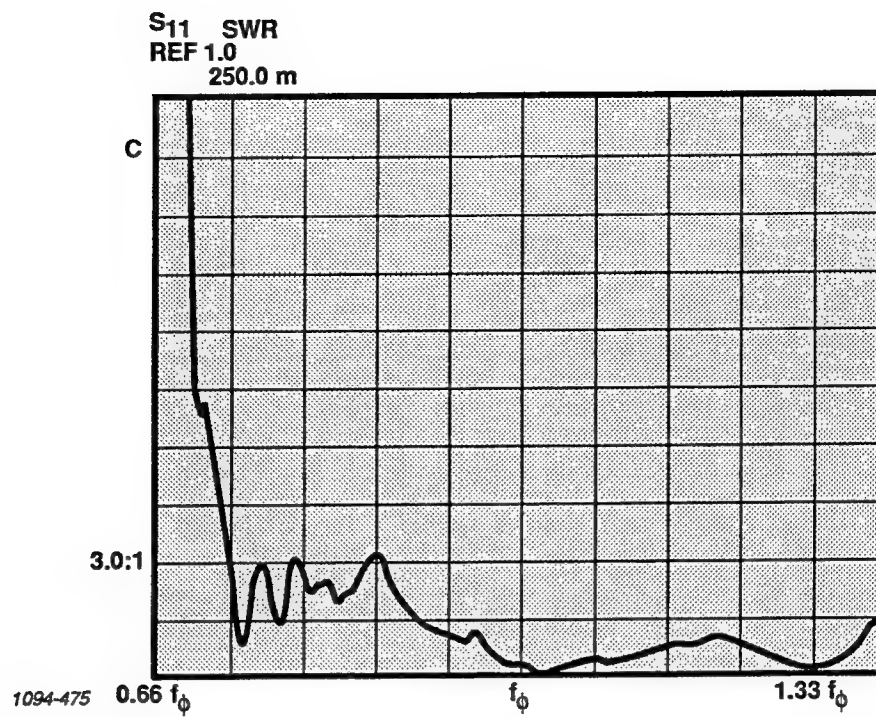


Figure 14. Passive VSWR of a High-Band Antenna Element in the Array Environment

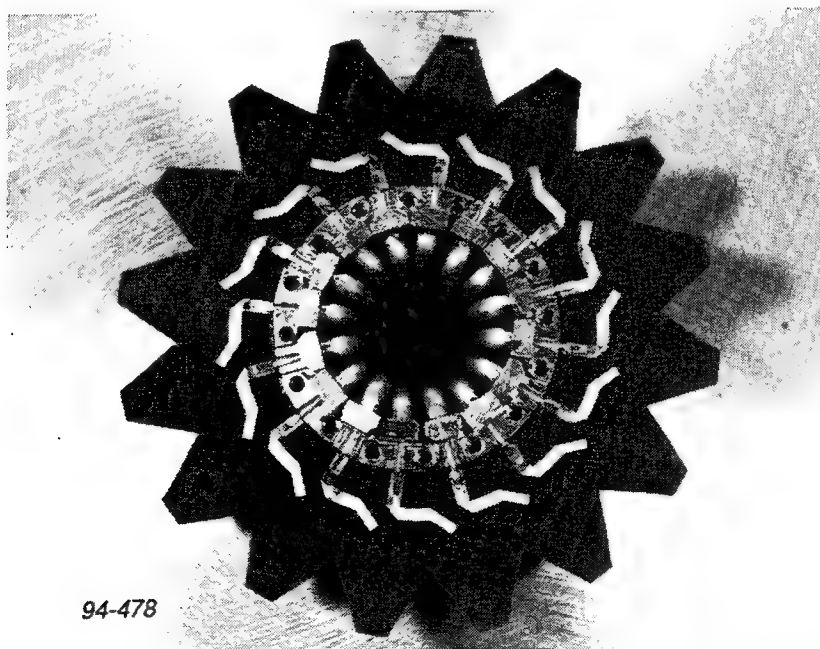


Figure 15. Feed for the 3:1 Bandwidth 16-Element Flared-Notch Array

The block diagram of this antenna was given earlier in Figure 3. The antenna aperture is fed by a 16 x 16 Butler matrix to provide access to the omnidirectional phase modes of the CAI. To mask the insertion loss of the feed network, each Butler matrix input is preceded by a low-noise amplifier. Eleven of the sixteen available Butler matrix output phase modes are used to form the high-gain mode directive beam while the remaining five highest-order modes are terminated. Signal from four of these omnidirectional modes is coupled-off to provide 360-deg IFOV AOA determination.

The through signals from the omnimode couplers are then fed into 11 separate MMIC phase-shifter channels where the required focusing phase distribution and progressive phase tilt are applied to form and steer the high-gain mode beam. The shifted modes then form the beam via an 11-way power-combining network. A sum/difference hybrid coupler provides the final monopulse amplitude DF outputs. The proposed midband subsystem is identical in operation.

#### **4.4 Low-Band Antenna Subsystem**

The low-band antenna subsystem covers a 4:1 frequency band and provides the omnimode of DF operation. The realized antenna, shown in Figure 16, is remarkable in that it comprises a complete eight-element DF array in a volume much smaller than is normally required for an antenna operating over a frequency band this wide. This is accomplished via a distributed resistive load over the dipole element surfaces [4]. This reduces the effects of the cylindrical groundplane on the element input impedance thus allowing the spacing of the elements to be much closer to ground than normal. The passive input VSWR of a dipole in the array environment is less than 2.0:1 over the entire operating band as shown in Figure 17. In addition, the entire state-of-the-art Butler matrix is contained inside the groundplane cylinder. The low-band subsystem weighs about 10 pounds.

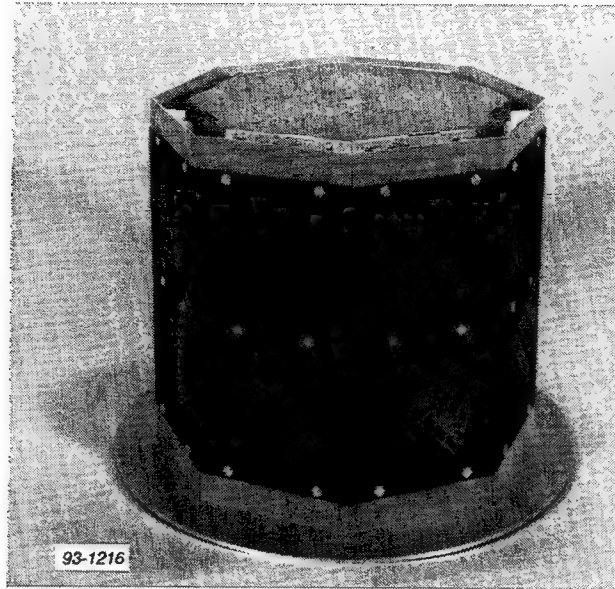


Figure 16. Low-Band Antenna Subsystem

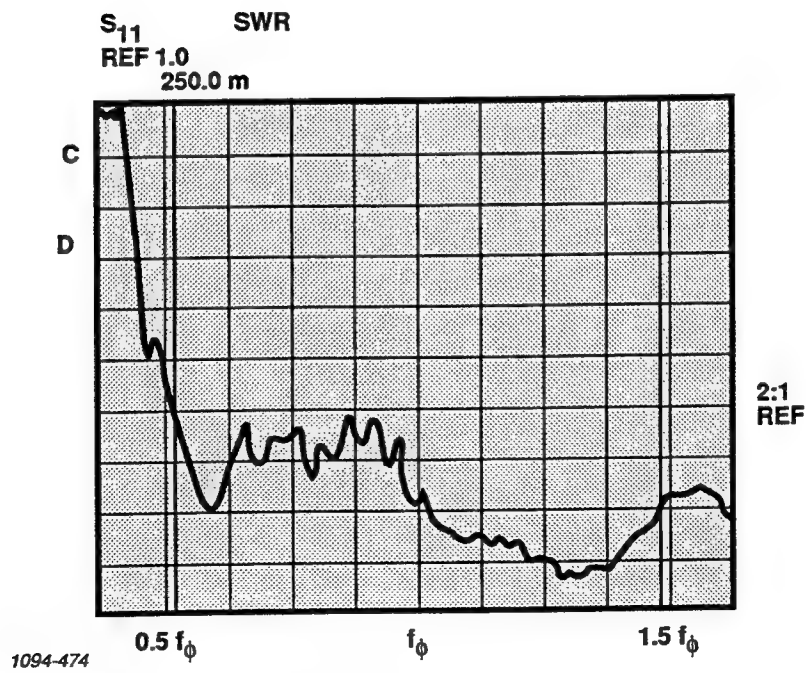


Figure 17. Passive VSWR of a Dipole in the Low-Band Antenna Array Environment



An example of the excellent modal phase linearity provided by this circular array is displayed in Figure 18, which shows the phase of mode +2 with respect to mode -2 versus azimuth angle at the low, mid, and high points in the frequency band. This phase linearity facilitates AOA determination with a very high degree of accuracy. This high-performance, low weight, small volume system is suitable for many DF applications including UAV's, submarine masts, and ground vehicle platforms.

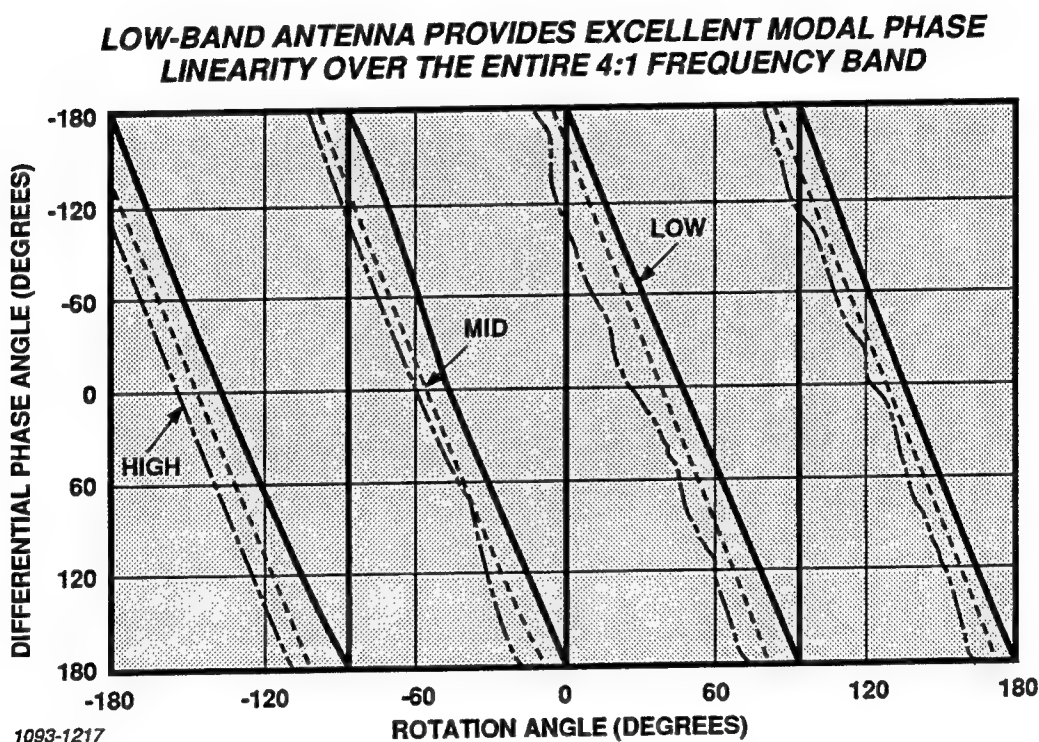


Figure 18. Measured Modal Phase of Low-Band Antenna Subsystem



## 5. Conclusions

This paper has presented a comprehensive introduction to the theory of operation of CAI systems. Using a Butler matrix in conjunction with a circular array provides direct access to the phase modes of the CAI. By simultaneously comparing pairs of phase modes AOA can be accurately determined to within 1- to 3-deg rms.

Low modal gain at the low end of the band and large phase ripple at the high end of the band were shown to limit conventional circular array designs to 3:1 or 4:1 operating bandwidths. AIL's Frequency Independent Circular Array Antenna eliminates this fundamental bandwidth limitation and, when development is complete, has the potential to provide 10:1 or 20:1 operating bandwidths for ground based and surface ship based ESM/ELINT systems.

An overview of AIL's present circular array technology was presented. This overview included CAI hardware which was under contracts for the U.S. Army, the U.S. Navy and on company funded IRAD projects. A unique CAI was presented; it can simultaneously provide both wide open full 360-deg IFOV AOA information and a narrower IFOV high-gain directional beam capable of full 360-deg coverage via electronic scanning. In addition, AIL's Butler matrices, the heart of a CAI, were presented; they provide cutting edge performance over the entire frequency band from UHF to millimeter wave frequencies.

## 6. References

- [1] United States Patent Number 4,980,692, "Frequency Independent Circular Array," Inventors: Ronald M. Rudish and Peter J. McVeigh; Assignee: AIL Systems Inc.
- [2] T. Rahim and D.E.N. Davies, "Effect of Directional Elements On The Directional Response Of Circular Antenna Arrays," *IEEE Proc.*, vol. 129, Pt. H, pp. 18-22, February 1982.

- [3] P. M. Eyring, "Computer Aided Optimization Of Wideband, Multi-Grating, Twist-Grid Polarizer Designs," *1993 IEEE Antennas and Propagation Society International Symposium Digest*, vol. 3, pp. 1368–1371.
- [4] R. E. Clapp, "A Resistively Loaded, Printed Circuit, Electrically Short Dipole Element For Wideband Array Applications," *1993 IEEE Antennas and Propagation Society International Symposium Digest*, vol. 1, pp. 478–481.

# A MULTIFUNCTION, MULTIPLE FREQUENCY APERTURE<sup>1</sup>

J. Yon  
L. Parrish  
T. Waterman  
G. Evans  
P. Hrycak

Westinghouse Electric Corporation  
Electronic Systems  
Design and Producibility Engineering Division  
Baltimore, Maryland 21203

## ABSTRACT

*A dual band radiating aperture was developed that is suitable for simultaneous operation in beacon antenna, L-Band surveillance radar, and S-Band dual polarized weather radar. The design uses S-Band patches between pairs of L-Band slots. Radiators were simulated analytically and tested experimentally in a multimode simulator. VSWR is typically less than 2:1 and isolation between bands is 30 to 37 dB, making it practical to operate the radars independently.*

---

<sup>1</sup> This effort was sponsored by the Federal Aviation Administration, Terminal Area Surveillance System Program Office, which is responsible for the development of the next generation airport surveillance radar.

## 1.0 OVERVIEW

In a variety of situations, multiple radar and communications requirements compete for limited real estate. It is especially true on aircraft and ship masts, but applies to airport surveillance situations as well. As part of this program, Westinghouse has successfully designed and developed a dual band shared aperture for the FAA's integrated sensor functions shown in Figure 1-1. The shared aperture provides beacon, a secondary source radar, and weather mapping with scan capability of  $\pm 45^\circ$  in azimuth and  $0^\circ$  to  $30^\circ$  in elevation. Beacon operation is provided vertically polarized at 1.0 to 1.1 GHz and the secondary source radar operation is provided vertically polarized at 1.25 to 1.35 GHz. S-Band weather radar is provided both vertically and horizontally polarized at 2.7 to 2.9 GHz. Furthermore, the shared aperture provides sufficient aperture isolation between bands to allow autonomous operation of L- and S-Band frequencies.

The shared aperture consists of L-Band elements interleaved with S-Band elements as shown in Figure 1-2. Each L-Band element utilizes a distributed feed to radiate between a set of paired slots formed by two S-Band elements high by two wide. The S-Band element utilizes a two layer patch construction fed in the back plane by a dual polarized feed which also forms the cavity used by the L-Band element. This configuration demonstrates sufficient isolation for autonomous

operation and the distributed L-Band feed establishes a periodicity that ensures grating lobe free S-Band patterns.

This effort demonstrated feasibility of the shared aperture through a combination of analytical and experimental evaluation. The baseline for the shared aperture was developed with the aid of computer modeling which solves Maxwell's equations using a finite difference approach. A multimode waveguide simulator, shown in Figure 1-3, provided empirical verification using two L-Band and eight S-Band elements. The effort concludes that all bands have VSWR of approximately 2:1 across the ranges of frequency and scan. Furthermore, the demonstration verified that there are no blind angles or resonances due to coupling from one band into the other radiator. Isolation from L- to S-Band is always better than 34 dB and from S- to L-Band it is better than 29 dB.

## 2.0 Requirements

Table 2-1 summarizes the system requirements. To include all options, the array would not be tilted back, therefore, allowing the possibility of a cylindrical array. Furthermore, the possibility of active devices and possibly adaptive azimuth processing leads us to organization in columns and a preference for a rectangular

grid of radiators rather than triangular. To obtain the required beamwidths the full aperture requires an approximate height of 14' and width of 24'. The chosen array dimensions and element spacings are shown in Figure 2-1. At S-Band the limitations are 2.5" spacing in height and 2.25" in width. By restricting ourselves to an integral number of S-Band elements per L-Band element, the L-Band element has a height of 5.0" and width of 4.5".

### 3.0 Aperture Analysis

Several obstacles were overcome during the analytical development. The limited L-Band aperture increased the difficulty of obtaining the scan volume and 30% bandwidth required for L-Band operation. This was compounded by the dual polarization requirement at S-Band. The vertical polarized S-Band signal could leak into the L-Band element if it is not properly choked. Conventional S-Band chokes could not be used without subtracting significantly from the already small L-Band aperture. This resulted in the resonant elements built into the L-Band feed network.

### 3.1 Integrated Radiator Development

The S-Band radiates from patches having a parasitic for bandwidth. It is not a conventional unbalanced patch which would be fed from one side. In order to avoid excitation of the various interconnected structures, this patch uses a dual polarized, balanced feed as shown in Figure 3-1. The symmetrical feed, similar to a crossed dipole, drives both sides with a balanced 2-wire line. Although this design works, considerable mechanical simplification would be justified if the full array construction were undertaken.

For wide angle scanning, the L-Band radiator should have an isolated pattern that is nearly a cosine shape in power. This matches the unavoidable variation in projected array area. A slot can be made to approximate this in the H-plane, but two parallel slots are needed in the E-plane. The shared aperture has natural scanning capability, but has a limited aperture. The limited aperture forces us to use multiple tuning components to achieve the require 30% bandwidth. These components comprise the L-Band feed, its surrounding cavity, and transition to free space.

The paired slot is driven with the L-Band feed shown in Figure 3-2. A necessary precaution during L-Band development is that line lengths joining slot pairs must be minimized. Otherwise, when the array is steered, the odd symmetry coupling from neighbors may be terminated in a reactance that resonates to produce a blind angle. An additional complication to the L-Band design results from the dual

polarization requirement at S-Band. It is impractical to insert S-Band chokes at the aperture face. That was found to significantly complicate L-Band matching. Instead, special tuning stubs were adapted to the L-Band feed to serve as filter elements without impeding L-Band match.

### 3.2 Analytical Results

The computed impedance match for S-Band operation is summarized in Table 3-1 and 3-2 for vertical and horizontal polarization, respectively. VSWR performance is summarized at four frequencies for four separate scan conditions. In general, the vertical polarization exhibits slightly larger VSWR resulting from the slots for L-Band radiation. Overall, the vertical polarization was always better than a VSWR of 2.3:1 and the horizontal polarization better than 1.7:1.

The computed impedance match for vertical polarized L-Band operation is summarized in Table 3-3. Overall, its VSWR was less than 2.2:1. These values would be considered reasonable even for separate, independently designed apertures, and are felt to be excellent for the composite array.



#### 4.0 Measurements

In this section, scan loss and isolation are empirically evaluated for the dual band aperture using a multimode waveguide simulator. In order to evaluate both bands the waveguide simulator walls must be repositioned as shown in Figure 4-1. During L-Band testing, the top and bottom walls are positioned half way between their feeds to produce the proper boundary conditions for simulating an infinite array environment. Likewise, the top and bottom walls are positioned half way between S-Band elements during S-Band testing. In both cases the side walls remain the same. In this fashion, the L-Band simulator consists of 1 element high by 2 wide, whereas, the S-Band simulator consists of 2 elements high by 4 wide.

The waveguide simulator enables us to accurately predict scan loss and isolation for the full array size by simulating an infinite array environment through the use of the waveguide walls. The propagating waveguide modes correlate to scanned plane wave conditions of the aperture. By utilizing superposition, a set of S-parameter measurements can be used to construct the multiple plane wave conditions and thereby determine impedance match and isolation responses. There were a total of six test performed: three for scan loss measurements and four for isolation measurements.

## 4.1 Scan Loss Measurements

Figure 4-2 summarizes the S-parameter sets needed to determine impedance match for L-Band and dual polarized S-Band. Only those modes are constructed that fall within our scan limits. At L-Band, only one mode is useful and it simulates a beam at 0° elevation and 41° at 1.0 GHz to 29° at 1.35 GHz in azimuth. At S-Band, there are enough elements to simulate a number of beams for each polarization. The beam directions are summarized for both bands in Table 4-1.

The measured L-Band impedance match is shown in Figure 4-3 for an azimuth scan of 30° (average). The match is better than a 2:1 VSWR except at the high end of the band with the worst VSWR being 2.5:1. This is comparable to predicted performance of 2.2:1 maximum. A 2% frequency shift would correct the discrepancy.

Figure 4-4a) summarizes the measured S-Band vertical polarization impedance match for the 0° elevation scan conditions and Figure 4-4b) for the 25° (average) elevation scan conditions. In almost all cases, the VSWR is generally better than 2.2:1. This is comparable to predicted performance of 2.3:1 maximum. At 25° elevation, 3 points at the band edge exceed our goal, and warrant further matching.

Figure 4-5 shows the S-Band horizontal polarization impedance match for the

25° (average) elevation scan conditions. A maximum VSWR of 2:1 was achieved across the band and scan angles. This is comparable to predicted performance of 1.7:1 maximum.

The overall scan loss tests are in good agreement with analytical predictions. Furthermore, both indicate that the two bands can be operated integrally without interaction, resonances, or blind angles.

#### 4.2 Band-to-Band Isolation Measurements

The total isolation between systems includes several contributors. While filters would provide the bulk of the rejection, some isolation is mandated at the aperture to ensure independent operation of each band. As a minimum, the aperture isolation needs to be better than 20 dB in order to sufficiently suppress coupling that would degrade sidelobe performance when scanning both bands independently.

Isolation between bands was determined from S-parameter measurements from each element of one band to a single element of the other band as shown in Figure 4-6. By using vector addition of the coupling values, with a weighting corresponding to the various waveguide modes, the band-to-band isolation can be

found for various scan angles.

The L-Band isolation between L-Band and vertical polarized S-Band is shown in Figure 4-7. The isolation corresponds to an azimuth scan of  $34^\circ$  (average). The simulator wall configuration for this measurement allows isolation to be determined at four of the eight S-Band elements. Due to symmetry, only the two unique isolation measurements were recorded. The isolation was found to be better than 34 dB across the band.

Figure 4-8 shows the L-Band isolation between L-Band and horizontal polarized S-Band for the same scan condition. The isolation is nominally better than 45 dB with a worst case of 40 dB.

The S-Band isolation between vertical polarized S-Band and L-Band is shown in Figure 4-9. The simulator wall configuration for this test permits isolation measurements at two of the four L-Band elements. Due to symmetry only one of the isolation measurements was recorded. At vertical polarized S-Band, there are three scan conditions within our scan volume corresponding to  $14^\circ$ ,  $28^\circ$ , and  $45^\circ$  average azimuth scan. The largest scan condition showed the worst isolation. However, for this waveguide mode, frequencies below 2.78 GHz correspond to azimuth scan angles greater than  $45^\circ$ . With the exclusion of those frequencies the isolation is

better than 29 dB.

Figure 4-10 shows the S-Band isolation between horizontal polarized S-Band and L-Band. For this measurement the average scan angles are  $0^\circ$ ,  $14^\circ$ , and  $45^\circ$  azimuth and  $25^\circ$  elevation. The isolation for the  $28^\circ$  azimuth scan condition can not be determined because it produces a null at the measured L-Band element. As before, the worst isolation occurs at the largest scan condition where the lower end of the band is excluded because it exceeds our scan limits. The isolation is better than 40 dB for all frequencies and scan angles within our interest.

## 8.0 CONCLUSIONS

The primary conclusion is that the shared L- and S-Band aperture is realizable. It is worth noting that achieving either the wide L-Band or the dual polarized S-Band performance individually would be a significant accomplishment. The feasibility of an integrated array face has been demonstrated and experiments show that it is possible to achieve both the match and the required isolation at the aperture needed to sustain autonomous operation.

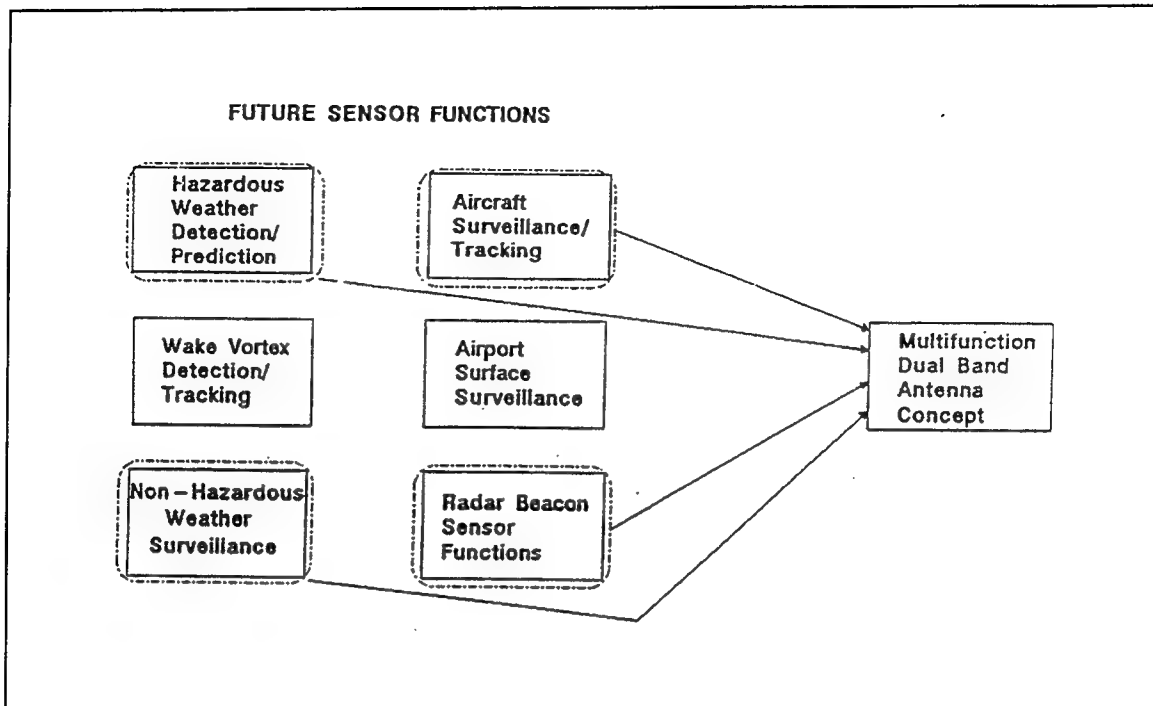


Figure1-1 Integrated Sensor Functions

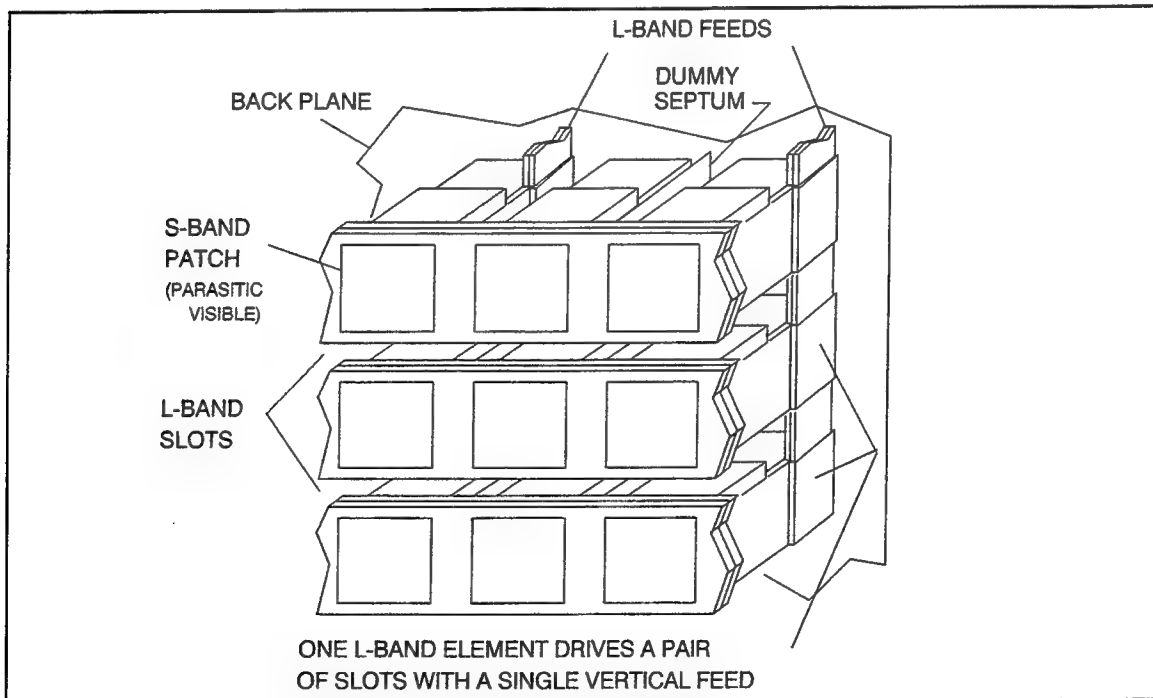


Figure 1-2 Integrated Dual Band Aperture

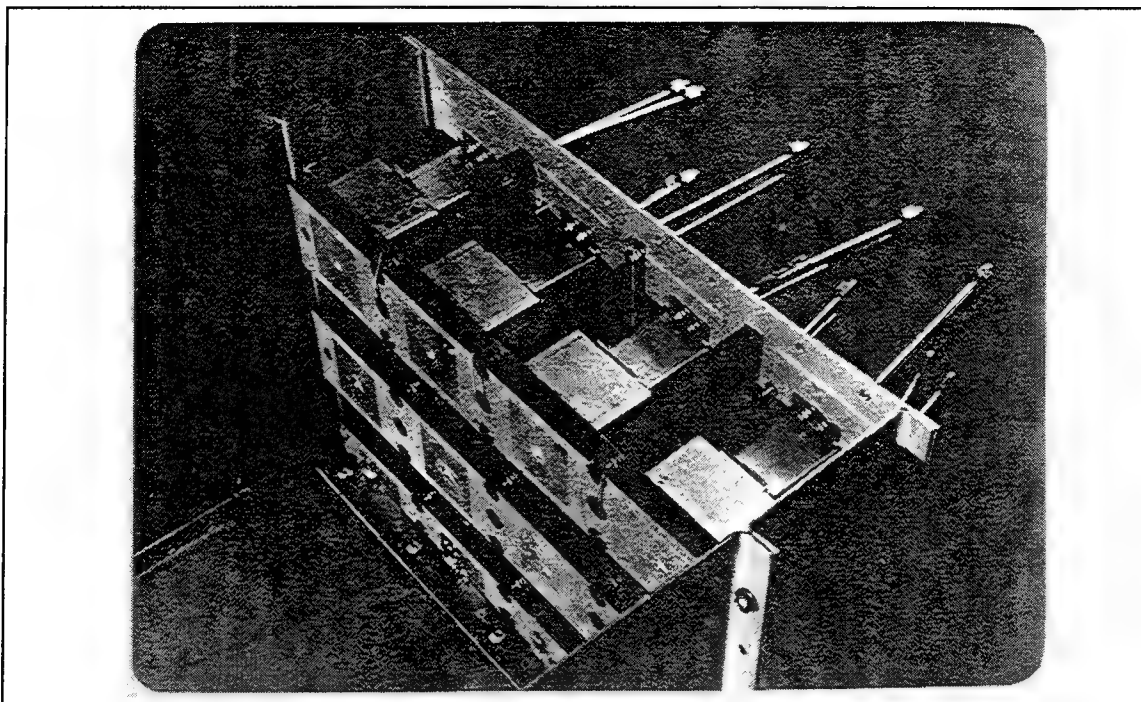


Figure 1-3 Multimode Waveguide Simulator

|                    | Beacon    | L-Band      | S-Band     |
|--------------------|-----------|-------------|------------|
| Frequency (GHz)    | 1.0 - 1.1 | 1.25 - 1.35 | 2.7 - 2.9  |
| Polarization       | vertical  | vertical    | selectable |
| Elevation Coverage | 30°       | 30°         | 30°        |
| Azimuth Scan       | ±45°      | ±45°        | ±45°       |
| Approx. Height     | 14'       | 14'         | 14'        |
| Approx. Width      | 24'       | 24'         | 24'        |
| Elevation BW       | 11° min   | 11° min     | 1.5°       |
| Azimuth BW         | 2.4° min  | 2.0° min    | 1.0°       |

Table 2-1 Integrated L/S Antenna Requirements

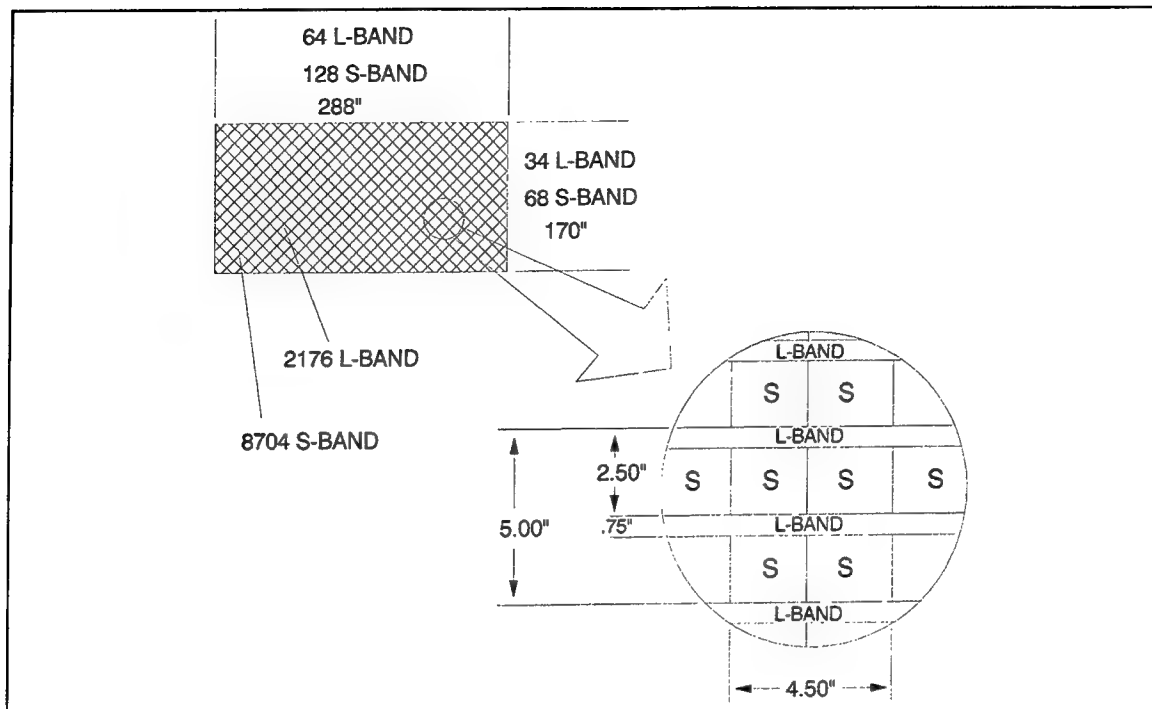


Figure 2-1 Integrated Array Geometry

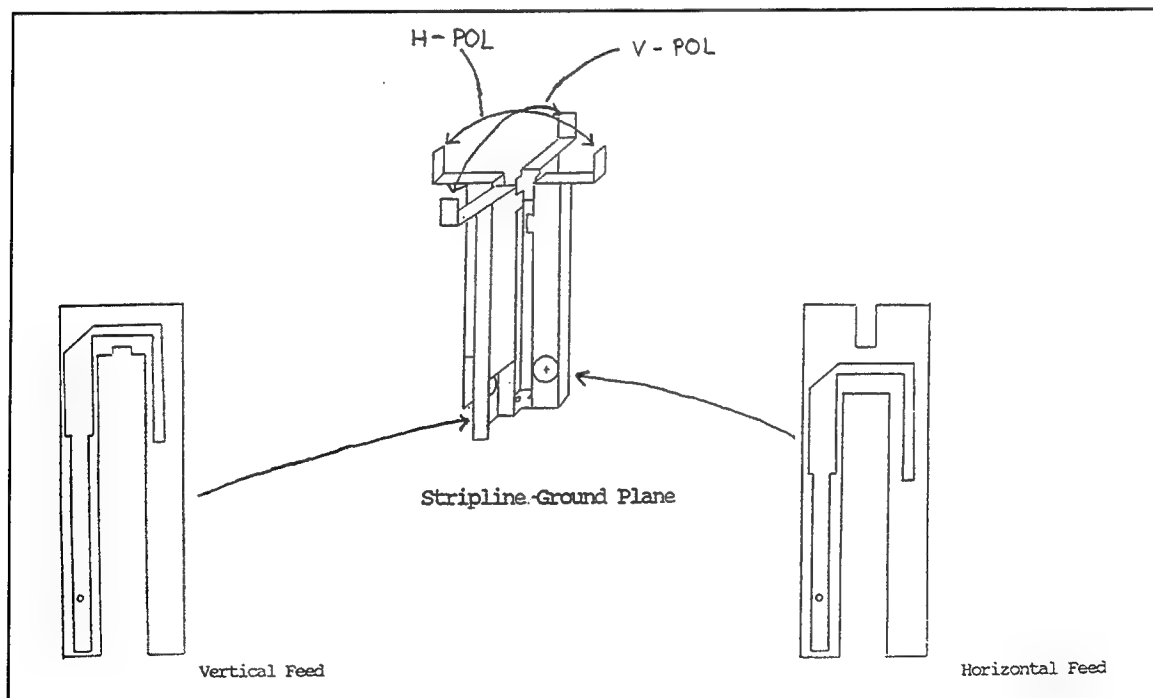


Figure 3-1 S-Band Balanced Feed Design



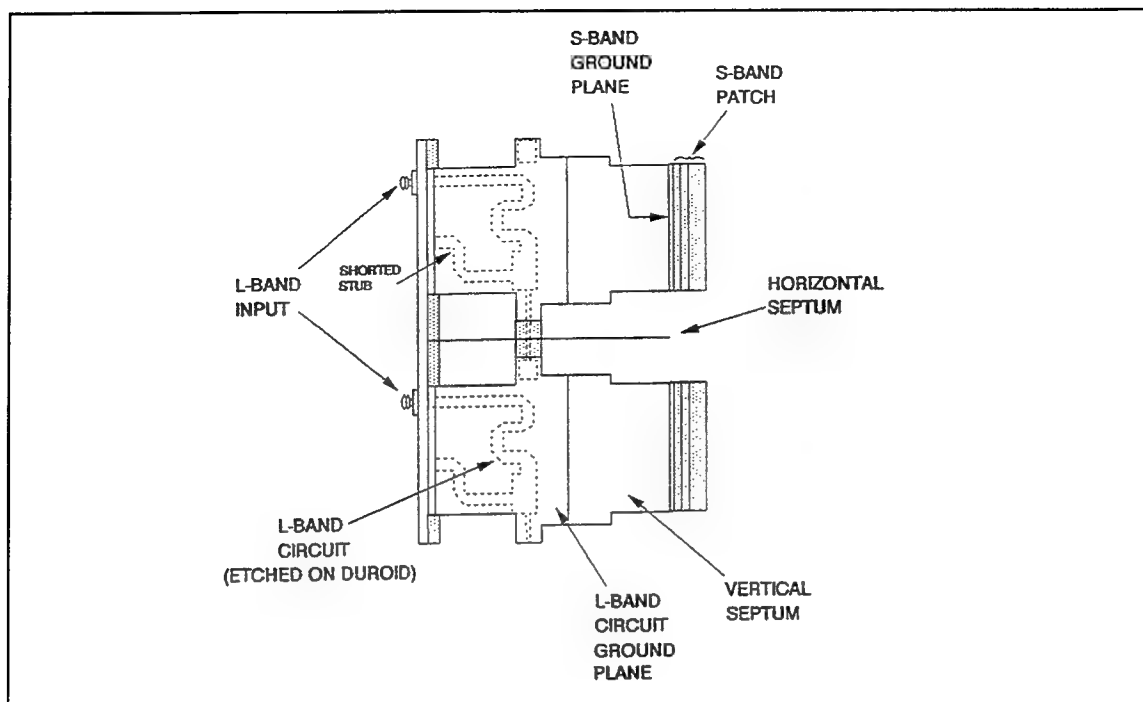


Figure 3-2 L-Band Feed Design

| FREQ<br>(GHz) | VSWR       |                |                |                            |
|---------------|------------|----------------|----------------|----------------------------|
|               | no<br>scan | 45° Az<br>scan | 30° El<br>scan | 45° Az &<br>30° El<br>scan |
| 2.70          | 1.65       | 2.0            | 1.3            | 2.3                        |
| 2.78          | 1.2        | 1.8            | 1.4            | 2.1                        |
| 2.86          | 1.3        | 1.9            | 1.7            | 2.1                        |
| 2.95          | 1.3        | 1.3            | 1.1            | 1.3                        |

Table 3-1 Vertical S-Band Computed VSWR

|               | VSWR       |                |                |                            |
|---------------|------------|----------------|----------------|----------------------------|
| FREQ<br>(GHz) | no<br>scan | 45° Az<br>scan | 30° EI<br>scan | 45° Az &<br>30° EI<br>scan |
| 2.70          | 1.6        | 1.4            | 1.3            | 1.5                        |
| 2.78          | 1.2        | 1.5            | 1.2            | 1.5                        |
| 2.86          | 1.4        | 1.7            | 1.5            | 1.5                        |
| 2.95          | 1.3        | 1.2            | 1.1            | 1.1                        |

Table 3-2 Horizontal S-Band Computed VSWR

|               | VSWR       |                |                |                            |
|---------------|------------|----------------|----------------|----------------------------|
| FREQ<br>(GHz) | no<br>scan | 45° Az<br>scan | 30° EI<br>scan | 45° Az &<br>30° EI<br>scan |
| 1.02          | 1.3        | 2.1            | 1.2            | 1.4                        |
| 1.11          | 1.2        | 2.2            | 1.3            | 1.6                        |
| 1.26          | 1.4        | 2.1            | 1.6            | 1.8                        |
| 1.35          | 1.7        | 2.1            | 2.0            | 2.2                        |

Table 3-3 L-Band Computed VSWR

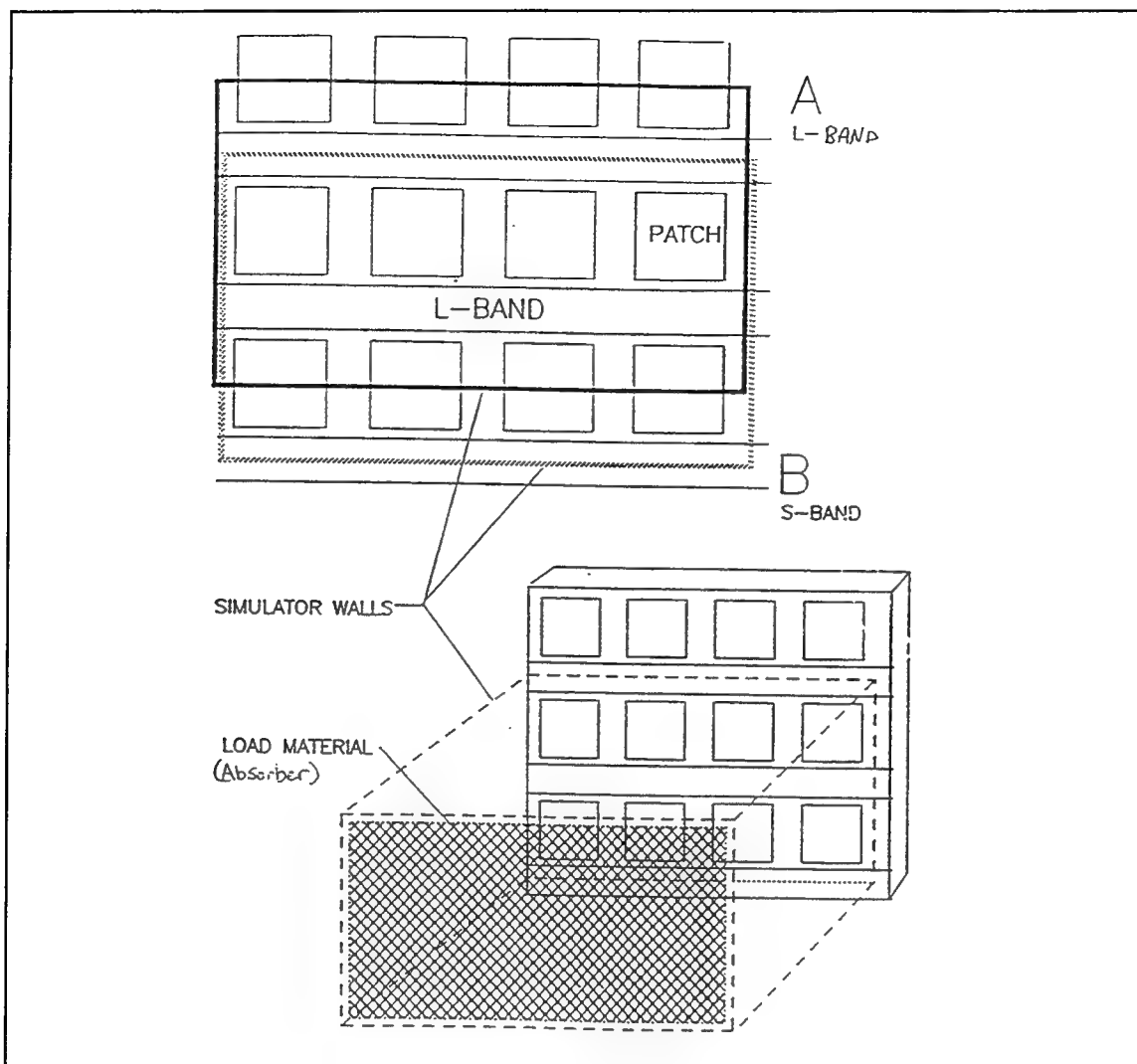


Figure 4-1 Waveguide Simulator Wall Configuration

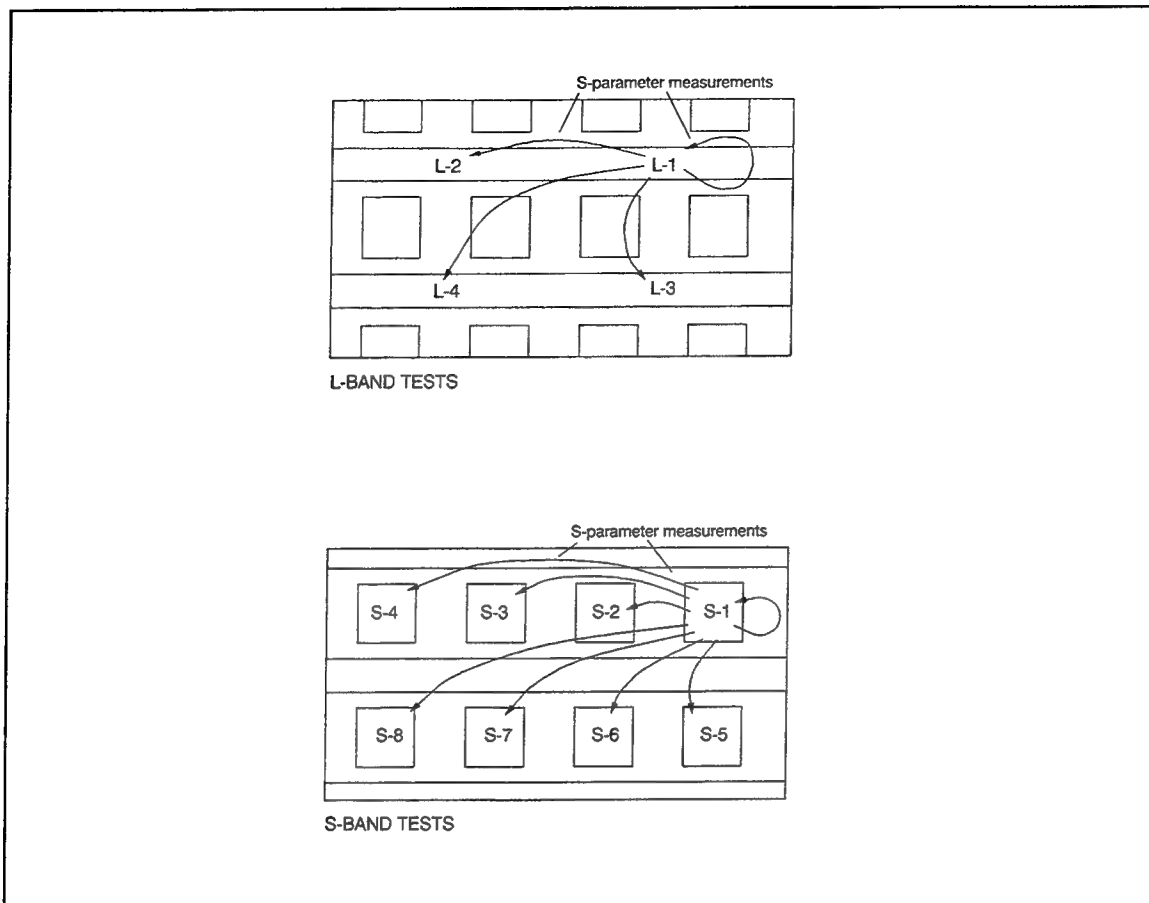


Figure 4-2 S-Parameter Set Required For Impedance Match

| Simulated Scan Angles |              |           |                   |
|-----------------------|--------------|-----------|-------------------|
| Band (GHz)            | Polarization | Elevation | Azimuth           |
| 1.06                  | V            | 0°        | 38°               |
| 1.30                  | V            | 0°        | 30°               |
| 2.8                   | V            | 0°        | 13°, 28°, 44°     |
|                       |              | 22°       | 13°, 28°, 44°     |
| 2.8                   | H            | 22°       | 0°, 13°, 28°, 44° |

Table 4-1 Simulated Scan Angles

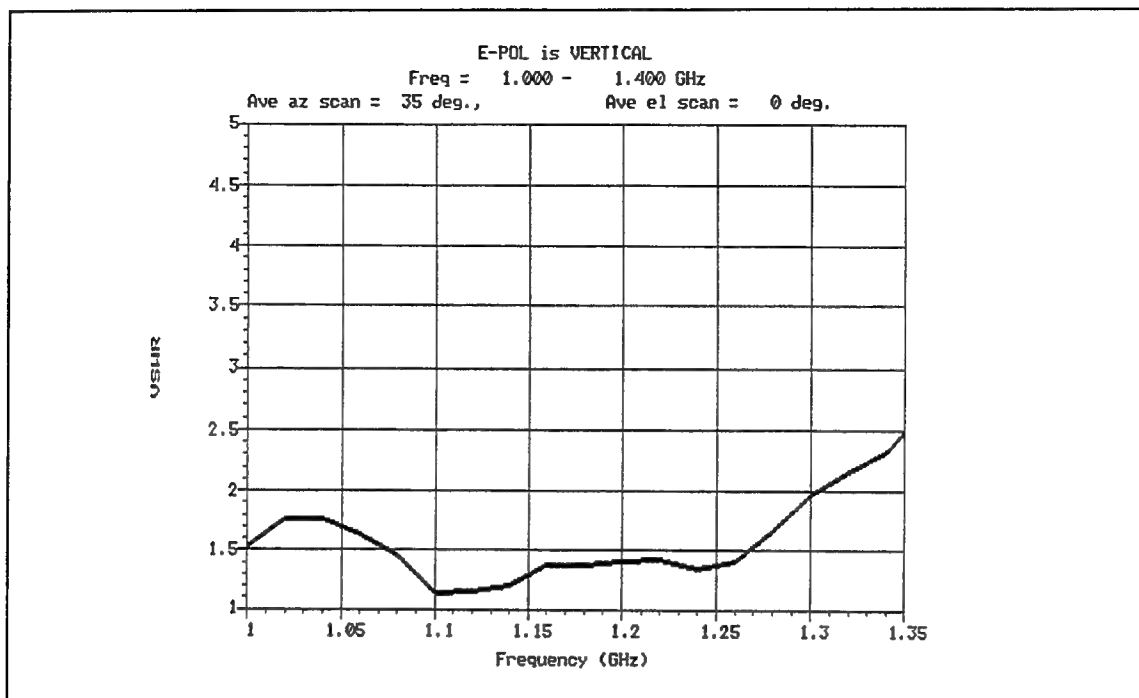


Figure 4-3 L-Band Measured Impedance Match

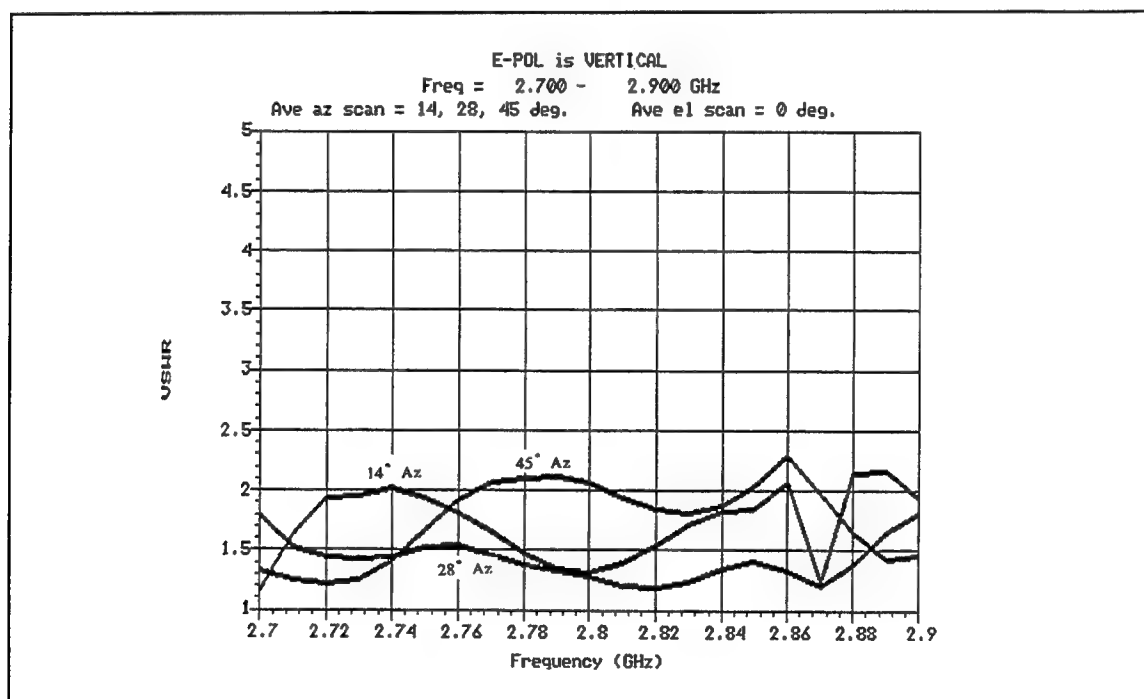


Figure 4-4a) Vertical Polarized S-Band Measured Impedance Match

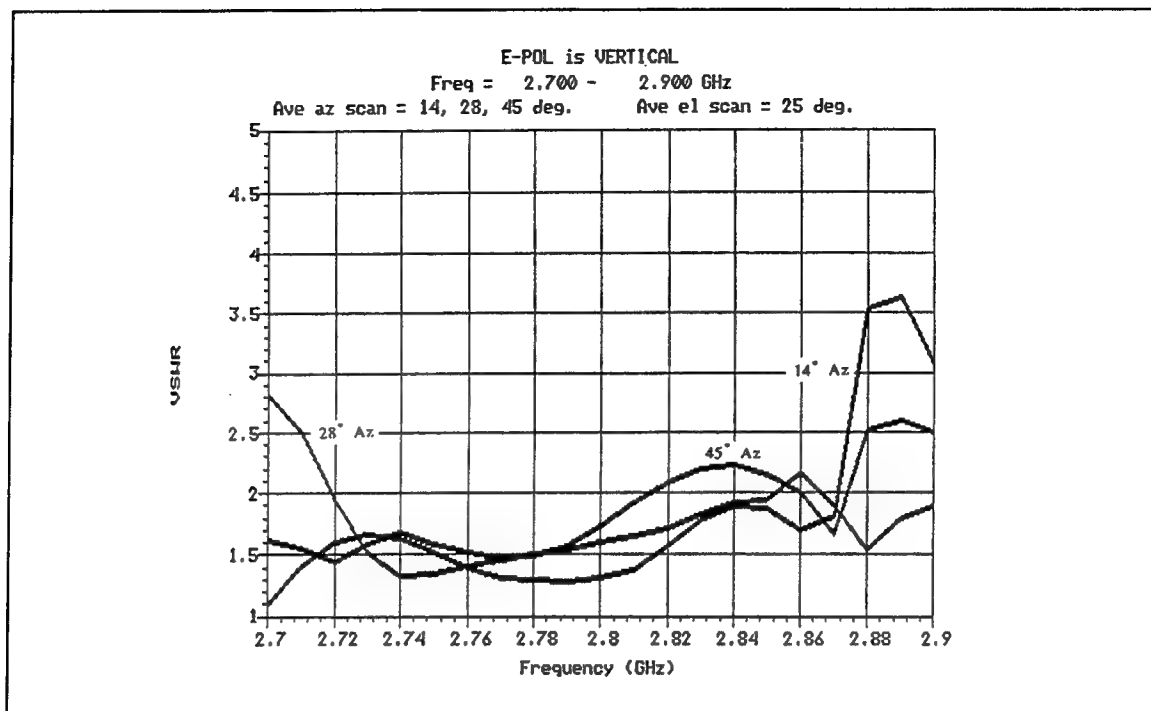


Figure 4-4b) Vertical Polarized S-Band Measured Impedance Match

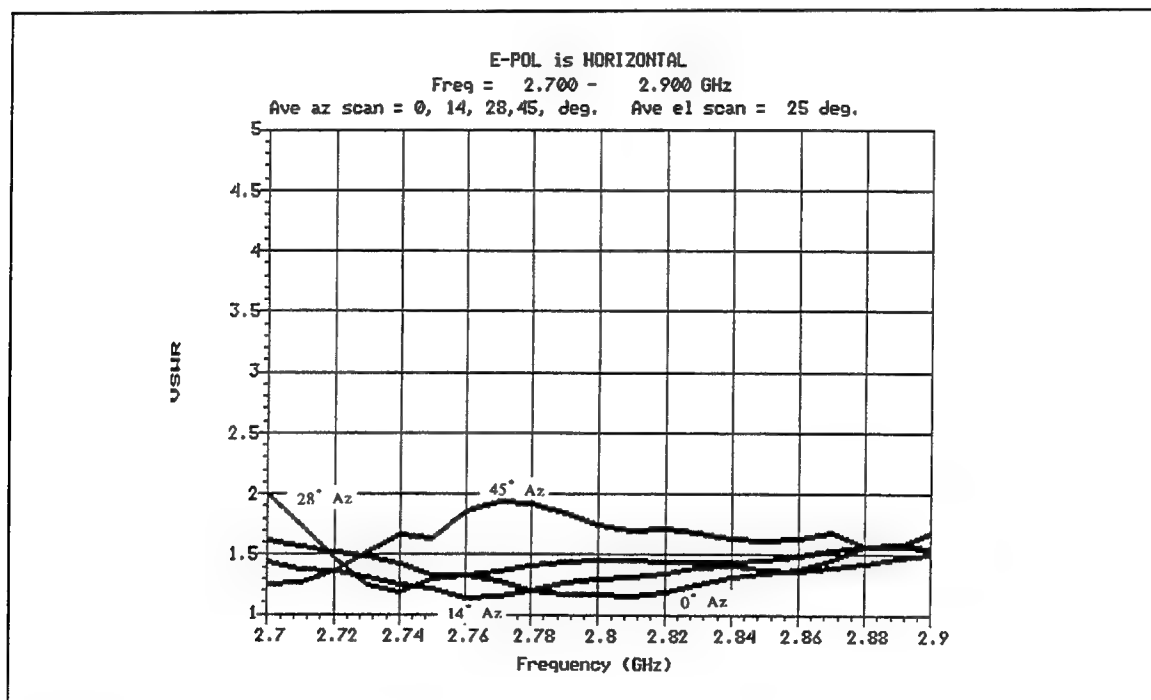


Figure 4-5 Horizontal Polarized S-Band Measured Impedance Match

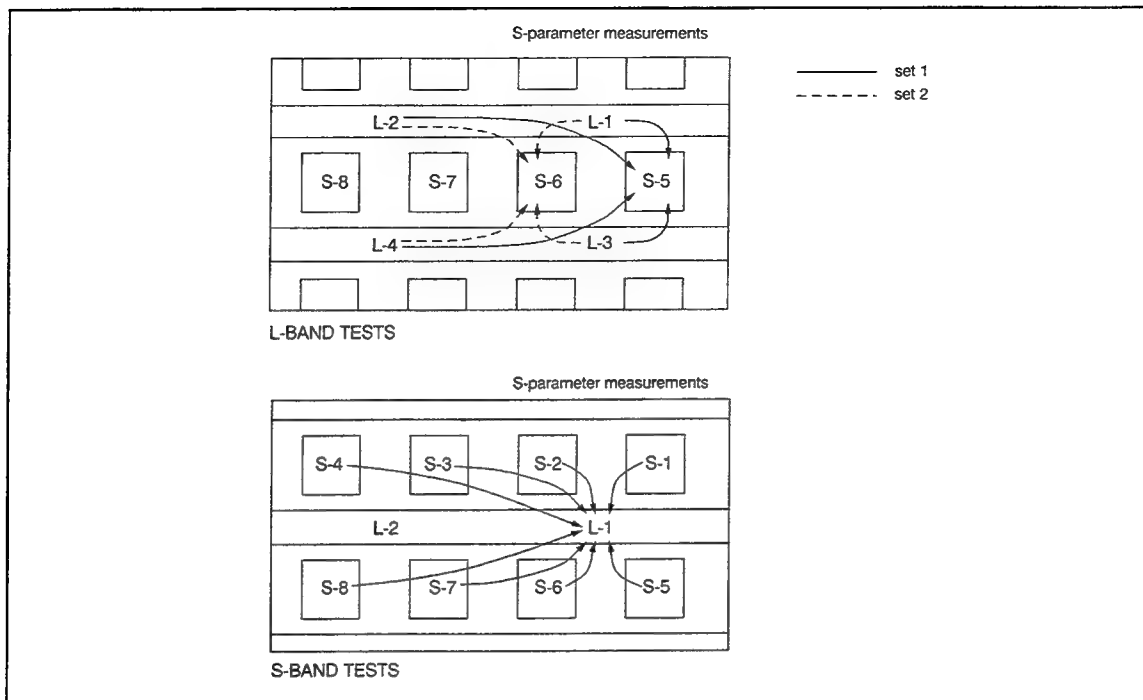


Figure 4-6 Summary Of Isolation Measurements

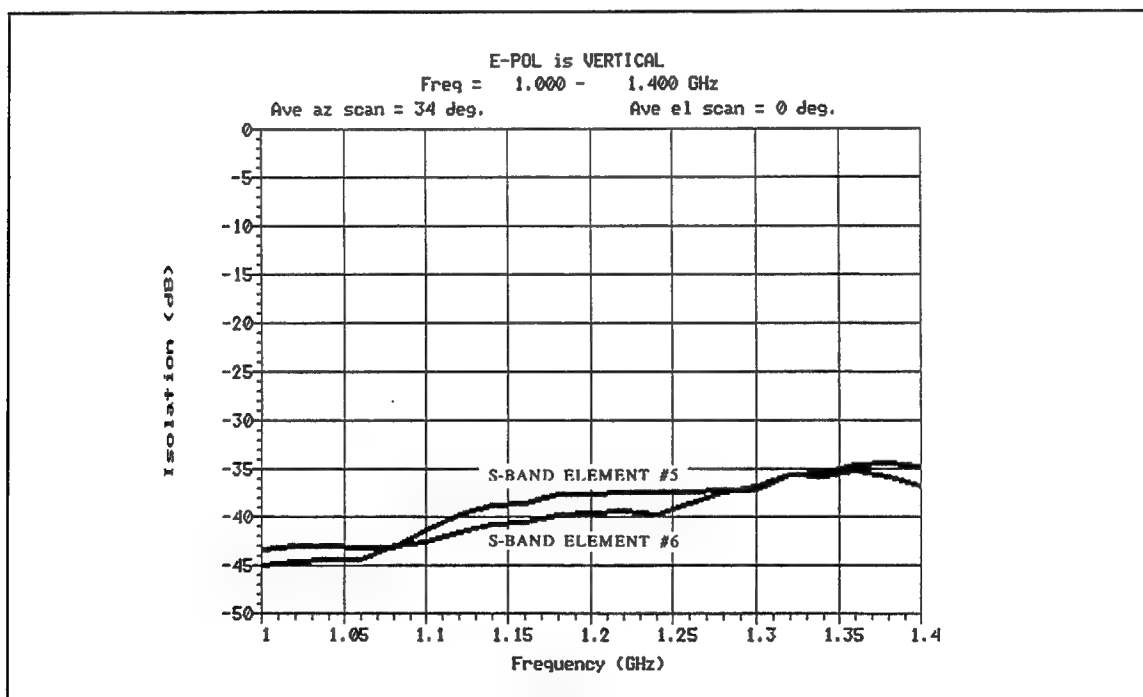


Figure 4-7 Measured Isolation From L-Band To V-Pol S-Band

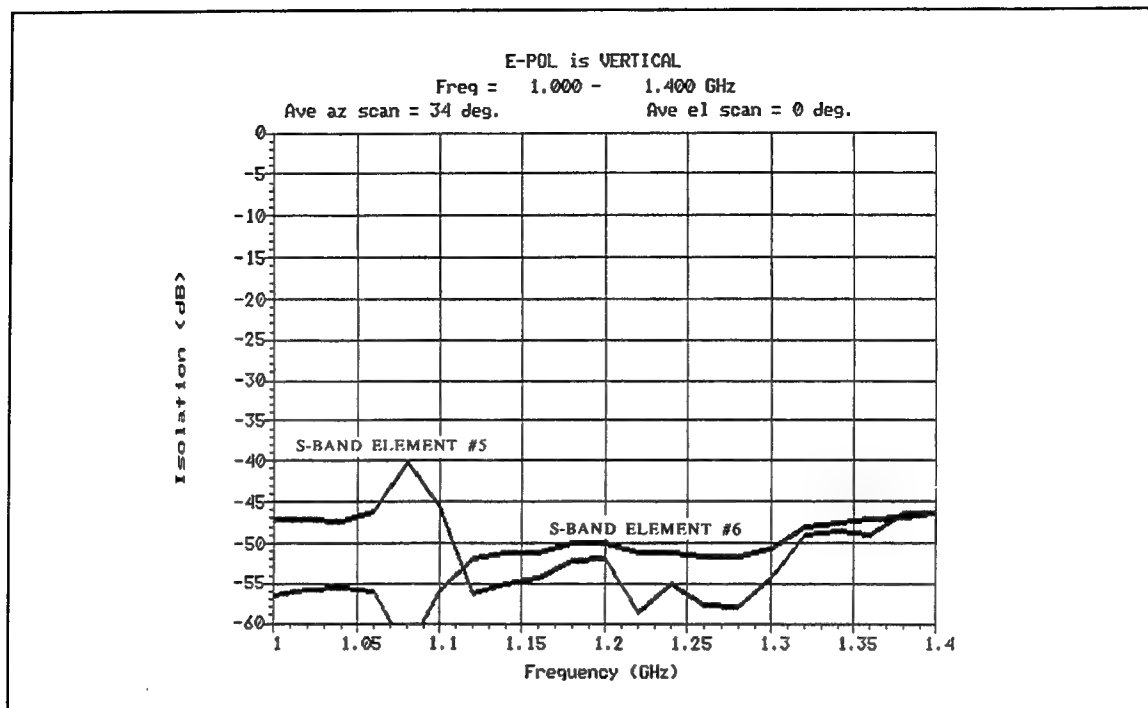


Figure 4-8 Measured Isolation From L-Band To H-Pol S-Band

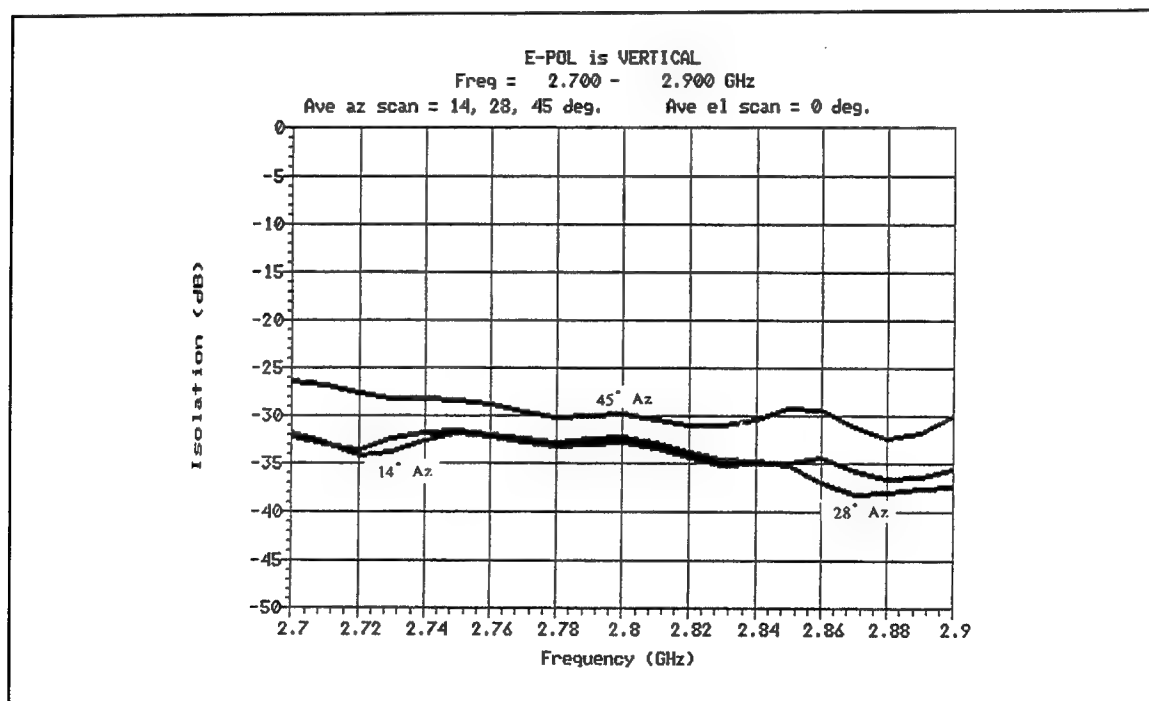


Figure 4-9 Measured Isolation From V-Pol S-Band To L-Band



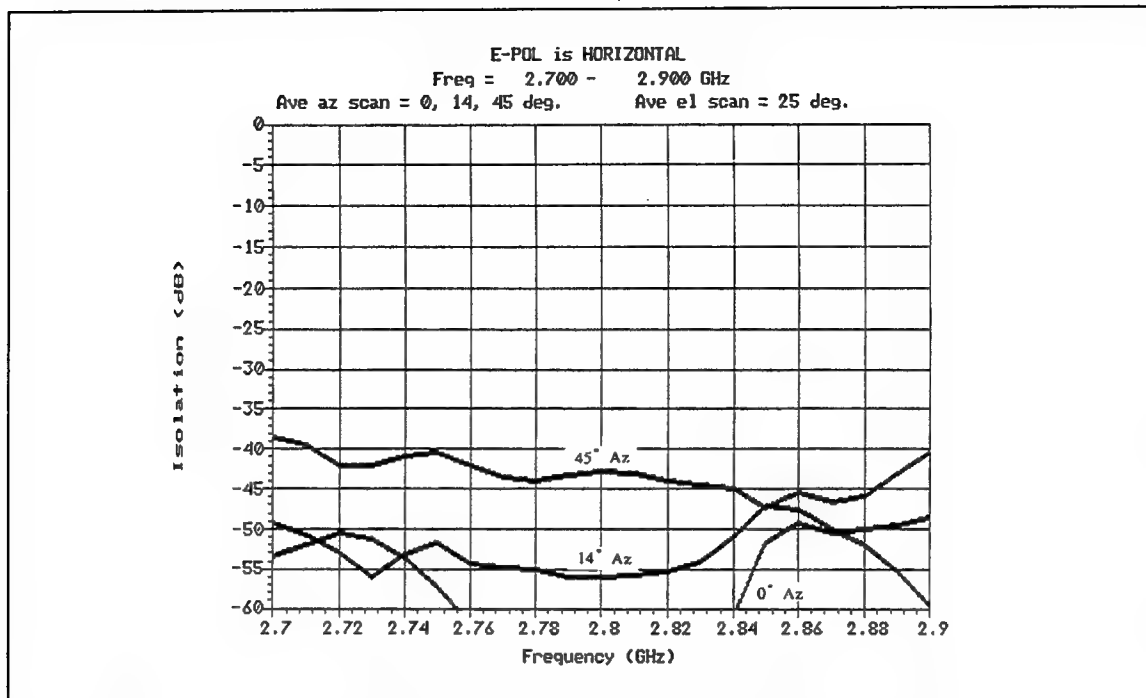


Figure 4-10

Measured Isolation From H-Pol S-Band To L-Band

## WIDEBAND PHASED ARRAY FOR IONOSPHERIC RESEARCH APPLICATIONS\*

Leon Susman, Paul Elliot, Vladimir Volman, Steve Carson, Peter Koert, James Cha

APTI+  
1250 24th St. NW, Suite 850  
Washington, DC 20037

**Abstract:** This paper describes the implementation studies and resulting design of an advanced high power HF transmitting array known as the Ionospheric Research Instrument (IRI). This array meets the requirements of the HF Active Auroral Research Program (HAARP), a program designed to study fundamental ionospheric physics by stimulating the ionosphere and via a variety of diagnostic instruments, measure its response.

The IRI surpasses the capabilities of existing HF facilities in its range of frequency coverage (2.8 to 10 MHz), its rapid scan capability (up to 30° off zenith), and its effective radiated power (86 to 97 dBW). Its overall flexibility is further enhanced by the range of modulation modes that can be accommodated (CW, AM, FM, pulse and biphasic). Real time amplitude and phase control across the 12 x 15 cross dipole array is achieved by the use of fiber optics links from a centralized control station to 30 transmitter shelters, each housing twelve 10 kW transmitters.

This paper discusses the array's expected performance based on NEC predictions of impedance, mutual coupling and element and array pattern behavior. Matching circuit considerations and phase correction techniques are discussed with special concern for improving low frequency performance. Finally, predicted performance is compared with results from measurements on a VHF scale model.

### 1. Introduction

The Ionospheric Research Instrument (IRI) is an HF transmitting array facility currently being constructed in the Gakona Alaska area as part of the HF Active Auroral Research Program (HAARP). This program will result in a World Class Ionospheric heater facility in the Auroral region, dedicated to the exploration of Ionospheric phenomena that can be induced by Ionospheric modification. The

---

\* Work performed under contract #N00014-92-C-0210 with the Office of Naval Research.

+ APTI, an E-Systems Company, was formerly ARCO Power Technologies, Inc.

requirements for the IRI were established during joint Office of Naval Research/Phillips Air Force Laboratory studies including preliminary tradeoff studies awarded to industry [1]. These requirements included the desire to cover the HF frequencies for which significant ionospheric heating could be achieved (namely 2.8 to 10 MHz), the requirement for rapid scan capability (without the generation of grating lobes), the need for high Effective Radiated Power (ERP up to 97 dBW), the need for polarization control of the radiated field, and the ability to radiate a variety of modulation waveforms. Instantaneous bandwidths up to 200 KHz were desired in the high power modes while still wider bandwidths in a low power mode were incorporated.

Figure 1 shows the layout of the IRI array. It is a 12x15 (180 elements) array on a 80 foot square lattice resulting in an effective antenna aperture area of 26 acres. Each antenna element is fabricated from tensioned wires, supported by one tower and four 6" diameter backbone elements. The element consists of two stacked broadband crossed grid dipoles, each grid dipole consisting of several wires arranged in a unique shape resembling a fan dipole. This element design was selected after a thorough analysis of alternatives, which considered multiple arrays, nested arrays, nested dipoles and caged dipoles, and wide biconical elements with folded stubs.

Figure 2 shows the predicted array ERP and beamwidth. Some of the unique features of this array are its high ERP (97 dBW), high power radiated (3.3 MW), very wide tunable impedance bandwidth of almost two octaves (2.8 to 10 MHz), while also providing wide scan capability over a conical region centered at zenith and extending 30 degrees from zenith in any azimuthal direction as shown in Figure 3, rapid scan capability, arbitrary polarization (any circular or linear polarization), low sidelobe and broad beam modes, high speed fiber optic phase control and data communication. The extremely stringent EMI objective, including -150 dBc from 88 to 200 MHz also posed unique design challenges. The mechanical design requirements were also difficult due to the array size and environmental specifications. The system is software expandable to provide pattern synthesis

capability.

Table 1 lists the sources of power loss. By far the largest source of loss is seen to be the mismatch loss, which justifies optimizing the radiating element and matching units for impedance bandwidth.

Table 1. RF Loss Budget

| Source of Loss                   | 2.8 MHz<br>Loss, dB | 10 MHz<br>Loss, dB |
|----------------------------------|---------------------|--------------------|
| Total Coax Length (175', 1-5/8") | 0.06                | 0.12               |
| Balun including Switch           | 0.07                | 0.13               |
| AMU including Switch             | 0.10                | 0.10               |
| Mismatch (Broadside: 2.2:1 VSWR) | 0.66                | 0.66               |
| Element Ohmic Loss               | 0.02                | 0.04               |
| Ground Screen Ohmic Loss         | 0.01                | 0.02               |
| Transmission thru Ground Screen  | <u>0.03</u>         | <u>0.28</u>        |
| Total Loss                       | 0.95                | 1.35               |

## 2. Array Design Approach using NEC

The array elements were designed using the Numerical Electromagnetic Code - NEC-4[2]. The NEC-4 computer models were run on SUN SparcStation 10, DEC Alpha, and other computers to predict the performance of the array. Various array sizes were computer modeled over an infinite ground plane by including different numbers of array elements. In addition to NEC predictions, the impedance performance was verified by measurements on a scale model array. The full size element performance will be verified by measurements on a smaller full scale version of the IRI, the Design Prototype (DP) array.

The element and array geometry was optimized to provide maximum performance for the normal mode of operation, a uniformly illuminated array with circular

polarization. The optimization concentrated on the performance of interior elements of the IRI array. The major performance parameter optimized was the active impedance bandwidth. The term "active" referring to the antenna load impedance with all the dipoles radiating. In addition another optimization objective was to provide smooth element pattern coverage over the scan region.

This optimization resulted in the element topology and dimensions, the square array lattice, and many other features of the antenna geometry. The optimization of the element and array was constrained by the presence of mutual coupling in the array which reduces the achievable bandwidth; the maximum element spacing which is limited by grating lobes; mechanical realizability and cost.

Each dipole is fed by its own transmitter as depicted in Figure 4. During operation of the array, the forward traveling RF wave amplitude and phase from each transmitter is prescribed by the central computer to provide the requested illumination taper, scan angle and polarization. Digital phase shifter within the transmitter and phase lock technology ensures that the prescribed forward wave is achieved. Due to mutual coupling, the active impedance and active reflection coefficient will be somewhat different for different tapers, scan angles and polarizations.

Figures 5, 6 and 7 show the active impedance calculated using NEC-4 at the terminals of an interior dipole of the array for uniform illumination, circular polarization. Figure 5 shows the active impedances for broadside which is the beam direction for which the greatest ERP is desired. Figures 6 and 7 show the impedances at maximum scan as well as broadside at the top and bottom frequency in each band. It is seen that the active impedances vary with frequency and scan direction. They also vary with dipole location in the array, illumination function (sidelobe taper, polarization, etc.), and of course array geometry. These dipole impedances will be matched using two circuits: a passive antenna matching unit (AMU) located near the feed point of each dipole, and a tuning circuit at each transmitter which can be autotuned or preset.

## 2.1 Radiation Patterns

Figures 8 through 11 show radiation patterns for individual dipoles and for the full IRI array. The patterns show good coverage over the scan volume and low power radiated towards horizon which reduces possible EMI. The phase patterns are also predicted with NEC which will be useful in phasing the array to compensate for different dipole phase patterns.

All sources of amplitude and phase error in the excitation and pattern of each dipole at the fundamental frequency of operation were analyzed and an error allocated to each in a detailed RF error budget. A correlation cell size was estimated for each error. Errors which are uncorrelated between elements have the least impact on performance, while those which are correlated over a large number of elements have an increased impact and need to be kept small. A correlated error could result from errors applied to all transmitters in one or more shelters. The distribution function of each error was also estimated so that the errors could be converted to rms values.

These errors effect the array pattern including sidelobes, gain, cross-polarization, ERP, and beam pointing angle, as shown in Tables 2, 3 and 4. The errors and their effect on pattern performance are random and are therefore statistically described. Table 2 is calculated at 10 MHz for a broadside main beam. The dynamic range of the transmitter control may limit realizability of low sidelobe tapers. Far away sidelobes are -40 dB or less for all cases in Table 2. NEC error is assumed correlated over 1/10 of array due to symmetry.

The IRI specification is to provide -20 dB cross-polarization level, and a -30 dB maximum sidelobe level for the low sidelobe mode when the main beam is at zenith. Due to the tolerance errors the sidelobe specification is more difficult to meet than the cross-polarization specification.

For an error of  $\pm 5^\circ$  in the NEC prediction of the phase pattern, the cross-polarization requirement of -20 dB would be met by 99.9% of main beams formed,

and the low sidelobe requirement of -30 dB would be met by 68% of beams formed. For NEC phase pattern error of  $\pm 10^\circ$  the cross-polarization requirement of -20 dB would be met by 97.4% of main beams formed and the low sidelobe requirement of -30 dB met by 33% of beams formed. It is therefore desirable to limit the NEC phase error to  $\pm 5^\circ$  if achievable.

Table 2. Effect of Random Errors on IRI Sidelobe Levels During Low Sidelobe Operation

| Loss                               | Taylor Taper Required to meet -30 dB Sidelobe (Spec. with 95% Probability) | Approximate ERP Loss |
|------------------------------------|--|----------------------|
| Without Errors:                    | 30 dB Taper  | -7.5 dB              |
| With $5^\circ$ NEC Error, no ice:  | 36 dB Taper  | -9 dB                |
| With $10^\circ$ NEC Error, no ice: | 42 dB Taper  | -10 dB               |
| With $10^\circ$ NEC Error and ice: | 44 dB Taper  | -10.5 dB             |

Table 3. Effect of Random Errors on IRI Sidelobe Levels for Uniform Illumination (Percentiles shown are fraction of sidelobes expected to be better than level shown)

| Expected Peak Sidelobe Levels (dB) |       |       |       |       |       |
|------------------------------------|-------|-------|-------|-------|-------|
|                                    | 1st   | 2nd   | 3rd   | 4th   | Far   |
| With No Errors:                    |       |       |       |       |       |
| 100%:                              | -13.2 | -17.5 | -20.1 | -21.8 | -25   |
| With Error Budget:                 |       |       |       |       |       |
| 50 %                               | -13.1 | -17.4 | -20.1 | -21.8 | -25   |
| 95 %                               | -11.5 | -15.7 | -18.7 | -20.8 | -24.4 |

Table 4. Approximate Polarization, ERP Loss and Beam Pointing Error Due to Random Errors

| Pattern Feature         | Error Level | % of Beams at or better |
|-------------------------|-------------|-------------------------|
| Main Beam Xpol / Copol  |             |                         |
| Broadside & Diagonals   | -26 dB      | 68 %                    |
| Parallel to Dipole Axes | -23 dB      | 68 %                    |
| ERP Loss                | 0.08 dB     | 50 %                    |
| Beam Pointing Error     | 0.1 degrees | 50 %                    |

## 2.2 RF Radiation Exposure

The RF radiation exposure due to the IRI was calculated using NEC and other computer models. Table 5 lists the required and predicted exposure levels. The field intensities near ground level meet existing U.S. Government standards outside the exclusion fence which surrounds the array. Field calculations over the array confirms the need for an aircraft warning radar with a cone of coverage +/- 45° from zenith for both the Design Prototype (DP) array and the IRI.

Table 5. RF Radiation Exposure for IRI

| <u>Hazard</u>        | <u>Requirement</u>         | <u>Predicted Performance</u>                      |
|----------------------|----------------------------|---|
| Personnel Safety     | 1 mW/cm.sq. (6 min. ave)   | <1 mW/cm <sup>2</sup> outside fence<br><15' high  |
| Fueling              | 5000 mW/cm.sq.             | < 3 mW/cm <sup>2</sup> at all points<br><15' high |
| EED                  | 0.001 mW/cm.sq. at 2 miles | < 0.001 mW/cm <sup>2</sup> at 2 mi.,<br><15' high |
| Cardiac Pacemakers   | 200 V/m                    | < 60 V/m outside fence &<br>< 15' high            |
| In-Band EMI/RFI      | "no problems at > 1 mile"  | < 0.025 mW/cm <sup>2</sup> at<br>ground level     |
| Out-of-Band EMI/RFI  | FCC, NTIA requirements     | Expected to meet require-<br>ment                 |
| Aircraft Electronics | Automatic Shutdown         | Handled by aircraft alert<br>radar                |



### 3. The AMU Design

One of the critical system interfaces for the HAARP IRI array is the interface between the antennas and the transmitters. Continental Electronics, Inc. has developed a tube based transmitter with variable tuning elements that can accommodate a wide VSWR range. However, because of the 3.5:1 operating bandwidth of the IRI array and the scan requirements, the VSWR range that can be tolerated by the transmitter is not adequate to supply power directly to the antennas under all operating conditions.

Antenna Matching Units (AMU) have been developed to alleviate this problem. The AMUs are connected at the antenna terminals in cascade between the transmitter and the antenna, and their function is to reduce the average VSWR at the output terminals of the transmitter. The AMU contains only fixed inductors and capacitors, therefore its impedance is a function of frequency alone.

The active impedance of the  $i^{\text{th}}$  antenna in the array is the ratio of the total voltage to the total current at the input to the  $i^{\text{th}}$  antenna. The active impedance seen looking into the  $i^{\text{th}}$  terminals of an  $N$  element antenna array is given by

$$Z_{a, i} = Z_{l, i} \frac{I_l}{I_i} + \dots + Z_{i, i} + \dots + Z_{N, i} \frac{I_N}{I_i} \quad (1)$$

where  $Z_{ij}$  the mutual impedance between ports  $i$  and  $j$ . The dependence of the active impedance on the exciting current implies that the active impedance is a function of scan angle ( $\theta, \phi$  in spherical coordinates), frequency, and array taper. The antenna matching units have been designed to match to an average impedance  $Z_m$  to minimize the swing in VSWR as a function of scan angle. The minimization of the mean square change in impedance for an assumed illumination can be formulated as:

$$\min \left( \sum_{i=1}^X \sum_{k=1}^Y (Z_a (\Theta_k, \phi_k, f_i) - Z_m (f_i))^2 \right) \quad (2)$$

which results in:

$$Z_m (f_i) = \frac{1}{Y} \sum_{k=1}^Y Z_a (\Theta_k, \phi_k, f_i) \quad (3)$$

The IRI antenna element requires a balanced feed, therefore, the AMU was implemented in balanced line, and was driven by the transmitter through a 2:1 balun. Two AMUs were designed, one each for the high and low band antennas, using a symmetric circuit model, so the circuit diagrams for these AMUs represent one half of the AMU circuit. The number of circuit elements in the AMUs were determined by trading off the increased cost, complexity and loss in the AMU against its matching performance. The circuit topologies for the high and low band AMUs are shown in Figure 12.

In the circuit simulation, the AMU was excited by a 50 Ohm generator, representing half of the 100 Ohm impedance of the balun, and the AMU was terminated in one half of the calculated mean active impedance as a function of frequency. The scanned impedances were calculated for the center element and a corner element of a 10 x 10 array using data from the NEC4. These calculations assumed a uniform illumination of the array.

The low band impedance data was averaged over 0 to 30 degrees off zenith and a full 360 degrees in azimuth. The high band impedance data was averaged over the entire scan volume required, as the maximum off zenith scan for the IRI decreases from 30 degrees at 8 MHz to 10 degrees at 10 MHz as shown in Figure 3. Figure 13 shows the VSWR performance of the two AMUs into the average active antenna impedance for a central element in the array. The average performance of both the high and low band AMUs reduces the input VSWR for the central antenna elements below 2.2, the level where the IRI transmitter can delivery full power into the load. The transmitter provides graceful degradation of power delivered into higher

VSWRs.

#### **4. Low Frequency Coupling Effects**

Analysis of the active impedance effects in arrays of closely spaced elements, (relative to a wavelength) reveals some unexpected features during low frequency operation of this array. Negative active impedance effects are found to exist for some excitations in the low frequency region of the IRI system, particularly in the peripheral elements, when extreme scan is attempted. The root cause of these effects has been identified. Studies demonstrate the dependence on local mutual coupling effects and lead to effective techniques to circumvent their influence. The negative impedance effects can be eliminated, with minimum impact on pattern performance, by phase perturbing the excitation of only a few antenna elements.

NEC calculations of the IRI array with more than 36 elements (6 x 6 array) has shown that at low frequency the essential mutual coupling has a local character. It is thus sufficient to take into account the mutual couplings between nearby elements. The following conclusions can be drawn from this data at low frequencies.

The strongest mutual couplings takes place between the collinear elements. The character of these couplings are close to static, i.e. they are proportional to  $r^{-2}$  and  $r^{-3}$ , where  $r$  is the distance between the elements.

For the same frequency, the mutual coupling values are practically independent of the excited element's position. For example, at 2.8 MHz, the mutual couplings between any excited element and the nearest collinear neighbor are -17 dB. The same is true for the middle and corner elements. Similar results are obtained for all other frequencies.

For low frequencies (<4 MHz) the nearest collinear elements have maximum effect on the active impedance. For frequencies close to 7 MHz, the nearest coplanar and collinear elements exercise almost equal effect on the active

impedance.

It can be shown that the collinear element excites in its nearest element, a current of the same direction as the driving current. Therefore, the net current in the nearest element increases resulting in a decrease of the active impedance. This effect is dominant in the corner and boundary elements of the array where a negative active impedance can result.

#### **4.1 Correction of the Negative Active Impedance**

The reflected waves in the feedline connected to each dipole are the superposition of two waves traveling toward the transmitter. One of them is the reflection from the dipole input, and the second is the wave received by this dipole because of the mutual coupling from the other dipoles in the array. In some cases, the total reflected wave magnitude can be more than the incident wave magnitude and the active resistance of this dipole becomes negative.

The fact that the reflected wave is the superposition of the two waves suggests a quite simple and effective method for removing the negative resistance. The idea is to introduce an additional phase shift in the forward wave such that the summation of the two reverse waves yields a larger positive active input resistance.

To be useful, the required phase correction of the boundary element excitation (beyond that needed to scan the array) must have negligible influence on the antenna pattern. When this correction is applied to the boundary and nearest boundary elements, it is expected that the sidelobe level will increase and the field nulls will fill. NEC was used to evaluate all these changes for a complex array with numerous and strong mutual couplings. This problem is complicated by the fact that phase correction of any element influences the active impedance of the neighboring elements. The only way to approach this problem is as a numerical simulation including NEC.

The efficacy of this technique is shown in Figures 14 and 15, which show the effect of a perturbation in the phase excitation of the corner and peripheral elements of a 6x6 array. These results are computed for a full model of the IRI element operating at 2.8 MHz, and scanned up to 30° in the elevation plane. Notice that for modest scan angles the active resistance of the elements are small, but positive. As the scan angle off broadside is increased, the resistance can become negative if the phase correction excitation is not applied. The phase correction needed to return to positive active impedances is modest. It has been verified that the introduction of this phase deviation has a negligible effect on the expected antenna pattern.

### **5. Scale Model Measured and Predicted Results**

The antenna array design for HAARP has relied on the use of NEC for the evaluation of expected performance. The accuracy of these codes is affected by the fineness to which the physical design can be modeled and the limitation of computer resources. To validate the NEC computer model a scale model measurement program was initiated. Extensive S-parameter measurements were performed on a 1/20th scale model for various array sizes (1x1 to 7x7). Sufficient self impedance and mutual impedance measurements were taken to fill the scattering matrix for the array size. For a 7x7 cross polarized dipole array the corresponding matrix size is 98x98. The active impedance for each antenna - i.e., for a given excitation of all the other antennas, can be calculated from this matrix.

Antenna Products, Inc. of Mineral Wells, Texas, the subcontractor responsible for the IRI antenna fabrication, manufactured the 1/20 scale models based on the APTI design of the full IRI antenna system. The antennas were positioned on a seven feet high platform covered by a wire grid ground screen. The raised platform allowed access to the measurement system. In addition to the IRI 1/20 scale model antenna array, standard dipoles were constructed to verify the calibration system.

Independent measurement of all the coupling in the 7x7 array would be excessive, taking over a month. However, since coupling between the more distant elements is negligible, measurement time could be reduced significantly by omitting them. In

addition, it was not necessary to measure some array elements because of symmetry.

The assumption that coupling between elements more than three elements apart could be ignored was confirmed in sample measurements. Figures 16 through 19 illustrate this by showing the spacing dependence of mutual coupling between the corner elements and various others. These figures show the  $S_{12}$  terms from the corner dipoles to  $S_{12}$  other dipoles along the side and on the diagonal for both the low and high bands. The reduction in coupling with distance is also seen to be sufficient to ensure the convergence of the active impedance summation with increasing array size. The two cases plotted (side parallel and diagonal orthogonal) are the best and worst cases in terms of agreement between NEC4 and measurements. Similar plots for the collinear dipoles along the side and the parallel dipoles on the diagonal are intermediate in accuracy.

The comparison with NEC showed certain consistent trends, namely: better agreement for small rather than larger arrays, better agreement for  $S_{12}$  coupling terms than for the  $S_{11}$  self impedance for the most part, and better agreement for  $S_{12}$  between dipoles in the same row or column than between dipoles on the diagonal, and very poor agreement for coupling below about -40 dB due to noise.

Figures 20 through 23 show broadside active impedances for the corner and center elements of the 7x7 array. Surprisingly, the agreement with NEC4 (which assumes an infinite conducting ground screen) for the corner element does not seem to be adversely affected by the nearby truncation of the ground screen in the scale model. Figure 24 shows low band impedances for the central element if the array were scanning a conical pattern at a constant 30 degrees off zenith over all azimuth angles. Figure 25 shows the same for the high band with theta equal to 30 degrees at 7 MHz and 10 degrees at 10 MHz. Agreement with measurement about the same as for broadside. The high band agreement for the most part is not as good as for the low band.

This paper shows results for the 7x7 scale model array. Smaller array sizes were

also measured and the comparison with NEC4 is even closer for the smaller arrays. Additional details on the scale model results have been given in the references [3][4].

## **6. Conclusions**

This paper describes the design and analysis that has been conducted in developing an antenna system capable of meeting the HAARP requirements. The requirements can be met in a single array of stacked cross-dipole elements dividing the 2.8 to 10 MHz band into manageable bands. For each band a separate antenna matching unit has been developed capable of producing reasonable VSWR to the transmitters. In the low frequency region, techniques to increase the active input resistance and prevent negative impedance effects were developed. The design and trade studies have relied heavily on the use of NEC4 to evaluate performance. In addition, extensive S-parameter measurements on a 1/20 scale model have confirmed the computational data. Further support for the IRI design will be generated during the upcoming demonstration prototype tests on a small subset of the IRI. These tests are scheduled to begin October, 1994.

## **7. Acknowledgments**

The contributions of Richard Groff and Thomas Collins of Penn State University in supporting the NEC calculations and the Scale Model Program is acknowledged. In addition, the authors wish to acknowledge the valuable guidance and suggestions from Mr. Ed Kennedy and Dr. Adrian Eley of the Naval Research Laboratory and from Peter Franchi of the Rome Air Development Center, during the course of this contract. In addition, the contributions of Dr. John Allen and Prof. Walter K. Kahn, who have acted as consultants to this project from its conception are gratefully acknowledged.

## **8. References**

[1] "HAARP Phase I Design Tradeoff Studies", ARCO Power Technologies, Inc. Technical Report 5006 on contract N0014-91-C-0023, Office of Naval Research, 30 May, 1991.

[2] "Numerical Electrical Code - NEC4 Method of Moments", Gerald Burke, Lawrence Livermore National Laboratory Report UCRL-MA-109338, January, 1992.

[3] "HAARP 1/20 Scale Model Measurement Program Test Results", ARCO Power Technologies, Inc. Report, 1250 24th Street, NW, Suite 850, Washington, DC 20037, 9 March 1994.

[4] P. Elliot, P. Koert, J. Cha, R. Groff, and T. Collins, "Computation of Phased Array Active Impedances and Comparison with Measurements," 10th Annual Review of Progress in Applied Computational Electromagnetics, Monterey, CA, March, 1994.



## IRI Array

30 Transmitter Shelters  
Each Containing 6 Dual 10 kW Transmitters

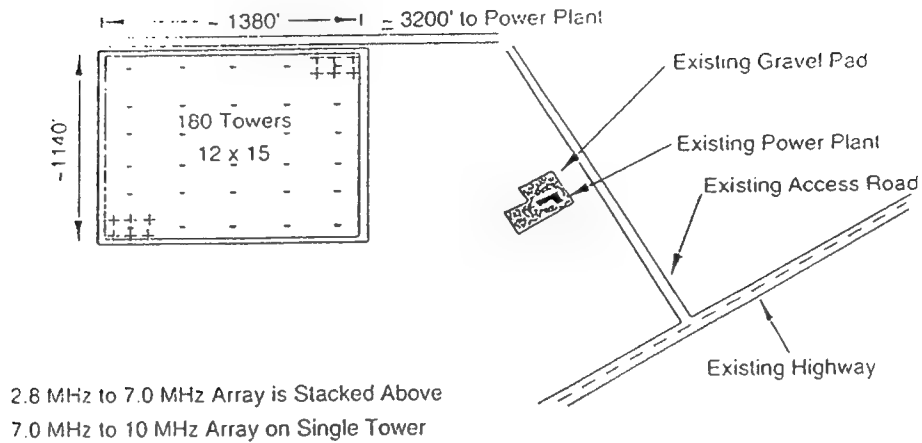


Figure 1.

## IRI Performance

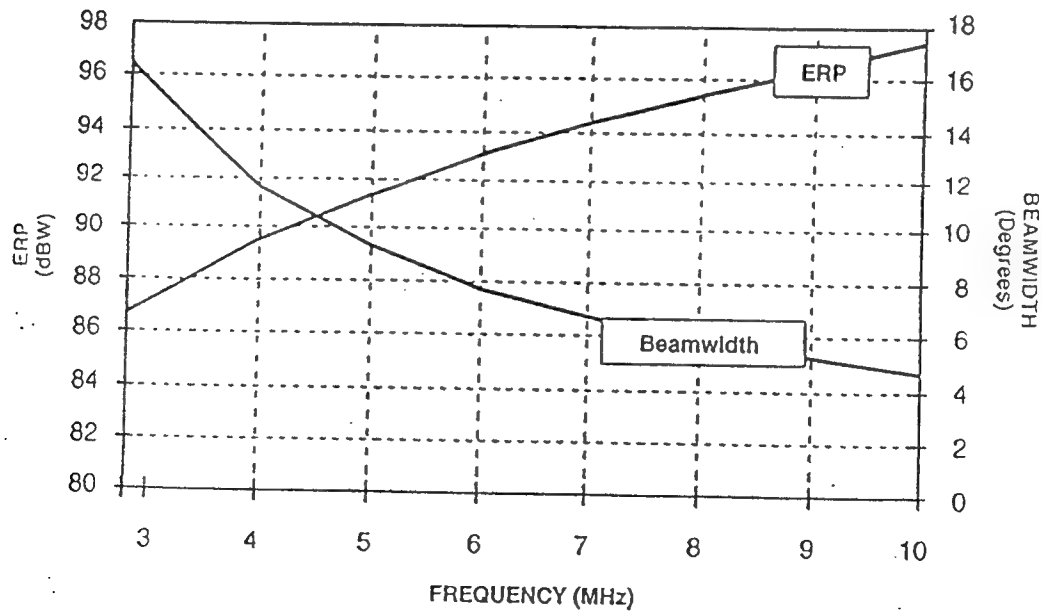


Figure 2.

## Slew Capability in all Directions from Zenith

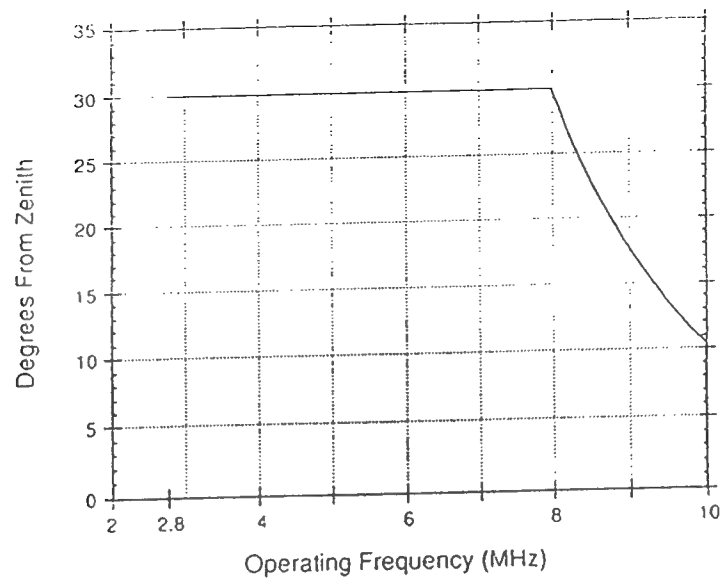


Figure 3.

## Array Excitations with Location in Feed

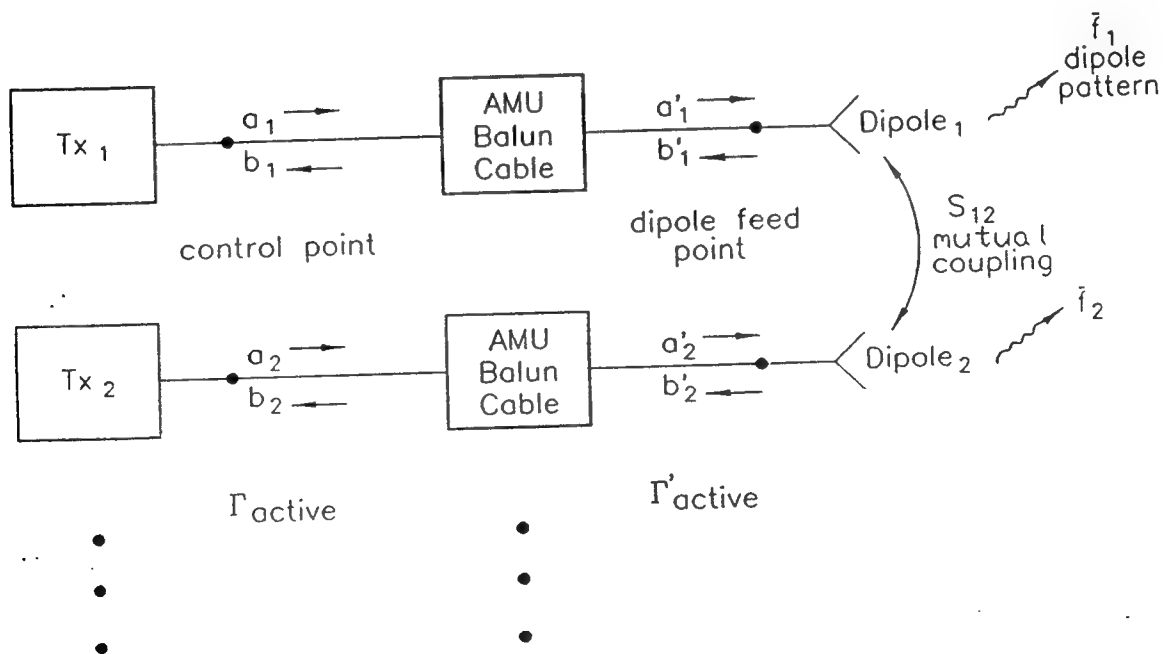


Figure 4.

### Broadside Active Impedance for Central Element

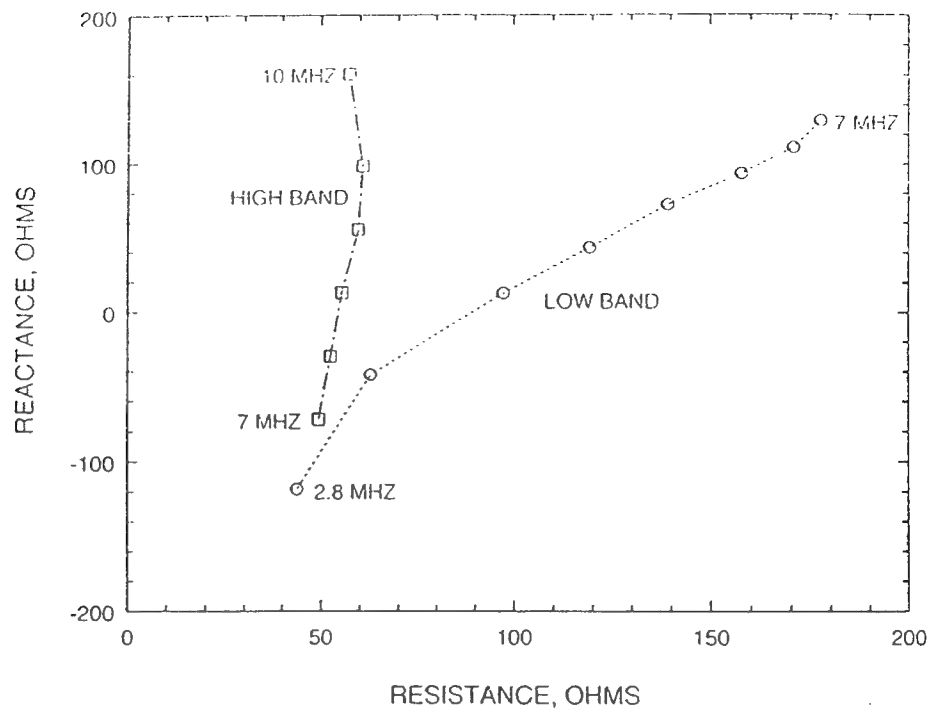


Figure 5.

### Active Impedance for Central Element High Band Top and Bottom Frequency Broadside and Max Scan Off Zenith for all Azimuth

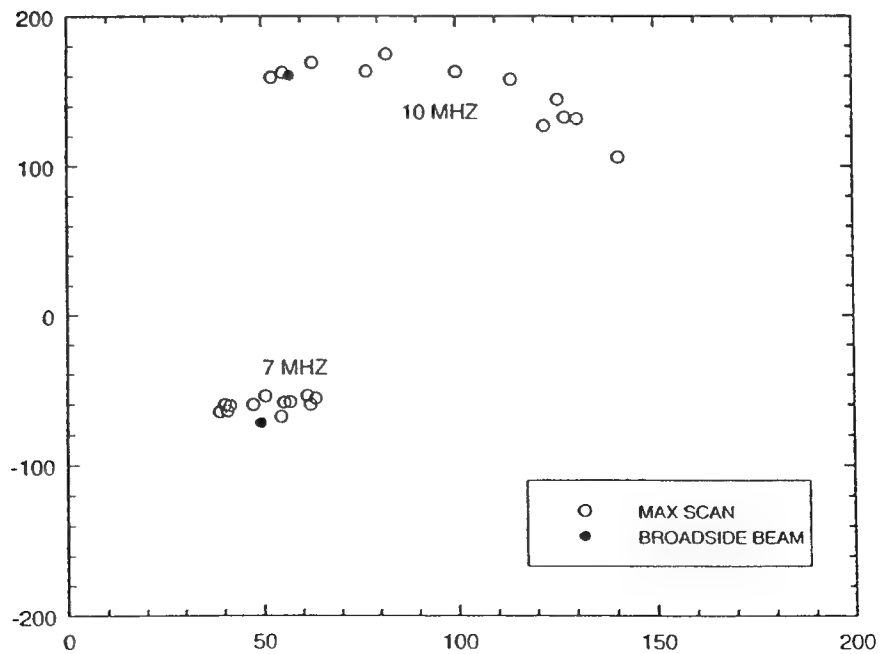


Figure 6.

Active Impedance for Central Element Low Band  
Top and Bottom Frequency  
Broadside and Max Scan Off Zenith for all Azimuth

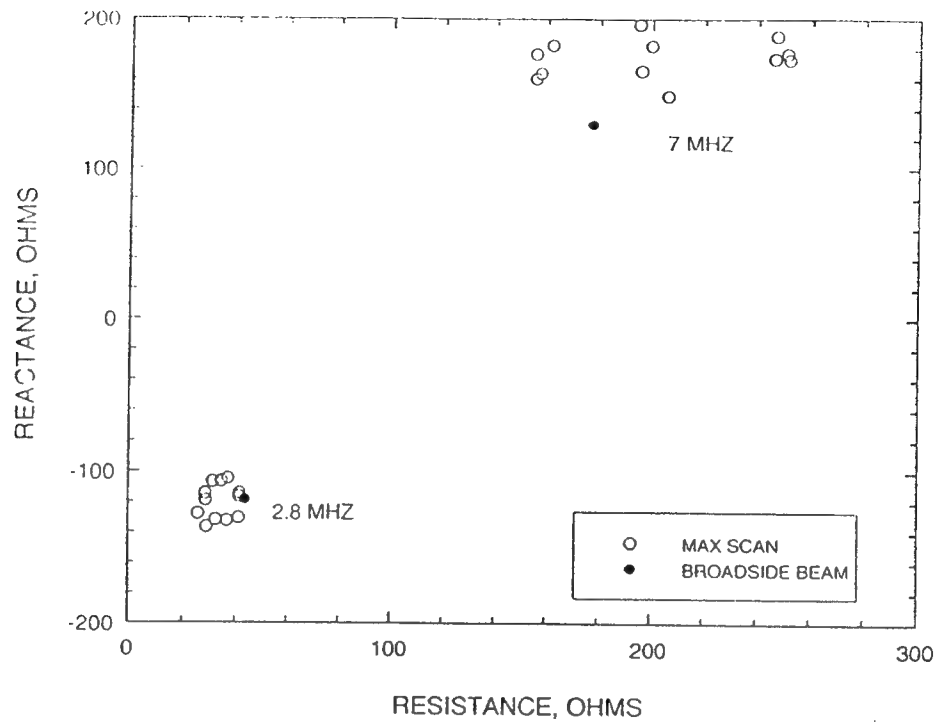


Figure 7.

2.8 MHz Low Band Center Dipole Pattern in 7x7 Array

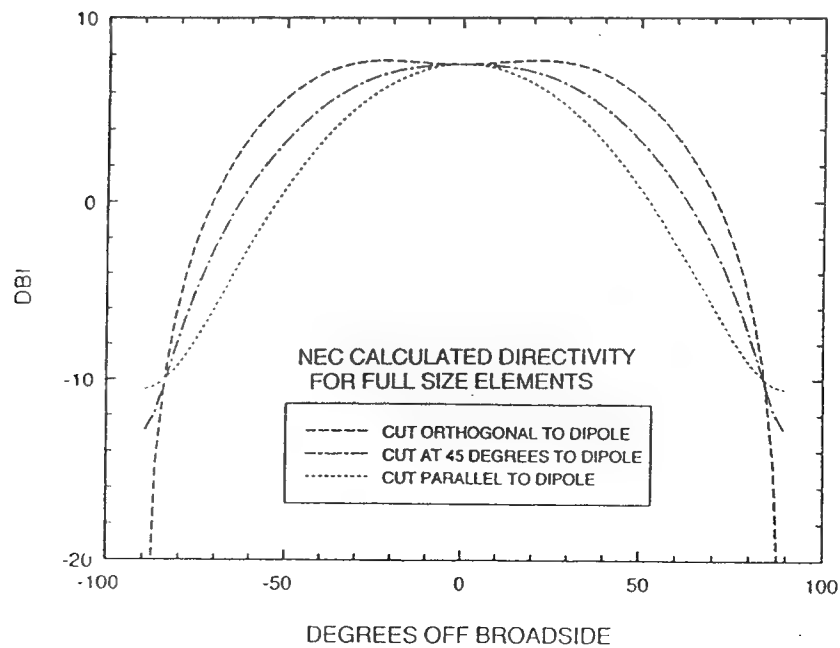


Figure 8.

# 10 MHz High Band Center Dipole Pattern in 7x7 Array

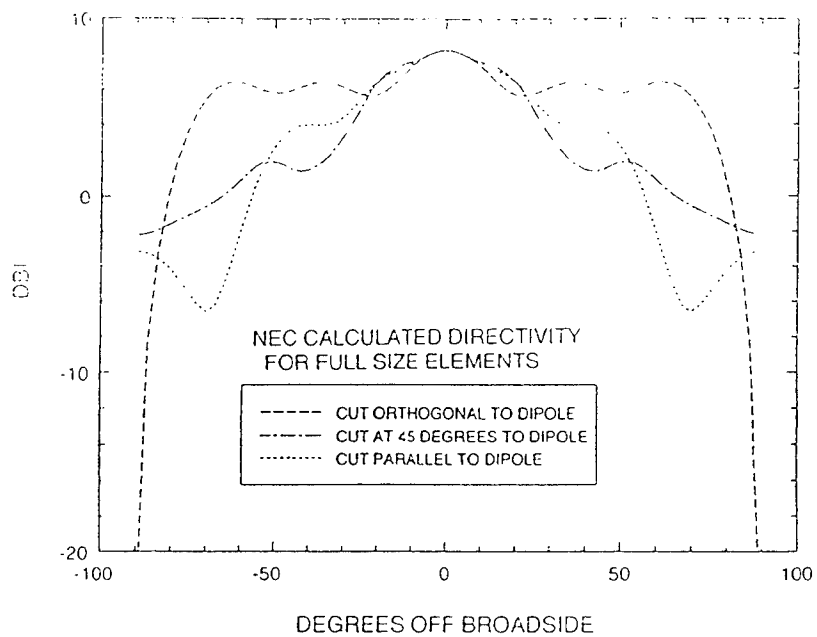


Figure 9.

## 12x14 Array Pattern at 2.8 MHz Using NEC Element Patterns Scanned to Theta, 30, Phi = 0 Circular Polarization

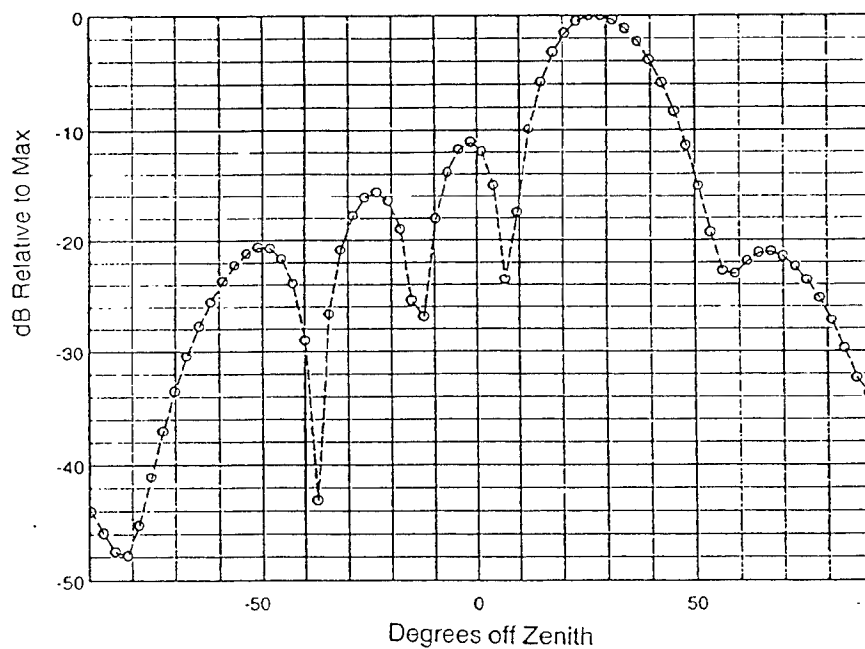


Figure 10.

12x14 Array Pattern at 2.8 MHz  
Using NEC Element Patterns  
Scanned to Theta, 30, Phi = 45 Circular Polarization

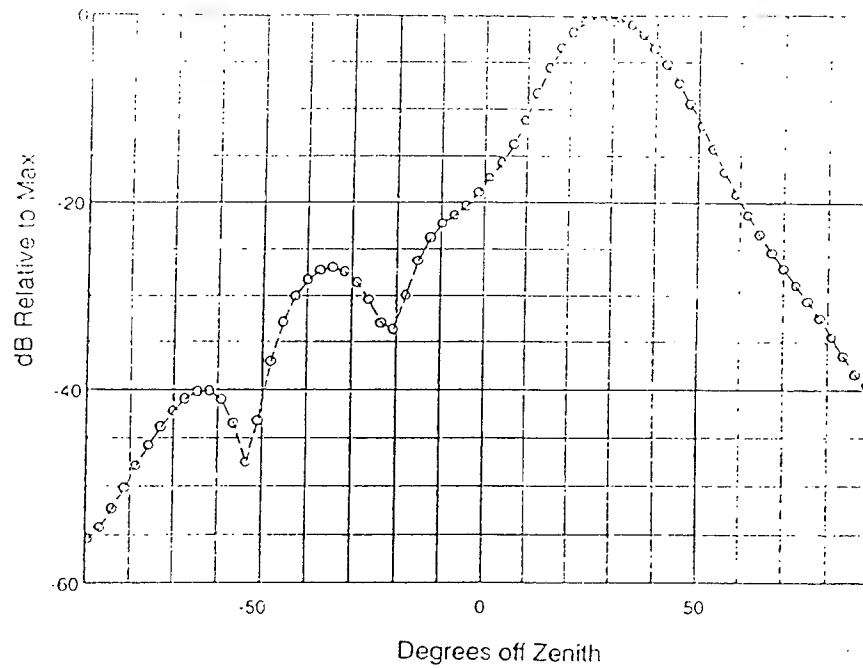


Figure 11.

Circuit Topologies for the High and Low Band AMUs

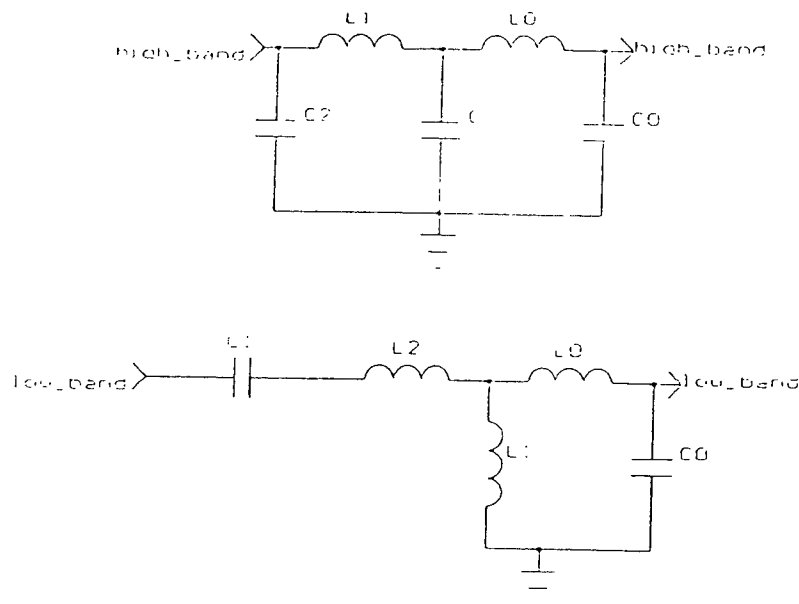
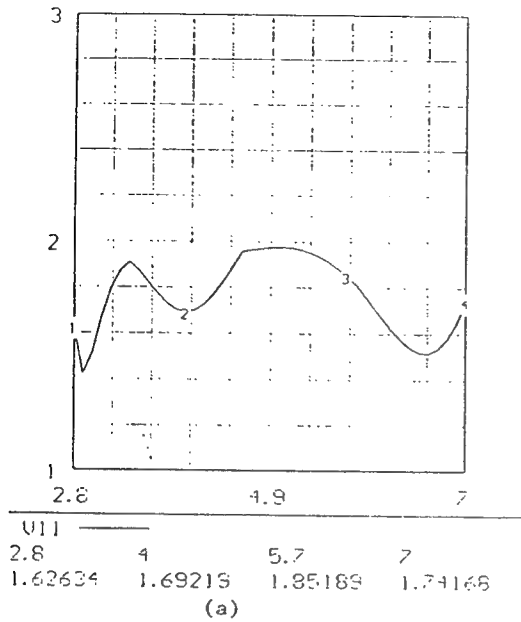


Figure 12.

Input VSWR Performance for the Low Band AMU



Input VSWR Performance for the High Band AMU

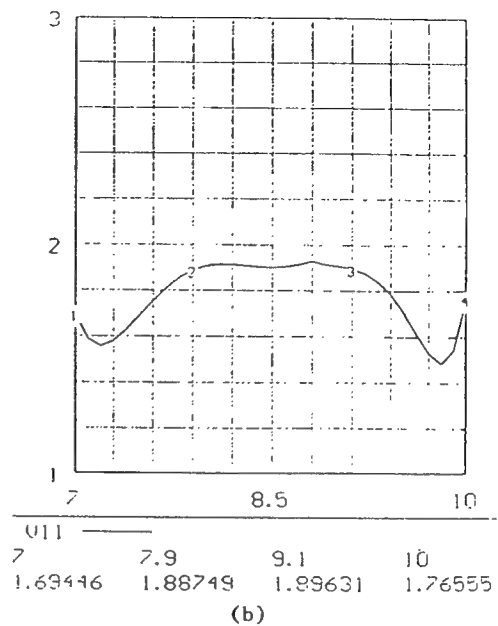


Figure 13.

Phase Perturbation Technique  
6x6 Array 2.8 MHz  $\Phi = 0^\circ$   
Corner Element

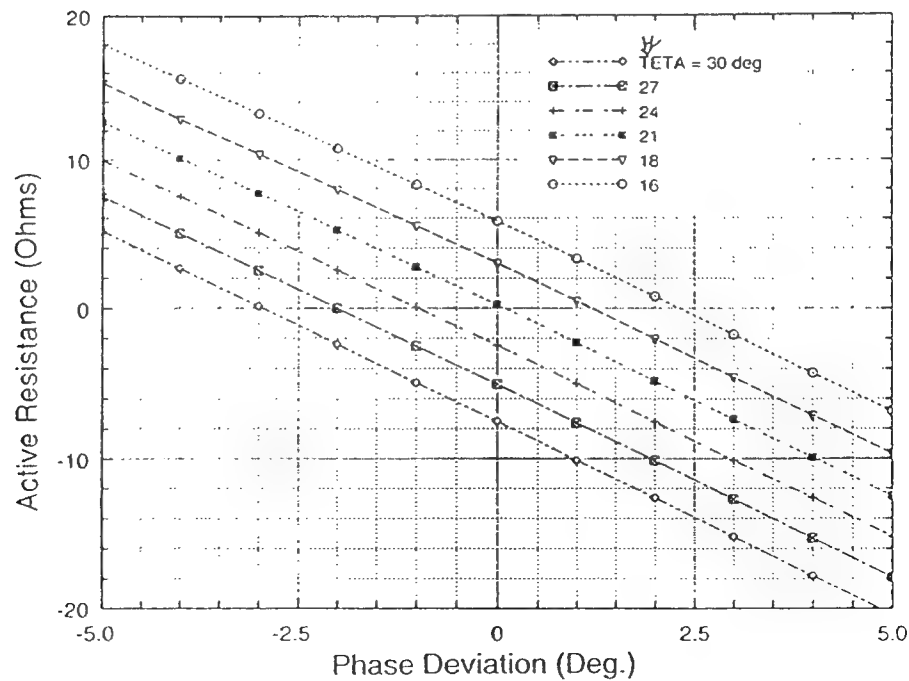


Figure 14.

Phase Perturbation Technique  
6x6 Array 2.8 MHz  $\Phi = 0^\circ$   
Perimeter Element

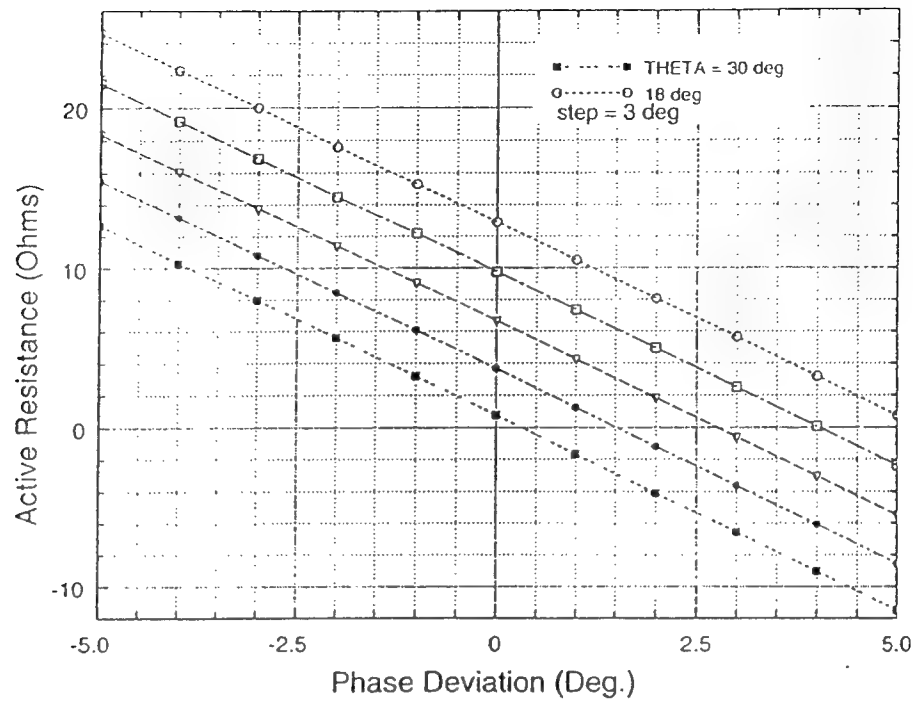


Figure 15.

Coupling from Corner Element (#11) to Parallel Dipoles Along Side

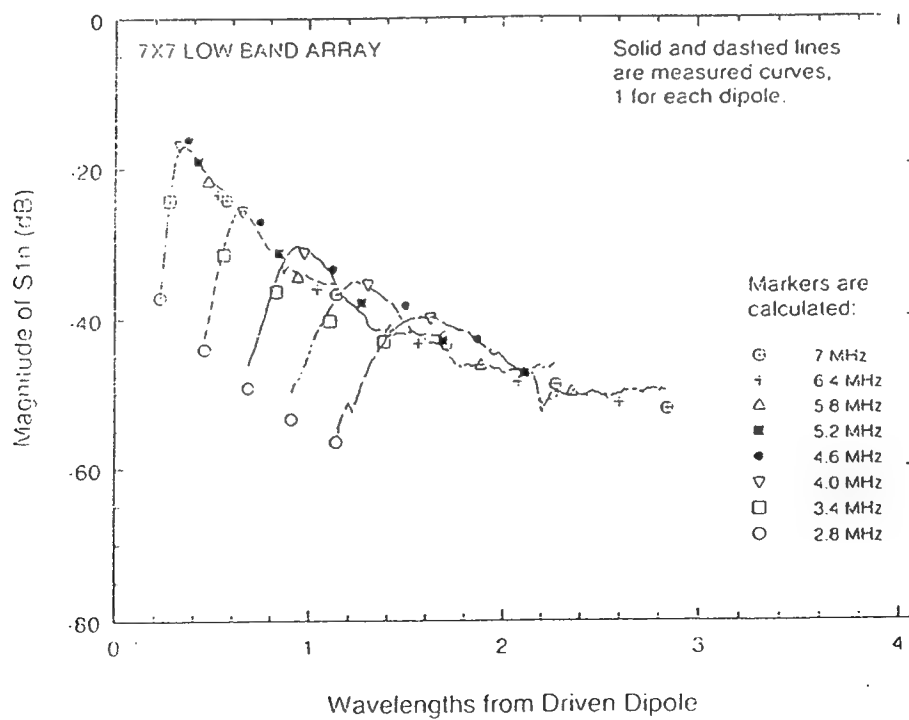


Figure 16.



## Coupling from Corner Element (#11) to Orthogonal Dipoles Along Diagonal

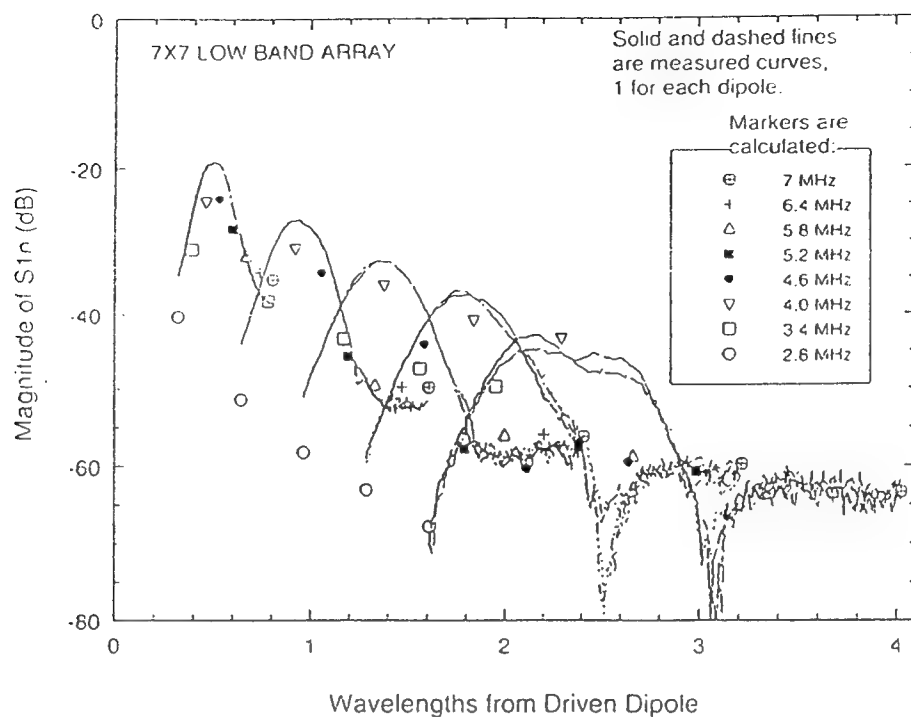


Figure 17.

## Coupling from Corner Element (#11) to Parallel Dipoles Along Side

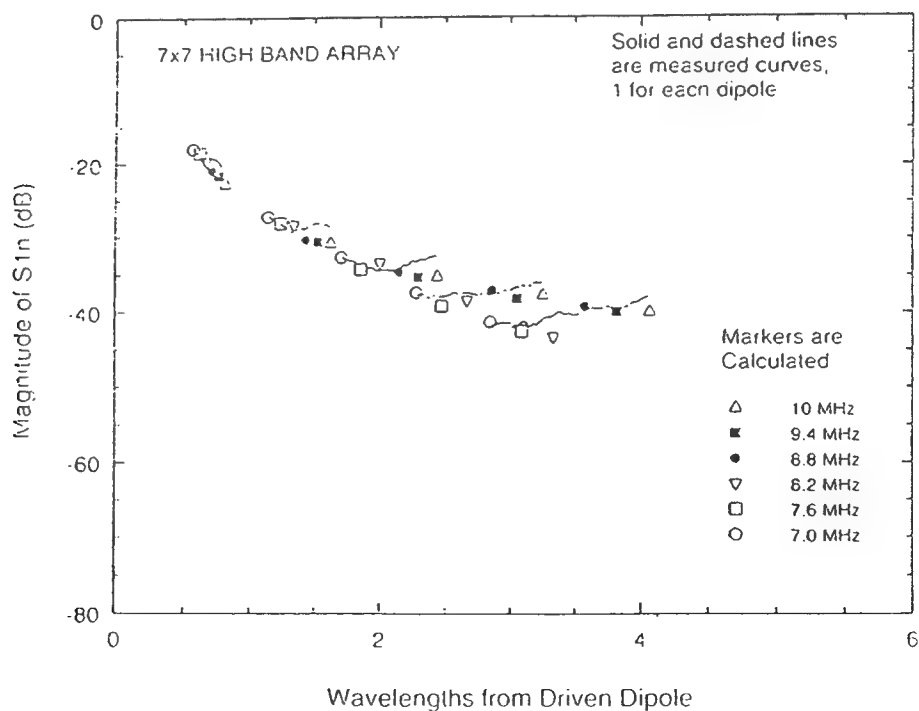


Figure 18.

# Coupling from Corner Element (#11) to Orthogonal Dipoles Along Diagonal

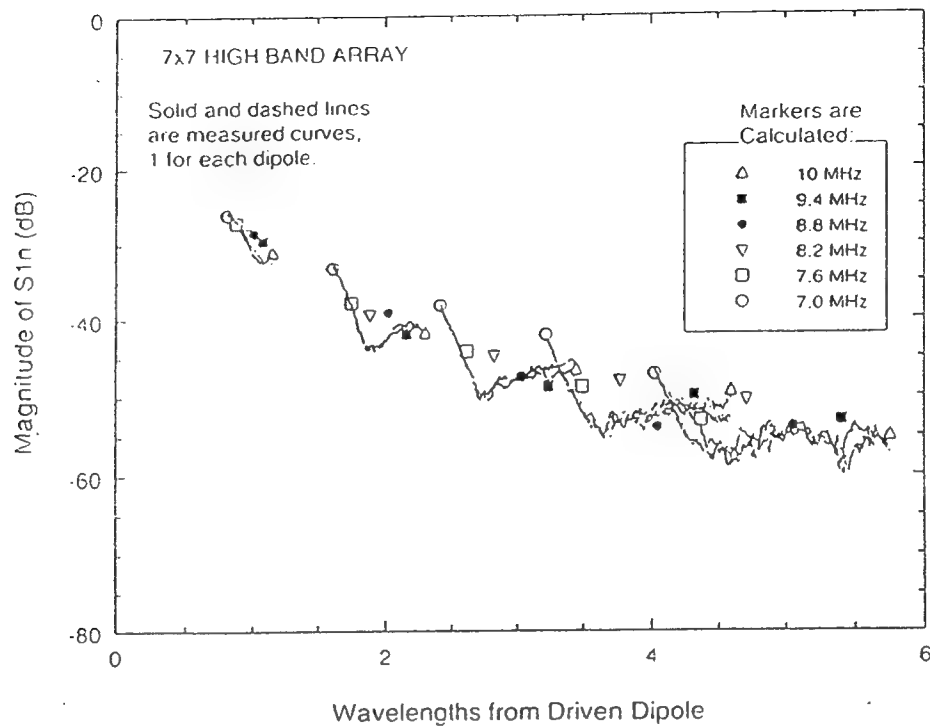


Figure 19.

## 7x7 Low Band Active Impedance for Corner Dipoles 2.8 - 7 MHz

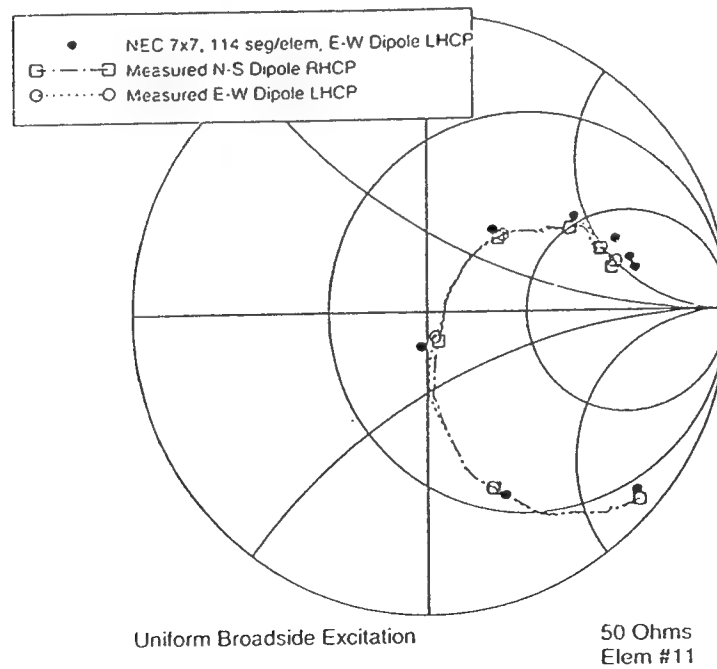


Figure 20.

# 7x7 Low Band Active Impedance for Center Dipoles 2.8 - 7 MHz

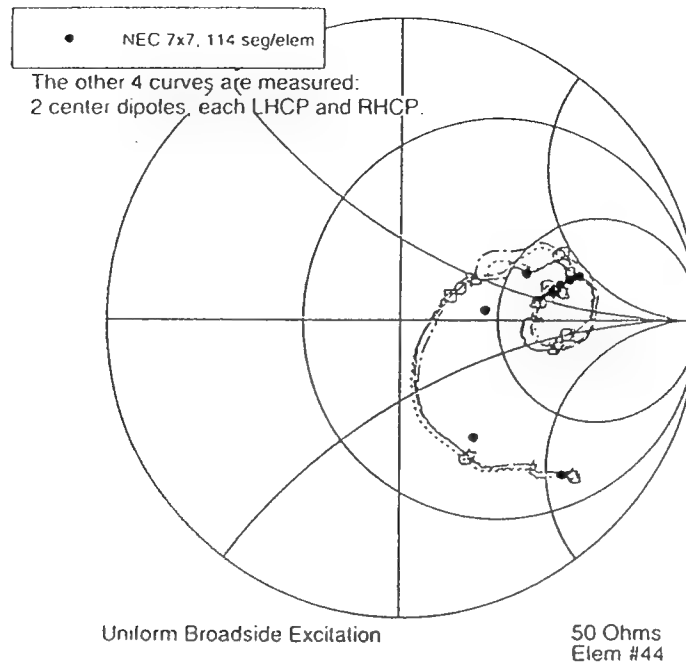


Figure 21.

# 7x7 High Band Active Impedance for Corner Dipoles 7 - 10 MHz

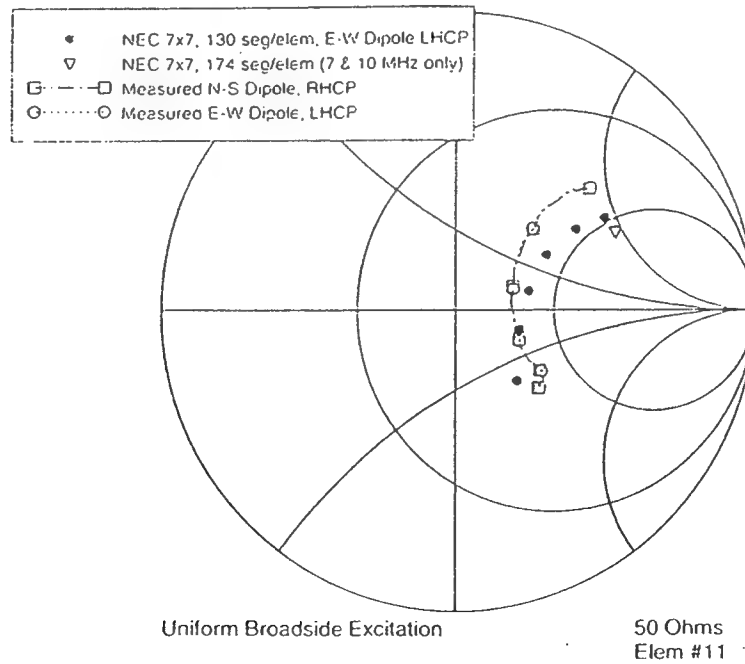


Figure 22.

## 7x7 High Band Active Impedance for Center Dipoles 7 - 10 MHz

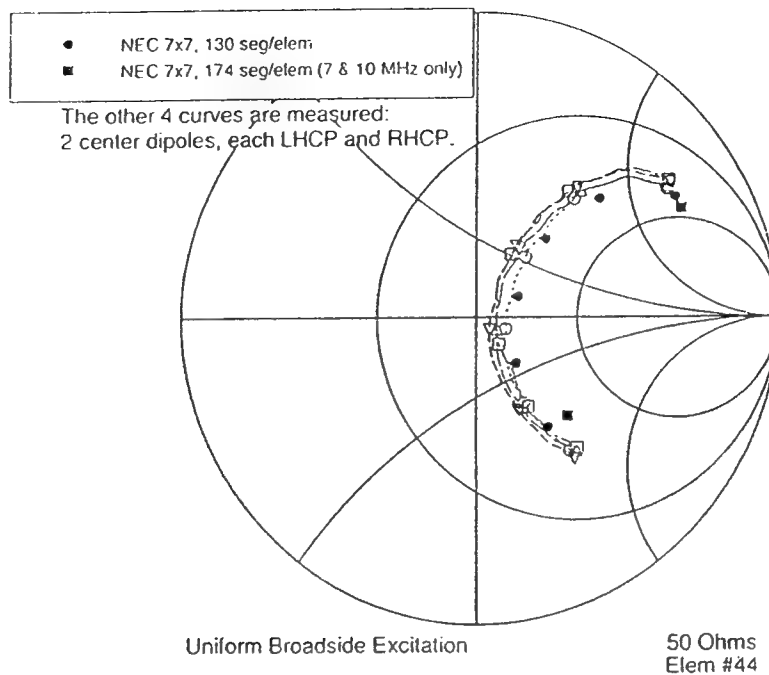


Figure 23.

## 7x7 Low Band Full Scan Active Impedance for Center Dipoles

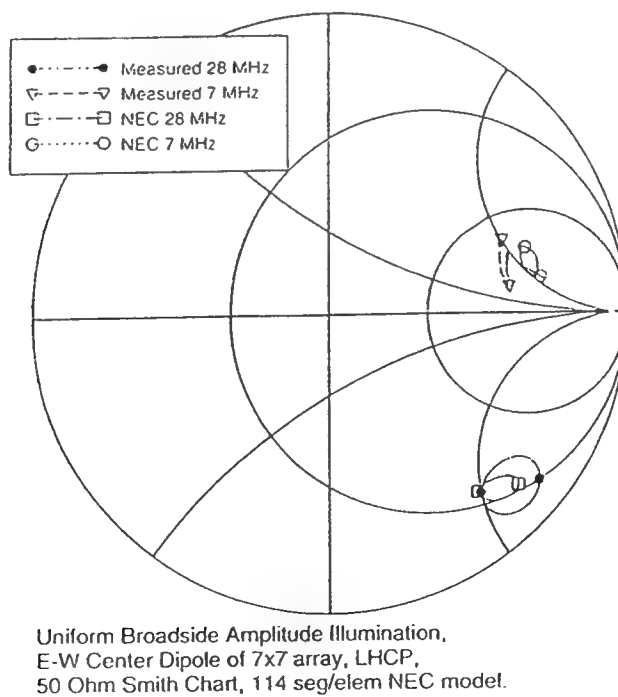
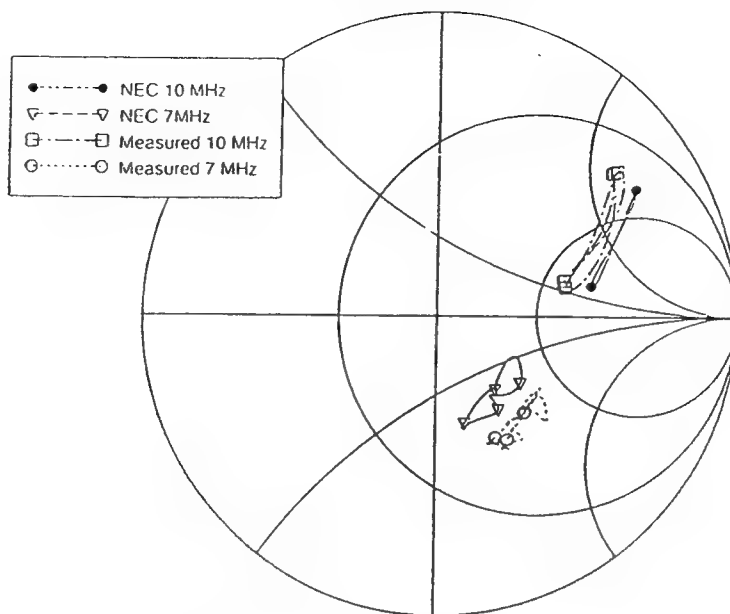


Figure 24.

## 7x7 High Band Full Scan Active Impedance for Center Dipoles



Uniform Broadside Amplitude Illumination,  
E-W Center Dipole of 7x7 array, LHCP,  
50 Ohm Smith Chart, 130 seg/elem NEC model.

Figure 25.

# **Infinite Microstrip Patch Array on a Biased Ferrite Substrate**

Fran Harackiewicz, and

(Electrical Engineering Dept., Southern Illinois University at Carbondale, Carbondale, IL 62901-6603)

Peter Rainville

(Rome Laboratory RL/ERAC, 31 Grenier St., Hanscom AFB, MA 01731-3010)

**Abstract** — An infinite periodic rectangular array of printed square antenna elements is on a biased bulk-ferrite substrate. The magnetic bias field is either normal to the plane of the array or in the plane of the array. As the magnetic bias increases, first the resonant frequency of the array tunes and then a magnetostatic surface wave enters which absorbs energy into the substrate. The magnetostatic surface wave causes a null in the RCS of the array at a frequency that also tunes with bias strength. Full-wave spectral-domain Galerkin numerical and waveguide-simulator experimental approaches are used to analyze the structure.

## **I. INTRODUCTION**

The possibilities of tuning the resonant frequency of a microstrip antenna over a much larger frequency region, of electronically changing the polarization of a microstrip antenna, and of tuning a null in the RCS of a microstrip array have motivated many antenna engineers to study the feasibility of building microstrip antennas on biased ferrite substrates [1]–[12]. For the same reasons, microstrip antennas with biased ferrite cover layers have also been studied [13], [14]. Experimentally, it has been shown that a 40% tuning of impedance bandwidth can be achieved for a single ferrite microstrip antenna (FMA) if a fixed permanent magnet is moved around the patch [1]. Experiments demonstrating the use of bulk ferrites [5] and thin film ferrites [11] to achieve circular polarization from a single probe fed FMA have also been reported. Analytically, the resonances of an FMA have been predicted by cavity models [8], [5], [10] by a spectral-domain immittance approach [6], and by a spectral-domain Galerkin approach for biases normal to the substrate [2] for biases in the plane of the substrate [3]. The surface wave modes of a ferrite slab have been analytically studied in particular for their effect on the scan performance of infinite dipole arrays [12] and infinite patch arrays [7] for general bias directions. In this paper, experimental and theoretical results are given which demonstrate resonance RCS peak tuning and surface-wave RCS null tuning with applied bias for an FMA array. The bias is considered to be in one of three orthogonal directions. Since the array is infinite and periodic the scattered wave is specular and scattering coefficients must be calculated instead of an RCS.

Here, RCS reduction is demonstrated using an in-plane-bias ferrite substrate rather than a normal-bias ferrite substrate. The in-plane-bias is conceivably easier to produce in a monolithic fashion since parallel wires carrying a dc current in the plane of the substrate would produce this bias. Experimental waveguide

simulator results for an infinite FMA array are presented here in addition to analytical results. In the waveguide simulator, incident angle varies with frequency, so the comparison of theory with this experiment actually checks the numerical results for various frequency and angle values. A Green dyad and an impedance matrix for the in-plane-bias case are carefully examined. This examination was found to be useful for speeding up the numerical computer code.

In section II, the theoretical model is explained. The specific geometry of the structure is described and terms referring to bias directions are defined. The tensor expression used for the ferrite's permeability, the full Green dyad including normal components used in modeling the probe load, and the choice of basis functions for the Galerkin model is given. Since the Green dyad expression is cumbersome for the in-plane-bias case, one element of it is plotted for two different bias conditions. This plot helps in visualizing what the program is calculating. Also, a plot of an impedance matrix versus frequency is given for two different bias cases to explain how interpolation techniques may or may not be used to increase computing efficiency.

In section III, the special theoretical considerations for modeling a waveguide simulated infinite FMA array are given. In particular, the theory treats a break in certain symmetries, which are usually required for waveguide simulators. The amount of asymmetry was found not to be that great and the theory still compared well with experiment.

In section IV, the experimental waveguide simulator geometry is described, and measurements of the magnitude of  $S_{11}$  versus frequency are given. This scattering coefficient from the experiment corresponds to the total reflection coefficient of the theory and the two are compared.

In section V, some more numerical results are given showing scattering coefficients as a function of the various parameters including 3 dB line width, bias strength, and frequency. Finally, comments on algorithm speed and efficiency are given. A discussion of the results appears in section VI.

## II. THEORETICAL ANALYSIS

Both full-wave and cavity models were developed and used. The cavity model can predict a range of frequency tuning of the patch and the full-wave model can predict a range of RCS null tuning of the ferrite substrate. Both models start by calculating the elements of the permeability tensor given by:

$$\bar{\mu} = \mu_0 U^T \begin{pmatrix} \mu & -j\kappa & 0 \\ j\kappa & \mu & 0 \\ 0 & 0 & 1 \end{pmatrix} U$$

where

$$U = \begin{pmatrix} \cos\theta_B \cos\phi_B & \cos\theta_B \sin\phi_B & -\sin\theta_B \\ \sin\phi_B & -\cos\phi_B & 0 \\ \sin\theta_B \cos\phi_B & \sin\theta_B \sin\phi_B & \cos\theta_B \end{pmatrix}$$

and

$$\mu = 1 + \frac{\overline{\omega_0} \omega_m}{\overline{\omega_0}^2 - \omega^2} \text{ and } \kappa = \frac{\omega \omega_m}{\overline{\omega_0}^2 - \omega^2}$$

with

$$\omega = 2\pi f$$

$$\omega_m = \gamma 4\pi M$$

$$\omega_0 = \gamma H_0$$

$$\overline{\omega_0} = \omega_0 + j/T$$

$$T = 2/\gamma \Delta H$$

where  $f$  is the frequency of the rf field,  $H_0$  is the internal applied dc bias,  $4\pi M$  is the internal dc magnetization that is greater than the applied bias,  $\Delta H$  is the 3dB line width that is usually proportional to frequency and  $\gamma$  is the gyromagnetic ratio, and the angles  $\theta_B$  and  $\phi_B$  specify the direction of the internal bias. Here, we consider only the normal (N) bias case  $\theta_B = 0^\circ$  and the two in-plane bias cases  $\theta_B = 90^\circ$  one with the applied bias field normal to the direction of the rf electric field (IX) and the other with the applied bias field parallel to the direction of the rf electric field (IL).

Assuming the ferrite slab is infinite in the x and y directions, the relation between the internal dc bias and the external dc bias is

$$H_z^{\text{internal}} = H_z^{\text{external}} - 4\pi M$$

and

$$H_x^{\text{internal}} = H_x^{\text{external}},$$

$$H_y^{\text{internal}} = H_y^{\text{external}}.$$

The relation between  $4\pi M$  and H internal is given by a hysteresis curve specific to each ferrite material.

Once the Polder tensor elements are known, either the spectral-domain dyadic Green's function for a grounded slab of a given thickness can be calculated or an effective permeability not dependent on thickness can be calculated. The frequency-dependent, scalar, effective permeability can be used in a cavity model or in a full-wave model.

#### A. Cavity Model



For the cavity model analysis an effective relative permeability is calculated as either

$$\mu_{eff} = (\mu^2 - \kappa^2) / \mu \text{ or } \mu_{eff} = 1$$

The first being for IL and N bias and the second for IX bias.

### B. Spectral-domain Green dyad

For the full-wave analysis the Green dyad is calculated from the permeability tensor and the thickness of the substrate. For the normal bias case the Green dyad can be expressed as in [9]. For the in-plane bias cases the Green dyad can be expressed as:

$$\overline{\overline{G}}^{EJ}(k_x, k_y) = \begin{pmatrix} G_{xx}^{EJ} & G_{xy}^{EJ} \\ G_{yx}^{EJ} & G_{yy}^{EJ} \end{pmatrix} = \overline{\overline{Z}}_T (\overline{\overline{T}}_J + \overline{\overline{G}}_0^{JE} \overline{\overline{Z}}_T)^{-1}$$

and

$$G_{z(x)z(y)}^{VJ} = \frac{Z_0 k_{(x)(y)}}{k_0 \epsilon_r} \int_0^d \overline{\overline{T}}_J(z) dz \cdot \overline{\overline{Z}}_T^{-1} \overline{\overline{G}}^{EJ}(k_x, k_y)$$

and by the modified reciprocity theorem

$$G_{z(x)z(y)}^{EJ}(k_x, k_y, \kappa) = G_{z(x)z(y)}^{VJ}(-k_x, -k_y, -\kappa)$$

where the matrices  $\overline{\overline{Z}}_T$ ,  $\overline{\overline{T}}_J$ , and  $\overline{\overline{G}}_0^{JE}$  are as in [15] for the in-plane bias case and are taken to be evaluated at  $z=d$  unless otherwise specified.

The Green dyad elements in the spectral domain for biased ferrites behave quite differently than those elements in the spectral domain for dielectrics or for unmagnetized ferrites. Since, the dyad elements times Fourier transformed currents must be integrated (for the single patch) or summed (for the periodic and infinite array of patches) in the spectral domain it is useful to look at a plot of the magnitude of these elements (see Fig. 1). Notice that the usual TM surface wave mode for thin grounded dielectric substrates shows up in all the plots as a crown of radius  $\beta_{sw}$  that lies between one and  $\sqrt{\epsilon_r}$ . Notice also that the magnitudes deform considerably as a bias field is applied. This deformation which looks like a curved peak is due to the backward volume waves [12] which are guided modes that give rise to scan blindness when the array is transmitting. However, if the array is not actively transmitting, these modes also work to reduce the reflection from an incoming plane wave [3].

### C. Galerkin Method for Infinite Array Excited by a Plane Wave

The spectral-domain Galerkin method was used to solve the boundary condition that the total tangential electric field on the patch is zero. The expanded and weighted boundary equation enforced on the patch is

$$[V^{inc}] = [Z][I] - I_L[V^{pt}]$$

where  $[I]$  is the unknown column vector,  $[V^{inc}]$  includes the incident plane wave and the plane wave reflected from the grounded biased ferrite slab,  $[V^{pt}]$  includes the field due to the probe,  $[Z]$  is the impedance matrix for the field due to the patch current, and  $I_L$  is the current in the load calculated as the scattered field voltage at the probe divided by the load impedance. The experiments were done with no probe load.

The expansion modes for the current induced on the patch are entire domain trigonometric modes and so are the testing modes. The impedance matrix varies more rapidly with frequency for a biased case than it does for an unmagnetized or dielectric slab. This means that to use interpolation of the impedance matrix elements as in [N] requires more finely placed sample points than usual, but still interpolation can be used to speed the computation.

### III. WAVEGUIDE SIMULATOR THEORY

Waveguide simulators can be used to measure the reflection coefficient of a large periodic structure if certain assumptions listed in [16] are met. There is one assumption that is not rigorously true when a grounded biased ferrite is used to terminate the waveguide. The reflection coefficients for the two simulated plane waves are not exactly the same as would be measured for a single plane wave incident on the infinite periodic structure from free space. This asymmetry results from the biased ferrite itself being asymmetric [2]. To determine the degree of asymmetry consider the fields involved.

The total field in the problem of a plane wave reflection from an infinite array of patches can be broken into three parts:  $E^i$  the plane wave incident when no substrate or patches are present,  $E^r$  the plane wave reflected due to the grounded slab with no patches, and  $E^s$  the plane wave(s) scattered due to the induced current on the patches. If the patch spacing is such that only one wave is scattered, then the total reflection coefficient matrix

$$\bar{R}^{TOT} = \begin{pmatrix} R_{\theta\theta}^{tot} & R_{\theta\phi}^{tot} \\ R_{\phi\theta}^{tot} & R_{\phi\phi}^{tot} \end{pmatrix}$$

can be written as the sum of the reflection coefficient matrix due to the grounded substrate alone

$$\bar{R} = \begin{pmatrix} R_{\theta\theta} & R_{\theta\phi} \\ R_{\phi\theta} & R_{\phi\phi} \end{pmatrix}$$

plus the scattering coefficient matrix due to the patch currents

$$\bar{\bar{S}} = \begin{pmatrix} S_{\theta\theta} & S_{\theta\phi} \\ S_{\phi\theta} & S_{\phi\phi} \end{pmatrix}.$$

Also a measurement of  $S_{11}$  when the waveguide is terminated in a grounded card without patches is the same as the reflection coefficient of a plane wave from an infinite grounded slab if certain symmetry requirements are met. For the case of the unmagnetized ferrite or an isotropic dielectric slab,

$$R_{\phi\phi}(\phi_0) = R_{\phi\phi}(\phi_0 + \pi)$$

and

$$R_{\theta\phi} = R_{\phi\theta} = 0$$

so the symmetry requirement is easily met and a measurement of  $S_{11}$  is the same as  $R_{\phi\phi}(\phi_0)$  with

$$\theta_0 = \arcsin(\lambda/2b)$$

for the dominant mode of the waveguide where  $b$  is the longest dimension of the guide's cross section.

For the IX biased ferrite card in a waveguide simulator (see Fig. 2), the symmetry relation that does exist is

$$R_{\phi\phi}(\phi_0) = R_{\phi\phi}(\phi_0 + \pi)$$

and

$$R_{\theta\phi}(\phi_0) = -R_{\phi\theta}(\phi_0 + \pi) \neq 0$$

This causes the reflected wave to be

$$\begin{aligned} \bar{E}' = & -\hat{x}R_{\phi\phi} 2j \sin(\pi y/b) \exp(-jk_0 \cos\theta_0) \\ & + \hat{y}R_{\theta\phi} 2 \cos\theta_0 \cos(\pi y/b) \exp(-jk_0 \cos\theta_0) \\ & + \hat{z}R_{\phi\theta} 2 \sin\theta_0 \sin(\pi y/b) \exp(-jk_0 \cos\theta_0) \end{aligned}$$

where the first term is a  $TE_{10}$  waveguide mode but the last two term are not zero at the waveguide walls  $x = 0, a$  and are therefore not waveguide modes. This violation of the boundary and symmetry condition is not severe since in most cases of interest

$$|R_{\phi\phi}| = |2G_{xx}(0, k_0 \sin\theta_0) + 1/\cos\theta_0| \approx 1$$

and

$$|R_{\phi\phi}| = |2G_{xx}(0, k_0 \sin\theta_0)| \approx 0.01.$$

For the IL biased ferrite card in a waveguide simulator, there are no symmetry relations that exist between  $\bar{\bar{R}}(\phi_0)$  and  $\bar{\bar{R}}(\phi_0 + \pi)$ . For the cases of interest this symmetry break is not too large as  $|R_{\phi\phi}(\phi_0)|$  is within 2% of  $|R_{\phi\phi}(\phi_0 + \pi)|$  and  $|R_{\theta\phi}(\phi_0)|$  and  $|R_{\phi\theta}(\phi_0 + \pi)|$  are both less than 0.01. Thus, despite the break in symmetry required to use a waveguide simulator, the theory calculation of

$$\left( R_{\uparrow\uparrow}(\phi_0) + R_{\uparrow\uparrow}(\phi_0 + \pi) \right)/2 \text{ and of } \left( R_{\uparrow\uparrow}^{tot}(\phi_0) + R_{\uparrow\uparrow}^{tot}(\phi_0 + \pi) \right)/2$$

are expected to compare well with the measurement of  $S_{11}$  for a waveguide simulator without patches on a ferrite termination and with patches on a ferrite termination respectively.

#### IV. WAVEGUIDE SIMULATOR EXPERIMENT

The waveguide simulator experiments were done using a geometry as shown in Fig. 2. First  $S_{11}$  was measured for a waveguide terminated in a ferrite slab coated with a metal short. This measurement corresponds with the  $\phi\phi$  component of the reflection coefficient described above. Then a card of patches on a grounded ferrite substrate was used to terminate the waveguide, and  $S_{11}$  was measured again. This second measurement compares with the  $\phi\phi$  component of the total reflection coefficient described above. The dc magnetic bias field was applied by an electromagnet with pole faces outside of the waveguide. Since the pole faces were much larger than the ferrite card, the applied bias was assumed uniform throughout the ferrite. The bias field was aligned so as to apply a N, IX, or IL bias to the ferrite. Results for the magnitude of  $S_{11}$  versus frequency for various bias values is shown in Fig. 3. The experiment uses a CBAND waveguide that has a dominant mode cutoff at 3.95. Not much tuning occurred for the IX and N bias directions. For IL biasing, the resonance of the patch tuned and then an absorbing mode of the ferrite appeared and tuned. (Fig. 4)

#### V. NUMERICAL RESULTS

As shown in section I a ferrite substrate is characterized by the parameters of thickness  $d$ , gyromagnetic ratio  $\gamma$ , a hysteresis curve relating  $4\pi M$  to  $H_0$ , the dielectric constant  $\epsilon_r$ , and the loss terms  $\Delta H$  and  $\tan \delta$ . All of these parameters are fixed once a particular substrate is chosen; however, a wide range of possible ferrites exist with a variety of saturation magnetizations  $4\pi M_s$  and 3dB line widths  $\Delta H$ . The effect of varying  $\Delta H$  is shown in Fig. 5.

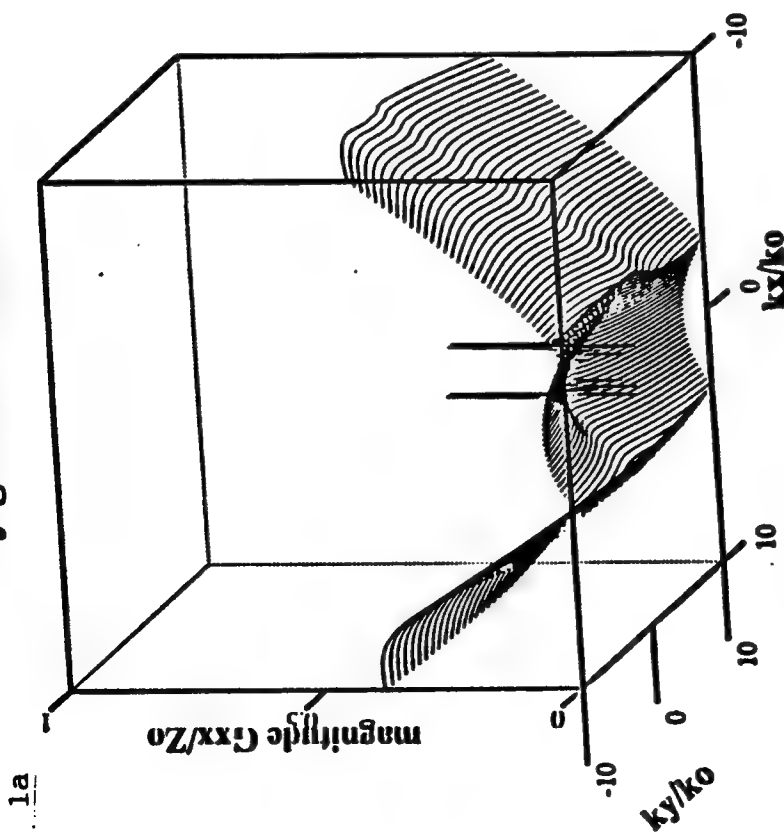
#### VI. CONCLUSION

An infinite periodic rectangular array of printed square antenna elements on a biased bulk-ferrite substrate was studied with a waveguide simulator. The magnetic bias field was either normal to the plane of the array or in the plane of the array. For IL bias, as the magnetic bias increases, first the resonant frequency of the array tunes and then a magnetostatic surface wave enters which absorbs energy into the substrate. The magnetostatic surface wave causes a null in the RCS of the array at a frequency that also tunes with bias strength. Full-wave spectral-domain Galerkin numerical technique can predict these frequencies as can the cavity model to a certain extent. Some differences between experiment and theory are due to the phase calibration of the experiment not being done fully at the ferrite card plane. Others are due to all the defining parameters of the ferrite such as internal bias not being completely known.

## REFERENCES

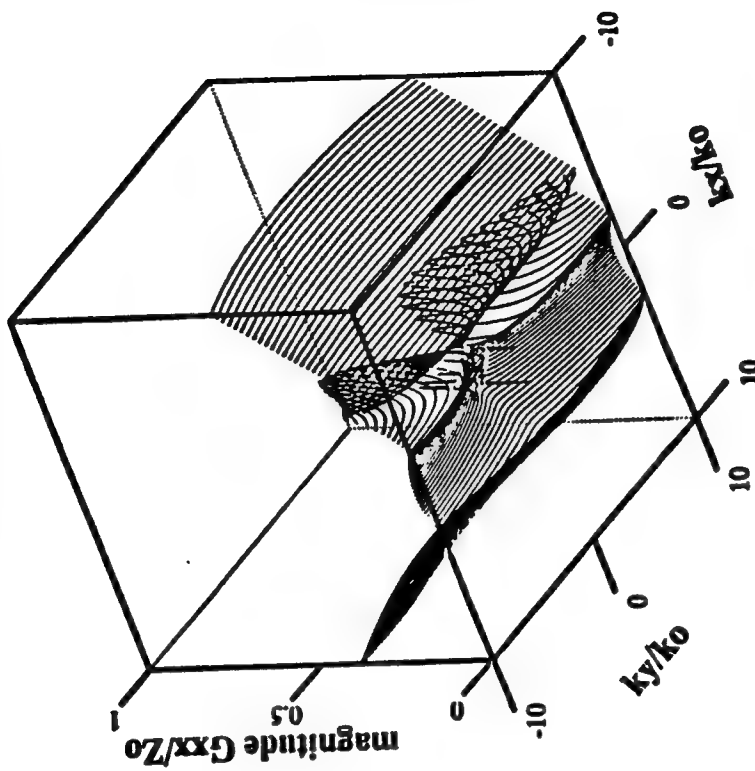
- [1] D. Pozar and V. Sanchez, "Magnetic tuning of a microstrip antenna on a ferrite substrate," *Electron. Lett.*, vol. 24, pp. 729-731, June 9, 1988.
- [2] D. Pozar, "Radar cross section of a microstrip antenna on a normally biased ferrite substrate," *Electron. Lett.*, vol. 25, pp. 1079-1080, August 3, 1989.
- [3] F. Harackiewicz, "Plane wave scattering from infinite microstrip arrays on ferrite substrates," *1990 AP-S Symposium Digest*, pp. 417-420.
- [4] H-Y. Yang, J. A. Castaneda and N. G. Alexopoulos, "Surface wave modes of printed circuits on ferrite substrates," *IEEE Trans. Microwave Theory Tech.*, vol. 40, pp. 613-621, April 1992.
- [5] J. S. Roy, P. Vaudon, A. Reineix, F. Jecko and B. Jecko, "Axially magnetized circular ferrite microstrip antenna," *1992 IEEE-APS International Symposium Digest*, pp. 2212-2215.
- [6] Z. Cai and J. Bornemann, "Spectral-domain analysis of patch radiators on lossy ferrite substrates," *9th Annual Review of Progress in Applied Computational Electromagnetics*, pp. 821-827, March 1993.
- [7] H-Y Yang and J. A. Castaneda, "Infinite phased arrays of microstrip antennas on generalized anisotropic substrates," *Electromagnetics*, vol. 11, pp. 107-124, 1991.
- [8] D. Pozar, "RCS reduction for a microstrip antenna using a normally biased ferrite substrate," *IEEE Microwave Guided Wave Lett.*, vol. 2, pp. 196-198, May 1992.
- [9] D. Pozar, "Radiation and Scattering Characteristics of Microstrip Antennas on Normally Biased Ferrite Substrates," *IEEE Trans. Antennas Propagat.*, vol. 40, pp. 1084-1092, Sept. 1992.
- [10] H. How, P. Rainville, F. Harackiewicz and C. Vittoria, "Radiation frequencies of ferrite patch antennas," *Electron. Lett.*, vol. 28, p. 1405-1406, July 16, 1992.
- [11] P. J. Rainville and F. J. Harackiewicz, "Magnetic tuning of a microstrip patch antenna fabricated on a ferrite film," *IEEE Microwave Guided Wave Lett.*, vol. 2, pp. 483-485, Dec. 1992.
- [12] N. E. Buris, T. B. Funk and R. S. Silverstein, "Dipole Arrays Printed on Ferrite Substrates," *IEEE Trans. Antennas Propagat.*, vol. 41, pp. 165-176, Feb. 1993.
- [13] H-Y. Yang, J. A. Castaneda, and N. G. Alexopoulos, "Multifunctional and low RCS nonreciprocal microstrip antennas," *Electromagnetics*, vol. 12, pp. 17-31, 1992.
- [14] D. Pozar, "A Magnetically Switchable Ferrite Radome for Printed Antennas," *IEEE Microwave Guided Wave Lett.*, vol. 3, pp. 67-69, Mar. 1993.
- [15] E. B. El-Sharawy and R. W. Jackson, "Coplanar Waveguide and Slt-Line on Magnetic Substrates: Analysis and Experiment," *IEEE Trans. on Microwave Theory and Techniques*, vol. 36, no. 6, pp. 1071-1079, June 1974.
- [16] C. C. Liu, J. Shmoys, A. Hessel, J. D. Hanfling, and J. M. Usoff, "Plane Wave reflection from Microstrip-Patch Arrays — Theory and Experiment," *IEEE Trans. Antennas Propagat.*, vol. 33, pp. 426-435, Apr. 1993.

yig ferrite  $f=5\text{GHz}$



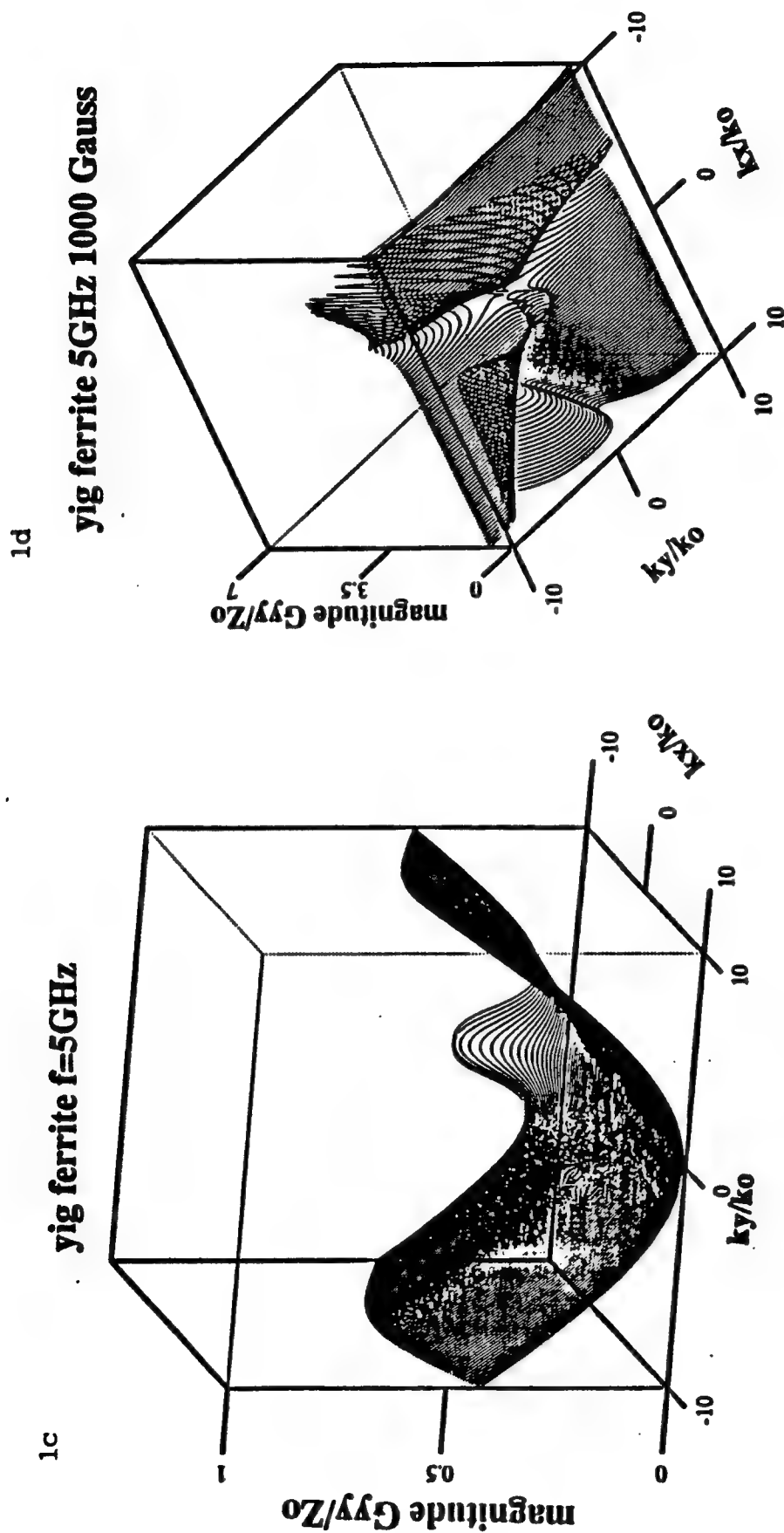
Magnitude of  $G_{xx}$  for 5GHz and  $H_0 = 0$  Gauss

1b yig ferrite 5GHz 1000 Gauss



Magnitude of  $G_{xx}$  for 5GHz and  $H_0 = 1000\text{G}$  (Gauss)

Figure 1 - Normalized magnitude of a Green dyad element  $G^{EJ}$  for IL biased yig at 5ghz vs. the spectral variables  $k_x$  and  $k_y$ . a)  $xx$  element for latched case; b)  $xx$  element for 1000 G internal bias; c)  $yy$  element for latched case; d)  $yy$  element for 1000 G internal bias.



Magnitude of  $G_{yy}$  for 5GHz and  $H_0 = 0$  Gauss

Magnitude of  $G_{yy}$  for 5GHz and  $H_0 = 1000j$  (Gauss)

Figure 1 - Normalized magnitude of a Green dyad element  $G_{ij}^E$  for IL biased yig at 5ghz vs. the spectral variables  $k_x$  and  $k_y$ . a)  $xx$  element for latched case; b)  $xx$  element for 1000 G internal bias; c)  $yy$  element for latched case; d)  $yy$  element for 1000 G internal bias.

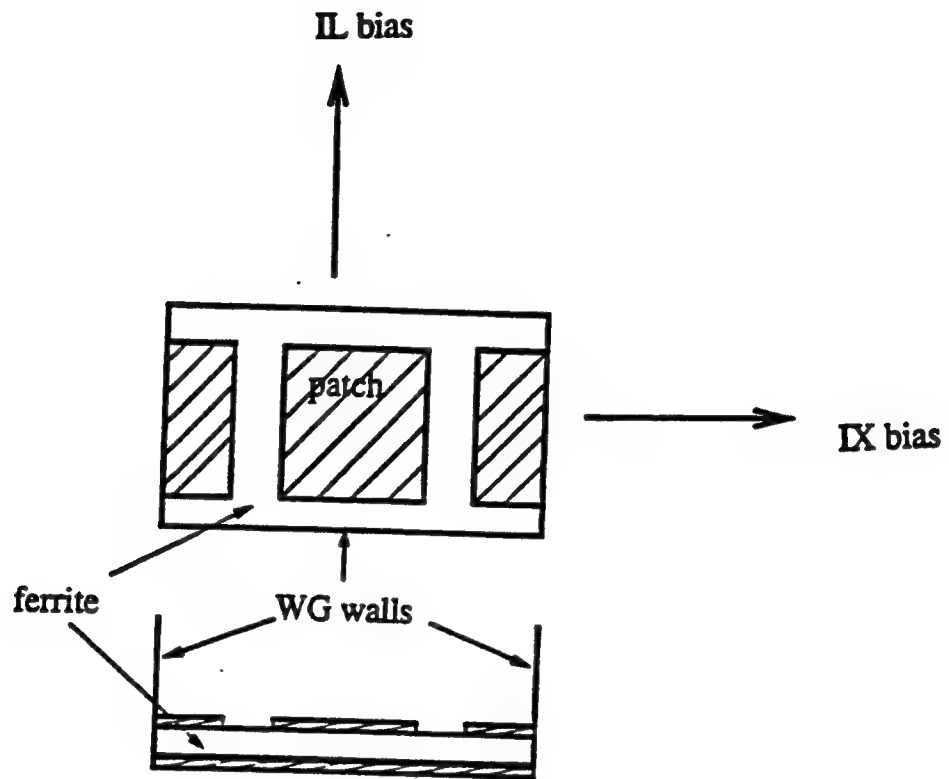


Figure 2 - waveguide simulator geometry and three orthogonal bias directions defined.



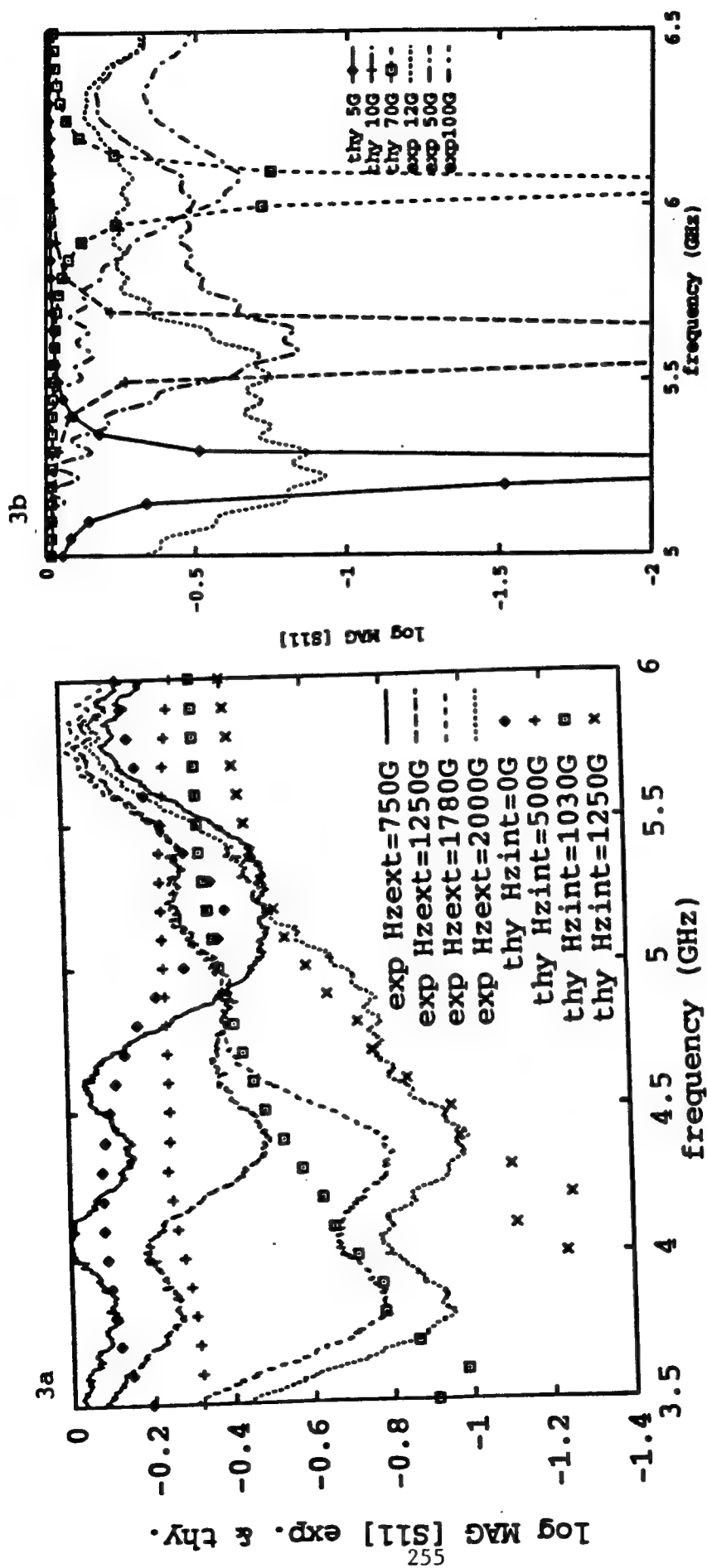


Figure 3 - Magnitude of S11 vs. f for waveguide simulator experiment and theory with 1mm thick yig substrate a) for 10.5mm-square patches with N bias; b) for 10.5mm square patch with IL bias; c) for no patches with IL bias.

3c

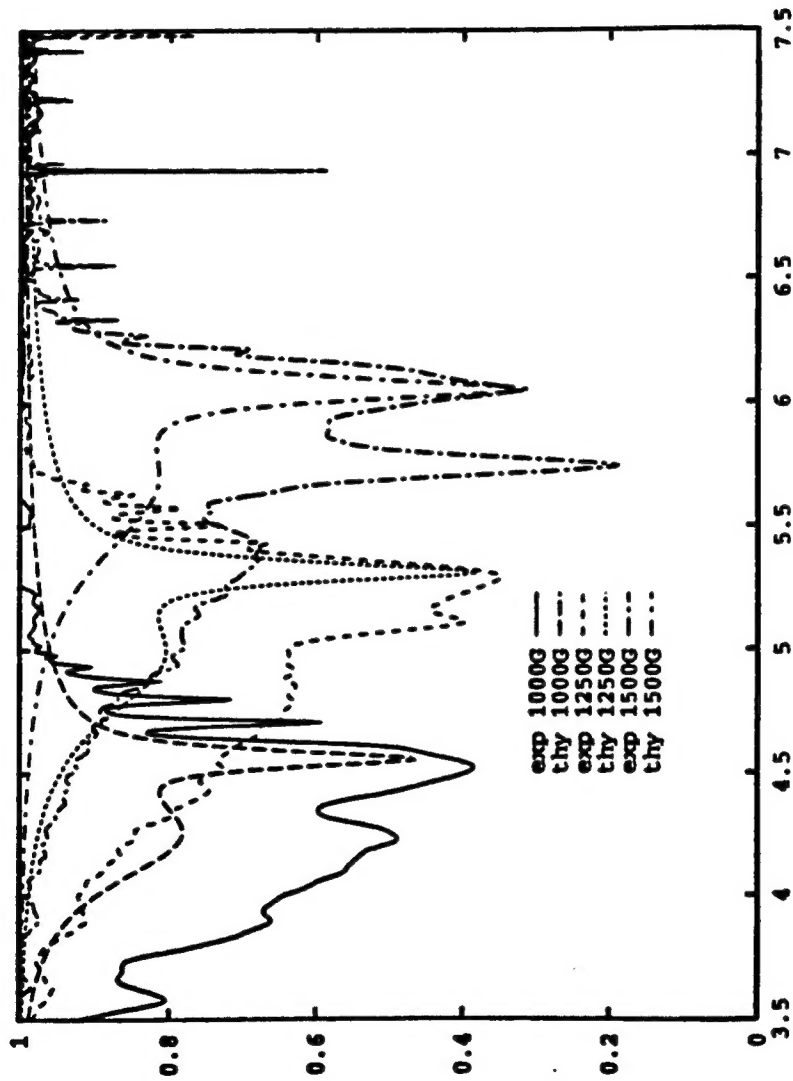


Figure 3 - Magnitude of  $S_{11}$  vs.  $f$  for waveguide simulator experiment and theory with 1mm thick yig substrate a) for 10.5mm-square patches with N bias; b) for 10.5mm square patch with IL bias; c) for no patches with IL bias.

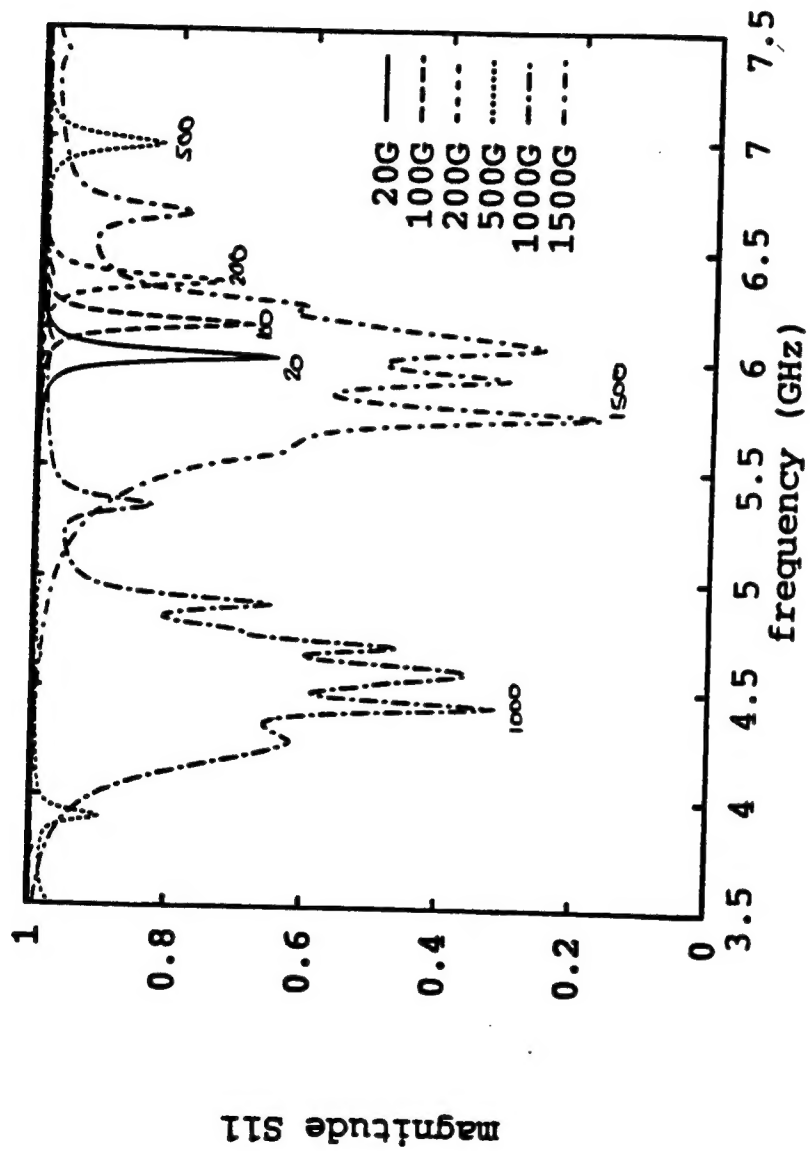


Figure 4 - Theory for magnitude of  $S_{11}$  vs.  $f$  for waveguide simulator with 1mm thick yig and no patches.

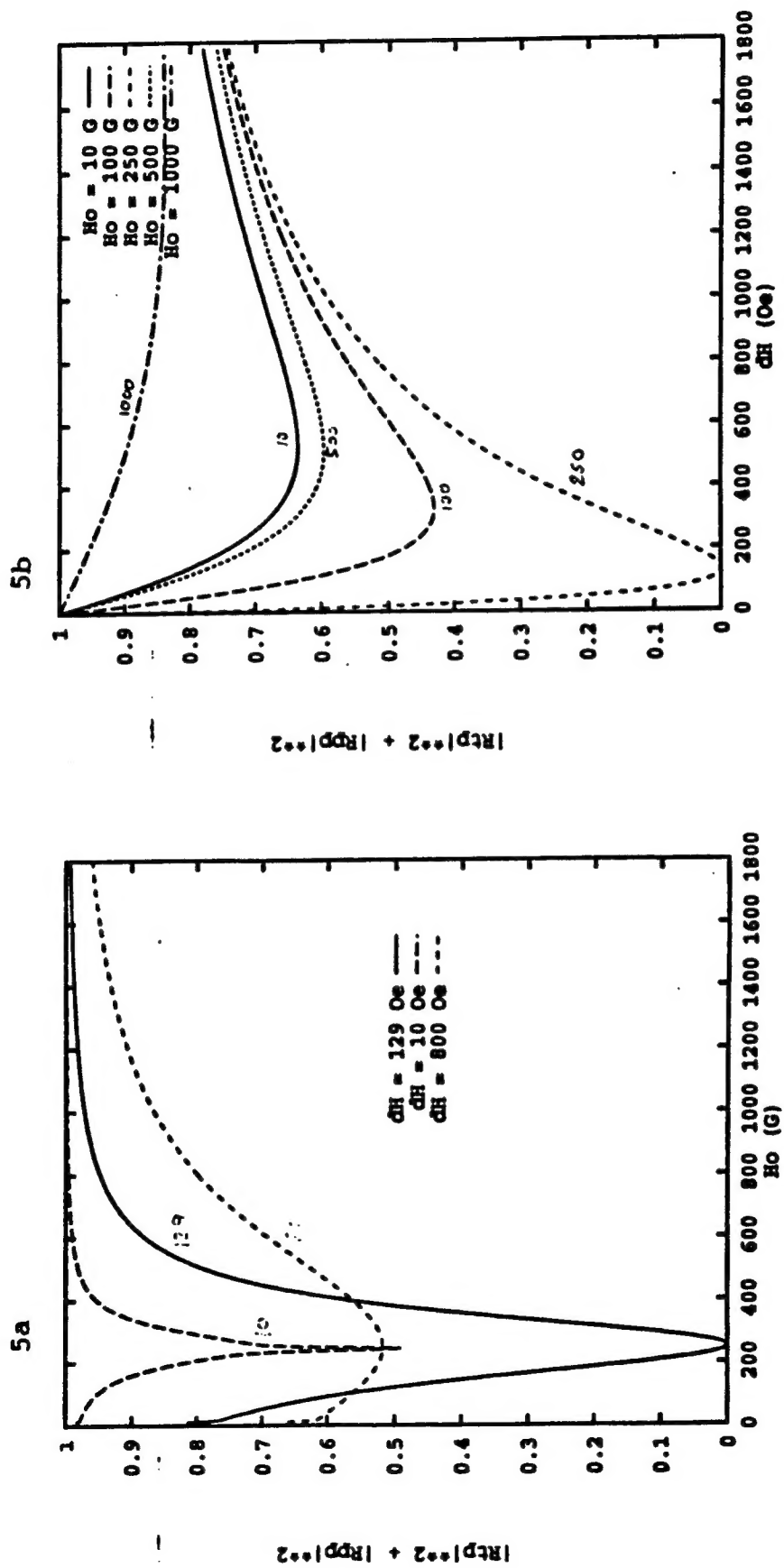


Figure 5 -  $|R_{cp}|^{+2} + |R_{cp}|^{-2}$  for a plane wave normally incident on an IL biased yig ferrite  
 a) vs.  $H_0$  (G) the internal bias; b) vs.  $\Delta H$  (Oe) the 3dB line width.

**MISSION  
OF  
ROME LABORATORY**

*Rome Laboratory plans and executes an interdisciplinary program in research, development, test, and technology transition in support of Air Force Command, Control, Communications and Intelligence (C<sup>3</sup>I) activities for all Air Force platforms. It also executes selected acquisition programs in several areas of expertise. Technical and engineering support within areas of competence is provided to ESD Program Offices (POs) and other ESD elements to perform effective acquisition of C<sup>3</sup>I systems. In addition, Rome Laboratory's technology supports other AFSC Product Divisions, the Air Force user community, and other DOD and non-DOD agencies. Rome Laboratory maintains technical competence and research programs in areas including, but not limited to, communications, command and control, battle management, intelligence information processing, computational sciences and software producibility, wide area surveillance/sensors, signal processing, solid state sciences, photonics, electromagnetic technology, superconductivity, and electronic reliability/maintainability and testability.*